The densest stellar systems in the Universe : the nuclear stellar disc

Niels Nieuwmunster

UNIVERSITÉ CÔTE D'AZUR | ÉCOLE DOCTORALE SCIENCES FONDAMENTALE ET APPLIQUÉES

LUND UNIVERSITY

Les systèmes les plus denses de l'Univers : le disque nucléaire

Niels NIEUWMUNSTER

Laboratoire J-L. Lagrange - Observatoire de la Côte d'Azur

Présentée en vue de l'obtention du grade de docteur en Sciences de la Planète et de l'Univers **d'**Université Côte d'Azur

Dirigée par : Mathias Schultheis / Nils Ryde

Soutenue le : 27 septembre 2024

Devant le jury, composé de :
Marie-Anne Bizouard, Professeur, OCA
Livia Origlia, Professeur, INAF/Bologna
Patricia Sanchez-Blazquez, Professeur, Universidad Complutense de Madrid
Mattia Sormani, Professeur assistant, University of Insubria/Como
Paola di Matteo, Astronome, GEPI Observatoire de Paris
David Hobbs, Professeur, Lund University

UNIVERSITÉ CÔTE D'AZUR | ÉCOLE DOCTORALE SCIENCES FONDAMENTALE ET APPLIQUÉES

LUND UNIVERSITY

The densest stellar systems in the Universe: the nuclear stellar disc

Niels NIEUWMUNSTER

Lund Observatory - Department of Physics - Lund University

Presented with a view to obtaining the degree of Doctor in Astronomy and Astrophysics **from** Lund University

Directed by : Mathias Schultheis / Nils Ryde

Defended on : September 27, 2024

In front of the jury, composed of :
Marie-Anne Bizouard, Professor, OCA
Livia Origlia, Professor, INAF/Bologna
Patricia Sanchez-Blazquez, Professor, Universidad Complutense de Madrid
Mattia Sormani, Assistant professor, University of Insubria/Como
Paola di Matteo, Astronomer, GEPI Observatoire de Paris
David Hobbs, Professor, Lund University

Les systèmes les plus denses de l'Univers : le disque nucléaire

Présidente du jury
Marie-Anne Bizouard, Professeur, OCA

Rapporteuses
Livia Origlia, Professeur, INAF/Bologna

Patricia Sanchez-Blazquez, Professeur, Universidad Complutense de Madrid

Examinateurs
Mattia Sormani, Professeur assistant, University of Insubria/Como

Paola di Matteo, Astronome, GEPI Observatoire de Paris

David Hobbs, Professeur, Lund University

Directeurs de thèse
Mathias Schultheis, Astronome, Observatoire de la Côte d'Azur

Nils Ryde, Professeur, Lund University

Résumé

Comprendre la formation et l'évolution des galaxies, et en particulier de leurs centres galactiques, est l'une des questions les plus intrigantes de l'astrophysique moderne. De nombreuses galaxies spirales comme la Voie lactée présentent en leur centre un disque nucléaire (NSD). Celui de la Voie lactée est, avec l'amas central et le trou noir super massif central, l'une des principales composantes internes et l'un des meilleurs laboratoires locaux disponibles pour étudier l'évolution des galaxies. En raison de la forte extinction, de l'importante densité d'étoiles et de la superposition de multiples structures le long de la ligne de visée, les études des régions internes de la Voie Lactée sont cependant très difficiles et très peu ont été réalisées jusqu'à présent. Grâce à des données récentes, cette thèse vise à dévoiler les processus physiques qui ont conduit à la formation du NSD et ses liens avec les autres composantes de la Voie Lactée. Ce manuscrit est divisé en trois parties correspondant aux différentes méthodologies utilisées.

Pour la première partie, grâce à la spectroscopie en proche infrarouge à haute résolution, j'ai effectué une analyse chimique d'étoiles géantes froides situées dans le bulbe Galactique interne. J'ai mesuré les abondances détaillées des éléments alpha : silicium, magnésium et calcium, en utilisant des données théoriques récentes et précises telles qu'une liste de raies mise à jour, des paramètres d'élargissement et les corrections de l'équilibre thermodynamique non local. Sur la base des abondances dérivées, un modèle d'évolution chimique adapté au bulbe Galactique interne a été construit. J'ai également utilisé l'analyse spectrale pour mesurer automatiquement le rapport isotopique du carbone dans les étoiles géantes du voisinage solaire afin d'établir une relation avec la masse stellaire astérosismique. Cela permettrait d'estimer les âges stellaires dans des régions éloignées telles que le NSD.

Dans la deuxième partie de cette thèse, j'ai étudié la dynamique des étoiles observées dans le NSD de la Voie Lactée en faisant une analyse orbitale. J'ai calculé les orbites dans un potentiel gravitationnel non-axisymétrique tenant compte des effets de la barre Galactique et j'ai dérivé leurs fréquences fondamentales. Cela m'a permis d'identifier les résonances orbitales et les différentes familles d'orbites qui peuvent être présentes dans le NSD.

En plus des observations, les simulations sont d'un grand intérêt pour comprendre

les processus physiques qui ont formé les régions internes de la Galaxie. Dans cette dernière partie, j'ai utilisé une simulation hydrodynamique à N-corps d'une galaxie isolée semblable à la Voie Lactée afin d'étudier la formation de son NSD. Cette simulation a permis de faire une première comparaison entre les observations et les simulations en termes de chimie et de dynamique.

Mots clés: Etoiles: abondances, phases évoluées - Galaxie: dynamique, bulbe, centre, structure.

Abstract

Understanding the formation and evolution of galaxies and in particular their galactic centres is one of the most intriguing questions in modern astrophysics. Many spiral galaxies like the Milky Way feature a nuclear stellar disc (NSD) in their centre. The Milky Way's NSD is, together with the nuclear star cluster and the central super massive black hole, one of the main inner components and best local laboratories available for studying galaxy evolution. Because of high extinction, crowding, and the superposition of multiple structures along the line of sight, studies of the inner regions of the Milky Way are however very challenging and very little has been done so far. Thanks to recent data, this thesis aims at unveiling the physical processes which led to the formation of the NSD and its links with the other components of the Milky Way. This manuscript is divided into three parts corresponding to the different methodologies used.

For the first part, thanks to high-resolution near-infrared spectroscopy, I carried out a chemical analysis of cool giant stars located in the inner Galactic bulge. I measured detailed abundances of the alpha-elements: silicon, magnesium and calcium, using recent and precise theoretical data such as an updated line list, broadening parameters and non-local thermodynamic equilibrium corrections. Based on the derived abundances, a tailored chemical evolution model for the inner Galactic bulge was constructed. I also used spectral analysis to measure the carbon isotopic ratio automatically in solar neighbourhood giant stars in order to establish a relation with asteroseismic stellar mass. This would allow to estimate stellar ages in distant regions such as the NSD.

In the second part of this thesis, I studied the dynamics of stars observed in the Milky Way's NSD by doing an orbital analysis. I computed orbits in a non-axisymmetric gravitational potential accounting for the effects of the Galactic bar and derived their fundamental frequencies. This allowed me to identify the orbital resonances and then the different orbit families that may be present in the NSD.

In addition to observations, simulations are of great interest to fully understand the physical processes that formed the inner regions of the Galaxy. In this final part, I used a N-body hydrodynamic simulation of an isolated Milky Way like galaxy in order to study the formation of its NSD. This simulation allowed to do a first comparison between observations and simulations in terms of chemistry and dynamics.

Keywords: Stars: abundances, late-type - Galaxy: dynamics, bulge, centre, structure.

Acknowledgements / Remerciements

Firstly, I would like to thank Livia Origlia and Patricia Sanchez-Blazquez for accepting to be rapporteurs and for taking the time to read this thesis. I also thank all the other members of the jury, for accepting to be part of it.

Since my thesis was conducted under a cotutelle agreement between Nice and Lund, I had the opportunity to be guided by two great supervisors.
I would like to thank my "main" supervisor, Mathias, for his insightful ideas and for proposing this thesis topic, which I found both challenging and immensely interesting to work on. Merci beaucoup Mathias pour ta bienveillance, ta gentillesse et ton soutien durant ces 3 années !
I would like to thank my swedish supervisor, Nils, for allowing me to discover Sweden thanks to this cotutelle agreement. I would like to thank you for your kindness, your support, for all your very interesting explanations about spectroscopy but also for picking me up by car at Lund C :) !
I consider myself very lucky to have had you both as supervisors.

I would like to thank Francesca Fragkoudi for supervising me through our collaboration, and for inviting me to Durham.

For the Lund side of my thesis, I want to thank Govind for always taking the time to help me in my spectroscopic projects and also Rebecca and Bibi for their kindness and for always being a pleasure to meet. I also want to thanks the other ISA group members I have not mentioned yet, Brian, Martin and Henrik for the nice ISA meetings we had during the first part of my thesis.

Pour la partie Nice de ma thèse:
Je voudrais remercier Philippine pour sa sympathie et gentillesse et pour m'avoir fait visiter Copenhague à plusieurs reprises.
I would like to thank Spitoni for his sympathy and creating a good atmosphere in the building and at the bus stop. I also thank his faithful sidekick Pedro for helping me on so many occasions.
Je voudrais aussi remercier le fameux Sab pour ses apparitions toujours aléatoires dans mon bureau et pour toutes nos sorties à notre QG le VD avec Gab et JB le trader (j'en

profite pour le remercier pour les discussions mentalisme et trading).

Je remercie Amaël pour toutes ces discussions et tous ces midis passés à l'observatoire (et aussi sorties dans Nice) !

Je tiens à remercier sans doute l'un des meilleurs collègues de bureau sur lesquels j'aurais pu tomber, Gabriele ou devrais-je dire le Plombier. Merci d'avoir amené de la gaieté et de l'ambiance à cet environnement parfois trop grisâtre, et pour tous ces moments passés à l'observatoire et en dehors (e.g. Soy el fuego, among MANY others). J'en profite pour remercier Raphaël qui a permis de créer un trio parfait et tout terrain (Paris, Palma..).

Je souhaite remercier mes frères bordelais, Rémulus et Jaliffe, pour toutes ces années d'amitié. C'est toujours un plaisir de partir dans nos aventures diverses et variées (avec notre cher Pierrot évidemment) et cela m'a notamment été très bénéfique pour sortir du rythme soutenu de cette thèse.

Je m'adresse maintenant à celle que je n'aurais jamais pu imaginer rencontrer. Je ne te remercierai jamais assez pour ton soutien quotidien, ta sensibilité et ton amour. Merci d'avoir croisé mon chemin et de partager ma vie. Merci Elisa.

Enfin, je ne remercierai jamais assez ma famille pour tout ce qu'elle m'a apporté pendant toutes ces années. Merci à ma mère et mon père de m'avoir transmis de si belles valeurs de vie, pour tous leurs sacrifices sans lesquels je ne serais sans doute pas là à écrire ma thèse, et pour tout leur amour.
Je voudrais m'adresser à Inès, ma sœur jumelle, mon témoin de vie. Je ne te remercierai jamais assez pour tout l'amour et le soutien que tu m'apportes constamment depuis que l'on est tout petits. Je me sais très chanceux d'avoir comme grande sœur une si belle et talentueuse personne que toi et tu es et restera toujours un exemple à suivre pour moi.

Contents

List of Figures

List of Tables

1

Overview

"The world is, of course, nothing but our conception of it."

Anton Chekhov

This chapter is the main introduction of the thesis and aims to provide the context for the subsequent chapters. I present the field of galactic archaeology and give a detailed overview about the inner structures of the Milky Way. The different methodologies employed throughout this thesis are presented in individual chapters.

1.1 The *Milky Way*

1.1.1 Context

Our home galaxy, the *Milky Way*, is just one galaxy among millions of billions in the observable Universe. However, well before our awareness of its existence and our humbling place in this vast cosmic panorama, various civilisations bestowed upon it diverse names and mythologies throughout time. The predominantly adopted term, "*Milky Way*", is a legacy of the Greeks and refers to the spilled milk of the goddess Hera.

Ethymology: the term "*Milky Way*" originates from the Latin "*via lactea*", and its roots can be traced further back to the Greek "γαλαξίας κύκλος" (galaxías kýklos), which translates to "milky circle".

Undoubtedly, mankind has consistently shown a profound fascination with the celestial sphere. Stars served diverse purposes, from guiding orientation and navigation to marking seasons, establishing calendars, and even playing a role in religious practices. In essence, these celestial bodies were our sole guides shaping our understanding of space and time and aiding us in seeking meaning in our existence. Throughout the ages, advancements in science and technology have allowed us to expand our understanding of the sky, enabling increasingly precise studies of our universe. Renowned figures like

Galileo Galilei, *Johannes Kepler*, *Isaac Newton*, *Margaret Burbidge*, *Albert Einstein*, and *Edwin Hubble* to name but a few, have played instrumental roles in laying the foundation for modern astrophysics. Their contributions, spanning from challenging geocentrism to elucidating the expanding universe, have reshaped our understanding of the cosmos. In recent decades, a novel field of astrophysics has emerged, commonly referred to as ***galactic archaeology***. Its main purpose is to unravel the evolutionary history of galaxies, starting by our own. Just as palaeontologists or archaeologists who study traces of past life through fossils or excavated remnants, galactic archaeologists use stars, gas and other observable structures as fossils. Various observational techniques like photometry, spectroscopy, and astrometry are used to analyse the properties of stars. By meticulously examining chemical compositions, ages, spatial distributions and kinematics of stellar populations, galactic archaeology provides valuable insights into the mechanisms underlying galaxy formation, the construction of galactic structures, and the interactions among galaxies across cosmic epochs. Given our technical capabilities, the Milky Way is the only galaxy for which it is presently possible to measure very detailed chemical abundances and resolve stars even in its centre. Its scales are truly staggering, it spans a distance of about 100 000 light-years ($\sim$ 3 billion billion kilometres or 30 kiloparsecs) and hosts at least 100 billion stars.

1.1.2 Structure and evolution

One of the greatest outstanding questions in modern astrophysics is how galaxies form and evolve across the Universe. The current cosmological framework, known as the Λ cold dark matter (CDM) paradigm, provides a broad understanding of the evolution of structures in the Universe (Springel et al., 2006). According to this model, galaxies form through the hierarchical merging of smaller proto-systems. While this theory has seen considerable success, particularly on large scales, the detailed process of galaxy formation remains incompletely understood. Discrepancies between the predictions of the model and observations, such as the "missing satellites" problem [1], highlight its limitations, particularly when applied to our Galaxy and its closest neighbours (Klypin et al., 1999; Nierenberg et al., 2016). Consequently, investigating the properties of the Milky Way and its components becomes essential for advancing our understanding of galaxy formation.

Types of galaxies

Numerous galaxy clusters populate the Universe, each hosting a wide variety of galaxies. Already in the 1920s, the astronomer Edwin Hubble developed a morphological classification of galaxies known as the *Hubble tuning fork diagram* (or *Hubble sequence*, see Figure 1.1). Nowadays, galaxies can be classified into four main categories: **elliptical**,

[1] The *"missing satellites"* problem refers to the disparity between the number of satellite galaxies predicted by simulations of Milky Way-type galaxies and the observed number of dwarf galaxies around our own Milky Way: we do not observe enough satellites.

spiral, **lenticular**, and **irregular/peculiar**. The belief that he mistakenly considered elliptical galaxies as evolutionary precursors to spiral and irregular galaxies, leading to the classification of ellipticals as *"early-type"* and spirals/irregulars as *"late-type"*, remains widespread. However, this classification system is now understood to be primarily based on morphological differences rather than evolutionary sequences (see Figure 1.2).

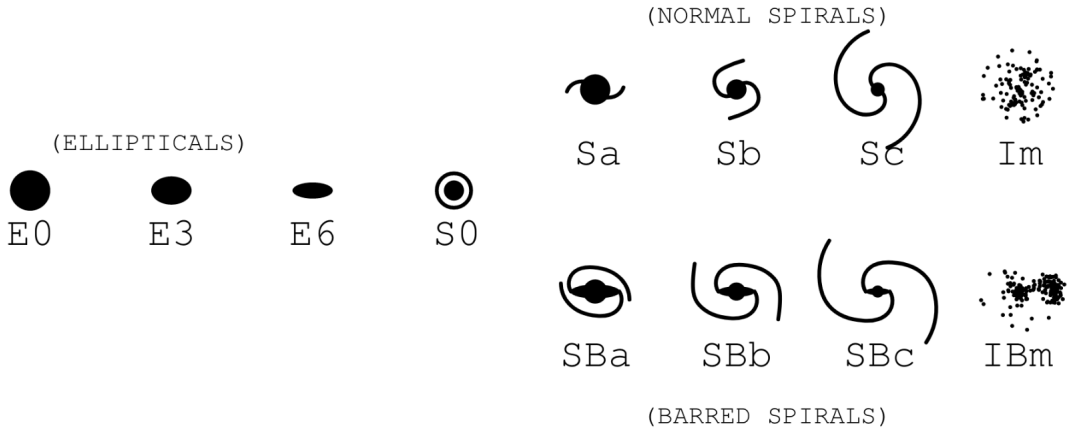

Figure 1.1: *Hubble sequence from Hubble, 1926. Elliptical galaxies range from nearly spherical (E0) to highly elongated (E7). Spiral galaxies are divided in barred and unbarred spirals and are subdivided based on the tightness of their spiral arms and the prominence of their central bulge.*

➤ **Elliptical galaxies**

Elliptical galaxies (*E* type in the Hubble sequence) exhibit a range of shapes, varying from nearly spherical to elongated ovals, which is why they are called "*elliptical*". They have bright nuclei and faint outer envelopes, with surface brightness decreasing strongly with distance from the centre. They are among the most massive and luminous known stellar systems, show very little organisation or features and contain no stellar disc and almost no cold gas or dust. They generally have red colours because their stars are mostly old, indeed cold gas is necessary to form new stars (Conselice, 2006). The majority of elliptical galaxies are believed to form either through the mergers of smaller galaxies (J. E. Barnes and Hernquist, 1992) or from the rapid collapse of non-rotating gas (van Albada et al., 1982). This explains why they are often found close to the centre of galaxy clusters.

➤ **Spiral galaxies**

Spiral galaxies stand in contrast to elliptical galaxies with their distinctive features. They contain a flattened, rotating disc component and are defined by prominent spiral arms extending outward from the galactic centre. Spiral galaxies are categorised into two primary types: normal spirals (*S* type) and barred spirals (*SB* type), distinguished by the presence of a central bar structure in the latter. Both types contain a central bulge and all these components are encompassed within a more diffuse region: a halo. The morphologies of these galaxies can vary widely,

with some exhibiting tightly wound, symmetric arms and others displaying more open and asymmetric structures. The stellar populations within spiral galaxies can have a wide range of ages but tend to be younger on average compared to those found in elliptical galaxies (Trager et al., 2000). Spiral galaxies harbour significant amounts of dust and gas, facilitating intense star formation primarily within the spiral arms. Until now, the origins of the different spiral patterns remain elusive, with no definitive explanation for how and when they form. Nonetheless, numerical simulations propose that minor mergers might play a role in shaping spiral patterns (Bottema, 2003; Dobbs et al., 2010; Cimatti et al., 2020).

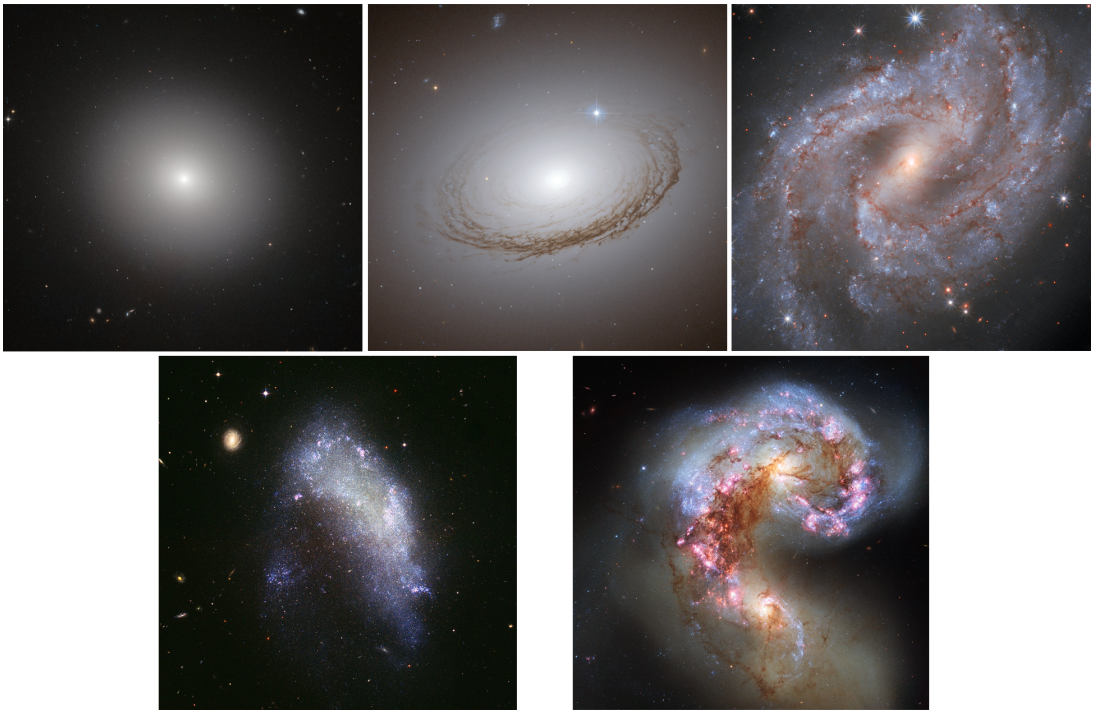

Figure 1.2: *Upper left panel: elliptical galaxy (M87). Upper middle panel: lenticular galaxy (NGC3489). Upper right panel: spiral galaxy (NGC3147). Lower left panel: irregular galaxy (NGC1427A). Lower right panel: peculiar galaxy (Antennae galaxies). Images from the Hubble Space Telescope.*

➤ **Lenticular galaxies**
Lenticular galaxies (*S0* type) can be viewed as intermediate between elliptical and spiral galaxies, exhibiting certain properties of both types. More precisely, they contain a bulge, a rotationally supported disc and some have a bar. However, they do not have spiral arms, have almost no cold gas and therefore their colours, gas content and star formation properties are more similar to elliptical galaxies (Caldwell et al., 1993). It is suggested that they could originate from spiral galaxies due to environmental effects (e.g. spirals highly depleted in gas Haynes et al., 1986).

➤ **Irregular and peculiar galaxies**
Galaxies that do not fit to any of the previous classes are called *"irregular"*

or *"peculiar"*. Dwarf galaxies with substantial amounts of gas and active star formation typically exhibit irregular structures, earning them the classification of *"irregular"* galaxies (e.g. the Large and Small Magellanic Clouds). In contrast, gas-deficient systems lacking young stars are categorised as dwarf ellipticals (*dE*) and dwarf spheroidals (*dSph*). Therefore, the irregular galaxies are usually smaller and less massive than commonly studied elliptical, spiral and lenticular galaxies. They lack any obvious symmetry and do not contain any nuclear bulge or disc components. On the other hand, *peculiar* galaxies can exhibit large sizes and are characterised by unusual features, including distorted shapes, abnormal amounts of gas and dust, or other atypical characteristics. They appear to have experienced strong perturbations in the recent past and are currently far from being in dynamical equilibrium (Mo et al., 2010). This suggests that they are undergoing a transformation process and are, therefore, usually associated with recent mergers or tidal interactions.

A closer look on the Milky Way

The galaxy group including the Milky Way, known as the *Local Group*, consists primarily of two main collections: our Galaxy and Andromeda moving toward another, along with their respective satellites. While at least 80 members are identified, the majority are dwarf galaxies. This group is a component of a more extensive structure known as the *Virgo Supercluster*. The Milky Way has been shown to have accreted several dwarf galaxies over time. Evidence of ongoing accretion is observed through the presence of stellar streams originating from the Sagittarius dwarf galaxy (e.g. Malhan et al. 2018; Ramos et al. 2020; Antoja et al. 2020)
The Milky Way is a barred spiral galaxy and its corresponding class on the *Hubble tuning fork diagram* is **SBbc** and it is supposed that it was previously a **SBb**. Its structure is often divided into three major components: the ***halo***, the ***disc*** and the ***bar / bulge*** as shown in Figure 1.3 (a more detailed illustration of the Milky Way is shown in Figure 1.4). However, there exist embedded within the latter component a hidden structure, called ***"nuclear bulge"***, and is just as important to mention.

- ✦ **Halo**
  The ***Galactic halo*** is the roughly spherical region surrounding the Milky Way, that extends beyond the main disc. It is primarily composed of very old stars and globular clusters, as well as dark matter. A notable portion of the stellar halo is believed to have formed through a hierarchical process involving the disruption and subsequent mixing of dwarf galaxies (Searle et al., 1978; Bullock et al., 2005; Bell et al., 2008; Helmi, 2008). Although it is relatively smooth, the debris from accretions in the last few gigayears can remain in relatively distinct structures. We can cite the three major tidal tails resulting from the disruption of the Sagittarius dwarf galaxy, the low-latitude stream, and the Virgo overdensity. The stellar halo is supported against gravity mainly by its velocity dispersion. Its stars are found to

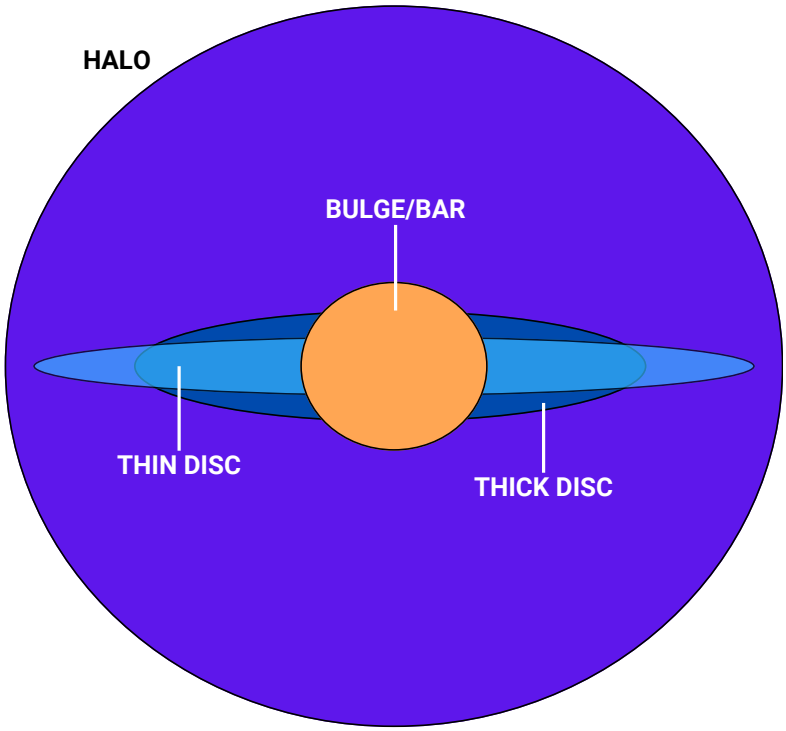

Figure 1.3: *Very schematic edge-on view of the Milky Way. Only the main components of the Galaxy are shown: the halo, thin and thick discs, and bulge/bar.*

be metal-poor (i.e. $[Fe/H] \leq -1.5$), α-enhanced and have a mean rotation velocity almost null. Considering these properties, the Galactic halo is expected to hold some of the best preserved fossils of the formation history of our Galaxy. The dark matter halo is much more extended than the stellar halo and dominates the mass of the Galaxy at these large scales (van der Marel et al., 2012).

✦ **Disc**

With a mass about $6 \times 10^{10}\ M_{\odot}$, the ***Galactic disc*** represents 75% of the total mass of the Galaxy and is therefore the most massive stellar component of the Galaxy (Sofue et al., 2009; Bland-Hawthorn et al., 2016). It can be divided into two different structures: the ***thin*** and ***thick discs*** (Gilmore et al., 1983). Their corresponding stellar populations have been distinguished by ages, chemical abundances, and kinematics and show that the thin component is younger than the thick one. Since the sun is located in the disc, this structure, and especially the solar neighbourhood, has already been well studied. The ***thick disc*** has a scale height of $\sim 1\ kpc$ and contains most of the gas, its stars are more metal-rich than those of the halo ($-1.5 \leq [Fe/H] \leq -1.0$), are α-enhanced and have rotation velocities about 150 $km\ s^{-1}$ (Belokurov et al., 2022; Conroy et al., 2022). The ***thin disc*** is $\sim 300\ pc$ thick, has ongoing star formation and its stars ($[Fe/H] > -1.0$) have rotational velocities about 220 $km\ s^{-1}$ which is higher than in the thick disc.

Recent galactic surveys focusing on the chemistry and kinematics of nearby stars suggest that the formation of the disc, and in particular that of the thick disc, occurred relatively early, within the first $1-2\ Gyr$ (Belokurov et al., 2022; Conroy et al., 2022; Rix et al., 2022; Xiang et al., 2022). The thin disc is supposed to have formed during the settling down of the disc that corresponds to when the galaxy achieves a constant star formation rate and an equilibrium rotating disc. To account for the distinct chemical compositions of thin and thick disc stars, two main mechanisms are proposed: intense star formation episodes triggered by the infall of pristine gas from the accretion of smaller satellite galaxies, or as a consequence of a merger event between the Milky Way and a massive dwarf galaxy (Helmi et al., 2018).

✦ **Bar / bulge**
The ***Galactic bar / bulge*** refers to the central kiloparsec scale and vertically extended over-density of the Galaxy. Its nature has long been unclear but thanks to the technological advancements that appears during these last decades, this structure is more and more understood. It is further detailed in Section 1.1.3.

✦ **Nuclear bulge**
The ***nuclear bulge*** is embedded in the Galactic bulge and is therefore the most challenging structure of the Galaxy to observe. That is why it remains presently poorly studied. It encompasses a variety of substructures that surrounds the supermassive black hole located at the centre of the Galaxy. The latter are further discussed in Section 1.1.4.

Main surveys of particular interest for this thesis

Galactic surveys:

- **VVV** (*Vista Variables in the Via Lactea*, Minniti et al., 2010; Saito et al., 2012) is an infrared variability survey focused on observing the Milky Way bulge and a portion of the disc. It is conducted using the 4.1-meter VISTA, is equipped with a near-IR camera containing 67 million pixels of mean size 0".34 and operates in five passbands: Z, Y, J, H, and KS. Morever, the VVVX (*Vista Variables in the Via Lactea eXtended*, Saito et al. 2024) has expanded both the temporal as well as spatial coverage of the original VVV survey.

- **GES** (*Gaia-ESO Survey*, Gilmore et al., 2012) targeted approximately 10^5 stars across the major components of the Milky Way. Observations were conducted using the VLT-FLAMES fibre that provided a field of view with a diameter of 25 arcminutes for two different spectrographs: GIRAFFE and UVES. The main

Figure 1.4: *Artistic face-on view of the Milky Way galaxy. Constellations and the known most prominent components are annotated. Credit: NASA/JPL-Caltech/ESO/R. Hurt and Pablo Carlos Budassi.*

purpose was to better understand the Galactic and stellar evolution by quantifying the kinematic and multi-element chemical abundance distribution functions across various components of the Milky Way.

- **APOGEE** (*Apache Point Observatory Galactic Evolution Experiment*, S. R. Majewski et al., 2016) observes in the near-infrared H-band ($1.5\mu m - 1.7\mu m$) at high spectral resolution ($R \simeq 22500$) and high signal-to-noise ratios ($S/N > 100$). The primary goal is to obtain precise and accurate radial velocities and chemical abundances for approximately 10^5 red giant branch stars, red clump stars, and asymptotic giant branch stars. It focuses on regions of the dust-enshrouded Galactic mid-plane and inner Galaxy, which are typically overlooked by optical surveys.

- **Gaia** (Gaia Collaboration et al., 2016a) survey aims to determine precisely the positions, distances, movements, and changes in brightness for a billion of stars in the Milky Way and in neighbouring galactic regions. Additionally, its radial velocity spectrometer (RVS) covers the wavelength range $846 - 870\ nm$ with a medium resolving power about $R \simeq 11500$. This allows the determination of stellar parameters and the measurement of chemical abundances for millions of stars.

- **MOONS** (*Multi-Object Optical and Near-Infrared Spectrograph*, Cirasuolo et al., 2014) survey conducted on the 8.2m VLT has medium to high resolution set ups ($R \simeq 9000$ in the optical and $R \simeq 20000$ in the infrared) covering the near-IR wavelength range. The main objective is to probe the Galactic bulge by determining precise radial velocities, metallicities, and chemical abundances for bulge stars in heavily obscured regions.

Extragalactic surveys:

- **TIMER** (*Time Inference with MUSE in Extragalactic Rings*, Gadotti et al., 2019a) survey uses the VLT–MUSE integral-field spectrograph and aims to establish the epoch in cosmic history when galactic discs transitioned into dynamically mature states (processes like disc settling, bar formation and gas accretion in discs are studied).

- **PHANGS** (*Physics at High Angular resolution in Nearby GalaxieS*, `www.phangs.org`) survey uses various telescopes, including ALMA, Hubble, JWST, and the VLT, to conduct high-resolution observations of nearby galaxies. The objective is to investigate the intricate interactions between small-scale phenomena such as gas dynamics and star formation with broader galactic structures and the evolutionary processes of galaxies.

1.1.3 The Galactic bulge and bar

Galactic bars

Many disc galaxies (i.e. spiral and lenticular galaxies presented in Section 1.1.2) feature a central elongated structure known as a bar. The Milky Way, as two thirds of external spiral galaxies, is barred (Sellwood et al., 1993) and this was only confirmed in the 1990s via the arrival of near-infrared photometry (Blitz et al., 1991; Weiland et al., 1994; Dwek et al., 1995; J. J. Binney et al., 1997) and dynamical models (Jenkins et al., 1994; Englmaier et al., 1999, among others). Bars can form naturally at the centre of stellar discs that are massive enough and dynamically cold to become gravitationally unstable (A. Toomre, 1964). According to cosmological zoom-in simulations, bar formation coincides with the settling of the disc, particularly when the thin disc emerges (Kraljic et al., 2012). This

timing aligns with observations of the Milky Way: its thin disc is estimated to have formed approximately 8 Gyr ago (Misha Haywood et al., 2013; Conroy et al., 2022), which corresponds to the proposed time of the formation of its bar (Wylie et al., 2022; Sanders et al., 2022b). Also, interactions between galaxies, whether through tidal interactions or mergers, have been demonstrated to significantly impact their morphology and play a role in the formation of bars (Alar Toomre et al., 1972; Athanassoula et al., 1999; J. E. Barnes et al., 1992; Kraljic et al., 2012).

Following their formation, bars evolve as they exchange angular momentum[2] with the dark matter halos (Weinberg, 1985; Debattista et al., 2000), and with the stellar and gaseous disks (Friedli et al., 1993; Bournaud et al., 2002). This process can strengthen bars when they lose angular momentum, but it can also weaken and ultimately destroy them in the other case (Bournaud et al., 2005). For instance, a bar can lose angular momentum by capturing disc stars from quasi-circular orbits outside the bar and moving them into elongated orbits in its outer part. In this way, the bar will become longer and thus stronger (Athanassoula, 2003). In the other hand, stars located outside the bar will be pushed into larger circular orbits. Considering this, bars redistribute stars within the galactic disc through radial migration processes, consequently altering the metallicity gradients in discs (Sellwood et al., 2002; Roškar et al., 2008; Minchev et al., 2010; Kubryk et al., 2013; Kubryk et al., 2015a; Kubryk et al., 2015b).

The growth of central mass concentrations can also weaken or destroy bars (Hasan et al., 1990; Pfenniger et al., 1991; Hasan et al., 1993; Juntai Shen et al., 2004) but has little impact if these central concentrations have sufficiently low mass or low mass growth (Athanassoula, 2005a). Additionally, comparisons between barred and unbarred galaxies indicate that the inner regions of barred galaxies consistently exhibit higher metallicities and star formation rates (Ellison et al., 2011). Furthermore, these regions tend to show increased nuclear activity and accretion onto central black holes (Alonso et al., 2018). As a result, bars are believed to play a key role in driving the secular phase of galaxy evolution.

Bars can vary in size depending on the galaxy host however in early-type galaxies there is a general tendency for them to be larger relative to the size of the disc (B. G. Elmegreen et al., 1985). They are believed to rotate with a well-defined pattern speed and are often classified into two categories: fast-rotating bars and slow-rotating bars (Debattista et al., 2000). The pattern speed of the Milky Way bar is about $39.0 \pm 3.5 kms^{-1}kpc^{-1}$ according to Portail et al., 2017a and the bar angle between the bar major axis and the Sun-Galactic centre line is around $25 - 30°$ (Christopher Wegg et al., 2013).

More details about orbital resonances within bar potentials are presented in Part II.

[2] In an isolated galaxy, the total angular momentum must be conserved. Therefore, different structures of the galaxy will either absorb or emit angular momentum, in equilibrium.

The concept of *"bulge"*

Nowadays, every astrophysicist with an interest in galaxies is familiar with the concept of *"bulge"*. However, it is noteworthy that this term has a more recent origin than one might assume. As explained by Madore (2016), there was no widely adopted term to describe the bulge of the Milky Way and those of other galaxies. *"Central condensation"*, *"lens-like feature"*, *"amorphous feature"*, *"bulge-like"*, various descriptions and terms were used before converging to the common name *"bulge"*. Indeed, it was only in the vicinity of the 1950s that the latter emerged, coinciding with the initial identification of the Galactic bulge as a distinct component of the Milky Way by Baade (1946) and Stebbins and Whitford (1947). It was not until mid 1970s that *"bulge"* and *"disc"* became the commonly used terms to describe the outer and inner features of disc galaxies. The growth in galaxy studies and the arrival of digital detectors (i.e. CCDs) in the 1980s resulted in the shift from visual descriptions to quantitative measurements, particularly with the use of the "bulge-to-disc" ratio. It allowed to identify more rigorously bulges in other galaxies with various morphology. Fisher and Drory (2011) showed that bulges are very common: they are found in upwards of 80% of bright galaxies ($> 10^9 M_\odot$).

> **Historical fact:** The bulge of M31 (or Andromeda galaxy) is the first extragalactic object observed in the northern hemisphere, thanks to its visibility to the naked eye.

Accordingly, we can now ask what does the term "*bulge*" truly mean ? Moreover, does it align with a singular, unequivocal definition ? In its simplest terms, one might depict a bulge as a central mass concentration. Alternatively, it can be defined more quantitatively, when examining the radial photometric profile of disc galaxies, as an extra light in the central part of the disc. Nevertheless, these definitions remain overly broad, categorising many objects as bulges. Indeed, they were found in elliptical galaxies but also in lenticular and spiral galaxies. Those with blue, young stellar populations have been shown to harbour very different bulges than those observed in red, old galaxies (Drory and Fisher, 2007). Some bulges share similarities with ellipticals, while others lean towards a more disc-like structure, and even others have peanuts or boxed shapes (John Kormendy and Kennicutt, 2004a; Athanassoula, 2005b). Only recently, a significantly growing number of studies have reported on a bimodal nature of bulges. The two categories that are commonly used to describe bulges, thanks to morphology, photometry and kinematics studies, are:

- **Classical bulges**
  The term "*classical*" pertains to the prevalent notion about bulges for a considerable part of the twentieth century. They are found in nearly half of early-type spirals and are absent in Sc and later-type systems. These bulges, that exhibit properties resembling elliptical galaxies, are supposed to form early, during the hierarchical formation of the galaxy, through violent processes (i.e. mergers Aguerri et al. 2001; Hammer et al. 2005) followed by strong relaxation. Other formation scenarios

are also discussed like the coalescence of massive gas clumps (Noguchi, 1999) or the rapid collapse of baryons in dark matter halo. Classical bulges contain stars that are smoothly distributed, old and dominated by random motions (i.e. kinematically hot) that allow these structures to be dynamically supported.

✦ **Pseudo-bulges**[3]

Contrary to classical bulges, *pseudo*-bulges (see review by John Kormendy and Kennicutt 2004a, Athanassoula 2008) are supposedly formed slowly via secular evolution processes. They are spread over all types of spiral galaxies, and their scale lengths are related to the disc scale length. Their structure is also very different and they present very distinct properties like active star formation, rotation kinematics and the presence of young stars. The term *"pseudo-"* became commonly used to distinguish these structures from classical bulges. For all these reasons, there is a growing debate about the potential abandonment of the term "bulge" for this category. They are divided into two types:

- **Boxy/peanut bulges**

  The concept of *boxy* bulges can be traced back to as early as 1959, when Burbidge and Burbidge (1959) found such a structure in NGC 128. Then later, thanks to other extragalactic observations (de Souza and Dos Anjos 1987, Lütticke et al. 2000) and N-body simulations (Athanassoula et al., 2002), the existence of *boxy/peanut* bulges was confirmed. This type of bulge is formed via the natural evolution of barred galaxies through slow secular evolution processes (John Kormendy and Kennicutt, 2004a; Athanassoula, 2005b). After their formation, stronger bars can undergo several episodes of buckling instability. This process entails distortions of the bar out of the equatorial plane of the disc, leading to the weakening and thickening of the bar (Athanassoula (2016)). When observed edge-on, this thickened bar adopts the characteristic boxy/peanut shape. Therefore, these bulges appears after the bar formation and represent its vertically extended inner part.

- **Former "discy bulges"**

  The discovery of flat central structures in other galaxies led to the conclusion that certain (pseudo-)bulges may exhibit a "disc-like" shape (J. Kormendy, 1993). Subsequently, to avoid potential confusion, Athanassoula (2005b) referred to them as "disc-like" bulges. These "discy bulges" are supposed to form through the inward flow of gas material towards the galactic centre, leading to subsequent star formation. These last couple decades, knowing that they correspond to small central discs in the plane of the galactic disc, the concept of "discy-bulge" has been abandoned in favour of the "nuclear disc"

[3] The term *"pseudo-bulge"* is not universally applied in the same manner. A part of the astronomy community restricts its usage to *discy-bulges*, categorising *boxy/peanut bulges* separately.

definition, more in alignment with their inherent characteristics (Gadotti et al., 2019a). Nuclear discs are further discussed Section 1.1.4.

Therefore, being able to determine the type of bulge within a galaxy is essential to understand both the specific properties of the host galaxy and the overall processes driving galaxy evolution. While this differentiation is crucial for a more comprehensive understanding of galaxy structures, it is essential to emphasise that pseudo-bulges do not always serve as the counterpart to classical bulges. Numerous studies demonstrate that bulges of varying types often coexist within the same galaxy (see Athanassoula 2005b; Athanassoula 2008; Nowak et al. 2010; Méndez-Abreu et al. 2014; Erwin et al. 2015). This reinforces, again, the necessity to revise the bulge definition.

Figure 1.5: *Artist's impression of the bulge of the Milky Way. Credit: ESO/NASA/JPL-Caltech/M. Kornmesser/R. Hurt.*

The Milky Way bulge

The existence of a bar-like structure in the inner regions of the Galaxy was firstly suggested by de Vaucouleurs et al. (1964) and then predicted thanks to infrared observations by Blitz et al., 1991. Soon after, the COBE data (B. J. Smith et al., 2004) confirmed the presence of a bar (Weiland et al., 1994; J. J. Binney et al., 1997). Additionally, a structurally distinct triaxial bulge separate from the main bar has been identified (Dwek et al., 1995, among others) and corresponds to the so called Galactic bulge. The old age of the bulk of stars (older than $5 - 8\ Gyr$ as suggested by Ortolani et al., 1995 and later refined to approximately 10 Gyr, as shown in Zoccali et al. 2003; Clarkson et al. 2008; Renzini et al. 2018) located in this structure has long been a convincing argument to categorising it as a *classical bulge*. Also, the combination of the first chemical evolution models and the observation of high-α abundances[4] led to the hypothesis that the bulge was formed early and rapidly (Francesca Matteucci et al., 1990; Molla et al., 1995; Ferreras et al., 2003; McWilliam et al., 1994) as inspired by dissipative collapse models (Richard B. Larson,

[4] See Chapter 3 for detailed review on chemical elements

1974). In the last two decades, our understanding of the nature of the Galactic bulge has undergone significant transformation. Star counts of red clump giants revealed an X-shape component in the bulge (McWilliam and Zoccali 2010; Nataf et al. 2010). It was later explained via the reconstruction of the 3D density of the bulge by C. Wegg and Gerhard (2013) which demonstrated the belonging of a large part to the *boxy/peanut bulge* category (see Figure 1.6). As explained previously, B/P bulges are the product of buckling instabilities that occur throughout the lifetime of stellar bars. According to simulations, this thickening predominantly occurs in the inner part of the bars. This is observable in our Galaxy, as Hammersley et al., 1994 documented the outer part of the Galactic bar, often referred to as the *"flat bar"* or *"long bar"*. The concept of a double bar system has been debated due to the perceived misalignment between the bulge and the long bar (Martinez-Valpuesta et al., 2011, among others). However, recent findings by Christopher Wegg et al., 2015 have shown them to have a consistent angle in addition to a smooth transition between them. Similarly to other barred galaxies (Kuijken et al., 1995; Bureau et al., 1999; Erwin et al., 2013), the B/P bulge transits at 2–3 kpc along the long axis into a planar long bar. Therefore, both components are thought to constitute a unified bar structure.

Being inside the Milky Way provides a significant advantage: the ability to resolve and observe individual stars. Nevertheless, when looking towards the Galactic centre, our view is limited to pencil beam areas around it because of high extinction, crowding, and the superposition of multiple structures along the line of sight. Making studies of the inner Galactic regions can thus become very challenging. The Galactic bulge is commonly defined as the inner 10 degrees of the Milky Way in Galactic coordinates (i.e. $(l, b) \leq (\pm 10^{\circ}, \pm 10^{\circ})$, Barbuy et al. 2018a). Given the technical challenges expressed before, a problem that stems directly from this definition is the necessity to cover homogeneously about 400 sq. deg. of sky and to separate bulge stars from foreground and background disc stars. Various photometric and spectroscopic surveys, such as VVV, Gaia-ESO, APOGEE, and Gaia, have been established to address this challenge, while others like MOONS are currently in development (see Barbuy et al., 2018a, for a comprehensive review of bulge surveys). These initiatives enable or will enable a more detailed exploration of the bulge, facilitating the discrimination between different stellar populations through precise measurements of kinematics, photometry, and stellar spectra.

Today, one can state that several stellar populations are part of the Galactic bulge and show evidence for a multiple component scenario, with different morphological and dynamical characteristics. The metallicity distribution function in the bulge region spans a wide range of metallicities ($-3.0 \leq [Fe/H] \leq +1.0$ according to Ness et al., 2016, with the bulk of the stars found within $-1.5 \leq [Fe/H] \leq +0.5$) and presents several peaks corresponding to different populations. However, the bulge can be divided into two main populations, a metal-rich one ($[Fe/H] > -1$) and another metal-poor

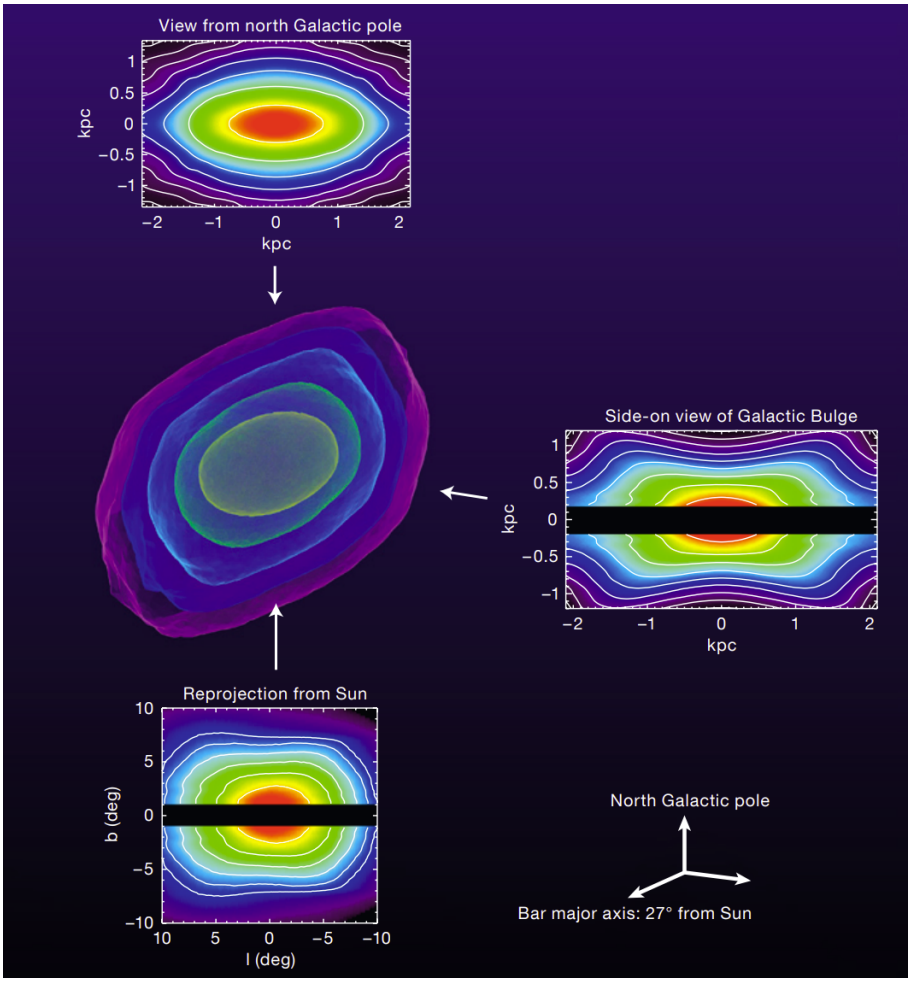

Figure 1.6: *Figure from C. Wegg and Gerhard (2013) showing the Galactic bulge seen from different directions. In the centre an image of the 3D iso-density contours of the measured Bulge density is shown. Three projections are shown as surrounding plots: from above (i.e., from the north Galactic Pole), from the side (i.e. along the intermediate axis of the bar) and the re-projected surface density from the Sun. The three projections show the surface density of Bulge red clump stars with isophotes spaced by 0.5 mag.*

($[Fe/H] < -1$). Vertical metallicity gradients were observed multiple times and show that the metal-rich population is concentrated to low latitudes (Ness et al., 2013a; A. Rojas-Arriagada et al., 2014; A. Rojas-Arriagada et al., 2017a; Johnson et al., 2020; Johnson et al., 2022). Most of the bulge stars exhibit a cylindrical rotation but differ in their vertical velocity dispersion profiles: it decreases steeply with latitude for metal-rich stars while it is approximately constant for the metal-poor ones. Also, only the metal-rich stars have a kinematic vertex deviation[5](Zhao et al., 1994; Soto et al., 2007; Babusiaux et al., 2010; Hill et al., 2011). Even if about 90% of the stars, with various metallicities, are barred, only the metal-rich ones constitute the B/P component (Ness et al., 2012; Dékány et al., 2013; Pietrukowicz et al., 2015; Gran et al., 2016). As said previously, studies of the

[5] The *vertex deviation* measures the covariance between radial and tangential motions (from the Sun's point of view). While a stationary, axisymmetric disc exhibits no vertex deviation, a triaxial bar inevitably introduces a vertex deviation.

age distribution of stars in the bulge have generally found old stars ($> 10\ Gyr$) leading to the hypothesis of a uniform old bulge. However, young ($< 5\ Gyr$) and intermediate age stars ($> 5\ Gyr$ and $< 8\ Gyr$) were also observed in other studies (Bensby et al., 2011; Bensby et al., 2013; Bensby et al., 2017) indicating a wider spread (M. Haywood et al., 2016). The age of the bulge remains a subject of debate, but consensus suggests that young stars are primarily or exclusively found at high metallicities, and thus not expected to be prevalent at high Galactic latitudes, where metal-poor stars dominate (Zoccali et al., 2017).
These results could explain the presence of a compound bulge in the Milky Way containing both a B/P bulge formed from secular evolution and classical bulge originated from accretion events (Athanassoula, 2005a; Debattista et al., 2005; Babusiaux et al., 2010; Hill et al., 2011; Zoccali et al., 2014). According to Grieco et al., 2012, such a compound bulge can easily produce the vertical metallicity gradient observed via the variation of the relative importance of two components.
Expanding the coverage of bulge stars and standardising the metallicity measurements across various surveys are crucial steps toward gaining a more comprehensive understanding of this structure.

1.1.4 The nuclear bulge

As presented in Section 1.1.3, the bulge component of galaxies has been the main subject of study until recently. With significant progress made in understanding this structure, attention has now turned towards exploring the intricate features of the inner regions, referred to as the nuclear bulge. Let's delve deeper into the heart of our Galaxy, all the way to its centre.

The Galactic centre

The old paradigm of putting humanity at a special place in the Universe has persisted throughout the ages. Even at the beginning of the twentieth century, the prevailing consensus among astronomers was that the Sun resided near, albeit not precisely at, the centre of the Milky Way, and that the Milky Way encompassed the entirety of the universe (Berendzen, 1975). However, in the 1910s, astronomer Harlow Shapley analysed the distribution of globular clusters in space and found its centre to be located within the Sagittarius constellation at a distance around 13 kpc from Earth. This discovery marked the first time that the Galactic centre was found to be much farther away than previously thought (Shapley, 1918). In 1927, Jan Oort made a significant observation regarding the rotation of stars within the Galaxy. He noticed that stars closer to the centre of the Galaxy exhibited higher rotational velocities compared to those located at greater distances from the Galactic centre. Numerous studies aimed to precisely determine this distance, employing various methodologies. Seventy-five years later, by the end of the twentieth century, most of these studies converged to a value between 7 and 9 kpc (Reid, 1993).

Figure 1.7: *Overview of the Galactic centre of the Milky Way. Galactic north is up and east to the left. Credit: NASA/JPL-Caltech/S. Stolovy (Spitzer Science Center/Caltech).*

The enormous quantities of gas and dust present along the line of sight towards the Galactic centre prevent the visible light to travel to us. It was not until the advent of radio astronomy by Karl Jansky in the 1930s that direct observations of the central region became possible. The origin of *Sgr A**, a radio source observed in the Sagittarius constellation, was not known for quite some time. As telescopes advanced in power and capability, infrared imaging and spectroscopy emerged as valuable tools for tracking the orbits of individual stars at the Galactic centre. Lynden-Bell and Rees suggested in 1971 that the Milky Way might host a supermassive black hole (Lynden-Bell et al., 1971). However, it took nearly four decades to provide compelling evidence to support this hypothesis. Indeed, in 2009, after 16 years of extensive observations on stellar orbits around *Sgr A**, Gillessen et al., 2009 demonstrated conclusively that the central mass concentration, surpassing $4 \times 10^6 M_\odot$, must be a black hole. It is now assumed that almost every galaxy contains a central super-massive black hole. The radio source *Sgr A** is thought to emanate from near the black hole, possibly originating either inside an accretion disc around the black hole or from a jet. Thanks to recent studies using highly precise measurements of the orbit of the closest star to *Sgr A**, named S2, to determine the distance to the supermassive black hole with unprecedented accuracy, the latter is estimated to be $8248.6 \pm 8.8\ pc$ (GRAVITY Collaboration et al., 2020). Also, thanks to observations made by the Hubble Space Telescope, we know that many low to intermediate mass galaxies contain exceptionally dense stellar systems at their centre, ranking among the densest known stellar structures in the Universe. Moreover,

photometric and kinematic studies of the GC have unveiled a variety of structures surrounding *Sgr A**.

The nuclear star cluster

Originally identified by Becklin et al., 1968, a nuclear star cluster (MWNSC) resides at the heart of our Galaxy, encircling its supermassive black hole. More than three decades later, it has been described by Launhardt et al., 2002a as a spherically symmetric structure embedded within a larger disc-like one that will be presented further in this section. Today, the MWNSC is considered as an elliptical structure flattened along the Galactic plane (Schödel et al., 2014a; Chatzopoulos et al., 2015a). According to several recent studies, its effective radius (i.e. where half of the cluster light is contained) is estimated to range between $4.2 \pm 0.4\ pc$ and $7.2 \pm 2.0\ pc$ (Schödel et al., 2014a; Fritz et al., 2016). Additionally, its mass has been determined to be approximately $2.1 \pm 0.7 \times 10^7 M_\odot$ to $4.2 \pm 1.1 \times 10^7 M_\odot$ (Schödel et al., 2014a; Feldmeier et al., 2014; Chatzopoulos et al., 2015a; Fritz et al., 2016; Feldmeier-Krause et al., 2017b). Also, it was shown that it is rotating in the same direction as the Galactic disc (McGinn et al., 1989; Lindqvist et al., 1992a; R. Genzel et al., 1996; Feldmeier et al., 2014). Infrared spectroscopy unveils that many of the observed bright stars in the MWNSC are old and evolved, such as late-type red giants, supergiants, and asymptotic giant branch stars. These findings align with the typical composition anticipated in an aged nuclear star cluster (Blum et al., 2003; Reinhard Genzel et al., 2010; Feldmeier-Krause et al., 2017a). In addition to this old population, several B-stars have been discovered as close as $\sim 0.04\ pc$ from *Sgr A**. These young stars, with an age of around $10 - 10^2\ Myr$, are part of a young star cluster that extends up to several parsecs, with the closest ones forming the inner part often referred to as the "S-cluster" (or S-star cluster). The MWNSC contains therefore both an old and a young stellar populations providing valuable insights into its origins. Additionally, the mean metallicity of the MWNSC appears to be solar to supersolar, which suggests a relatively high metallicity of the MWNSC (Feldmeier-Krause et al., 2017a; Feldmeier-Krause, 2022).

Among the variety of external galaxies, nuclear star clusters (NSCs) are found in most of spirals (Böker et al., 2002), are absent in giant ellipticals and their existence is still not clear in very low mass galaxies Neumayer et al., 2012; Neumayer et al., 2020. By definition, NSCs are located at the dynamical centre of their host galaxies and are described as very dense, massive and bright compact stellar systems exceeding the luminosity of any other stellar clusters. Several NSCs are found to to be flattened as shown by Seth et al., 2006. The typical effective radius of a NSC, independently of the galaxy type, is about $2 - 5\ pc$ but extreme values can reach $40\ pc$. In terms of stellar mass, NSCs are much more massive than globular clusters on average, ranging from $10^5\ M_\odot$ to $10^8\ M_\odot$. For massive galaxies (i.e. $> 10^9\ M_\odot$), the metallicities of NSCs are always higher than those of their hosts. However, in less massive galaxies, they are found to vary widely and are often lower (Koleva et al., 2009; Paudel et al., 2011; Kacharov

et al., 2018). Empirical relationships have been observed between NSCs and their host galaxies, hinting at a potential co-evolutionary process. Their study could thus provide significant understanding of galaxy evolution. The measurements of observed NSCs found in external galaxies confirm that the MWNSC has very typical properties. The advantage of the MWNSC is its proximity, indeed, it is the only NSC sufficiently close to us to resolve its stars. It offers a unique opportunity to study the extreme conditions and environment effects that characterised galactic centres (e.g. extreme stellar density, extreme tidal shear, strong magnetic fields).
Today, the two main formation scenarios proposed to explain the origin of a NSC are:

1. In situ formation through the infall of gas and subsequent star formation near the galactic centre (Shlosman et al., 1990), dissipative nucleation (Kenji Bekki et al., 2006; K. Bekki, 2007), tidal compression (Emsellem et al., 2008) or magneto-rotational instability (Milosavljević, 2004).

2. Inspiral of (globular) clusters due to dynamical friction and their subsequent merger (Tremaine et al., 1975; Capuzzo-Dolcetta, 1993; Antonini, 2013; Antonini, 2014; Arca-Sedda et al., 2014).

The dominant formation scenario for NSCs in massive galaxies is believed to be in situ formation, while in low-mass galaxies, the dominant mechanism is thought to be globular cluster accretion according to Neumayer et al., 2020. The dominance is proposed to switch between both processes at galaxy masses of around $\sim 10^9 M_\odot$ (Ordenes-Briceño et al., 2018; Sánchez-Janssen et al., 2019).
As previously said, the MWNSC contains a young stellar population dominant below $R_{GC} < 0.5\ pc$ (Buchholz et al., 2009) and an older one above this value. Additionally, there is also evidence for intermediate age stars (Blum et al., 2003; Pfuhl et al., 2011). Although the presence of young stars is a clear evidence for very recent star formation (i.e. in situ formation), the discovery of a recently identified population of metal-poor stars could potentially be attributed to an infalling globular cluster (Feldmeier-Krause et al., 2020; Arca Sedda et al., 2020a). Therefore, both scenarios could have contributed to the formation of the MWNSC. Due to the extreme conditions near the SMBH, the star formation in its vicinity is highly unlikely. As a result, the origin of the S-stars remains a mystery.
The most probable scenario for the formation and evolution of the MWNSC is described as follow. The bulk of the stars (80% of the MWNSC stellar mass) was formed during a starburst that started 10 Gyr ago and dropped to a minimum about $1-2\ Gyr$ ago. Then, an increase of star formation happened over the past few hundreds of millions years (Blum et al., 2003; Pfuhl et al., 2011; F. Nogueras-Lara et al., 2019b).
Unfortunately, comprehensive chemical abundance studies in the MWNSC are still lacking. Initial research by Thorsbro et al., 2020 indicates an enhancement in [Si/Fe] at super-solar metallicities which may suggest a past starburst event but it still needs to be confirmed.

So far, only small portions of the Galactic centre, comprising approximately 1% of the projected area, have been thoroughly explored. For further details about NSCs, see the reviews by Reinhard Genzel et al., 2010, Schödel et al., 2014c, Neumayer et al., 2020 and Schödel et al., 2020a.

The nuclear stellar disc

The existence of a remarkably dense molecular cloud complex with a ring-like shape in the central few hundred parsecs of our Galaxy, commonly known as the ***"central molecular zone"*** (CMZ), has been firmly established since the early 1970s (R. Genzel et al., 1987; Mezger et al., 1996; Henshaw et al., 2023). Its observed mean gas densities are much higher than those observed in the Galactic disc but the observed star formation rate (SFR) is not ($\simeq 0.1\ M_\odot\ yr^{-1}$, A. T. Barnes et al., 2017). However, stars are believed to originate from the dense regions, known as "clumps", within giant molecular clouds that fragment further into gravitationally bound "cores" which will form individual stellar systems (Bergin et al., 2007; Robert C. Kennicutt et al., 2012). Therefore, a higher SFR would be expected but is not. To explain this deficiency of star formation, environmental causes are proposed but still in debate. For instance, variations in the SFR could stem from fluctuations in the total gas mass of the CMZ, potentially influenced by irregular accretion driven by the Galactic bar (Sormani et al., 2018b; Sormani et al., 2020; Tress et al., 2020). As explained in Section 1.1.3, the Galactic bar redistributes angular momentum within the Galaxy which leads to an inflow of gas towards the centre. The current measured bar-driven mass inflow rate onto the CMZ is $\dot{M} = 0.8 \pm 0.6\ M_\odot\ yr^{-1}$ (Sormani et al., 2019; Hatchfield et al., 2021). This phenomenon can lead to the formation of inner structures.

Hidden within this vast gaseous nuclear ring lies a stellar structure that was, until very recently, largely unknown. After early indications found in studies such as Catchpole et al., 1990 and Lindqvist et al., 1992a, the first detailed depiction of the ***nuclear stellar disc*** (MWNSD) can be traced back to Launhardt et al., 2002a that used COBE infrared photometry to derive the large-scale distribution of stars and interstellar matter in the nuclear bulge. Both structures, the MWNSD and the CMZ, overlap in radius and have comparable scale-heights (Molinari et al., 2011; Henshaw et al., 2016; Longmore et al., 2017). The initial estimations from Launhardt et al., 2002a of the mass, radius and height of the MWNSD are $M_{MWNSD} = 1.4 \pm 0.6 \times 10^9\ M_\odot$, $R_{MWNSD} \simeq 230 \pm 20\ pc$ and $z_{MWNSD} \simeq 45 \pm 5\ pc$ respectively. More recent studies, however, suggest a slightly lower radius, around $R_{MWNSD} \simeq 100 - 200\ pc$ (Shogo Nishiyama et al., 2013; Gallego-Cano et al., 2020a; Sormani et al., 2022). Schönrich et al., 2015a utilised infrared spectroscopy from APOGEE data to measure the radial velocity of stars in the MWNSD, revealing a rotation velocity of approximately $V \simeq 120 km\ s^{-1}$, comparable to the gas in the CMZ. Schultheis et al., 2021, via the KMOS survey (Fritz et al., 2021), showed that the MWNSD

is kinematically cold compared to the kinematically hot Galactic bulge. They observed a decrease in velocity dispersion with increasing metallicity and found the MWNSD to be more metal-rich than the bulge yet less so than the MWNSC, with the metal-rich population exhibiting faster rotation than the metal-poor component. The correspondence between the rotation velocities of the gas of the CMZ and the observed metal-rich stars of the MWNSD provides compelling evidence that the latter likely originated in the CMZ. All these findings reinforce the presence of a rotating nuclear disc, distinct from both the MWNSC and the Galactic bulge, within the inner regions of the Milky Way.

Nuclear stellar discs (NSDs) are also detected in extragalactic systems. Indeed, as explained in Section 1.1.3, the structures observed at the centre of certain galaxies formerly called "discy bulges" are NSDs like the MWNSD[6]. Pizzella et al., 2002 were among the first to detect such structures in spiral galaxies. NSDs are, however, observed across a wide range of galaxy types, including both late-type (Zasov et al., 1999; Pizzella et al., 2002; Dumas et al., 2007) and early-type galaxies (Scorza et al., 1998; John Kormendy et al., 2001; de Zeeuw et al., 2002; Emsellem et al., 2004; Trujillo et al., 2004; Krajnović et al., 2008; Ledo et al., 2010). In very recent years, advancements in observational techniques, particularly through projects like MUSE-TIMER (Gadotti et al., 2019a), have revealed that NSDs are very common in spiral barred galaxies. These studies have provided a more precise characterisation of NSDs properties, leading to improved insights into their formation and evolution. NSDs span a range of sizes from a few parsecs to around a kiloparsec in radius. A correlation between bar lengths and NSDs sizes is observed (Gadotti et al., 2020) and smaller NSDs are found to be associated with younger bars (de Sá-Freitas et al., 2023c). NSDs are clearly distinguishable from the other galaxy components: they appear younger, more metal-rich, and less α-enhanced compared to their immediate surroundings. They are rapidly rotating and have low velocity dispersion (Gadotti et al., 2020). They exhibit a large range of ages with a tendency for young stars to be present and there are evidence of age gradients (i.e. stellar ages decrease with increasing radius, Bittner et al., 2020). All these results are consistent with a bar-driven secular evolution in the case of barred galaxies. According to this process, because of their non-axisymmetric potential, bars exert tangential forces on the gas of the main disc that makes it shocks and loses angular momentum. This results in a gas inflow towards the inner regions of the galaxy along features known as the bar "dust-lanes" (Bruce G. Elmegreen et al., 2009; Shimizu et al., 2019; Sormani et al., 2019)). Then, the gas accumulates with high rotational velocities in the central region and forms gaseous rings where active star formation occurs. The nuclear disc forms through an accumulation of nuclear stellar rings that were formed at larger radius successively (see Chapter 6 for more details about this process). For this reason, this formation scenario is commonly called "inside-out formation". However, since NSDs are also found in bar-less galaxies, it suggests that other formation mechanisms

[6] Both terms, *"discy bulge"* and *"nuclear disc"*, were used but referred in fact to the same type of structure.

would be possible. Proposed processes include gas inflows triggered by spiral arms and tidal interactions (Cameron et al., 2010). Additionally, bars could have formed these NSDs before being destroyed (see Section 1.1.3 for further details). Nevertheless, many studies show the long lived properties of bars in the absence of major mergers (Kraljic et al., 2012; Cavanagh et al., 2020, among others). Therefore, the most probable formation scenario involves a non-axisymmetric potential, particularly that of the bar.

The insights gained from extragalactic observations, simulations, and theories, combined with the measured properties of the MWNSD, have significantly enhanced our understanding of this structure. Moreover, several studies were carried out to derive the SFH of the MWNSD. While it was initially thought that the MWNSD had a quasi-constant SFR during the last 10 Gyr (Figer et al., 2004), more recently using the GALACTICNUCLEUS data (F. Nogueras-Lara et al., 2018a), Francisco Nogueras-Lara et al., 2020a argued that 80% of the stars were formed more than 8 Gyr ago, followed by a quenching phase and by a recent increase in star formation during this last Gyr, in which about 5% of the MWNSD mass was formed. In addition, F. Nogueras-Lara et al., 2023a observed an age gradient as detected in extragalatic NSDs. Now, most of studies agree that the MWNSD has a relatively early formation time and that the inside-out formation is the most probable, however the detailed SFH is still under discussion (see e.g. F. Nogueras-Lara et al. 2023a; Sanders et al. 2024).

While the MWNSD was uncovered only two decades ago[7], our comprehension of it has significantly advanced. However, it continues to be underexplored primarily due to the observational hurdles it still presents.

1.2 Motivation and goals of the thesis

In the previous sections, I discussed the complex structure of the Milky Way and showed that the inner regions are still poorly studied. This thesis aims at understanding the formation processes of these inner structures and in particular those of the MWNSD. The manuscript is divided into three parts corresponding to the different methodologies used.

- In Part I, I introduce stellar evolution and spectroscopy (Chapter 2) and present two projects: a chemical analysis of inner bulge M-giants (Chapters 3) and a study of the relation between the isotopic carbon ratio $^{12}C/^{13}C$ and asteroseismic mass of K-giants. (Chapter 4).

- In Part II, I introduce stellar dynamics (Chapter 5) and present an orbital analysis of MWNSD stars (Chapter 6). Additionally, a co-author paper on the relation between metallicity and orbits of these stars, which has been submitted for publication, is

[7] I will be 26 years old by the end of my thesis, which further highlights how recent this discovery is.

included in Chapter 7.

- In Part III, I present the study of the inner structures of an isolated barred disc galaxy constructed with a N-body hydrodynamic simulation. The formation processes of these structures are analysed in Chapter 8, followed by an orbital analysis (similar to Chapter 6) of their stars in appendices of Chapter 8.

Finally, in Chapter 9, I summarise the different projects presented in this thesis highlighting the main findings and perspectives.

1.3 List of publications

1.3.1 First author publications

- *Detailed α abundance trends in the inner Galactic bulge*
  N. Nieuwmunster, G. Nandakumar, E. Spitoni, N. Ryde, M. Schultheis, R. M. Rich, P. S. Barklem, O. Agertz, F. Renaud, and F. Matteucci (2023) A&A 671, A94
  Project presented in Chapter 3.

- *Orbital analysis of stars in the nuclear stellar disc of the Milky Way*
  N. Nieuwmunster, M. Schultheis, M. Sormani, F. Fragkoudi, F. Nogueras-Lara, R. Schödel, P. McMillan, L. C. Smith, and J. L. Sanders (2024) A&A 685, A93
  Project presented in Chapter 6.

- *A common in-situ formation pathway for nuclear discs and nuclear star clusters: Clues from a hydrodynamic N-body simulation*
  N. Nieuwmunster, F. Fragkoudi, M. Schultheis, in prep.
  Project presented in Chapter 8.

1.3.2 Co-author publications

- *First r-process enhanced star confirmed as a member of the Galactic bulge*
  R. Forsberg, R. M. Rich, **N. Nieuwmunster**, H. Jönsson, M. Schultheis, N. Ryde, and B. Thorsbro (2023) A&A 669, A17
  Not discussed in this thesis.

- *Smooth kinematic and metallicity gradients reveal that the Milky Way's nuclear star cluster and disc might be part of the same structure*
  F. Nogueras-Lara, A. Feldmeier-Krause, R. Schödel, M. C. Sormani, A. de Lorenzo-Cáceres, A. Mastrobuono-Battisti, M. Schultheis, N. Neumayer, R. M. Rich, and **N. Nieuwmunster** (2023) A&A 680, A75

Not discussed in this thesis.

- *Composition of Giants* 1° *North of the Galactic Center: Detailed Abundance Trends for 21 Elements Observed with IGRINS*
  G. Nandakumar, N. Ryde, G. Mace, K. F. Kaplan , **N. Nieuwmunster**, D. Jaffe, R. M. Rich, M. Schultheis, O. Agertz, E. Andersson, C. Sneden, E. Strickland, and B. Thorsbro (2024) The Astrophysical Journal, 964:96 (14pp)
  Not discussed in this thesis.

- *Metallicity-dependent kinematics and orbits in the Milky Way's nuclear stellar disc*
  F. Nogueras-Lara, **N. Nieuwmunster**, M. Schultheis, M. C. Sormani, F. Fragkoudi, B. Thorsbro, R. M. Rich, N. Ryde, J. L. Sanders, L. C. Smith (submitted)
  Included in Chapter 7.

Part I

Chemical fingerprints

2

Introduction

"Not just beautiful, though - the stars are like the trees in the forest, alive and breathing."

Haruki Murakami

Soon after the Big Bang, the Universe was primarily composed, in terms of baryonic matter, of hydrogen and helium, with trace amounts of lithium and beryllium. The stars belonging to the first generation known as *Population III* formed from this pristine gas and synthesised many heavier elements during their lifetimes. As these stars released these new elements into the interstellar medium, subsequent generations of stars further enriched the Universe's chemical composition, a process that continues to this day with *Population I* stars. As a result, the chemical composition of stars can be seen as their DNA since it carries the information of their origins and the environment from which they formed. I will give in this chapter a short introduction about stellar evolution, nucleosynthesis, stellar spectroscopy and chemical evolution models.

2.1 Stellar evolution

Stars are formed through the gravitational collapse of molecular gas clouds. These clouds are maintained against this collapse by their thermal pressure, however when their mass exceeds a certain threshold, the *Jeans mass*, gravitational forces become dominant, causing the clouds to begin collapsing. This process continues until individual gas clumps in the cloud become dense enough to ignite nuclear fusion. The latter produces a stronger pressure gradient which stops the collapse. A star is born.
Depending on their initial mass, stars will have different evolutionary paths, lifetimes and ultimate fates. However, stellar evolution can be summarised into several phases that almost all stars live. As long as stars have hydrogen to burn, they remain on the *main sequence*. This is the longest phase in the life of a star but its duration will vary strongly depending on the initial stellar mass: the supply of hydrogen will exhaust

quicker the more massive the star is[1]. After this exhaustion in the core, stars begin to fuse hydrogen in a shell outside the core that causes the stars to expand, turning them first into *subgiants* and then, becoming brighter but colder, turning them into *red giants branch* stars. When the necessary temperatures for central helium ignition are reached, the core of helium formed through the fusion of hydrogen will start burning. This is the *horizontal branch*. Stars light enough for the core to be degenerated will experience a *helium core-flash* which corresponds to the ignition of the helium core practically all at once. More massive stars will start the helium fusion more gradually. Once the helium supply is exhausted in the core and the stars are not massive enough to fuse carbon, hydrogen and helium burning continues in outer shells while stars enter the *asymptotic giant branch* (AGB). During this variable phase, intense stellar winds will expel a significant portion of the stars material. Eventually, the outer layers will expand and create a *planetary nebula*, while the leftover core transitions into a *white dwarf* (mainly composed of carbon and oxygen). More massive intermediate mass stars will partially ignite carbon fusion in their core but will not be able to burn more elements. They will follow a similar scenario as the less massive stars but as *super-AGB* instead of AGB and will end their lives as white dwarfs (mainly composed of oxygen and neon). Massive stars ($> 10 M_\odot$) will burn successively carbon, neon, oxygen and silicon before reaching an iron core that cannot produce energy through fusion. This incapacity to continue to produce energy in appreciable amounts will lead these stars to being torn apart in *core-collapse supernovae*. Depending on the mass of the star, the remnant will be a *neutron star* or a *black hole*.
Along all these evolutionary paths, stars increase and decrease in luminosity and temperature and their current phase can be identified through the *Hertzsprung-Russell diagram* (HR) which shows the relation between the luminosity of a star and its surface temperature (see Fig.2.1).

The purpose of this section was not to detail every evolutionary paths that exist but to provide a big picture of stellar evolution. For more details about the different phases of a star depending on the initial mass, see the schematic view Fig.2.2 from the review Karakas et al., 2014.

[1] 1 $M_\odot$ stars spend about 10 Gyr on the main sequence while 10 $M_\odot$ stars spend only $\sim$ 20 Myr

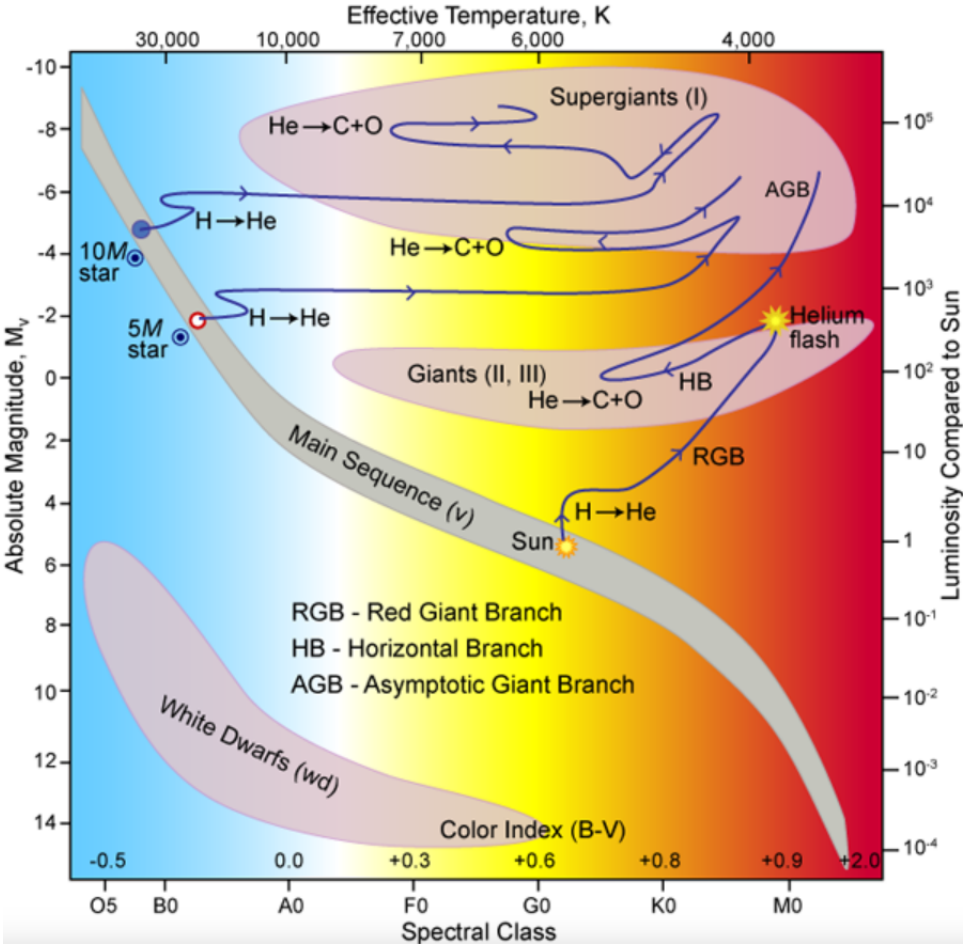

Figure 2.1: *Hertzsprung-Russell diagram. Illustration: Robert Hollow, Commonwealth Science and Industrial Research Organisation (CSIRO), Australia, adapted by Carin Cain*

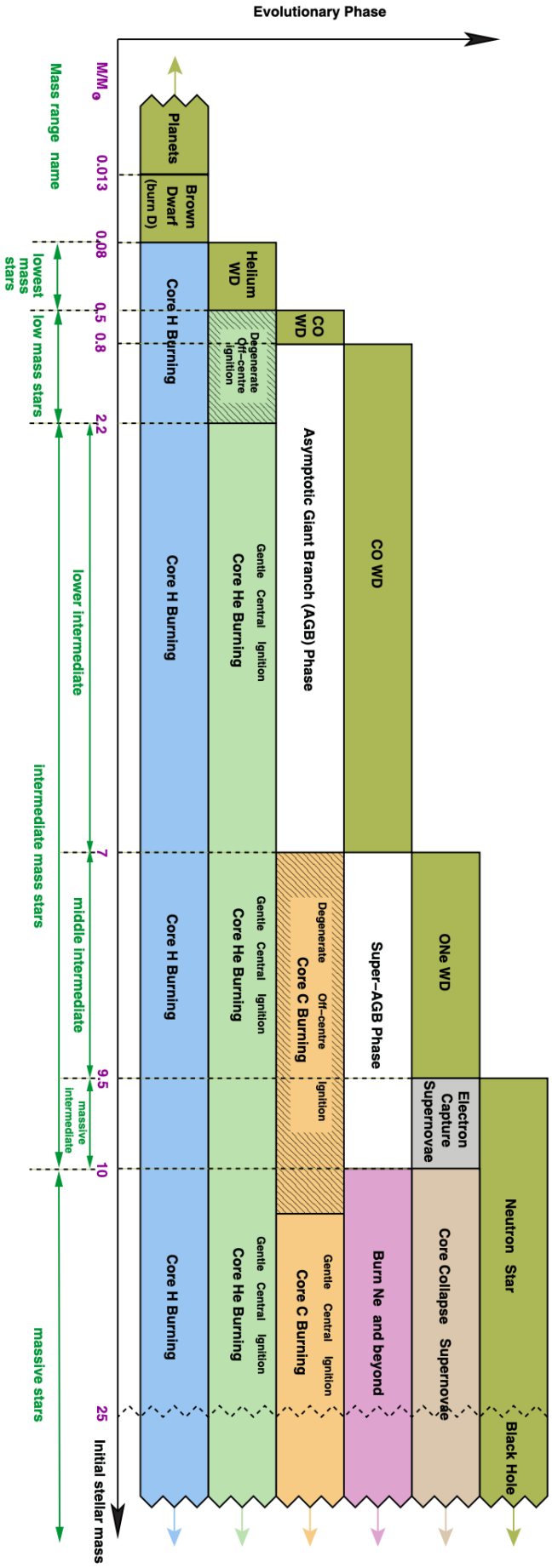

Figure 2.2: *The different evolutionary paths a star can take depending on its initial mass. (Karakas et al., 2014)*

2.2 Chemical elements

As discussed in Section 2.1, many chemical elements are produced through nuclear fusion in stars. However, other physical processes occur throughout the lifetimes of stars, resulting in the formation of specific elements. Figure 2.4 shows the periodic table of elements with their corresponding cosmic origin(s). In the following of this section, I present the main types of chemical elements in the context of stellar nucleosynthesis.

2.2.1 α and iron-peak elements

The α-elements are predominantly formed through fusion with a helium nucleus ^4He (also called α particle), resulting in their most abundant isotopes having nucleon numbers that are multiples of 4 (e.g. O, Ne, Mg, Si, S, Ar, Ca, Ti). They are mainly formed in *core-collapse supernovae* (*CCSNe* or *Type II SNe*) which correspond to the death of massive and therefore stars with relatively short lifetime. These elements are thus enriched in the interstellar medium (ISM) on a short timescale.
Iron-peak elements correspond to elements with atomic numbers close to iron (e.g. V, Cr, Mn, Co, Ni, Cu, Zn). In contrary to α-elements, they are produced in *Type Ia* (or *thermonuclear*) *supernovae* (*Type Ia SNe*) due to the explosive oxygen and silicon fusion. This type of SNe is believed to occur either through the merger of two white dwarfs or via the explosion of a white dwarf that has accumulated mass from a companion star, surpassing the Chandrasekhar mass limit. Only low and intermediate-mass stars become white dwarfs and since they have long lifetimes (see Section 2.1), *Type Ia SNe* appear only at large timescales in comparison to *Type II SNe*. These elements are thus enriched in the ISM on a longer timescale. Thanks to chemical evolution models that are detailed in Section 3.4.3, it is possible to understand chemical element abundance trends. In the case of α-abundances, the different timescale between these two kinds of SNe gives a typical trend, shown Fig.2.3, composed of a plateau at low metallicity (i.e. [Fe/H] see Section 2.4 for more details) and a decrease at higher metallicity values. The first part of the trend is due to the early enrichment of α-elements produced by *Type II SNe* and the second part corresponds to the enrichment in iron-peak elements via *Type Ia SNe*. This suggests that [α/Fe] abundance can be seen as a "galactic clock" indicating the duration of star formation, in the absence of other influencing factors.
A detailed study of α-elements in the inner Galactic bulge is presented in Chapter 3.

2.2.2 Neutron capture elements

In Section 2.1, the main stellar evolution scenarios were presented along with an explanation of how nuclear fusion produces elements up to iron. In the contrary, those heavier than iron cannot be produced through these processes but are instead produced by **neutron-capture** processes in different phases of stellar evolution. Depending on the strength of the neutron flux and the ability of unstable nuclei to decay between neutron captures, two distinct neutron-capture processes emerge: the rapid neutron-capture

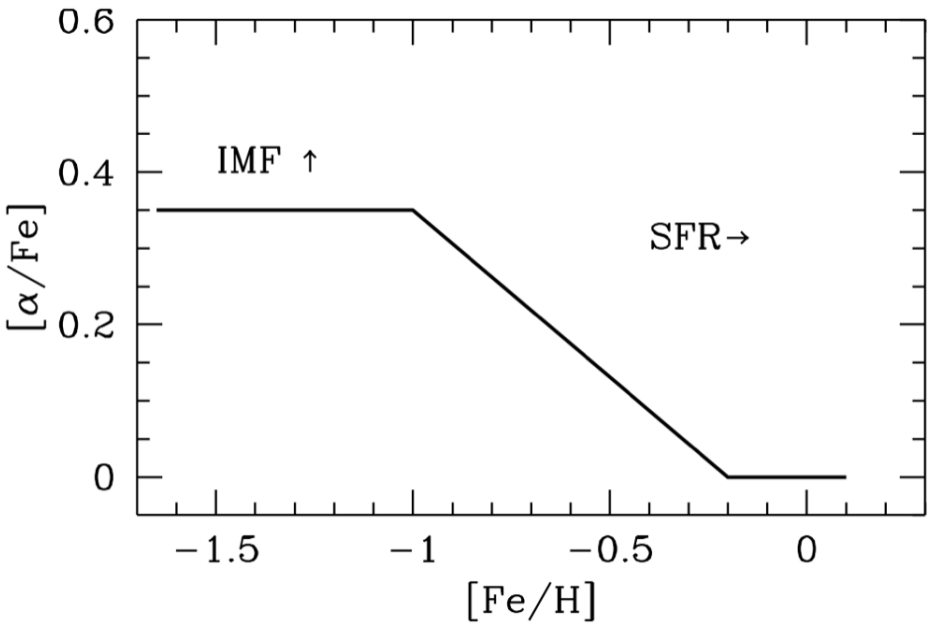

Figure 2.3: *Typical [α/Fe] vs. [Fe/H] trend (McWilliam, 1997)*

process (*r-process*) and the slow neutron-capture process (*s-process*). The former takes place in CCSNe and in mergers of neutron stars while the latter occurs in the interior of AGB stars. Nevertheless, the cosmic origin of these processes are still not entirely understood. Neutron-capture elements are therefore very different from the already well studied α and iron-peak elements and could help to better understand the Galactic evolution. These elements were recently measured in the Galactic disc with the Gaia survey (Contursi et al. 2023, Contursi et al. 2024) and with high-resolution spectrographs in both the disc and bulge (Forsberg et al. 2019, Forsberg et al. 2023).

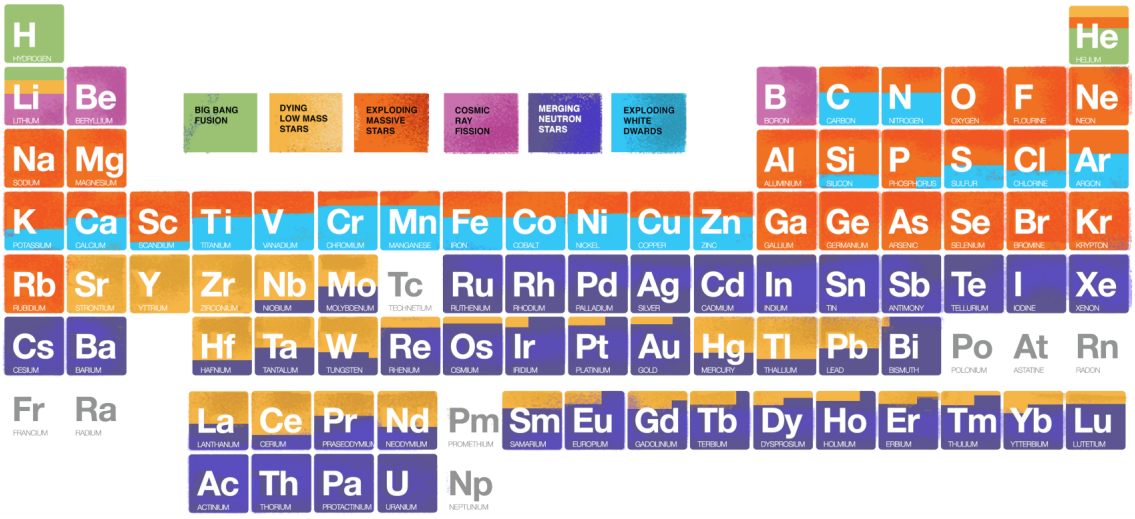

Figure 2.4: *Periodic table with indications of the cosmic origin(s) for each chemical element. Credit: NASA/CXC/K. Divona; SDSS blog, J. Johnson*

2.3 Chemical evolution models

Galactic chemical evolution seeks to elucidate the origins of chemical elements, how their abundances have evolved over time and their distribution throughout space. While the main nucleosynthesis processes were presented in Sections 2.1 and 2.2, this section shifts focus to **chemical evolution models** (CEM). Their objective is to track the temporal and spatial evolution of chemical element abundances within the interstellar medium (ISM). Such an evolution depends on various parameters that are used by CEM to simulate the galactic chemical enrichment:

- **Initial conditions** involve determining whether to adopt an open or closed model. In addition, the initial gas in which stars form can be primordial or enriched.
- The **star formation rate** (SFR), which corresponds to the masses that become stars per unit of time, and the **initial mass function** (IMF), which is the distribution of stars at birth as a function of mass, are used to determine the star formation history (SFH).
- **Stellar yields** quantify the amount of chemical elements produced by stars of different masses (i.e. released into the ISM upon the death of a star or stellar remnant). These yields are determined through comprehensive nucleosynthesis calculations that incorporate all the main nuclear reactions occurring within stars.
- **Gas flows** like infalls, outflows and radial flows, have to be taken into account in order to understand their effects on galactic chemical enrichment. For instance, abundance trends may reflect accretion events, and thus, their signatures can be discerned through observations.

For a more detailed description, see the review by Francesca Matteucci, 2021.

2.4 Stellar spectroscopy

2.4.1 Star light

As mentioned in the introduction of this chapter, the chemical composition of a star reflects the makeup of the gas from which it formed, making these "chemical fingerprints" a valuable record of its history and the conditions of its origin. To measure it, we analyse the light of the stars and more precisely their spectra which are a measurement of the intensity of the light as a function of the wavelength. The energy flux emitted in the burning core of stars is transported through the exterior via radiative diffusion, heat conduction and convection. Given the high opacity of stellar matter, photons have a very short mean free path and can take up to millions of years to travel to the photosphere. In the deeper regions of the star, the material is dense enough to emit light following a black body spectrum: a spectrum with a very specific shape which is determined by the temperature of the material. The latter is reshaped by both line and continuous absorption coming from atoms, ions and molecules as it passes through the

less dense outer layers of the stellar atmosphere. Observed stellar spectra thus provide rich information about the chemical composition of the star. By examining the position and shape of spectral lines, it is possible to identify the elements present in the star and measure their abundances.
In principle, the stellar spectrum reflects everything occurring in the outer layers of the star. However, it can be reproduced with radiative transfer codes and models of stellar atmosphere that only require elemental abundances and several key stellar parameters, provided that some assumptions are made. Indeed, the photosphere is often modelled only in the radial direction using one-dimensional (1D) models: the atmosphere is only assumed to change with depth. Three-dimensional (3D) stellar atmosphere models exist and are sometimes more precise, but are computationally very heavy. In the following, I will talk only of the stellar spectroscopy using 1D models.

2.4.2 Stellar parameters

The stellar parameters needed to model a stellar atmosphere are the following:

- The **effective temperature**, T_{eff}, is the temperature of an ideal black body that emits the same power per unit area as the star, $L = 4\pi R^2 \sigma T_{\text{eff}}^4$. Although stars are not perfect black bodies due to their varying emissivity across different wavelengths, the effective temperature is usually a good estimate of the temperature of the stellar photosphere.

- The **surface gravity** corresponds to $g = \dfrac{G\,M}{R^2}$ where M is the stellar mass, R the radius and G is the Newton's constant of gravity. Its 10-logarithmic form $\log(g)$ is commonly used. Since the hydrostatic equilibrium is assumed when computing chemical abundances, the surface gravity is strongly linked to the (gas and electron) pressure.

- The **metallicity** refers to the iron abundance given by:
  $[\text{Fe/H}] = \log_{10}\left(\dfrac{N_{Fe}}{N_H}\right) - \log_{10}\left(\dfrac{N_{Fe}}{N_H}\right)_{\odot}$
  It is the logarithm of the number density of iron atoms compared to hydrogen and scaled to the solar values. However, it can also be considered as a measure of the fraction of the star made up of elements other than hydrogen and helium. In this case it will be given by:
  $[\text{M/H}] = \log_{10}\left(\dfrac{N_M}{N_H}\right) - \log_{10}\left(\dfrac{N_M}{N_H}\right)_{\odot}$ with N_M the number density of metals. Metallicity is linked to the opacity of the atmosphere through the extra absorption contribution from additional metallic elements.

Because the turbulent motions in the stellar atmosphere cannot be described correctly in only 1D, two fudge parameters are necessary to take these motions into account:

- The **microturbulence**, ξ_{micro}, accounts for the small scale non-thermal motions.

More precisely it describes the gas cell movements in the stellar atmosphere that occur on a scale comparable to the mean free path of photons. These motions cause velocity shifts that are similar to those produced by thermal broadening (that is presented in Section 2.4.3) and are thus indistinguishable, and affects the line formation process.

- In the same way, the **macroturbulence**, ξ_{macro}, is used to describe the large scale motions of gas cells in the stellar atmosphere but this parameter only broadens the lines without affecting the line formation process.

2.4.3 Spectral line profile

It is worth noting that a line absorption is not evaluated independently, it is measured based on the difference between the line absorption and continuous absorption. The continuum arises from transitions such as bound-free, free-bound, and free-free processes. Hydrogen, which is abundant in stellar atmospheres, is the main contributor to continuous absorption: as neutral hydrogen in hot stars and as the ion H^- in cooler stars such as red giants. In the latter case, the extra electron required to form H^- originates from ionised metals[2], so the amount of continuous absorption is influenced by both the degree of ionisation and the chemical composition of the photosphere. For even cooler stars, molecules, and particularly the ionised state of H_2 and TiO, are also major contributors to continuous absorption.
The depth and width of spectral lines reflect the temperature, density, and other properties of the gas. As the concentration of an absorber increases, a spectral line goes through three main regimes: weak lines, saturated lines and strong lines. A weak line is initially narrow and mainly deepens as the abundance increases. The line will become stronger and deepen with the increasing amount of the absorbing species, until the core becomes saturated. At this stage, it no longer changes linearly with increasing absorption and the saturation grows asymptotically towards a constant value. In the final stage, the strength of the line increases approximately with the square root of the abundance, with most of the enhancement occurring in the wings of the line.

Line broadening

Although atomic line transitions are defined by a single wavelength value, the absorption lines observed in spectra display shapes that deviate significantly from a single Dirac delta function. In reality, these transitions can manifest various shapes depending on the conditions of the radiation medium and the characteristics of the absorbing atoms. Several broadening mechanisms can influence stellar spectral lines, often acting simultaneously.

- The **natural broadening** stems from the fact that the energy levels in an atom

[2] Magnesium is the most important electron donor in the atmosphere of cool giants.

cannot be perfectly precise due to Heisenberg's uncertainty principle. It gives the line profile a *Lorentzian* shape but is very small and does not affect stellar line broadening.

- The **thermal broadening** arises from Doppler shifts caused by the microscopic thermal movements of the absorbing atoms. These thermal motions adhere to the Maxwell-Boltzmann temperature distribution, resulting in a line profile that resembles a *Gaussian* shape. The addition of the microturbulence enters as an extra term in the thermal broadening.

- The **pressure broadening** is due to the perturbation of the transition energy levels made by the collisional interactions between the absorbing atoms and other particles in the atmosphere. This gives the line profile a *Lorentzian* shape and only affects the wings of strong lines.

- The spectrograph used to capture the spectrum introduces **instrumental broadening**. This is often assumed to create a *Gaussian* broadening, but in some cases, the instrumental profile may have a more complex shape. A higher spectral resolution leads to a smaller instrumental broadening. Instrumental properties are discussed in Section 2.4.4.

Other broadening processes can be considered as the line splitting due to hyperfine structure, isotopic structure, and Stark and Zeeman effects.

Local thermodynamic equilibrium and limitations

In *thermodynamic equilibrium*, energy exchanges within a system are balanced, but this concept fails to capture the behaviour of stars, which radiate massive amounts of energy. On the other hand, *local thermodynamic equilibrium* (LTE) describes a system in which, despite a potential net energy disparity, the rate of change is gradual enough that the temperature of a particle remains determined by collisions with its nearby environment. In other words, LTE assumes that the temperature does not vary significantly compared to the mean free path of photons. As a result, collisional excitation and de-excitation are the prevailing mechanisms that keep the populations of the energy levels at balance. When solving the radiative transfer equation, it means that absorption and emission at each location within the atmosphere conform to a black body spectrum corresponding to the temperature at that specific depth. In reality, the population of energy levels also relies on radiative mechanisms and consequently, the statistical equilibrium becomes linked with the radiation field.
Since stellar atmospheres become less dense as the depth decreases, the LTE approximation may become less valid in the outer layers and does not account for important radiative effects (in a NLTE analysis, one is not restricted to an LTE case). The latter are therefore especially important in giant stars. Typically, LTE predicts the cores of strong

lines to be shallower, as they primarily form further out in the atmosphere and are thus more susceptible to NLTE effects.

2.4.4 Instrumentation

Galactic archaeology critically depends on the extraction of stellar properties, their atmospheric parameters, and their chemical composition. As mentioned earlier, various physical processes contribute to and influence the formation of spectral lines and, consequently, the stellar spectra. In addition, the characteristics of the spectrograph used to collect starlight also affect the observed spectra.

- The **spectral resolution**, $R = \frac{\lambda}{\Delta\lambda}$ (where $\Delta\lambda$ is the smallest difference in wavelengths at a given wavelength λ), is an essential parameter to take into account in stellar spectroscopy. Depending on the observed type of star and the quantity to measure (e.g. stellar parameters, chemical abundances), the choice of resolution significantly impacts the precision of the measurement. A lower resolution tends to smear out weak lines, lines blend into each other and the surrounding continuum. Therefore, chemical abundances determination requires a sufficiently high resolution in order to derive precise values while stellar parameters can still be determined with low resolution stellar spectra. A visual comparison of different spectral resolutions corresponding to current or future spectrographs is shown in Figure 2.5. In the context of this thesis, high-resolution spectra were used to derive abundances (see the corresponding projects in Chapters 3 and 4).

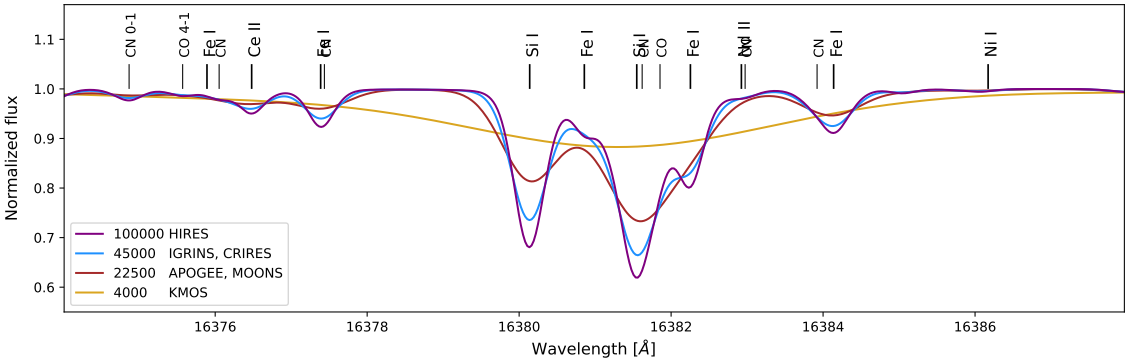

Figure 2.5: *Example of the effect of spectral resolution in the case of a K-giant (T_{eff} = 4738 K, $\log(g) = 2.39$, [Fe/H] = −0.81)*

- The **signal-to-noise ratio** (SNR) that comes from the discrete quantity of photons received by the spectrograph, the internal noise of the latter, and the sky noise to name but a few, measures how well the stellar spectrum is recovered. A higher SNR leads to more precise measurements.

Other parameters like the wavelength coverage, limiting brightness and number of stars observed have to be considered in order to get rigorous results and depend on the

purpose of the study.

2.4.5 Methods to analyse spectra

The determination of atmospheric parameters and abundances from stellar spectra can generally be achieved via two main methods: the measurement of the equivalent width and the spectral synthesis.

- The **equivalent width** (EW) is the width of a box from zero to the continuum with the same area as the absorption line. The EW is measured by fitting a Gaussian profile to the spectral line or by direct integration. A radiative transfer code is needed to derive the line abundance based on a specified set of initial atmospheric parameters. This method is really successful for weak isolated lines observed at high spectral resolution and high signal-to-noise ratio. However, if lines are blended, the derived abundance will be overestimated and that is why crowded spectral regions have to be discarded when using this method. Also, the determination of the continuum is essential to have a precise measurement of the abundance.

- The **spectral synthesis** technique consists in comparing the observed spectrum with synthetic spectra that are generated using a radiative transfer code and model atmospheres grids. A minimisation algorithm allows to find the best fit. If most of the spectral lines within the examined region are identified, blending is not an issue in the abundance measurement. However, as for the equivalent width method, the determination of the continuum is essential to derive precise abundances. Moreover, the latter depend also on the assumptions used (e.g. 1D or 3D model atmosphere, LTE or NLTE) and the precision of the parameters (e.g. stellar parameters, atomic data). Several tools exist for this task, but I used Spectroscopy Made Easy (SME) for the purposes of this thesis (see its detailed description in the following).

For more details, see the reviews from Nissen and Gustafsson (2018) and Blanco-Cuaresma (2019).

Spectroscopy Made Easy

Spectroscopy Made Easy (SME) is a code that allows to model stellar spectra and fit them to observed spectra (J. A. Valenti and Piskunov 1996a, Piskunov and Valenti 2017a). As a spectral synthesis software, SME operates by modelling the photosphere of a star and simulating the passage of light through it. To do so, it requires several inputs:

- Stellar parameters[3] (presented Section 2.4.3) and also chemical abundances[4]. The

[3] In SME, the macroturbulence parameter accounts for the stellar macroturbulence defined in Section 2.4.3, the stellar rotation and the instrumental profile.

[4] The reference solar abundances used in this thesis are from Grevesse et al., 2007a

quantities to be determined are set to "free" parameters.

- ✦ SME needs that the user specifies several masks: line masks to identify which spectral features to fit and continuum masks to do the continuum normalisation.
- ✦ To model the atmosphere of the studied star, SME generates an interpolated model based on a MARCS2014[5] model grid (Gustafsson et al., 2008b) and the input stellar parameters. In this thesis, I used 1D spherical symmetric models, particularly suited for giant stars[6].
- ✦ SME assumes that radiation transport in the stellar atmosphere occurs in LTE (see Section 2.4.3) but NLTE departure coefficients can be used to account for deviations from the LTE approximation. The latter are given to SME as grids.
- ✦ A line list that contains all the atomic/molecular data to describe the lines of the studied spectral region (e.g. central wavelengths, ionisation stage, oscillator strengths, upper and lower excitation energies of transition levels, line-broadening parameters).

When fitting synthetic spectra to observed spectra, SME minimises a goodness-of-fit metric χ^2_{SME} to derive chemical abundances or stellar parameters.

[5] *Model Atmospheres with a Radiative and Convective Scheme* (MARCS) is a code that models stellar atmospheres. It assumes a 1D atmosphere in hydrostatic equilibrium, utilising either a plane-parallel or a spherical geometry.

[6] Due to the large scale heights and extensions of the atmosphere of giant stars, spherical symmetry is required. In the contrary, plan-parallel symmetry works well for dwarfs.

Additional comments on stellar spectroscopy in the context of this thesis

Observing in *near-infrared* (NIR) is necessary to avoid as much as possible the heavy extinction in the central regions of the Galaxy. In addition, *red giants* are of particular interest since their high luminosity allows to get spectra with higher SNR at larger distances. However, they present several disadvantages that we have to deal with:

- Their *low effective temperature*, ranging from $3000K$ to $5000K$, leads to spectra containing many molecular lines more complicated to analyse because of blending and a less well defined continuum.

- Their *low surface gravity* ($\log(g) < 3.5$) and then lower electron pressure induce a lower continuum opacity. Lines are therefore more often saturated and less sensitive to the corresponding abundances. Line selection is even more important.

In order to measure detailed stellar metallicities and abundances for such cool stars, high-resolution spectroscopy is essential. That is why I used in this thesis data from CRIRES and IGRINS which have a spectral resolution about $R \sim 50000$. Moreover, accurate atomic and molecular data are very important to synthesise realistic spectra with SME. Giving the small number of stars observed in the central regions and the complexity of their spectra, each best fit between synthetic and observed spectra was visually checked. This time consuming work is necessary to get very precise measurements.

3

Detailed α abundance trends in the inner Galactic bulge

Published in Astronomy & Astrophysics | A&A 671, A94 (2023)
Authors: N. Nieuwmunster, G. Nandakumar, E. Spitoni, N. Ryde, M. Schultheis, R. M. Rich, P. S. Barklem, O. Agertz, F. Renaud, F. Matteucci

In order to understand the formation and evolution of galaxies, we must begin by studying our own. To this purpose, the kinematics, dynamics, and chemical composition of stars are analysed mainly using orbit simulations and spectroscopy in order to set constraints on their formation processes. The different chemical elements observed in stellar spectra are created and distributed into the Galaxy by a large variety of astronomical processes, from nucleosynthesis in stars to that in supernovae. Among these elements, the α-elements are the most commonly used for probing the stellar populations in the Galaxy. They are spread into the interstellar medium by means of core-collapse supernovae, which are violent events due to the death of the short-living massive stars. On the contrary, iron is mainly disseminated via thermonuclear supernovae, which happen on a longer timescale. This longer timescale means that the enrichment of the interstellar gas varies with time and thus the α-abundances found in stars depend on the time of their birth. α-elements are therefore useful for determining the spatial (e.g. in situ or accreted) and temporal origins of stars; see for example Agertz et al., 2021,Renaud et al., 2021b and Renaud et al., 2021a.

In addition to the already well analysed Galactic discs, the inner regions of the Milky Way, —the bulge, the nuclear stellar disc, and the nuclear star cluster— are of specific interest in the quest to attain a complete picture of Galactic history. However, dust extinction towards the inner regions has prevented studies of these regions. More studies are therefore needed to unveil the details of the various stellar populations occupying these structures. In the study of the Galactic bulge[1], industrial spectroscopy in both the optical and IR has become commonplace during the last decade, with surveys such as

[1] Here defined purely geometrically as the inner 10 degrees of the Milky Way (Barbuy et al., 2018b).

Gaia-ESO (Randich et al., 2022), APOGEE (Abdurro'uf et al., 2022a), and GALAH (Buder et al., 2021). These investigations have been powerful, especially in producing large numbers of abundance and composition measurements. However, nearly all industrial spectroscopy projects forego abundance analysis and spectrum synthesis for individual stars, instead developing a range of tools from label matching to machine learning, which exploit high-resolution spectra and speed up their analysis via an automated pipeline. Interestingly, some of the abundance trends and major conclusions, while showing the overall declining trend of [α/Fe] versus [Fe/H], also reveal significant differences in shape; for example, Queiroz et al., 2020 show two dominant trends: an alpha-enhanced thick disc trend, and a low alpha population that predominates in the central kiloparsec.

The original hypothesis that the bulge is alpha-enhanced relative to the thin and thick disc (McWilliam et al., 1994; Lecureur et al., 2007; Zoccali et al., 2008; Fulbright et al., 2007; Johnson et al., 2014) has begun to yield to abundance trends that appear increasingly similar to a thick disc that extends to higher metallicity, $\sim$ +0.5 dex (Meléndez et al., 2008; N. Ryde et al., 2010; A. Rojas-Arriagada et al., 2017b; Zasowski et al., 2019). A general picture has emerged according to which the dynamical bar becomes dominant at [Fe/H]> -0.5 dex (Soto et al., 2007; Ness et al., 2013b) and the metal-rich population is concentrated in the plane (Ness et al., 2013b; Johnson et al., 2020; Johnson et al., 2022). New data have therefore challenged the early paradigm that the bulge formed early, rapidly, and with high [α/Fe] set by Francesca Matteucci et al., 1990 and McWilliam et al., 1994. If the bulge/bar abundance trends are understood as resembling those of the thick disc but extended to +0.5 dex, this is an important paradigm shift that has implications for how we consider the formation history of the bar and its relationship to the disc.

There is accumulating evidence in support of the view that the bulge contains at least two different structures or populations: (i) a metal-rich population that is most likely associated with the bar and therefore with a secular formation origin from the early disc (see e.g. Ness et al. 2012, A. Rojas-Arriagada et al. 2017b; Alvaro Rojas-Arriagada et al. 2020a, Zoccali et al. 2017) and (ii) a metal-poor population that dominates away from the plane (Johnson et al., 2020; Johnson et al., 2022) and whose formation scenario is less clear; suggestions include association with an early merger event, metal-enriched outflows, or secular evolution of the thick disc.

These paradigm shifts regarding the bulge challenge us not only to increase the sample size of abundance measurements, but also to reconsider making the most careful possible abundance determinations on smaller samples, particularly in the IR, where the most immediate advances in high-resolution spectroscopy are anticipated.

High-resolution, detailed abundance measurements near the plane and Galactic centre

remain relatively sparse because of very high extinction. So far, the great majority of observations have been made in regions of relatively low extinction; for example, Baade's window, where many optical and IR studies exist. APOGEE used this window to obtain a high-quality set of chemical abundances (Schultheis et al., 2017). This is important if one wants to compare chemical abundances obtained by different instrument setups (e.g. wavelength range, spectra resolution, S/N, etc.) as each of those can introduce significant bias. However, a similar work but closer to the Galactic plane is missing. Nandakumar et al., 2018 provide the largest sample of stars with high-resolution spectroscopic measurements near the plane, with their work finding no asymmetry between the northern and southern bulge, and confirming the presence of a metal-poor peak near -0.5 dex.

Even in the era of industrial-scale spectroscopy, the development of small, high-quality samples analysed with different approaches has value, and especially in regions of high extinction and crowding near the plane. In this work, I therefore make use of the data sets provided by N. Ryde et al., 2015, N. Ryde et al., 2016a and Nandakumar et al., 2018 and reanalyse them consistently with updated methods. I apply new distance determinations and models of orbits, and use NLTE spectrum synthesis to give the best possible modern composition measurements of this sample. I additionally take advantage of new high-resolution, high-S/N IGRINS spectra of thin and thick disc stars in the solar neighbourhood. I report new trends in Si, Mg, and Ca in the inner galaxy, and fit the [Fe/H] distribution with chemical-evolution models.

3.1 Observations

I analysed high-resolution, near-IR spectra of stars in both the inner Galactic bulge and a local comparison sample. Observations were performed with the CRIRES and ISAAC spectrographs on the Very Large Telescope (VLT), the SOFI spectrographs on the New Technology Telescope (NTT), and the IGRINS spectrograph on the 4.3 m Lowell Discovery Telescope and the 2.7m McDonald telescope.

3.1.1 Inner bulge sample

The high-resolution, near-IR spectra of the 72 inner bulge giants analysed here for stellar abundances were observed in 2012-2013 with CRIRES (Kaeufl et al., 2004; Alan Moorwood, 2005; Käufl et al., 2006) mounted on the VLT, and are described in detail in Nandakumar et al. (2018) (Paper I). A relatively short wavelength coverage was observed in the K band, namely 20 818 – 21 444 Å, but at a spectral resolving power of $R \sim 50\,000$.

The effective temperatures of the stars needed for the analysis were determined in Paper I from low-resolution, K-band spectra ($R \sim 1000 - 2000$). These spectra were observed with the ISAAC (A. Moorwood et al., 1998b) on the VLT and the SOFI spectrographs

(A. Moorwood et al., 1998a) on ESO's NTT telescope on La Silla.

Stars in six fields along the minor axis, both south and north of the Galactic centre, were observed at both high and low spectral resolution; see Table 3.1 and 3.2. Among the 72 M giants, 44 belong to northern fields, 19 to southern fields, and 9 to a centre field. The stars in the latter field lie 2.5 – 5.5 arcmin north of the very centre of the Milky Way —which corresponds to a projected galactocentric distance of 5 – 10 pc— and probably belong to the nuclear disc and not the nuclear star cluster (cf. N. Ryde et al., 2016b; R. M. Rich et al., 2017).

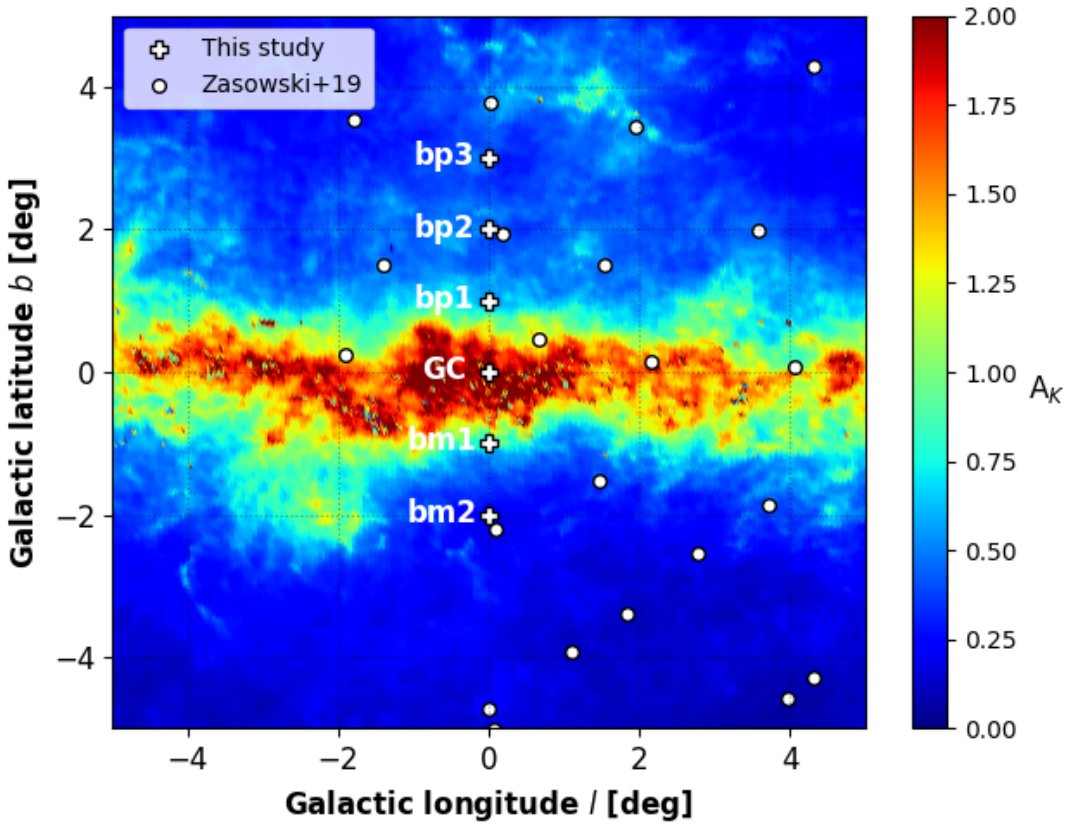

Figure 3.1: *Location of the inner Galactic bulge fields studied in this work and those from Zasowski et al., 2019 (only those visible in this frame) in Galactic coordinates superimposed on the interstellar extinction map of Gonzalez et al., 2012.*

3.1.2 Solar neighbourhood sample

In order to minimise possible systematic uncertainties in the analysis of the abundance trends for the inner Galactic bulge, I observed similar types of stars in the Galactic discs as locally as possible. With determined abundance trends from these stars, I can search and study possible differences in a differential way. This comparison sample of 37 solar neighbourhood K giants was observed with the Immersion GRating INfrared Spectrograph (IGRINS; Yuk et al., 2010; Wang et al., 2010; Gully-Santiago et al., 2012a; Moon et al., 2012; Park et al., 2014; Jeong et al., 2014) in 2016 on the 4.3

m Discovery Channel Telescope (DCT; now called the Lowell Discovery Telescope) at Lowell Observatory (Mace et al., 2018), and on the 2.7 m Harlan J. Smith Telescope at McDonald Observatory (Mace et al., 2016). The near-IR spectra provided by the IGRINS span the full H and K bands (1.45 - 2.5 μm) with a spectral resolving power of R $\sim$ 45000. Details of observations and data reduction are explained in detail in Nils Ryde et al., 2020, Montelius et al., 2022 and Nandakumar et al., 2022.

3.2 Analysis

In this study, I determined the abundance trends versus metallicity of the α-elements Mg, Si, and Ca for the inner bulge sample, as well as the local comparison sample with the same method. I made an effort to clarify the membership of the stars in my inner bulge sample by determining accurate distances and performing a dynamic analysis of the stars. In this way, I was able to disregard any star in the sample that is obviously not a bulge member. Furthermore, I adopted an updated K-band line list with determined astrophysical line strengths and improved van der Waals as well as Stark broadening parameters. I also applied and discuss non-LTE corrections for all spectral lines.

3.2.1 Spectroscopic analysis

Stellar parameters

Proper determination of the stellar parameters (i.e. $T_{\rm eff}$, $\log(g)$, [Fe/H], and $\xi_{\rm micro}$) of the stars is fundamental for an accurate and precise abundance determination. The effective temperatures used in this paper were determined in Paper I based on the relation between the effective temperature and the ^{12}CO-band-head strength in low-resolution spectra at 2.3 μm. The method is described in Schultheis et al. (2016) and results in typical uncertainties of ±150K. Furthermore, first estimations of the metallicities are determined using $\log(g)$ and $\xi_{\rm micro}$ from Paper I. Given these metallicities, new surface gravities and microturbulences were then determined with the iterative method from R. M. Rich et al. (2017) and the empirical relation between microturbulence and surface gravity from V. V. Smith et al. (2013a), respectively. Typical uncertainties in surface gravity are of ±0.3 dex after a few iterations.

The line shapes and widths are important in my analysis because I compare synthesised lines with observed ones. Therefore, I carefully analyse the widths of the lines and estimate a general macroturbulence, $\xi_{\rm macro}$, for each star using manually selected Gaussian-shaped spectral lines from Mg, Al, and Si. The updated broadening parameters for these lines will be important for the stronger lines.

The new stellar parameters are given in Tables 3.1 and 3.2. For my star sample, $T_{\rm eff}$ is in the range 3400 - 4400 K and $\log(g)$ is within 0.4 - 2.0 dex. Uncertainties in the derived

abundances[2] are due to the fitting procedure and to the uncertainties on the stellar parameters (as shown in R. M. Rich et al., 2017; N. Ryde et al., 2016a) and are already well discussed in Section 3.4 of Paper I. It has been shown that the fitting procedure is the main contributor to the abundance error. Therefore, as in Paper I, I adopt a main abundance uncertainty of ±0.15dex.

Line list

In order to determine reliable abundances for different elements from stellar spectra, information about the atomic physics data for the spectral lines corresponding to each element are needed: the central wavelength of the line, upper and lower excitation energies of transition levels, line strengths ($\log gf$), broadening parameters, and so on. The line list has all this information, which is necessary in order to synthesise spectral lines. VALD (Ryabchikova et al., 2015) assimilates this information from a large collection of sources, which I use as my base line list in this work.

However, the line list was primarily updated with $\log gf$ values for my lines of interest (without reliable experimental $\log gf$ values), which were determined astrophysically using the high-resolution IR solar flux spectrum of Wallace et al., 2003. This is done by finding the value of $\log gf$ for which the respective line in the solar-flux spectrum is best fitted by the synthetic spectrum.

The collisional broadening due to neutral hydrogen, and in some cases charged particles, is important for strong lines with damping wings. For collisional broadening due to hydrogen, where possible, I have used parameters from the ABO theory (Anstee et al., 1991; Anstee et al., 1995; P S Barklem et al., 1997; P S Barklem et al., 1998) taken from the spectral synthesis code BSYN based on routines from MARCS (Gustafsson et al., 2008a). For the Mg I lines at 21059.75 Å and the multiplet at 21060.71 - 21061.095 Å, the parameters used in Paper I for collisional broadening due to hydrogen were $\sigma(v = 10^4 \mathrm{m/s}) = 2927\, a_0^2$, with velocity parameter $\alpha = 1.313$[3]. These values were calculated using the impulse approximation (Kaulakys, 1985; Kaulakys, 1991; Hoang Binh et al., 1995; Osorio et al., 2015) based on Coulomb wave functions in momentum space (Hoang Binh et al., 1997; P. S. Barklem, 2015), but neglecting elastic contributions because of the problem of estimating the interference between the lower and upper level contributions. In this work, rather than neglecting the elastic contribution, the maximum and minimum possible contributions, that is respectively, the completely constructive and destructive interference cases, were estimated. The mean of these two extreme elastic contributions was then added to the inelastic contribution, and it

[2] The solar value used in this study is from Grevesse et al., 2007b

[3] Here σ is the broadening cross section and α describes the velocity dependence assuming a power law $\sigma \propto v^{-\alpha}$.

Table 3.1: *Stellar parameters of the observed stars in the northern fields of the inner Galactic bulge. The names of stars belonging to my Golden Sample (see Section 3.3.4) are marked in bold face.*

Star	$T_{\rm eff}$ [K]	$\log(g)$ (cgs)	[Fe/H]	$\xi_{\rm macro}$ [km s^{-1}]	$\xi_{\rm micro}$ [km s^{-1}]
Northern field at $(l, b) = (0°, +3°)$					
bp3-01	3780	0.75	-0.67	4.9	2.2
bp3-02	4111	1.83	0.08	4.2	1.8
bp3-04	3623	0.67	-0.34	6.0	2.3
bp3-05	3879	1.67	0.50	5.9	1.8
bp3-06	3755	0.63	-0.78	3.7	2.3
bp3-07	3962	1.77	0.40	5.5	1.8
bp3-08	3637	1.04	0.20	6.0	2.1
bp3-10	4052	1.74	0.12	4.4	1.8
bp3-11	3542	0.69	-0.06	6.4	2.3
bp3-12	3966	1.36	-0.21	6.4	1.9
bp3-13	3625	0.84	-0.05	7.2	2.2
bp3-14	3569	0.63	-0.26	6.4	2.3
bp3-15	3610	0.53	-0.55	5.9	2.4
bp3-16	3654	0.84	-0.13	7.0	2.2
bp3-17	3946	1.35	-0.16	5.3	1.9
Northern field at $(l, b) = (0°, +2°)$					
bp2-01	4054	1.93	0.38	5.6	1.8
bp2-02	3838	1.31	0.08	5.6	1.9
bp2-03	3889	1.45	0.14	6.6	1.9
bp2-04	4134	1.60	-0.32	4.9	1.9
bp2-05	4079	1.36	-0.55	5.0	1.9
bp2-06	3962	0.47	-1.80	5.6	2.4
bp2-07	4320	1.77	-0.59	4.0	1.8
bp2-08	3808	1.29	0.13	6.0	2.0
bp2-09	3813	0.79	-0.69	4.0	2.2
bp2-10	3774	1.29	0.20	5.2	2.0
bp2-11	3645	1.10	0.26	6.3	2.0
bp2-12	4032	1.17	-0.71	7.6	2.0
bp2-13	3899	1.10	-0.45	4.2	2.0
bp2-14	3559	0.85	0.11	5.5	2.2
bp2-15	4237	1.51	-0.74	5.7	1.9
Northern field at $(l, b) = (0°, +1°)$					
bp1-01	3918	1.69	0.40	5.6	1.8
bp1-02	4311	1.47	-0.99	5.0	1.9
bp1-03	3948	1.79	0.49	7.5	1.8
bp1-04	4060	1.67	-0.01	5.9	1.8
bp1-05	3731	1.34	0.37	5.2	1.9
bp1-06	3863	1.18	-0.18	6.3	2.0
bp1-07	4209	1.47	-0.73	3.9	1.9
bp1-08	4242	1.65	-0.56	5.3	1.9
bp1-09	3494	1.00	0.49	4.9	2.1
bp1-10	3879	1.40	0.10	5.6	1.9
bp1-11	4352	1.94	-0.42	5.4	1.8
bp1-12	4175	1.91	0.01	5.2	1.8
bp1-13	4151	1.45	-0.60	5.3	1.9
bp1-14	4070	1.63	-0.10	4.2	1.9

Table 3.2: *Stellar parameters of the observed stars in the southern fields of the inner Galactic bulge. The names of stars belonging to my Golden Sample (see Section 3.3.4) are marked in bold face.*

Star	$T_{\rm eff}$ [K]	$\log(g)$ (cgs)	[Fe/H]	$\xi_{\rm macro}$ [km s^{-1}]	$\xi_{\rm micro}$ [km s^{-1}]
Galactic Centre field at $(l, b) = (0°, 0°)$					
GC1	3668	1.12	0.23	5.6	2.0
GC20	3683	1.25	0.36	8.3	2.0
GC22	3618	1.13	0.36	4.9	2.0
GC25	3340	0.67	0.37	6.6	2.3
GC27	3404	0.68	0.26	5.5	2.3
GC28	3773	1.34	0.28	6.1	1.9
GC29	3420	0.86	0.46	6.4	2.2
GC37	3754	1.42	0.44	7.0	1.9
GC44	3465	0.96	0.49	4.9	2.1
Southern field at $(l, b) = (0°, -1°)$					
bm1-06	3814	1.54	0.46	6.1	1.9
bm1-07	3873	1.44	0.17	5.1	1.9
bm1-08	3650	1.21	0.39	6.0	2.0
bm1-10	3787	1.10	-0.09	4.9	2.0
bm1-11	3812	1.48	0.38	6.8	1.9
bm1-13	3721	0.44	-0.93	4.9	2.4
bm1-17	3775	0.56	-0.91	5.6	2.4
bm1-18	3780	1.48	0.46	5.6	1.9
bm1-19	3958	1.76	0.40	5.3	1.8
Southern field at $(l, b) = (0°, -2°)$					
bm2-01	3946	1.51	0.08	3.5	1.9
bm2-02	4013	1.44	-0.22	6.7	1.9
bm2-03	3668	1.24	0.39	6.0	2.0
bm2-05	3450	0.86	0.39	6.1	2.2
bm2-06	4208	1.29	-0.97	5.1	2.0
bm2-11	4005	1.16	-0.65	6.0	2.0
bm2-12	4003	1.73	0.23	6.5	1.8
bm2-13	3727	1.05	0.00	5.0	2.1
bm2-15	3665	1.31	0.52	6.3	1.9
bm2-16	3886	1.58	0.32	4.7	1.9

led to $\sigma(v = 10^4 \mathrm{m/s}) \approx 4440\, a_0^2$ and $\alpha = 1.10$. The error in the cross section due to the uncertainty in the elastic contribution is roughly 15%, with the overall uncertainty from this method probably being at least of order 30%.

Further, for the 21059 Å line, data for Stark broadening were extracted from the Stark-B database (Sahal-Bréchot et al., 2015), the data originating from Dimitrijevic et al., 1996. Combining the data for broadening due to electrons (e) and protons (p) with the assumption $N_p = N_e$, and converting to the format conventionally used in many spectrum-synthesis codes for quadratic Stark broadening, $\log \Gamma/N_e = -2.56$ at $T = 10000$ K was found, where Γ is the full-width at half maximum in rad/s and N_e is in cm^{-3}. No data was found for the 21060.71 - 21061.095 Å multiplet. As this multiplet is analogous to the 21059 Å transition but in the triplet term system, the Stark broadening for this multiplet is assumed to be the same as the line in the singlet system. The combination of the increased collisional broadening due to hydrogen and the strong Stark broadening significantly improved the agreement with the observed spectrum in the Sun.

In addition to the Sun spectrum, the high-resolution (R ~ 100000) IR spectrum of the well-studied Arcturus from the Arcturus atlas (Hinkle et al., 1995) was used to validate the updated line strengths of Fe, Mg, Si, and Ca lines. Arcturus is a well-studied reference star with reliable stellar parameters determined using various methods and is a cool giant similar to the stars investigated in this work. Mean values of -0.5, 0.22, 0.27, and 0.29 dex were determined for [Fe/H] (excluding four Fe lines that were noisy or telluric affected in the Arcturus spectrum), [Mg/Fe], [Si/Fe], and [Ca/Fe], respectively, with less than 0.05 dex line-by-line dispersion for each element assuming the stellar parameters from Ramírez et al., 2011. In addition, the same line list was used to determine the elemental abundances of the 37 solar neighbourhood giants using the same set of lines (see Section 3.2.1 and upper panels of Figure 3.7).

The central wavelengths, updated $\log gf$ values, and broadening parameters for the spectral lines used in this work are listed in Table 3.3. For the molecular lines, the line data from G. Li et al. (2015), Sneden et al. (2014), and Brooke et al. (2016) were used for CO, CN and OH respectively.

Spectral synthesis

I used Spectroscopy Made Easy (SME version 583, J. A. Valenti et al. (1996b) and Piskunov et al. (2017b)) for the spectral analysis. For a given set of stellar parameters, in order

[4] a: Collisional broadening by neutral hydrogen gives either the broadening cross section $\sigma(v = 10^4 \mathrm{m/s})$ in atomic units (a_0^2), with velocity parameter α (see text for more details), or if the value is negative and no α given, then the line width is given in the standard form $\log \Gamma/N_H$ at $T = 10000$ K, where Γ is the full-width at half maximum in rad/s and N_H is in cm^{-3}. 1: Kurucz, 2007, 2: BSYN based on routines from MARCS code Gustafsson et al., 2008a, 3: see text, 4: Brault et al., 1983, 5: Civiš et al., 2013, 6: Kurucz, 2014, 7: manual entry by NIST lookup, *: astrophysical estimate

Table 3.3: *Spectral line data for the lines used in the present study.*

Element	Wavelength ()	log (gf)	Broadening by H [a]	α
Si	20804.225 [1*]	-1.026 [1*]	861 [2]	0.292
	20890.415 [1*]	-1.613 [1*]	859 [2]	0.292
	20908.625 [1]	-1.453 [1*]	-6.990 [1]	
	20917.151 [1]	0.288 [1*]	1485 [2]	0.324
	20926.149 [1]	-1.076 [1*]	1484 [2]	0.324
	21056.379 [1*]	-0.505 [1*]	-7.032 [1*]	
	21139.759 [1]	-0.501 [1*]	-6.880 [1]	
	21143.260 [1*]	-0.619 [1*]	-6.880 [1]	
	21204.492 [1*]	-0.388 [1*]	-6.880 [1]	
Mg	21059.757 [4*]	-0.384 [5*]	4440 [3]	1.10
	21060.710 [4*]	-0.530 [5]	4440 [3]	1.10
	21060.896 [4*]	-1.587 [5]	4440 [3]	1.10
	21060.896 [4*]	-0.407 [5]	4440 [3]	1.10
	21061.095 [4*]	-3.383 [5]	4440 [3]	1.10
	21061.095 [4*]	-1.583 [5]	4440 [3]	1.10 [4]
	21061.095 [4*]	-0.298 [5]	4440 [3]	1.10
Ca	20962.570 [1*]	-0.784 [1*]	-7.230 [1]	
	20972.529 [1]	-1.002 [1*]	-7.230 [1]	
	20973.378 [1]	-1.436 [1*]	-7.230 [1]	
Fe	20798.893 [6]	-3.525 [6]	-7.280 [6]	
	20799.685 [6]	-0.613 [6*]	-7.021 [6*]	
	20805.113 [7*]	-0.065 [7*]	-7.076 [7*]	
	20840.835 [6*]	0.104 [6*]	-7.134 [6*]	
	20882.233 [6]	-0.935 [6*]	-7.330 [6]	
	20948.086 [6]	-0.796 [6*]	-6.861 [6*]	
	20991.083 [6*]	-3.058 [6*]	-7.730 [6]	
	21036.355 [6]	-0.817 [6*]	2656 [2]	0.330
	21095.401 [6]	-0.658 [6*]	-7.000 [6*]	
	21105.217 [6]	-0.749 [6*]	-7.320 [6]	
	21124.505 [6*]	-1.647 [6*]	975 [2]	0.302
	21162.095 [6*]	-0.605 [6*]	1364 [2]	0.328

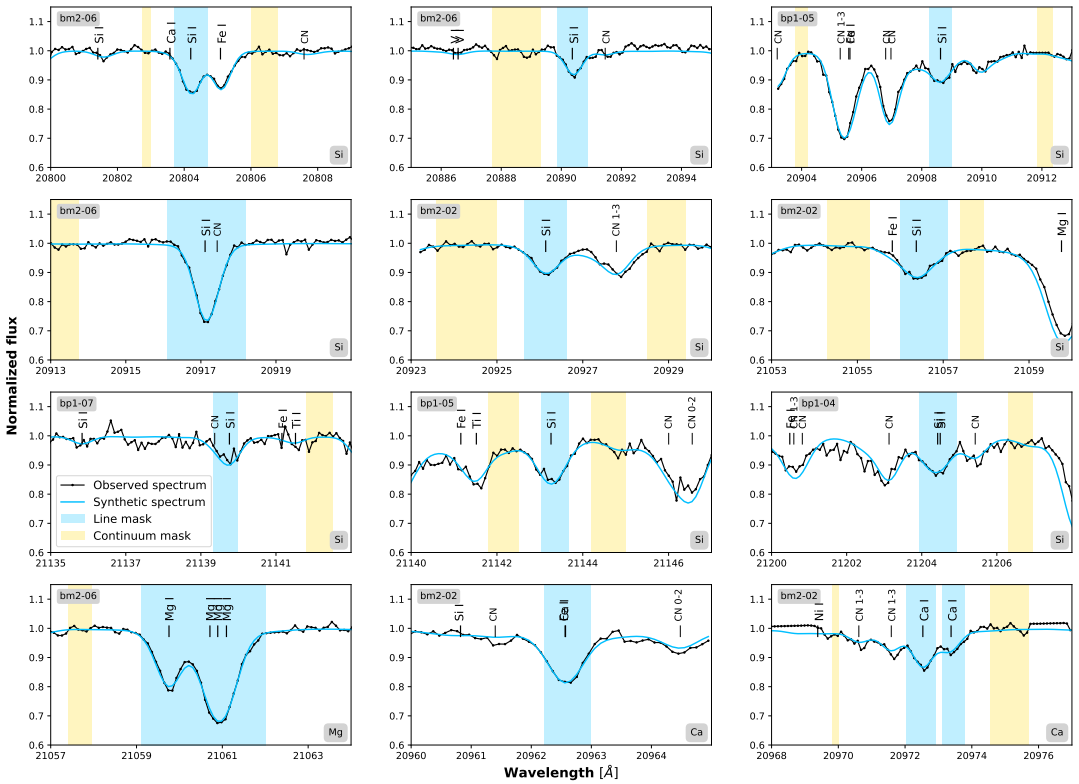

Figure 3.2: *Typical spectral fits for Si (the nine upper plots), Mg (lower left), and Ca lines (lower middle and right) used in the analysis. The stellar name is given in the upper left corner of every subplot. The black observed data are fitted with the blue synthetic spectrum. The lines of interest are marked with the blue line masks. The yellow masks show the regions in the spectrum that are used to normalise the local continuum around the lines. In some of the plots, these continuum regions are outside of the figure. The linear local continuum is always fitted with at least three continuum windows in every segment close to the line of interest.*

to generate synthetic spectra, SME interpolates a model atmosphere from a grid of spherically symmetric MARCS models computed using LTE. To account for non-LTE effects, SME applies departure coefficients by interpolating in grids. In this study, I used this type of non-LTE grid for which the departure coefficients were computed using the MPI-parallelised non-LTE radiative transfer code `Balder`. This code is based on the code `Multi3D` (Leenaarts et al., 2009), which calculates the level populations for model atoms based on model atmospheres, forcing a statistical equilibrium for all levels in the ambient radiation field. For a further description of the general approach to the calculations, see Amarsi et al., 2020. Specifically, in this analysis I used the grids for Si, Mg, and Ca from Amarsi et al., 2020 and for Fe from Lind et al., 2017 and Amarsi et al., 2016 (with subsequent updates Amarsi priv. comm.).

Moreover, SME needs the user to select spectral intervals within which the studied spectral lines lie and a line list containing the atomic and molecular data for these segments (see more about my line list in Section 3.2.1). Regions free from spectral lines

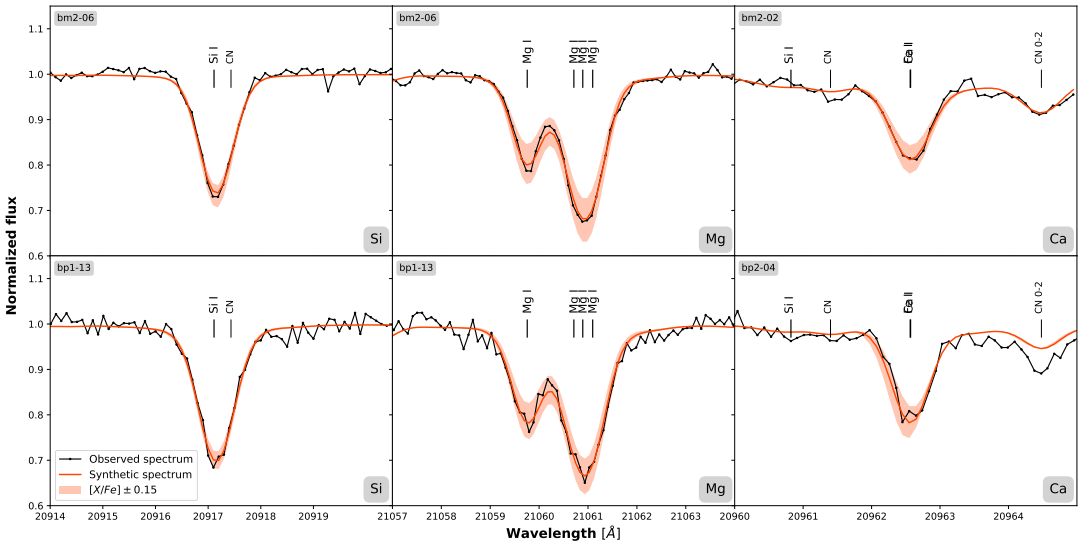

Figure 3.3: *Typical spectral fits for Si, Mg, and Ca lines with a variation band of* ±0.15 *dex in abundance. The upper panel shows fitted lines for stars with a good S/N whereas the lower panel shows those for stars with a poor S/N.*

and other features are marked manually as continuum masks allowing a local linear continuum normalisation within the interval. In the same way, the line of interest has to be marked with a line mask. Therefore, for measuring the abundance or other parameters, SME generates synthetic spectra and compares them with the observed spectrum using a χ^2-minimisation in the region within the line masks.

As explained in Section 3.2.1, for the abundance analysis, firstly I determined the metallicity [Fe/H] using the iterative method from R. M. Rich et al. (2017). For each chemical element studied, namely iron, silicon, magnesium, and calcium, I chose a set of good-quality spectral lines (the ones used in my study are shown in Figure 3.2 and listed in Table 3.3). Among these, I meticulously selected the best available lines for each star. To this end, each line and spectral interval were examined by eye so as to evaluate S/N and to detect disturbing artefacts or cosmic hits. In addition, line blending and fitting quality were appraised. In order to determine the final abundance value, the mean of the abundances derived from the selected lines is computed. This process permits me to obtain a precise estimate of the chemical abundances of my stars.

Given that metallicity is essential in the determination of stellar models and then in the estimation of the chemical fingerprints of stars, the iron abundances were directly determined with non-LTE corrections, contrary to the three other chemical elements for which LTE and non-LTE cases were explored and compared.
In the case of magnesium, I used the line at 21059.757 and the multiplet lines at 21060.710 − 21060.896 . As shown in Fig. 3.2, these lines are wide and very well defined and are therefore good candidates for the abundance determination as I have precise broadening values. Moreover, due to the proximity of these spectral features, I fitted all

these lines simultaneously using one line mask.
Compared to the other elements of this study, there are only a few Ca lines available and these all lie on the edge of one of the detector chips. I was therefore only able to obtain Ca abundance estimates for 42 stars of the sample. Because of their proximity to CN lines, and in order to fit the selected Ca lines correctly, I fitted the nitrogen abundance via these molecular lines. The aim is not to have an accurate estimation of nitrogen (which is a difficult chemical element to study because of its complicated molecular equilibrium with carbon and oxygen) but only to correctly fit the CN lines. Two additional Ca lines, located at 20956.394 and 20962.570, are heavily blended with CN lines, and are therefore insensitive to the Ca abundance. As a consequence, I discarded them from the study.

I ensured that all the spectral lines used were not blended with any other line of my line list. Even if no suspicious line has been retained, it should be noted that there is always a risk that unknown blends or lines with unknown line strengths are not accounted for, especially for metal-rich and cool stars.
I chose a final sample, which I refer to as the Golden Sample (see Section 3.3.4), based on a sufficiently high S/N (> 40) and low line-by-line discrepancy (σ_{lines} < 0.3 dex).

Solar neighbourhood

The 37 solar neighbourhood stars used for comparison in this work are a subset of the Giants In the Local Disk (GILD) stellar catalogue (Jönsson et al. in prep.; which builds upon and improves the analysis described in H. Jönsson et al. 2017a). The fundamental stellar parameters, effective temperature ($T_{\rm eff}$), surface gravity ($\log(g)$), metallicity ([Fe/H]), and microturbulence ($\xi_{\rm micro}$) were estimated from carefully analysed optical spectra. These parameters were benchmarked against independently determined effective temperatures, $T_{\rm eff}$, from angular diameter measurements and surface gravities, $\log(g)$, from asteroseismological measurements (see H. Jönsson et al., 2017a, for more details) with uncertainties of ±50K for $T_{\rm eff}$, ±0.15 dex for $\log(g)$, ±0.05 dex for [Fe/H], and ±0.1 km/s for $\xi_{\rm micro}$. Stellar parameters of these 37 stars are in the range of 4000 - 5100 K in $T_{\rm eff}$, 1 - 3.5 dex in $\log(g)$ and -1 - 0.3 dex in [Fe/H]. Therefore, even though there is an overlap in $T_{\rm eff}$, the solar neighbourhood sample is strictly above 4000 K. There may therefore exist unknown systematic uncertainties in $T_{\rm eff}$ which should be kept in mind while comparing the two samples. This is an improvement that could be made in the future when such observations exist.

With accurate stellar parameters known, a detailed analysis of the same set of Si, Mg, and Ca lines used for the bulge stars was carried out in order to determine their respective abundances. In addition, the same set of stellar atmosphere grids, the same version of the SME, the same non-LTE corrections, and the same line list as I used for the bulge stars were used. Therefore, a consistent spectroscopic analysis of the bulge and solar neighbourhood giant stars was carried out to determine their elemental abundances.

Needless to say, one obvious difference between the IGRINS spectra of the bright nearby solar neighbourhood stars and the CRIRES spectra of the faint and distant bulge stars is the better S/N, which naturally affects the precision of the abundance estimates.

3.2.2 Dynamical analysis

While my sample size is relatively modest, I undertook a basic dynamical analysis in order to ensure membership of the inner Galactic bulge. Therefore, astrometric parameters are necessary as initial conditions to study dynamics. Among the 72 stars, 63 were cross-matched with Gaia EDR3 (Gaia Collaboration et al., 2016b; Gaia Collaboration et al., 2021) in order to obtain their proper motions. To ensure reliable values, a proper motion error limit is set at 0.3 mas yr^{-1}. In addition, updated distances were determined (see Section 3.3.2) and radial velocities were measured using the strong and clear Mg lines.

I used the software package AGAMA (Vasiliev, 2019) to compute the orbits of my stars up to 10 Gyr. As I am studying inner bulge stars, I used a combination of three gravitational potentials: a disc, a halo, and a bulge/bar. More precisely, I used the disc and halo components of the `MWPotential2014` (Bovy, 2015) and the bar potential from Launhardt et al., 2002b. A typical (clock-wise) rotation pattern speed about $\Omega_b = 40$ km s^{-1} kpc^{-1} was taken into account for the bar (Portail et al., 2017a) which is at an angle of $\alpha = 25°$ from the line of sight towards the Galactic centre. I use these orbital parameters to assign the bulge membership in addition to the calculated distances (see Sect. 3.3.3).

For more details about stellar dynamics, see Part II.

3.3 Results

In this section, I discuss the new abundance measurements of α elements for giants in the inner Galactic bulge. Moreover, I discuss the re-determined distances of the stars and therefore their bulge-membership.

3.3.1 Abundances

Figure 3.3 shows typical fits of a Si line, Ca line, and the Mg lines. The sensitivity of the abundance determination is shown by varying the abundance by ±0.15 dex (the choice of this uncertainty value is explained Section 3.2.1) plotted as a band around the observed spectrum.

LTE and non-LTE comparison

In order to investigate the effects of non-LTE corrections and to be able to compare my results with those from Paper I, in which only the LTE case was explored, I determined Si, Mg, and Ca abundances calculated both with LTE and non-LTE level populations,

affecting both the source function and the line opacity. Therefore, LTE and non-LTE abundance trends for [Si/Fe], [Mg/Fe], and [Ca/Fe] are shown Figure 3.4 with the LTE results from Paper I superimposed (except for Ca which was not measured in Paper I). In addition, the running mean of each trend was computed and is plotted in Figure 3.4.

A few differences between LTE and non-LTE can be seen. For [Si/Fe], the non-LTE trend is indeed slightly stronger and by looking at its running mean, we see that this trend is only slightly lower than the LTE one. For [Mg/Fe], the difference is clearly noticeable; the non-LTE trend is much stronger, showing less scatter, especially for higher metallicities. Moreover, there is a significant offset of ~0.1-0.15 dex between the two trends. Finally, for [Ca/Fe] there is almost no difference between the two cases, and only a very slight offset is visible. This latter fact is further discussed in Section 3.4.2. By comparing the line-by-line discrepancy values for LTE and non-LTE cases, we see that they are lower in the latter case, which justifies my choice to take into account non-LTE effects, as this appears to improve the accuracy of my spectral analysis. Moreover, we note that using non-LTE decreases the scatter in the [α/Fe] versus [Fe/H] trends. From now on, I therefore focus on the non-LTE abundances.

Silicon and magnesium

In Fig.3.4 I show my new [Si/Fe] and [Mg/Fe] trends as function of metallicity compared to the ones derived in Paper I. The uncertainties are the same for the old and the new abundances: 0.15 dex. Besides the fact that my [Si/Fe] and [Mg/Fe] trends follow a typical α-element trend, we observe that there is no plateau at supersolar metallicities for either silicon or magnesium; my trends keep going down. Also, my Si abundances are slightly higher (+0.14 dex in average) and my Mg abundances slightly lower (-0.14 dex in average) than the results from Paper I. Compared to the latter, where [Si/Fe] results were showing a lower dispersion than [Mg/Fe], I get the opposite in my study. This is explained by the fact that the Mg lines used are more sensitive to non-LTE effects than the Si lines (see Figure 3.4).

Calcium

The determination of calcium abundances for my inner bulge stars is new compared to Paper I and is therefore one of the major novelties of this study. As mentioned in Section 3.2.1, only the few stars with satisfactory Ca lines have a calcium abundance estimation (see final values in Table 3.2). We can see that my Ca trend is more dispersed (which could be simply due to the lack of stars) and higher values are seen for metal-rich stars, which is different from my Si and Mg trends.

Table 3.4: *Si abundances of the observed stars in the northern fields. The names of stars belonging to my Golden Sample (see Section 3.3.4) are marked in bold face.*

Star	[Si/Fe]								σ_{lines}	[Si/Fe]$_{mean}$
	20890.37	20908.62	20917.11	20926.14	21056.37	21139.76	21143.26	21204.42		
Northern field at $(l, b) = (0°, +3°)$										
bp3-01	0.27	-	0.34	0.24	0.44	-	0.21	-	0.08	0.30
bp3-02	-0.00	-	0.03	-0.06	0.14	-	-	-	0.07	0.03
bp3-04	0.38	-	-	0.58	-	-	-	-	0.10	0.24
bp3-05	-0.21	-	-0.42	-0.28	-0.21	-	-	-	0.09	-0.22
bp3-06	0.41	-	0.59	-	-	-	-	-	0.09	0.50
bp3-07	-	-0.10	-0.15	-0.24	-0.05	-	-0.25	-0.30	0.09	-0.18
bp3-08	-	0.35	0.09	-	0.09	-	-	-	0.12	0.11
bp3-10	0.03	-	-0.06	-0.11	0.07	-	-	-0.14	0.08	-0.04
bp3-11	0.07	-	0.43	0.28	-	-	-	-	0.15	0.20
bp3-12	0.20	-	0.23	0.22	0.20	-	-	-	0.01	0.14
bp3-13	0.01	-	-	-	-0.03	-	-	-	0.02	-0.01
bp3-14	0.03	-	-	-	-0.03	-	-	-	0.03	0.00
bp3-15	0.33	-	0.13	-	-	-	0.21	-	0.08	0.22
bp3-16	0.09	-	0.47	-	0.08	0.16	-	-	0.16	0.20
bp3-17	-	-	0.07	-	0.02	-	-	-	0.02	0.03
Northern field at $(l, b) = (0°, +2°)$										
bp2-01	-0.10	-	-0.21	-0.07	0.06	-	-	-	0.10	-0.08
bp2-02	0.23	0.76	-	0.57	0.88	-	-	-	0.25	0.61
bp2-03	0.01	-	0.46	0.05	0.06	-	-	-	0.18	0.14
bp2-04	0.28	-	0.29	0.25	0.37	-	-	-	0.04	0.30
bp2-05	0.30	-	0.44	0.39	0.40	-	-	-	0.05	0.26
bp2-06	-	-	-	-	-	-	-	-	-	-
bp2-07	0.05	-	0.24	0.02	0.26	0.12	-	-	0.10	0.14
bp2-08	0.10	0.99	0.62	-0.03	0.27	-	-	-	0.37	0.39
bp2-09	0.17	-	0.45	0.09	0.35	-	-	-	0.14	0.21
bp2-10	0.31	-	0.24	-0.02	-	-	-	0.02	0.14	0.14
bp2-11	0.10	-	0.39	0.08	-0.09	-	-	-	0.17	0.12
bp2-12	0.41	0.46	0.50	0.48	0.49	0.26	0.53	0.18	0.12	0.41
bp2-13	0.11	-	0.33	0.43	0.50	0.16	0.21	-	0.14	0.29
bp2-14	0.05	0.52	0.40	0.15	0.16	-	-	-	0.18	0.26
bp2-15	0.37	-	0.32	-	0.51	0.35	0.31	-	0.07	0.37
Northern field at $(l, b) = (0°, +1°)$										
bp1-01	-0.15	0.58	0.32	-	-0.17	-	-	-	0.32	0.14
bp1-02	0.60	-	0.52	0.32	0.52	0.61	0.49	-	0.10	0.51
bp1-03	-	-	0.14	-0.06	-0.12	-	-0.08	-	0.10	-0.03
bp1-04	-0.04	0.02	0.10	-	0.02	-0.04	0.03	-	0.05	0.02
bp1-05	-0.16	0.12	0.04	-0.27	-0.14	-	0.10	-	0.14	-0.05
bp1-06	0.17	-	0.20	0.65	0.29	-	-	-	0.19	0.33
bp1-07	0.31	-	0.43	0.40	0.51	0.39	-	0.41	0.06	0.41
bp1-08	0.20	-	0.20	0.15	0.33	-	-	-	0.06	0.15
bp1-09	-0.13	-	-0.10	-	-0.43	-	-	-	0.15	-0.22
bp1-10	0.03	-	0.22	0.04	0.41	-	-	-	0.16	0.12
bp1-11	0.29	-	0.20	-	0.34	-	0.10	-	0.09	0.23
bp1-12	0.02	0.07	-	0.08	0.10	-	-	-	0.03	0.07
bp1-13	0.06	-	0.24	-	0.02	-	0.07	-0.08	0.11	0.06
bp1-14	-	-	0.07	0.06	0.32	-	-	-	0.12	0.07

Table 3.5: *Si abundances of the observed stars in the southern fields. The names of stars belonging to my Golden Sample (see Section 3.3.4) are marked in bold face.*

Star	[Si/Fe]							σ_{lines}	$[Si/Fe]_{mean}$
	20801.41	20804.20	20890.37	20908.62	20917.11	20926.14	21056.37		
Galactic Centre field at $(l, b) = (0°, 0°)$									
GC1	-	-	-	-	0.17	-	0.59	0.21	0.38
GC20	-	-	0.50	-	0.16	-	-0.26	0.31	0.14
GC22	0.01	-	-0.04	-	0.07	-	-	0.05	0.02
GC25	-	-	-0.29	-	-0.34	-0.37	-0.22	0.06	-0.31
GC27	0.27	-0.04	-0.24	-	0.71	-0.26	-0.27	0.36	0.03
GC28	-	-0.32	-0.23	-	-0.53	-0.36	-0.08	0.15	-0.3
GC29	-	-	-	-	-0.51	-	0.18	0.34	-0.16
GC37	-	-0.52	-0.14	-	0.04	-	0.09	0.24	-0.13
GC44	-	-0.39	-0.12	-	-0.46	-0.33	-0.43	0.12	-0.35
Southern field at $(l, b) = (0°, -1°)$									
bm1-06	-	-	-	-	-0.01	-0.18	-0.02	0.08	-0.07
bm1-07	-	-	0.11	-	0.14	-	-0.04	0.08	0.07
bm1-08	-	-0.26	-0.14	-	-0.23	-	-0.13	0.06	-0.19
bm1-10	-	-0.03	0.10	-	0.09	-	0.06	0.05	0.05
bm1-11	-	-	-	-	0.16	-0.19	0.05	0.14	0.01
bm1-13	-	0.20	0.27	-	0.32	-	0.52	0.12	0.32
bm1-17	-	0.45	0.23	-	-	-	-	0.11	0.34
bm1-18	-	-	-0.29	-	0.00	-0.11	0.08	0.14	-0.08
bm1-19	-	-0.05	-	0.26	-0.09	-0.01	0.47	0.21	0.12
Southern field at $(l, b) = (0°, -2°)$									
bm2-01	-	-0.09	0.16	-	0.13	0.03	-	0.1	0.06
bm2-02	-	0.07	0.18	-	0.21	0.20	0.37	0.1	0.21
bm2-03	-	0.03	0.05	-	0.11	-	0.20	0.07	0.1
bm2-05	-	-	-0.18	-	0.40	-	-0.04	0.25	0.06
bm2-06	-	0.19	0.39	-	0.18	0.31	0.28	0.08	0.27
bm2-11	-	0.33	0.20	-	0.33	0.35	0.54	0.11	0.35
bm2-12	-	-	-0.06	-	-0.04	-0.21	-	0.08	-0.1
bm2-13	-	0.04	-	-	0.41	-	0.20	0.15	0.22
bm2-15	-	-	-	-	-0.05	-	-0.16	0.06	-0.1
bm2-16	-	-0.13	-	-	0.22	-	0.27	0.18	0.12

Table 3.6: *Mg and Ca abundances of the observed stars in the northern fields. The names of stars belonging to my Golden Sample (see Section 3.3.4) are marked in bold face.*

Star	[Mg/Fe]$_{mean}$	[Ca/Fe]					σ_{lines}	[Ca/Fe]$_{mean}$
	21059.76 + triplet	20937.90	20956.39	20962.57	20972.53	20973.38		
Northern field at $(l, b) = (0°, +3°)$								
bp3-01	0.19	0.38	0.36	0.30	-	-	0.02	0.35
bp3-02	-0.19	0.30	-	0.36	-	-	0.03	0.33
bp3-04	0.18	-	-	-	-	-	-	-
bp3-05	-0.38	0.09	0.39	0.25	-	-	0.09	0.24
bp3-06	0.27	0.51	-	0.23	-	-	0.14	0.37
bp3-07	-0.29	0.40	0.10	-	0.14	-	0.09	0.22
bp3-08	-0.21	-	-	-	-	-	-	-
bp3-10	-0.03	-	0.34	0.26	-	0.18	0.04	0.26
bp3-11	-0.14	0.44	0.16	0.23	-	-	0.09	0.28
bp3-12	-0.10	0.38	-	0.37	-	-	0.01	0.37
bp3-13	-0.15	0.55	0.07	-	-	-	0.24	0.31
bp3-14	-0.10	0.36	0.09	-	-	-	0.13	0.22
bp3-15	0.16	0.23	-	-	-	-	-	0.23
bp3-16	0.08	0.54	-	-	-	-	-	0.54
bp3-17	-0.09	0.30	0.33	-	-	-	0.02	0.32
Northern field at $(l, b) = (0°, +2°)$								
bp2-01	-0.32	-	-	-	-	-	-	-
bp2-02	-0.09	0.11	-	0.18	-	-	0.03	0.15
bp2-03	-0.22	0.17	-	-	-	-	-	0.17
bp2-04	0.05	0.55	0.52	0.50	-	-	0.01	0.52
bp2-05	0.18	0.03	-	-	0.16	-	0.07	0.10
bp2-06	-	-	-	-	-	-	-	-
bp2-07	0.09	-	-	-	-	-	-	-
bp2-08	-0.12	0.56	0.65	0.46	-	-	0.05	0.55
bp2-09	0.11	-	-	0.29	-	-	-	0.29
bp2-10	-0.28	0.23	-	0.06	-	-	0.09	0.15
bp2-11	-0.17	0.38	0.15	0.05	-	-	0.10	0.19
bp2-12	0.25	0.57	-	-	-	-	-	0.57
bp2-13	0.15	-	-	-	-	-	-	-
bp2-14	-0.00	-	-	-	-	-	-	-
bp2-15	0.34	0.22	-	-	-	-	-	0.22
Northern field at $(l, b) = (0°, +1°)$								
bp1-01	-0.32	0.30	0.58	0.31	-	-	0.09	0.40
bp1-02	0.46	0.64	-	0.77	-	-	0.07	0.70
bp1-03	-0.41	-	0.38	0.19	0.32	-	0.06	0.30
bp1-04	-0.15	0.20	0.16	0.17	-	-	0.01	0.18
bp1-05	-0.25	0.09	0.27	0.22	-	-	0.05	0.19
bp1-06	-0.09	0.50	0.38	-	-	-	0.06	0.44
bp1-07	0.32	0.03	-	0.55	-	-	0.26	0.29
bp1-08	0.12	-	-	0.04	0.13	-	0.04	0.09
bp1-09	-0.42	-0.25	0.01	-0.19	-0.18	-0.11	0.04	-0.15
bp1-10	-0.15	0.20	-	-	-	-	-	0.20
bp1-11	0.01	-	-	-	-	-	-	-
bp1-12	-0.09	0.29	0.29	0.20	-	-	0.03	0.26
bp1-13	0.01	-	-	-	-	-	-	-
bp1-14	-0.02	-0.28	-	0.17	-	-	0.22	-0.06

Table 3.7: *Mg and Ca abundances of the observed stars in the southern fields. The names of stars belonging to my Golden Sample (see Section 3.3.4) are marked in bold face.*

Star	[Mg/Fe]$_{mean}$	[Ca/Fe]					σ_{lines}	[Ca/Fe]$_{mean}$
	21059.76 + triplet	20937.90	20956.39	20962.57	20972.53	20973.38		
Galactic Centre field at $(l, b) = (0°, 0°)$								
GC1	-0.1	0.20	0.26	-	-	-	0.03	0.23
GC20	-0.25	0.74	0.46	0.40	0.28	0.22	0.09	0.42
GC22	-0.28	0.40	0.37	0.20	-	-	0.06	0.32
GC25	-0.36	-	0.57	0.38	-	-	0.10	0.48
GC27	-0.21	0.13	-	0.27	-	-	0.07	0.20
GC28	-0.25	0.36	0.37	0.19	0.13	0.23	0.05	0.26
GC29	-0.16	-	-	-	-	-	-	-
GC37	-0.45	-0.19	0.08	-	-	-	0.14	-0.06
GC44	-0.36	-	-	-	-	-	-	-
Southern field at $(l, b) = (0°, -1°)$								
bm1-06	-0.12	0.68	0.32	0.31	-	-	0.12	0.43
bm1-07	-0.11	0.19	0.17	-	-	-	0.01	0.18
bm1-08	-0.25	-	0.34	0.29	-0.12	0.01	0.11	0.13
bm1-10	0.02	-	-	-	-	-	-	-
bm1-11	-0.27	0.24	0.58	-	-	0.24	0.11	0.35
bm1-13	0.4	-	-	-	-	-	-	-
bm1-17	0.54	-	-	-	-	-	-	-
bm1-18	-0.14	-0.61	-	-	0.10	-	0.35	-0.26
bm1-19	-0.14	-0.64	0.32	-	-	0.25	0.31	-0.02
Southern field at $(l, b) = (0°, -2°)$								
bm2-01	0.04	-0.20	0.17	-	-	-	0.19	-0.01
bm2-02	0.13	0.36	0.26	0.28	0.21	0.19	0.03	0.26
bm2-03	-0.04	0.19	-	0.18	-0.03	0.10	0.05	0.11
bm2-05	-0.08	0.31	0.36	-	-	-	0.03	0.33
bm2-06	0.29	-	-	0.43	-	-	-	0.43
bm2-11	0.2	0.21	-	0.19	-	-	0.01	0.20
bm2-12	-0.31	-0.05	0.31	0.24	0.15	-	0.08	0.16
bm2-13	0.11	0.16	-0.16	-	-	-	0.16	0.00
bm2-15	-0.27	0.16	0.18	0.12	-	0.07	0.02	0.13
bm2-16	-0.01	0.14	-	0.14	0.09	0.22	0.03	0.15

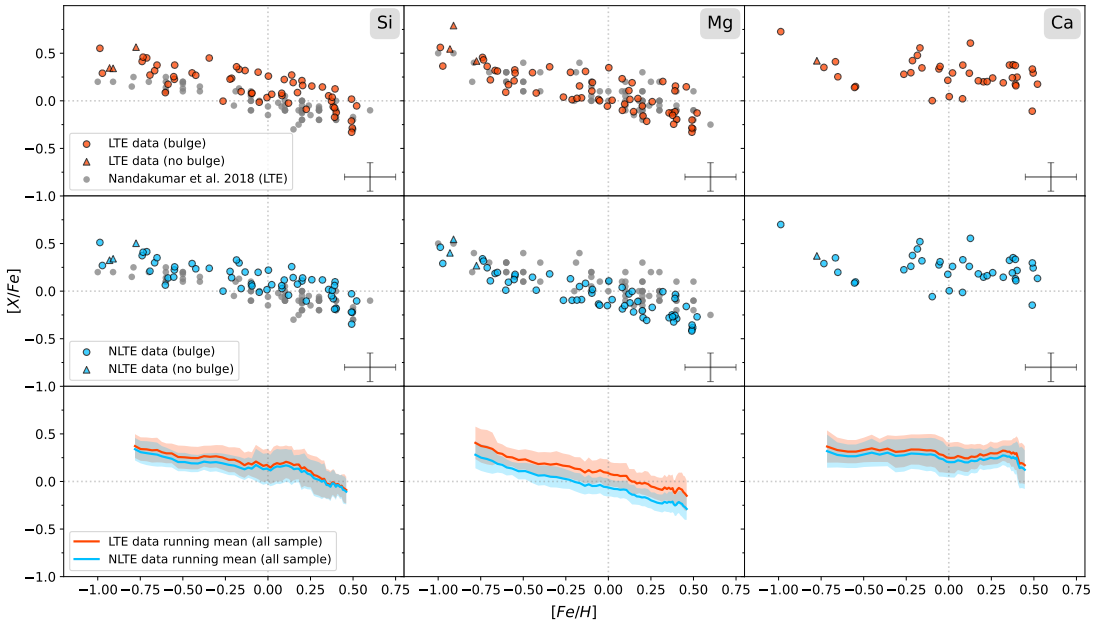

Figure 3.4: *Comparison of my [Si/Fe], [Mg/Fe], and [Ca/Fe] versus [Fe/H] trends in LTE and non-LTE. The comparison sample for Si and Mg is from Nandakumar et al. (2018) and is shown in grey. The upper row shows my trends in red while assuming LTE in the line formation. The middle row shows my trends in blue when assuming non-LTE instead. The lower row shows the running mean of my trends with and without LTE in order to demonstrate the differences more clearly.*

3.3.2 Distances

I determined the spectro-photometric distances using the stellar parameters $T_{\rm eff}$, $\log(g)$, and [Fe/H] (Rojas-Arriagada, A. et al., 2014; Schultheis et al., 2017) together with the near-IR photometry J, H, and K and associated errors, in order to simultaneously compute the most likely line-of-sight distance and reddening by isochrone fitting using PARSEC isochrones. Here I use the same method as that described in A. Rojas-Arriagada et al. (2017b), where I consider a set of isochrones spanning ages from 1 to 13 Gyr in steps of 1 Gyr and metallicities from -2.2 to +0.5 dex in steps of 0.1 dex. As in A. Rojas-Arriagada et al. (2017b), besides computing the distance from the observed stars to the whole set of model stars, I calculate weights for each star, which depend on: the evolutionary speed of the model stars; the fact that the number of stars per mass is not uniform, which is given by the IMF; and an exponential weight associated with the distance of the observed stars with respect to the model. The typical uncertainties are on the order of 20%-40% but I find no systematic differences in comparison to distances obtained by a Bayesian approach for example (e.g. Santiago et al. 2016). The obtained distances permit us to analyse the bulge membership of my sample; see Section 3.3.3. I note that I do not calculate the distances of the Galactic centre field because I lack the J magnitudes. From the heliocentric distances, I computed the Galactocentric radial distance $R_{GC} = \sqrt{(X_{GC}^2 + Y_{GC}^2)}$ where X_{GC} and Y_{GC} are the cartesian coordinates.

Table 3.8: *Distances of the observed stars in the northern fields. The names of stars belonging to my Golden Sample (see Section 3.3.4) are marked in bold face.*

Star	R_{GC} [kpc]	Distance error [kpc]	Population
Northern field at $(l, b) = (0°, +3°)$			
bp3-01	0.3	0.7	bulge
bp3-02	0.4	1.0	bulge
bp3-04	1.7	1.1	bulge
bp3-05	2.2	0.8	bulge
bp3-06	11.9	0.9	No bulge
bp3-07	1.9	0.9	bulge
bp3-08	1.3	0.8	bulge
bp3-10	1.1	1.0	bulge
bp3-11	0.9	0.6	bulge
bp3-12	1.6	1.1	bulge
bp3-13	0.4	0.9	bulge
bp3-14	1.6	0.6	bulge
bp3-15	1.8	0.6	bulge
bp3-16	0.2	0.9	bulge
bp3-17	1.9	0.7	bulge
Northern field at $(l, b) = (0°, +2°)$			
bp2-01	1.8	0.9	bulge
bp2-02	0.6	0.8	bulge
bp2-03	2.0	0.7	bulge
bp2-04	2.2	0.6	bulge
bp2-05	0.9	0.9	bulge
bp2-06	8.7	2.1	No bulge
bp2-07	1.8	0.8	bulge
bp2-08	1.4	0.7	bulge
bp2-09	1.9	1.1	bulge
bp2-10	1.8	0.7	bulge
bp2-11	1.1	0.7	bulge
bp2-12	0.2	1.1	bulge
bp2-13	1.5	1.1	bulge
bp2-14	1.6	1.3	bulge
bp2-15	1.4	0.7	bulge
Northern field at $(l, b) = (0°, +1°)$			
bp1-01	1.7	0.9	bulge
bp1-02	0.6	0.8	bulge
bp1-03	2.1	0.9	bulge
bp1-04	2.1	0.8	bulge
bp1-05	0.3	1.0	bulge
bp1-06	1.0	1.0	bulge
bp1-07	0.1	0.8	bulge
bp1-08	1.1	0.7	bulge
bp1-09	0.1	0.9	bulge
bp1-10	1.1	0.7	bulge
bp1-11	1.5	0.9	bulge
bp1-12	1.8	0.9	bulge
bp1-13	1.3	0.6	bulge
bp1-14	0.5	0.7	bulge

Table 3.9: *Distances of the observed stars in the southern fields. The names of stars belonging to my Golden Sample (see Section 3.3.4) are marked in bold face.*

Star	R_{GC} [kpc]	Distance error [kpc]	Population
Galactic Centre field at $(l, b) = (0°, 0°)$			
GC1	-	-	-
GC20	-	-	-
GC22	-	-	-
GC25	-	-	-
GC27	-	-	-
GC28	-	-	-
GC29	-	-	-
GC37	-	-	-
GC44	-	-	-
Southern field at $(l, b) = (0°, -1°)$			
bm1-06	1.5	0.9	bulge
bm1-07	0.2	1.1	bulge
bm1-08	1.4	0.9	bulge
bm1-10	1.1	1.1	bulge
bm1-11	1.8	0.8	bulge
bm1-13	3.9	0.4	No bulge
bm1-17	6.6	0.6	No bulge
bm1-18	0.6	1.1	bulge
bm1-19	1.6	1.0	bulge
Southern field at $(l, b) = (0°, -2°)$			
bm2-01	1.4	1.1	bulge
bm2-02	1.0	0.8	bulge
bm2-03	1.4	1.1	bulge
bm2-05	0.2	0.8	bulge
bm2-06	1.8	0.8	bulge
bm2-11	0.2	1.0	bulge
bm2-12	1.8	0.9	bulge
bm2-13	1.1	1.0	bulge
bm2-15	1.8	0.8	bulge
bm2-16	1.1	0.9	bulge

3.3.3 Bulge membership

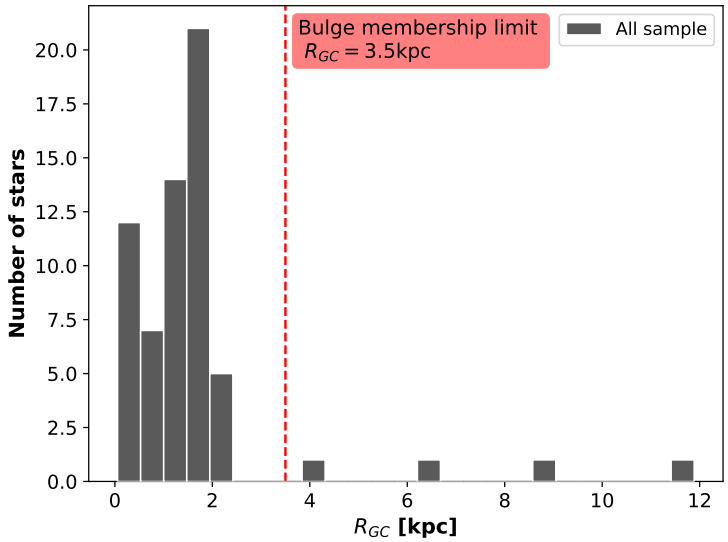

Figure 3.5: *Histogram of the Galactocentric radial distances (computed in Section 3.3.2) of the stars in my sample for which values are available. The typical intrinsic depth of the bulge is indicated by the red dashed line.*

Figure 3.5 displays the distribution of the Galactocentric distances (R_{GC}) where we see a peak in the distribution at $R_{GC} \sim 1.5$ kpc. I also indicate the typical intrinsic depth of the bulge with $R_{GC} \leq 3.5$ kpc (see e.g. A. Rojas-Arriagada et al. 2017b, Alvaro Rojas-Arriagada et al. 2020a, Zasowski et al. 2019). Four stars (bp3-06, bp2-06, bm1-13, bm1-17) show larger distances going up to $R_{GC} \sim 12.0$ kpc, indicating that those do not belong to the inner bulge. They all have low metallicities ([Fe/H] ~ -1.0) and are enhanced in the $\alpha-$elements and could therefore belong either to the thick disc or to the halo population. Thus, compared to Paper I where no star was found outside of the bulge, in this study I exclude those four stars from further analysis, resulting in a total sample of 59 stars with determined distances.

All the stars of my sample were spectrally analysed using the method explained in Section 3.2.1, except the star bp2-06. Indeed, due to the very low metallicity of this latter object (the estimation for bp2-06 from Paper I gives −1.8 dex), none of my Fe lines are usable for determining it directly. However, thanks to my dynamical analysis introduced in Section 3.2.2 and to my broad Mg lines, I can estimate its metallicity. As explained in Section 3.3.2 and shown in Table 3.8, the Galactocentric radial distance of bp2-06 is about 8.7 kpc (using its metallicity estimation from Paper I), which demonstrates that it does not belong to the inner bulge. In addition, its simulated orbit shown in Figure 3.6 supports the latter finding and provides further information about its movements in the Galaxy.

These results lead us to conclude that bp2-06 may be a halo star and therefore it ought

to have a typical Mg abundance for a halo star of about ~ 0.4 dex (see e.g. Edvardsson et al., 1993). A magnesium-based metallicity can therefore be estimated by selecting a range of iron abundances [Fe/H] and corresponding $\log(g)$ and ξ_{micro} and by fitting my Mg spectral feature for each of these sets of values. I finally obtain a metallicity of about −2.03 dex, which allows me to obtain a Mg abundance of about 0.4 dex for this star. Such a low metallicity, together with its orbits, leads me to reject the notion that this star is in the inner bulge. It is therefore excluded from my inner bulge sample.

I also checked the derived orbital parameters for my bulge stars sample, such as apocentric radius (R_{apo}) and maximum vertical height (z_{max}). Except for the four stars with larger distances mentioned above (bp3-06, bp2-06, bm1-13, bm1-17), my sample shows typical orbital parameters for the bulge, with the majority of stars lying within $R_{apo} < 3$ kpc and $z_{max} < 1.5$ kpc and with high eccentricities. I do not find any trends in the orbital parameters with metallicity and/or abundances, but a larger sample is clearly needed in order to obtain statistically significant results.

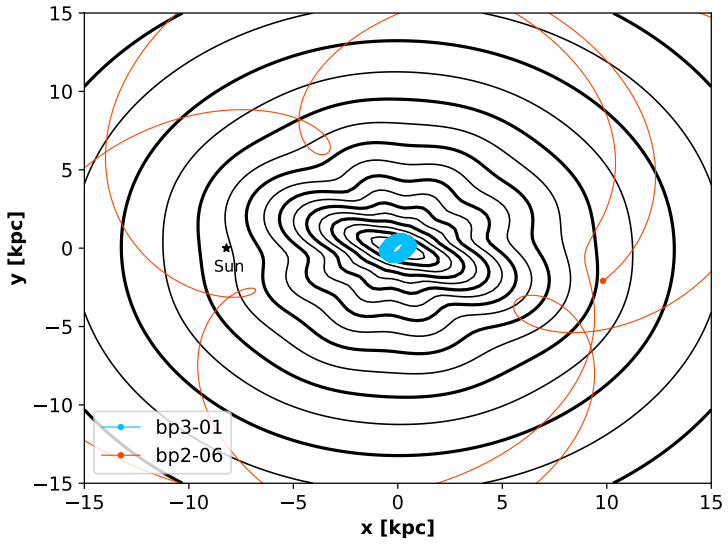

Figure 3.6: *Comparison of the orbits in the Cartesian Galactocentric (x,y) plane of bp3-01 found in the bulge and bp2-06 found outside of the bulge. The black contours show the surface density of the stellar component of my combination of gravitational potentials.*

3.3.4 The Golden Sample

The objective of this work is to derive the most precise abundance trends as possible for the inner Galactic bulge. In this context, I construct a clean sample, referred to as the Golden Sample, which contains stars belonging to the inner bulge as determined in Section 3.3.2 and that have sufficiently high-quality spectra. To select these stars (i) I require a minimum S/N of 40 (see Section 3.2.1) and (ii) as explained in Section 3.3.3, I exclude stars with $R_{GC} > 3.5$ kpc.

Therefore, because of an insufficient S/N, I discarded the stars bp2-02, bp1-01, GC1, GC20, GC25, GC27, GC28, GC37, bm1-06, bm1-18, and bm1-19 from the abundance analysis. It should be noted that the latter are mainly from the Galactic centre field, which is expected as it corresponds to the innermost region studied here. Similarly, the stars bp3-06, bp2-06, bm1-13, and bm1-17 are excluded because of their excessive distances. From the original sample of 72 stars, my Golden Sample is therefore reduced to 57 stars. The latter are highlighted in bold face in Tables 3.1, 3.2, 3.4, 3.5, 3.6, 3.7, 3.8, and 3.9.

Moreover, I computed the line-by-line discrepancy, σ_{lines} (given in Table.3.4,3.5,3.6 and 3.7), for every star abundance, which is the standard deviation of the used line abundance values. Therefore, in addition to the selection made for the construction of my Golden Sample, I require $\sigma_{lines} < 0.3$ for each chemical element. As explained in Section 3.2.1, due to the fact that I used only one spectral feature for magnesium, the line-by-line discrepancy is zero for this element. This selection criterion is therefore useful to my analysis, but as its value strongly depends on the number of used lines, caution must be taken when using it; for example, abundances determined with only one line cannot be evaluated by this criterion.

3.4 Discussion

Here, I discuss my results presented in Section 8.2 and compare them to a local sample of solar neighbourhood stars, for which I used the same lines and spectral analysis method (I refer the reader to Section 3.1.2 and 3.2.1 for more details). Moreover, my abundance trends are also compared to the APOGEE inner bulge sample from Zasowski et al. (2019) (hereafter referred to as the APOGEE sample). The APOGEE sample has been updated with the latest APOGEE DR17 release (Abdurro'uf et al. 2022a) covering about 4000 stars with $R_{GC} < 4$ kpc. Finally, I discuss my abundances in context of a tailored chemical-evolution model for the inner bulge.

3.4.1 Silicon and magnesium

The NLTE Si and Mg abundance trends for my Golden Sample of the inner bulge are shown in Figure 3.7. These are compared to my local star sample in the upper panel of the figure. This comparison provides a more direct test to look for differences or similarities between the populations, as the analyses of the stars are designed to be as similar as possible, thereby minimising any systematic uncertainties. As indicated in Section 3.2.1, even if the local sample has been selected in the most reasonable way possible, the potential existence of unknown systematic uncertainties in $T_{\rm eff}$ should be kept in mind while comparing the two samples. However, a larger scatter is expected for the inner bulge sample, due to the most obvious and only significant difference between the analyses, which is the S/Ns. In general, we see that the Si and Mg trends for the

inner bulge and local thin and thick discs are in very good agreement.

However, my inner bulge stars extend to higher metallicities. Furthermore, although based on few stars, the local sample shows a tendency to 'flatten off' at [Fe/H]> 0.25 dex. The inner bulge sample, on the other hand, clearly shows a continuous downward trend with increasing metallicity (Johnson et al., 2013 report a similar result for several α elements in outer bulge fields; moreover, chemical-evolution models suggest this is indeed to be expected; see Sect. 3.4.3.), albeit with a significant scatter in the abundance ratios. This is true for both the [Si/Fe] and [Mg/Fe] trends. My derived Mg abundances show the steepest slope of decreasing Mg with increasing [Fe/H] with a mean dispersion of 0.10 dex (see Fig. 3.4). More stars and further investigations into the cause of the increased scatter at supersolar metallicities for the inner bulge stars are needed in order to be able to claim any difference in the slopes of the trends for the two populations.

In the lower panel of Fig. 3.7, the Si and Mg trends for my inner bulge stars are compared to those of the inner bulge APOGEE sample from Zasowski et al. (2019). These data result from different analysis methods and a systematic shift might therefore be expected. Silicon is the α-element with the lowest dispersion in APOGEE, which is also seen in other IR studies (R. Michael Rich et al. 2005, Schultheis et al. 2017, N. Ryde et al. 2010). We see good agreement overall, within the uncertainties, except for the highest metallicities. There is, on the other hand, a significant and systematic offset between the data sets for the [Mg/Fe] trends, with the metal-rich regime showing the largest differences, namely of up to 0.4 dex. We note that Mg and Si are hailed to be the α-elements measured with the greatest precision by APOGEE (see e.g. Henrik Jönsson et al. 2018, Schultheis et al. 2017) and Mg does not show signs of any temperature dependency. As this offset is also the case for my local disc sample, and the APOGEE [Mg/Fe] trend corresponds to what is expected for a bulge/thick disc trend (see e.g. Bensby et al., 2014), I believe that my [Mg/Fe] trend is systematically too low by a few times 0.1 dex. As noted above, such a shift might be expected in light of the differences in the analysis methods, such as the choice of lines used, whether or not NLTE effects are used, and whether or not those effects are correct in magnitude. Therefore, a differential comparison of the local and the inner bulge stars is very important.

We also note that a flattening in [Si/Fe] and [Mg/Fe] trends is seen for the APOGEE sample for metal-rich stars, that is, [Fe/H] > 0.0. Santos-Peral et al. (2020) demonstrated that the normalisation procedure has an important impact on the derived abundances and that narrow normalisation windows around the studied lines improves the precision and leads to a decreasing trend in the abundance even at supersolar metallicities. This might be an explanation for the differences. However, we note that this explanation would not explain this levelling-off tendency for my local sample.

The APOGEE sample suffers from some slight temperature dependencies of Si abundance,

which is not the case for my Golden Sample, as shown in Figure 3.8 (only an expected trend is visible: the warmer stars are more metal poor). This might affect the more metal-rich APOGEE stars, as these tend to be cooler. However, the [Si/Fe] difference in the slope at supersolar metallicities is less obvious when comparing with my inner bulge sample, up to [Fe/H]~ 0.3. As shown in Fig. 3.4, NLTE corrections for Si are also very small, and so this should not cause any differences.

3.4.2 Calcium

The Ca abundances determined for the local solar neighbourhood sample show only slightly larger scatter compared to the local [Si/Fe] and the [Mg/Fe] trends. However, the [Ca/Fe] trend for my golden sample of the inner bulge shows the largest intrinsic dispersion compared to Mg and Si. This is in part due to problems with the Ca lines, such as the fact that they are situated close to the edge of the detector in the CRIRES setup. This is not the case for the solar neighbourhood sample, which is observed with the IGRINS spectrometer, covering the full K band with no gaps. Nevertheless, we see a general agreement in [Ca/Fe] between the solar neighbourhood and the Golden Sample.

A clear offset compared with the APOGEE sample can be seen. Schultheis et al. (2017) noted that, for Baade's window, the Ca abundances of APOGEE are systematically ~ 0.15 dex lower than those reported by R. Michael Rich et al., 2005,Fulbright et al., 2007, and Gonzalez et al., 2011. The APOGEE trend is also lower compared to what is expected for the bulge/thick disc trend see e.g. Bensby et al., 2014. This shift would put my local sample and APOGEE's trend in closer agreement. The NLTE corrections for Ca could also be underestimated for the K band lines, leading to overly high Ca abundances with respect to APOGEE. However, the Ca NLTE corrections (Amarsi et al., 2020) for the H band are small and the solar disc trends with these NLTE corrections show good agreement with the [Ca/Fe] trends for the disc determined from optical lines (Montelius et al., 2022). There is therefore no direct reason to believe that these corrections should be underestimated. As for the other α-elements, here we again see the flattening in APOGEE for the high-metallicity stars.

3.4.3 A new chemical-evolution model of the inner Galactic bulge

In this section, I present a new chemical-evolution model designed to reproduce the NLTE abundance ratios and metallicity distribution function (MDF) of the inner bulge stars. First, in Section 3.4.3, I compare the new NLTE data for the inner bulge with the chemical-evolution model of F. Matteucci et al. (2019) based on the one-infall scenario designed for the Galactic bulge. Subsequently, in Section 3.4.3, I compare the data to a two-infall model. While such simple approaches to galaxy evolution cannot account for the full complexity of galaxy formation, they have served as useful reference models in the literature for studying the impact of single or multiple episodes of galactic star formation on the chemical signatures in stellar populations.

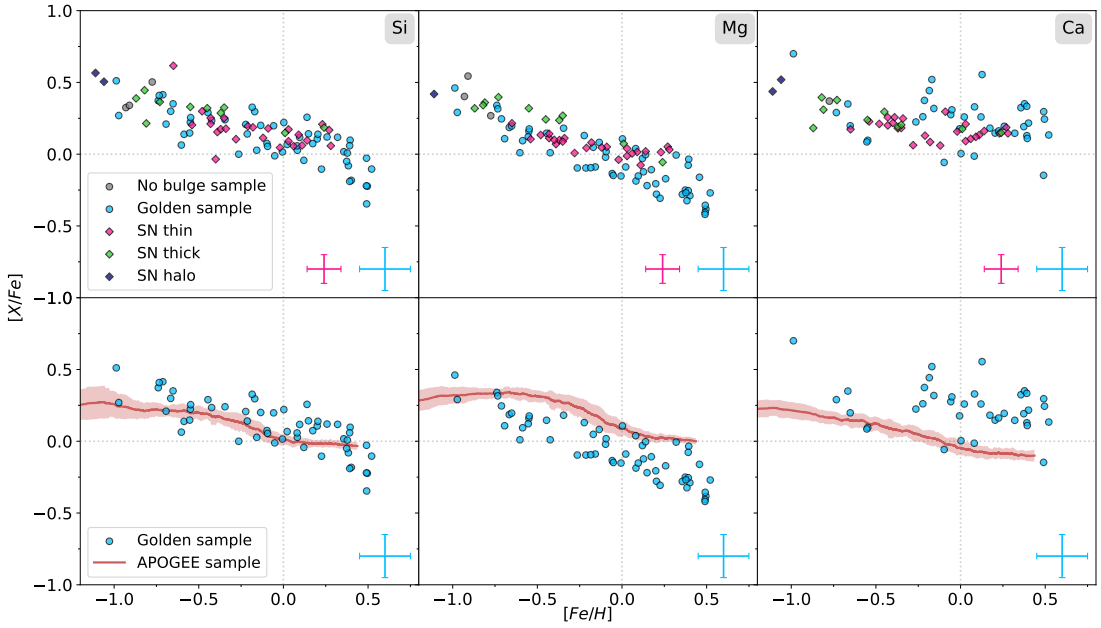

Figure 3.7: *NLTE [Si/Fe], [Mg/Fe], and [Ca/Fe] vs. [Fe/H] trends of my Golden Sample of the inner bulge shown in light blue and compared to solar neighbourhood stars in purple (thin disc), green (thick disc), and dark blue (halo) in the upper panel and compared to the running mean of the updated APOGEE DR17 sample from Zasowski et al., 2019 plotted in red in the lower panel.*

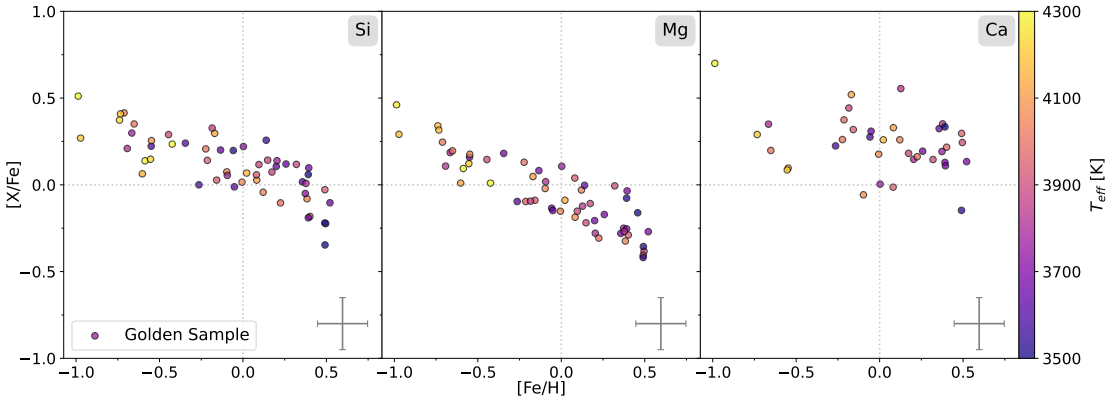

Figure 3.8: *NLTE [Si/Fe], [Mg/Fe], and [Ca/Fe] vs. [Fe/H] trends of my Golden Sample of the inner bulge colour coded with $T_{\rm eff}$ showing no bias with temperature.*

Testing the one-infall chemical-evolution model

In the left panel of Fig. 3.9, I compare the NLTE [Mg/Fe] versus [Fe/H] data presented in Section 3.3.1 with the one-infall chemical-evolution model for the Galactic bulge of F. Matteucci et al. (2019). In this model, the bulge follows a fast gravitational collapse scenario (R. B. Larson, 1976) and is supposed to form by accretion of a single fast gas-infall event on a timescale of τ = 0.1 Gyr. The proposed model was capable of reproducing Gaia-ESO bulge stars of A. Rojas-Arriagada et al. (2017b) adopting the Salpeter (1955) IMF. However, we note from Fig. 3.9 that the NLTE data presented in this study are not reproduced by the model. A better agreement is obtained with the Kroupa et al. (1993) IMF. As highlighted in the VINTERGATAN simulation (Agertz et al., 2021),

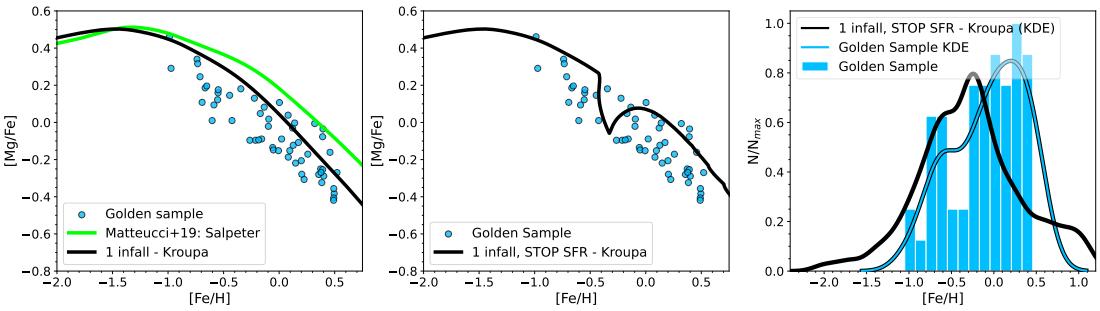

Figure 3.9: *One-infall chemical-evolution model predictions for the Galactic bulge. Left panel: Effects of different IMF on the one-infall chemical-evolution model. With the green line, I show the model presented in F. Matteucci et al. (2019) assuming the Salpeter (1955) IMF, whereas with the black line I show the same model but with the Kroupa et al. (1993) IMF. Blue dots are the [Mg/Fe] abundances for my Golden Sample. Middle panel: [Mg/Fe] vs. [Fe/H] for the one-infall model with the Kroupa et al. (1993) IMF, where a 250 Myr pause in star formation has been applied. Right panel: Kernel density estimation of the MDF of the same model as in the middle panel (black line) compared with the histogram and KDE of the NLTE stars distribution (blue histogram and line).*

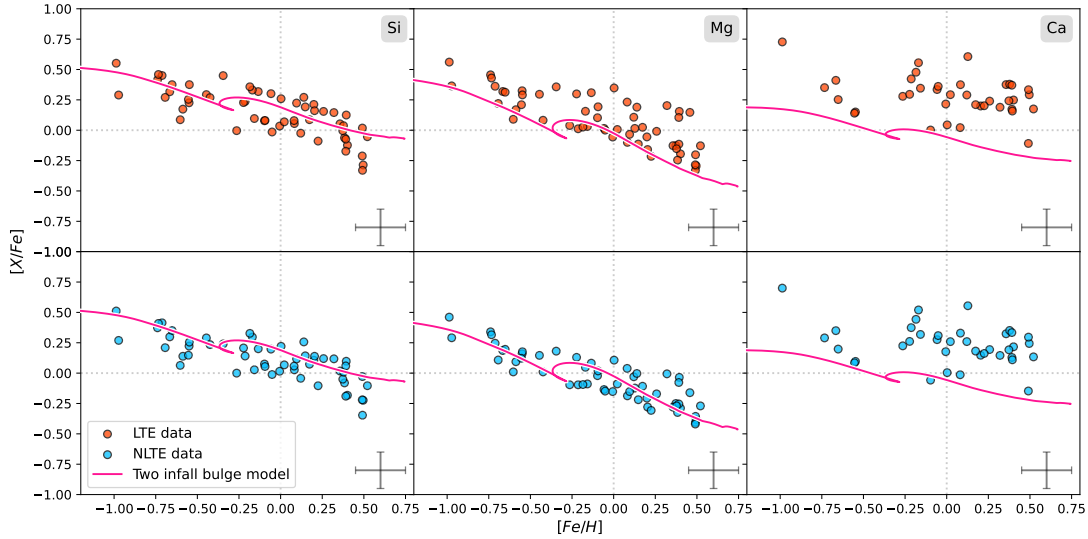

Figure 3.10: *LTE (upper panel) and NLTE (lower panel) [Si/Fe], [Mg/Fe], and [Ca/Fe] vs. [Fe/H] trends of my Golden Sample compared with the two-infall bulge chemical model constructed Section 3.4.3.*

the scatter in the data with high-[α/Fe] abundance ratio values across the entire galaxy is largely set by the gas -consumption timescales in star forming clouds (see Figure 9 in Renaud et al. 2021a). Gas with short depletion times shows the highest values of [α/Fe] at fixed [Fe/H] values. This is due to supernova-enriched gas being trapped more easily in dense clouds where the depletion time is short. It is worth noticing that in the VINTERGATAN simulation, the scatter in the high-alpha sequence is present in both the in situ formed stars and the accreted stars (see Figure 8 in Renaud et al. 2021a).

In the middle panel, following F. Matteucci et al. (2019), in order to reproduce the bimodality in both in the [Mg/Fe] versus [Fe/H] space and in the MDF, I try a 250

Myr pause in star formation. The chemical-evolution model characterised by a unique gas-accretion event coupled with a pause in star formation is able to predict the gap in the [X/Fe] versus [Fe/H] observed in APOGEE bulge data (middle panel), but completely fails to properly reproduce the two stellar populations in the MDF (see right panel).

Inner-bulge stellar populations with the two-infall model

In the previous section, I show that the classical one-infall chemical-evolution model does not seem to be the correct scenario to properly reproduce the chemical properties of the inner bulge.

Here, I consider the possibility that two gas-accretion events are responsible for the chemical signatures impressed in the NLTE abundance ratios. The presence of two distinct sequences in the chemical abundances in the Galactic bulge was pointed out by F. Matteucci et al. (2019) and Queiroz et al. (2020) based on analyses of APOGEE stars. In particular, in Queiroz et al. (2020), the Galactic disc dichotomy in the abundance ratios [α/Fe] versus [Fe/H] seemed to extend up to the innermost regions of the disc up to the bulge. The complex nature of the Galactic bulge structures has already been addressed by theoretical models with the introduction of two different stellar populations. Samland et al. (2003), by means of a dynamical model, predicted the existence of two bulge populations: one originating from an early collapse and the other formed late in the bar through secular evolution (e.g. Combes et al., 1990; Norman et al., 1996; John Kormendy et al., 2004b; Athanassoula, 2005a). These results suggest the two-infall chemical-evolution model may represent the scenario capable of reproducing the chemical evolution that I find in the Golden Sample.

In the context of the two-infall model, the adopted analytical expression for the gas infall rate is:

$$\mathcal{I}_i(t) = \overbrace{\mathcal{X}_{1,i}\mathcal{A}\, e^{-t/\tau_1}}^{\text{1st infall}} + \overbrace{\theta(t - t_{\max})\,\mathcal{X}_{2,i}\,\mathcal{B}\, e^{-(t-t_{\max})/\tau_2}}^{\text{2nd infall}}, \tag{3.1}$$

where $\tau_1 = 0.4$ Gyr and $\tau_2 = 2$ Gyr are the timescales of the two distinct gas-infall episodes. The Heaviside step function is represented by θ. $\mathcal{X}_{1,i}$ and $\mathcal{X}_{2,i}$ are the abundance by mass unit of the element i in the infalling gas for the first and second gas infall, respectively. The quantity $t_{\max}$ is the time of the maximum infall rate on the second accretion episode; that is, it indicates the delay between the two peaks of infall rates. In this model, gas outflow occurs during the first infall phase —in which the accretion of gas happens on a short timescale, and is therefore faster— with a rate proportional to the SFR through a free parameter. The outflow rate is defined as

$$\dot{\sigma}_w = -\omega \cdot \psi(t) \begin{cases} \omega = 10 & \text{if } t < t_{max} \\ \omega = 0 & \text{if } t > t_{max}, \end{cases} \tag{3.2}$$

where ω is the mass loading of the wind. Values of 10 or even greater for this latter parameter are expected in galaxies with stellar masses < 10^9 $M_\odot$ (e.g. Chisholm et al. 2017). Hence, the large mass-loading factors experienced by the inner bulge in a scenario of an early, fast collapse (first gas infall episode) can impose important constraints on the host environment of the stars residing in the bulge (or possibly even the mass of the MW bulge when these stars formed; see analysis for MW-mass systems by van Dokkum et al. 2013).

The star formation rate (SFR) is expressed as the R. C. Kennicutt Jr. (1998) law,

$$\psi(t) \propto \nu \cdot \sigma_g(t)^k, \tag{3.3}$$

where σ_g is the gas surface density and $k = 1.5$ is the exponent. The quantity ν is the star formation efficiency (SFE) and this has been set to the value of 10 Gyr^{-1}, a value compatible with previous chemical-evolution models for the Galactic bulge (F. Matteucci et al., 2019). Following Grieco et al. (2012), I impose that for the second gas infall, a chemical enrichment must be obtained from the model of the early collapse phase, corresponding to [Fe/H]=-1 dex.

From Fig. 3.10, we note that my model predictions accurately reproduce the Golden Sample data (NLTE) both in the [Mg/Fe] versus [Fe/H] and [Si/Fe] versus [Fe/H] relations. It is worth mentioning that, for Mg, the agreement between data and the model substantially improves if I consider NLTE stars. Nevertheless, the proposed two-infall model underestimates the data in the [Ca/Fe] versus [Fe/H] space. This is due to the adopted nucleosynthesis prescriptions. In fact, I make use of the ones suggested by Romano et al. (2010, in their model 15) and I refer the reader to this article for details. I stress here that in Fig. 22 of this latter paper, model predictions for the Ca in the solar neighbourhood also substantially underestimate that data sample in the [Ca/Fe] versus [Fe/H] space (see also the discussion in Spitoni et al. 2022).

The histogram and kernel density estimate (KDE) of the MDF of my Golden Sample (see Section 3.3.4 for more details about the star selection) is shown Fig. 3.11. In this figure, we can also appreciate that the two-infall model for the inner bulge accurately reproduces the MDF of the Golden Sample. It is important to underline that the purpose of this study is not to analyse the MDF in the inner Galactic bulge in detail, since the targeted stars have not been specifically selected using an unbiased method concerning this parameter. The stars were selected in such a way that they are sufficiently bright and therefore do not suffer from excessive interstellar reddening but cover a wide range in the colour and therefore effective temperature. Because of my limited sample size, I do not address any corrections concerning the selection function. However, MDF studies so far (see e.g. Alvaro Rojas-Arriagada et al. 2020a, Nandakumar et al. 2017) do not reveal strong selection effects on the shape of the MDF. Compared to Paper I, no particular offset is observed with my new metallicity values.

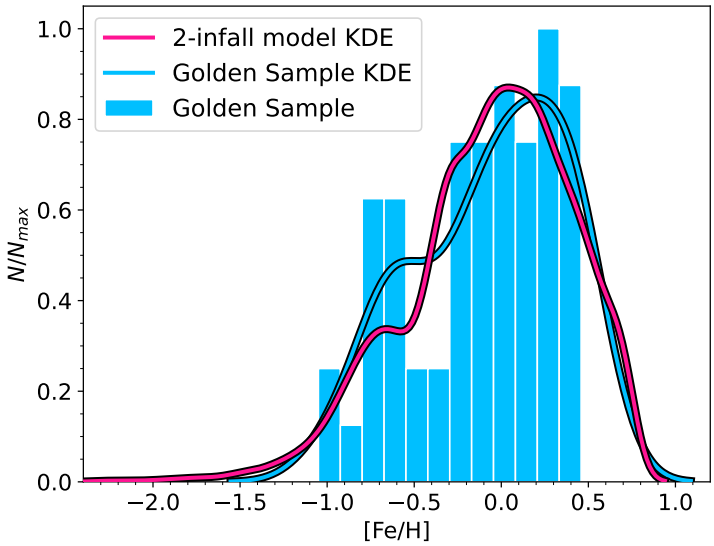

Figure 3.11: *Histogram and kernel density estimation of the metallicity distribution function of my Golden Sample stars (blue histogram and blue line) compared to those predicted by my chemical-evolution model (pink line) presented Section 3.4.3.*

3.5 Conclusions

I analysed the α-element composition of 72 M giants in the inner Galactic bulge from Nandakumar et al., 2018 using high-resolution CRIRES spectra. To this end, I determined precise silicon, magnesium, and calcium abundances using a meticulous star-by-star analysis. In addition, thanks to a recently updated K-band line list, improved broadening parameters, a more precise macro-turbulence estimation, and NLTE corrections, this paper provides one of the most detailed studies of α-abundance trends in the inner bulge carried out so far. This study can be used as a kind of benchmark for future spectroscopic surveys such as the upcoming MOONS galactic survey (Gonzalez et al. 2020).

Thanks to a membership study using distance estimations and simulated orbits, I find that four stars of my sample are not bulge members. With additional selections based on S/N and line-by-line discrepancy, I constructed a clean sample of my inner bulge stars.

I compare my α-abundance trends in LTE and NLTE cases and find the NLTE corrections reduce scatter overall, with Mg having the most reduction. However, the NLTE analysis results in $\sim$ 0.1 dex lower [Mg/Fe]; applying NLTE corrections gives a noticeably lower trend in [Mg/Fe] versus [Fe/H]. Calcium owes its higher dispersion to the lower quality of the Ca lines used.
NLTE [α/Fe] versus [Fe/H] trends of my inner bulge stars and those for thin/thick discs of my solar neighbourhood sample obtained using the same lines and spectral analysis show similar behaviour, with the bulge sample extending to +0.5 dex in [Fe/H], +0.3 dex beyond the solar neighborhood sample. For both Si and Mg, the bulge trend at

suprasolar metallicity is lower than the solar vicinity, especially for Mg. This is striking and is contradictory to the canonical alpha enhancement expected for bulge giants; this trend requires confirmation.

However, for metal-rich stars with [Fe/H]>0.3, we observe a flattening in the [Si/Fe] and [Mg/Fe] thin-disc trends, which I do not find in my inner bulge trends nor in my chemical-evolution model trends. Additional solar neighbourhood stars for these values of metallicity would be needed to validate this difference.

Based on my derived MDF and α-abundance trends, I constructed a tailored chemical-evolution model for the inner Galactic bulge. This latter is highly consistent with silicon and magnesium abundances. In the case of calcium, my model underestimates the abundance values because of the nucleosynthesis prescriptions selected in this work. According to this model, two gas-accretion events with timescales of 0.4 Gyr and 2 Gyr would explain the chemical fingerprints in the α-elements of these inner-bulge stars. However, a larger sample of high-quality abundances in the inner bulge is clearly needed in order to confront them with galactic chemical-evolution models.

4

Stellar ages through $^{12}C/^{13}C$ measurements

Unpublished project

Contributors: N. Nieuwmunster, G. Nandakumar, N. Ryde, M. Schultheis

Chemical abundances are, as shown in Chapter 3, very good assets to study the Galactic history. However, a precise estimate of stellar ages would be a crucial clue to complement this kind of studies. This is one of the hardest stellar parameters to determine. Indeed, the age of an individual star cannot be precisely measured, only estimates can be done. Moreover, no single method is effective for estimating the ages of a wide variety of stellar types or across the entire range of stellar ages. Various methods have been developed and are discussed in Soderblom, 2010. Their current accuracy is not satisfactory except for the asteroseismology technique that is, to this day, the most precise but also limited one. This method uses the analysis of the oscillating frequencies of stars combined with stellar models to derive their mass, radius, evolutionary state, and age. These last two decades, several surveys such as CoRoT (Baglin, 2003), Kepler (Borucki et al., 2010), K2 (Howell et al., 2014), TESS (Ricker et al., 2015) and PLATO (Rauer et al., 2014) have been developed. Unfortunately, almost only relatively bright and neighbouring stars are observed with this method and no mass measurements are available for more distant stars as it would be useful for the purpose of this thesis. When there is no asteroseismic data, less precise ages can be estimated by fitting models from a set of theoretical isochrones with accurate stellar parameters, colours and magnitudes. However, isochrone dating is meaningful only for stars in the turnoff and subgiant phase, where stars of different ages are clearly separated in the HR diagram (Casagrande et al., 2011; Kordopatis et al., 2023).

As exposed in previous chapters, more evolved stars like RGB are of specific interest to study the different structures of the Galaxy as they are more luminous and prevalent across most ages and metallicities. Since their luminosities and colours show relatively little variation with age, isochrones of different ages nearly overlap, making it impossible to obtain precise ages from stellar parameters regardless of the accuracy of their

measurements. Nevertheless, the mass of these evolved stars could serve as a strong constraint on determining their age.

The surface carbon isotopic ratio of main-sequence stars reflects the composition of the interstellar cloud from which the star formed. At the beginning of the ascent of the RGB, low and intermediate mass stars experience the *first dredge-up* (FDU) (Iben, 1965). During this phase, the star undergoes expansion and its outer convective envelope reaches its maximum mass extent and thus penetrates layers where the chemical composition has been partially modified by hydrogen burning via the CN cycle. Through convection, this newly formed material is transported to the stellar surface and modify the observed chemical composition of the star. Therefore, the measured abundances of the CNO group are affected by the FDU and this can be observed, for instance, in a decreased ratio of [C/N], as well as a notably reduced ratio of $^{12}C/^{13}C$. Standard stellar evolution models for stars similar in mass to the Sun predict a reduction in the $^{12}C/^{13}C$ ratio to around $\sim$ 30 from its initial value of $\sim$ 90 (Asplund et al. 2009; Charbonnel 1994). According to these models, no changes in carbon and nitrogen abundances are expected after the FDU. However, observations reveal decreases in carbon and increases in nitrogen as the star ascends the RGB (Mikolaitis et al. 2012, Tautvaišienė et al. 2016 among others). Standard stellar models assume convection is the only mixing mechanism present but extra mixing processes are found to occur on the upper part of the RGB (and also later through the AGB). The *thermohaline mixing* has become, these last years, a prominent theory that can explain many observations (Charbonnel and Lagarde, 2010). Thermohaline-induced mixing models that are stellar models that account for this process are more than necessary. Therefore, the abundances and ratios of certain atomic species, such as [C/N] or $^{12}C/^{13}C$, carry important information about stellar nucleosynthesis and mixing processes along the RGB and AGB. By combining measurements of the latter with thermohaline-induced mixing models, it is possible to get more precise estimates of the current evolutionary stage of the observed stars.

The main purpose of this project is to establish a relation between stellar mass and the $^{12}C/^{13}C$ ratio for RGB stars to be able to estimate stellar ages without the need of mass measurement. It would then be possible to get an age estimation for very distant RGB stars located for instance in the inner bulge, NSD or even NSC.
The steps for this project were initially the following:

1. Establishing a stellar mass - $^{12}C/^{13}C$ relation from analysis of solar neighbourhood stars with available asteroseismic masses.
2. Using this relation to estimate masses for cooler solar neighbourhood stars without asteroseismic masses but with the same range of temperature as the observed inner bulge stars for which I later want to measure the ages.
3. Estimate masses for the observed inner bulge stars.

In the next sections, only the first step of the project is described.

4.1 Observations

For this work, I used 17 giant stars observed in near-infrared with IGRINS (Yuk et al. 2010; Wang et al. 2010; Gully-Santiago et al. 2012b; Moon et al. 2012; Park et al. 2014; Jeong et al. 2014) that provides spectra spanning the full H and K bands (1.45 – 2.5 μm) with a spectral resolving power of $R \simeq 45\,000$. These stars are part of the Giants in the Local Disk (GILD) survey (H. Jönsson et al. 2017b, in prep) and their stellar parameters were determined by using optical spectra obtained with FIES (Telting et al., 2014). They were also observed with Kepler (Borucki et al., 2010) and are thus part of the Kepler Input Catalog (KIC) with measured asteroseismic masses (Pinsonneault et al., 2014). Their effective temperature, surface gravity, metallicity and mass values are given Table. 4.1. The spectra are corrected for telluric lines. In the following sections, the displayed telluric spectra will be used solely to point out the presence of any potential residuals. For further details about these stars, see Nandakumar et al., 2022.

Star	T_{eff} K	log(g) log(cm s^{-2})	[Fe/H] dex	Mass $M_\odot$
KIC3936921	4488	2.19	0.01	1.029
KIC3955590	4411	2.21	0.03	1.046
KIC4177025	4309	1.65	-0.37	0.802
KIC4659706	4428	2.52	0.24	1.811
KIC5113061	4100	1.65	-0.09	1.292
KIC5113910	4338	1.72	-0.48	0.983
KIC5709564	4687	2.15	-0.35	0.895
KIC5779724	4303	1.63	-0.45	0.864
KIC5859492	4511	2.38	0.09	1.324
KIC6547007	4738	2.39	-0.81	0.899
KIC6696436	4520	2.19	-0.40	1.090
KIC6837256	4731	2.33	-0.73	1.340
KIC7006979	4869	2.58	-0.34	1.287
KIC10186608	4676	2.50	-0.12	1.112
KIC11342694	4509	2.82	0.14	1.169
KIC11444313	4630	2.33	-0.18	1.319
KIC11569659	4838	2.42	-0.43	1.030

Table 4.1: *Stellar parameters and mass of the solar neighbourhood stars*

4.2 Method

In this section, I present the method developed to measure automatically the $^{12}C/^{13}C$ ratio of the observed stars.

The near-infrared spectra of cool stars contain many molecular lines, especially OH and CO. High-resolution spectroscopy is therefore necessary to be able to avoid blends and resolve as much as possible individual molecular lines. CO lines are of specific interest since the ^{12}CO lines are clearly distinct from the ^{13}CO lines and individual ^{12}CO and ^{13}CO can be analysed. This is often not the case for isotopic atomic lines. The isotopic shift for atoms is small but large for molecules. Additionally, the CO lines profiles are sensitive to the variation of $^{12}C/^{13}C$ and these lines are well represented and display a range of line strengths in high-resolution H and K bands.

As in Chapter 3, I used SME to analyse the observed spectra (1D spherical symmetric MARCS2014 models and NLTE grids for the available elements). However, since SME cannot measure $^{12}C/^{13}C$ directly, I developed an iterative method to estimate this ratio. SME was only used to fit the radial velocity (v_{rad}) and to generate synthetic spectra without any other free parameter. I used stellar parameters determined in Nandakumar et al., 2022 and CNO abundances values that have already been measured via OH, CN and CO lines in the H band with the same spectra. In order to generate synthetic spectra for different carbon ratio values, I calibrated the molecular linelists for carbon ratios ranging from 4 to 90 in steps of one. To do that, I used the relations Eq. 4.1 and 4.2 to simulate via the $\log(gf)$ value the change in carbon ratio for lines with ^{12}C and ^{13}C respectively. For high $^{12}C/^{13}C$, molecular lines with ^{12}C are stronger (larger $\log(gf)$) and those with ^{13}C are weaker (lower $\log(gf)$) than for lower $^{12}C/^{13}C$.

$$\log(gf)_{^{12}C}^{^{12}C/^{13}C} = \log(gf)_{^{12}C}^{100\%} + \log\left(\frac{\frac{^{12}C}{^{13}C}}{1+\frac{^{12}C}{^{13}C}}\right) \tag{4.1}$$

$$\log(gf)_{^{13}C}^{^{12}C/^{13}C} = \log(gf)_{^{13}C}^{100\%} + \log\left(\frac{1}{1+\frac{^{12}C}{^{13}C}}\right) \tag{4.2}$$

where $\log(gf)_{^{12}C}^{^{12}C/^{13}C}$, $\log(gf)_{^{12}C}^{100\%}$, $\log(gf)_{^{13}C}^{^{12}C/^{13}C}$ and $\log(gf)_{^{13}C}^{100\%}$ are the $\log(gf)$ corresponding to ^{12}C lines with a specific $^{12}C/^{13}C$ and 100% of ^{12}C, and ^{13}C lines with a specific $^{12}C/^{13}C$ and 100% of ^{13}C respectively.
The method has been developed only for the K band for the moment, but could be expanded to the H band too. Thus, I selected several spectral regions in K band where CO lines and band heads are located. The method that I describe below is used to automatically select the interesting CO lines for each star and measure their carbon ratio.

The method is iterative (see Fig. 4.1) and therefore follows several steps:

1. Initially the spectra are prepared to have wavelengths in the laboratory frame by fitting the radial velocity shift. This step is simply to improve the quality of the spectra for later fitting. Thus, I use SME to fit the observed spectrum with only v_{rad} as a free parameter. This relieve the need to consider radial velocity shifts in

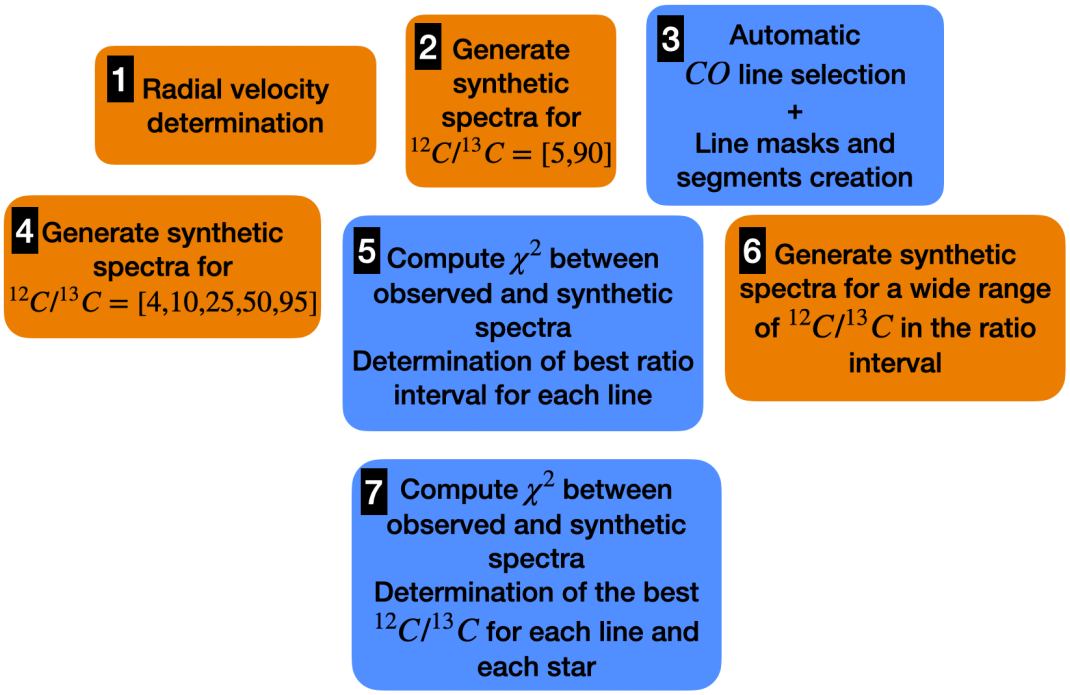

Figure 4.1: *Diagram of the method used to measure the carbon ratio. SME is used in the orange boxes and python scripts are used in the blue boxes.*

the next steps.

2. SME generates two synthetic spectra for carbon ratios of 5 and 90 for all segments with no free parameters (v_{rad} is measured at the previous step, stellar parameters and abundances are already determined).

3. A python script selects only CO lines sufficiently sensitive to $^{12}C/^{13}C$ by comparing the difference in intensity between the two generated synthetic spectra. It keeps only lines for which the difference is sufficiently high and without bad tellurics. The script needs two threshold parameters: one for the difference between both synthetic spectra and another for the difference between the telluric and observed spectra. Then, it defines automatically line masks and smaller segments in order to use SME for only these selected lines in the next steps.

4. SME generates synthetic spectra for carbon ratios of 4, 10, 25, 50 and 95 for the new spectral segments made in the previous step.

5. A python script computes the χ^2 between the observed spectrum and the different synthetic spectra in order to identify the closer minimum and maximum carbon ratio values ($\text{ratio}^{\text{line}}_{\text{min}}$ and $\text{ratio}^{\text{line}}_{\text{max}}$) for each line.

6. SME generates synthetic spectra for a wide range of ratios, with a step of 1, between

$\text{ratio}^{\text{line}}_{\text{min}}$ and $\text{ratio}^{\text{line}}_{\text{max}}$ for each selected line.

7. As in step 5, a python script computes the χ^2 between the observed spectrum and the different synthetic spectra in order to determined the best carbon ratio for each line. The final $^{12}C/^{13}C$ of the star is the mean of the carbon ratios of the lines.

Until now, this method has been used only for ^{13}CO lines analysis but ^{12}CO lines could be studied too. Among 94 identified ^{13}CO lines, 50 were used in total and the method led to a selection of 5 to 10 best quality lines for each star. I show Fig. 4.2, an example of several spectral lines for the star KIC5859492 in the final steps 6 and 7. We can clearly see that the selected lines are really sensitive to the carbon ratio: they are stronger as it decreases.

4.3 First results

In this section, I present the first results obtained after analysing the 17 solar neighbourhood giant stars with available asteroseismic masses.

The measured carbon ratio (listed in Table 4.2) as a function of stellar mass is shown Fig. 4.3. Since this work is not finished, uncertainties have not been computed yet. Among the different ratio values, four stars seem to have unexpected higher ratios. After visually checking the corresponding spectra, the stars KIC4659706, KIC6696436, KIC6837256, and KIC11342694 have poor quality data because of their very low metallicity and/or their very low SNR and therefore have very few available CO lines. They were discarded for the rest of the analysis.

The Kiel diagram of the stars superimposed with thermohaline-induced mixing models from Lagarde et al., 2012 for different stellar masses at solar metallicity is shown Fig. 4.4. We can see that the stars are in the helium-burning phase and more precisely located at the red clump or in the horizontal branch (see Fig. 4.5 for detailed indications of the evolutionary stages). The effects of the FDU but also of the thermohaline mixing can clearly be observed via the measured carbon ratios: less evolved stars seem to have a higher carbon ratio (close to 18) than the more evolved ones (close to 10).
In Figure 4.6, I compare the carbon ratios obtained in this work with the ones from V. V. Smith et al., 2013b and Gilroy, 1989. V. V. Smith et al., 2013b measured in high-resolution H band, the carbon ratio of four solar neighbourhood red giants. Gilroy, 1989 measured the mean carbon ratio of the red giants belonging to open clusters. The author estimated the stellar ages and masses by fitting theoretical isochrones to the colour-magnitude diagram of the clusters. As in both literature studies, we observe with these first results an increase for this range of mass ($< 2\ M_{\odot}$). Thermohaline-induced mixing models from Lagarde et al., 2012 predict also this increase at low stellar masses. This is due to

Star	$^{12}C/^{13}C$
KIC3936921	18.6
KIC3955590	17.4
KIC4177025	5.9
KIC4659706	26.3
KIC5113061	17.7
KIC5113910	9.1
KIC5709564	12.3
KIC5779724	8.6
KIC5859492	20.0
KIC6547007	18.0
KIC6696436	25.8
KIC6837256	41.7
KIC7006979	12.8
KIC10186608	17.0
KIC11342694	37.1
KIC11444313	14.0
KIC11569659	13.0

Table 4.2: *Measured carbon ratios of the solar neighbourhood stars*

the fact that the duration of all the evolutionary phases decreases when the initial stellar mass increases (Charbonnel, 1994). Low mass stars are therefore exposed for longer to mixing processes, i.e. more ^{13}C is transported to their stellar surface. Stellar models for lower masses ($< 1\ M_{\odot}$) would be needed to better compare the results.

4.4 Early conclusion

The first results of this project show that the method is promising and could allow me to estimate the ages of very distant giant stars provided that they are not too metal-poor and that I have high-resolution near-infrared spectra with a sufficiently high SNR. Even if the method works well with most of the stars studied in this work, it could still be improved. A better computation of the final carbon ratio of the stars could be done with, for instance, a weighted mean accounting for the quality of the selected lines. Also, the method still has to be extended to the H band (this work used only the K band).
Moreover, the method developed for $^{12}C/^{13}C$ can be used with any isotopic ratio. Additional parameters could be measured as C/N and other isotopic ratios like $^{16}O/^{17}O$ and $^{16}O/^{18}O$ that have been found to be dependant of stellar mass as explained in Lebzelter et al., 2015.

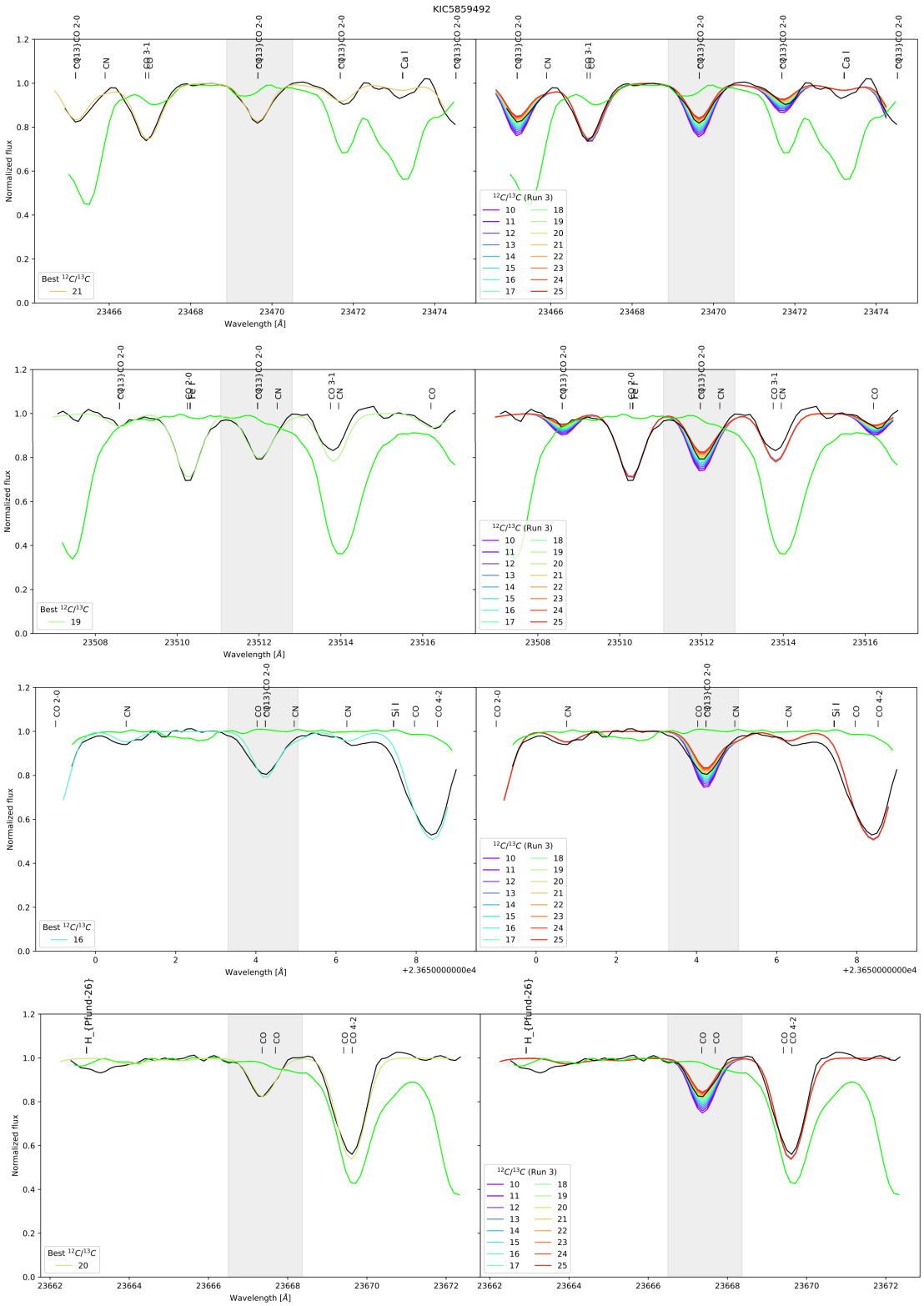

Figure 4.2: *Example of several lines used in the final steps for the star KIC5859492. For each line, the right panel corresponds to step 6 where synthetic spectra of different carbon ratio values are generated while the left panel shows the best fitting obtained in step 7. The black curve is the observed spectrum, the green curve is the telluric spectrum, and the coloured curves correspond to synthetic spectra for different carbon ratio values. The automatically defined line masks at step 3 correspond to the grey region.*

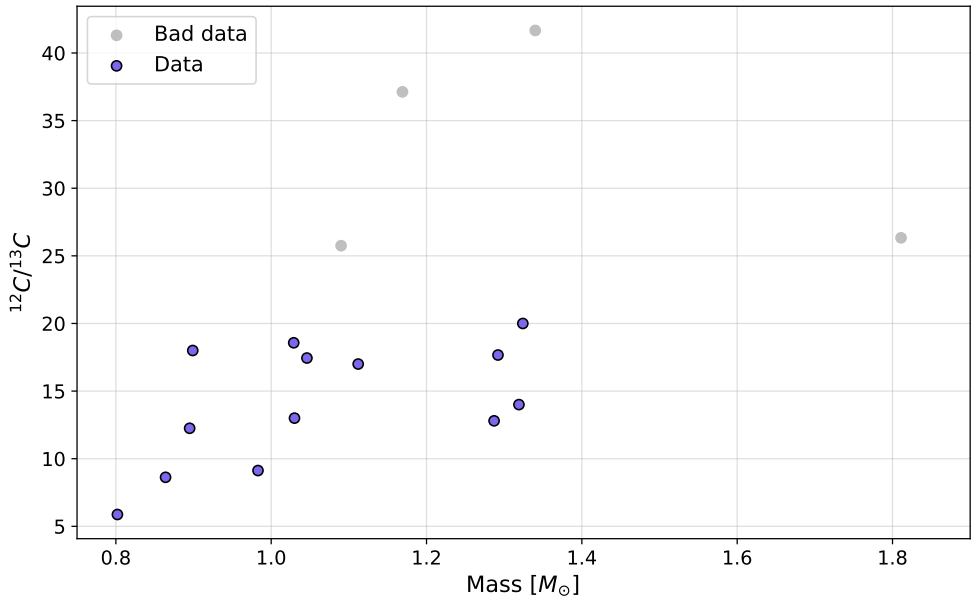

Figure 4.3: ***Carbon ratio vs. stellar mass*** *for the solar neighbourhood stars with available asteroseismic masses. Purple markers correspond to stars with qualitative enough spectra while grey points refer to stars with bad quality spectra.*

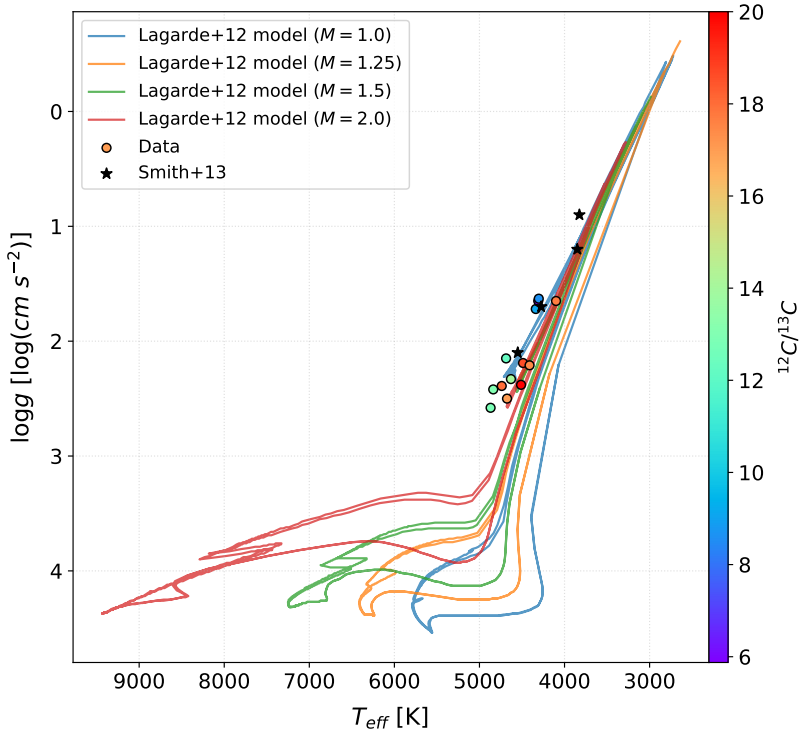

Figure 4.4: *Kiel diagram of the solar neighbourhood stars colour coded with their carbon ratio. Black stars correspond to V. V. Smith et al., 2013b stars. Thermohaline-induced mixing models from Lagarde et al., 2012 for solar metallicity ($Z = 0.014$) and stellar mass of 1.0, 1.25, 1.5 and 2.0 $M_{\odot}$ are the blue, orange, green and red curves respectively.*

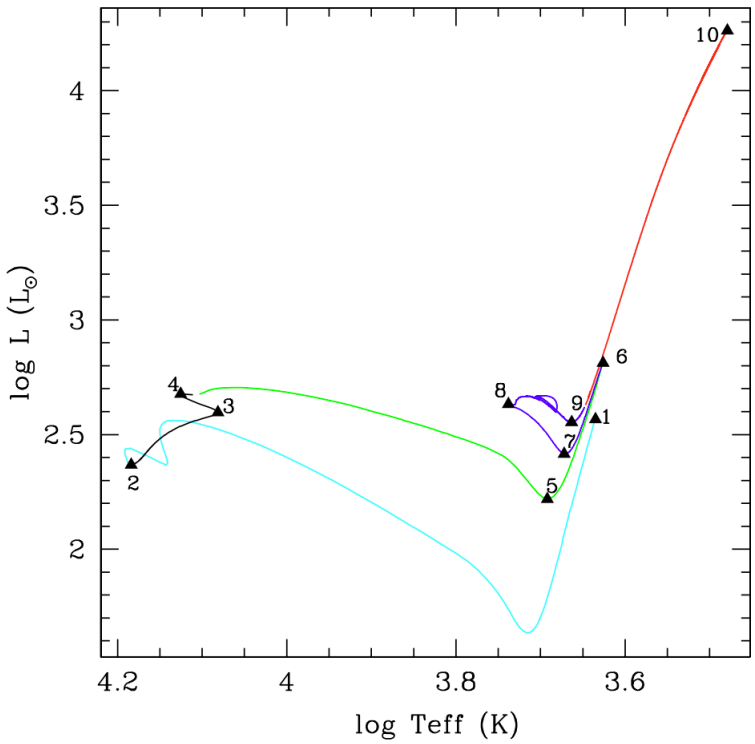

Figure 4.5: *Figure 1 from Lagarde et al., 2012 showing the evolution track in the Hertzsprung-Russell diagram of the standard 4.0 $M_{\odot}$ model at solar metallicity. Each phase is indicated by a different colour: pre-main sequence (cyan), main sequence (black), Hertzsprung gap and red giant branch (green), core helium-burning phase (blue), and asymptotic giant branch (red).*

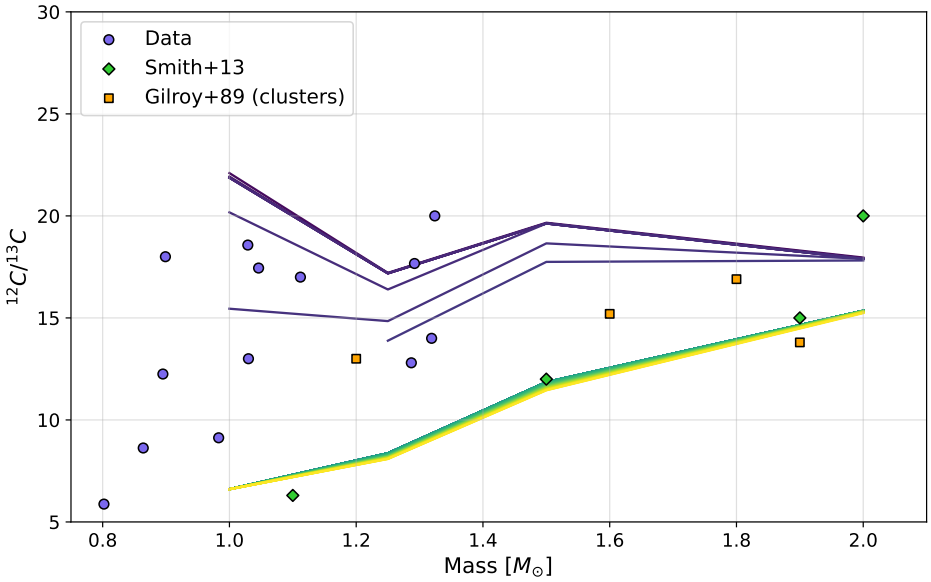

Figure 4.6: ***Carbon ratio vs. stellar mass*** *for the solar neighbourhood stars with available asteroseismic masses. Purple markers correspond to stars with qualitative enough spectra. Coloured lines correspond to the carbon ratios from the thermohaline-induced mixing models from Lagarde et al., 2012 for solar metallicity ($Z = 0.014$) and stellar mass of 1.0, 1.25, 1.5 and 2.0 $M_\odot$. Only values for model stars between the bottom of the RGB (purple) and the RGB-tip (yellow) with temperature between $4000 < T_{eff} < 4800$ K are shown (see Fig. 4.5).*

Part II

Stellar dynamics

5

Introduction

"Every star has its own orbit [...]"
George Bernard Shaw

Chemical analysis of stars is highly valuable for understanding Galactic history as presented in Part I, but it is also crucial to study the motions of stars (kinematics and dynamics) to gain a complete picture. Combining both approaches provides a comprehensive insight into the structure and evolution of the Galaxy. In this chapter, I delve into stellar dynamics and the approaches used to study orbits.

5.1 Stellar orbits

Until now, the Milky Way is the only galaxy where individual stars can be resolved in the inner regions, allowing for high-accuracy measurements of their positions and motions in three dimensions. While the motions of one- or two-body systems are relatively simple, it is widely known that systems with three or more bodies become complex and some are fundamentally unpredictable (Poincaré, 1892). Galaxies, containing numerous interacting stars, gas, and dark matter, can exhibit very complex dynamics and chaotic behaviours (Poincaré, 2017). The Milky Way consists of multiple components that evolve and interact with each other, while also being influenced by external perturbations from satellites like Sagittarius and the Large Magellanic Cloud. Stellar orbits are usually computed using numerical integration algorithms and using simplified, smooth, symmetric and static descriptions of galactic gravitational potentials. Since the timescale for galactic changes far exceeds the typical orbital timescale and because encounters between individual stars are rare, the latter approximations work well. However, in certain cases, accounting for more complex structures like galactic bars, spiral arms or rotation effects is necessary to calculate realistic orbits (this will be more discussed in Section 5.1.2).

5.1.1 Orbit definition

The trajectories that stars trace within the Galaxy are called *orbits*. They are initially set by the motions within the gas from which the stars formed, along with the influence of the gravitational potential. Over time, the movements of stars can be influenced by various processes such as radial migration (Sellwood et al., 2002), gravitational torques (Block et al., 2002), heating mechanisms (J. Binney et al., 1988), and resonances (Athanassoula, 1992a) among others.

Hamiltonian mechanics

The motion of a particle (a star in the case of this thesis) can be described by the Hamiltonian function $\mathcal{H}$ which is a function of coordinates $\mathbf{x}$ and velocities $\mathbf{v}$ and is equal to:

$$\mathcal{H}(\mathbf{x}, \mathbf{v}) = K(\mathbf{v}) + V(\mathbf{x}) \tag{5.1}$$

with the kinetic energy K and potential energy V.

The Hamilton equations are:

$$\dot{\mathbf{x}} = \frac{\partial \mathcal{H}}{\partial \mathbf{v}}, \ \dot{\mathbf{v}} = -\frac{\partial \mathcal{H}}{\partial \mathbf{x}} \tag{5.2}$$

A very useful set of variables to describe a stellar system are the action-angle denoted by ($\boldsymbol{\theta}$,$\mathbf{J}$). Actions are adiabatical invariants which means they are conserved under slow changes in the potential. For instance, this simplifies the treatment of multicomponent systems (e.g. when combining disc and halo potentials, Vasiliev 2019). This set of variables satisfies, in the case of an Hamiltonian only dependant of the actions $\mathcal{H} = \mathcal{H}(\mathbf{J})$:

$$\dot{\theta}_i = \frac{\partial \mathcal{H}}{\partial \mathrm{J}_i} = \Omega_i(\mathbf{J}), \ \dot{\mathrm{J}}_i = -\frac{\partial \mathcal{H}}{\partial \theta_i} = 0 \tag{5.3}$$

where $\Omega_i(\mathbf{J})$ is a constant and represents a frequency.
The actions are constant functions of time (when the stellar system is not perturbed) and the angles are therefore linear functions of time: $\theta_i = \Omega_i(t - t_{i0})$ (i.e. they increase linearly with time).

In the case of a star on a regular orbit, the entire 6D phase space is foliated into non-intersecting 3D orbital torus (or three-torus). The latter would allow three closed independent curves γ_i corresponding to the different (θ_i, J_i) pairs. An illustration of a 2D orbital torus is shown in Figure 5.1. As it moves along its orbit, a star spirals on the surface around the torus. Its motion can therefore be decomposed into three decoupled linear motions in θ_1, θ_2 and θ_3. The actions describe the extent of oscillations in each dimension (i.e. size of the torus) while the angles describe the motion. In other words, actions tell which orbit the star is on and angles where it is located on the orbit. Thanks to transformations $(\boldsymbol{\theta}, \mathbf{J}) \rightarrow (\boldsymbol{x}, \boldsymbol{v})$, it is possible to find the position and velocity at any time (McMillan and Binney (2008)).

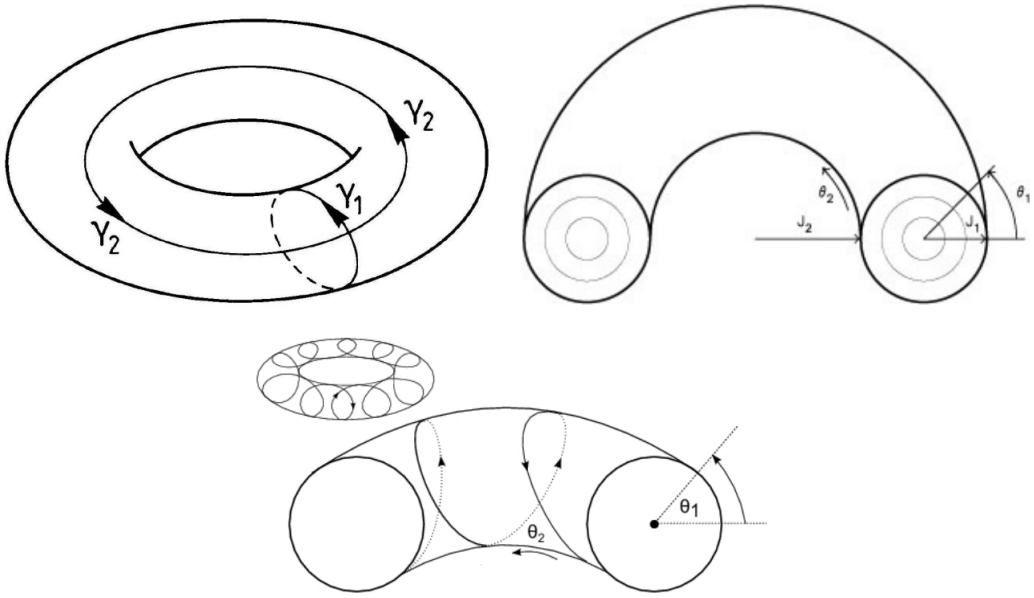

Figure 5.1: *Upper left panel: Two closed independent curves on the surface of a 2D-torus (J. Binney and Tremaine 2008). Upper right panel: The actions* J_i *represent the size of the torus (Merritt, 1999). Lower panel: A star orbiting periodically on the torus surface (Brink et al., 2015).*

An orbit can be characterised according to several definitions:

- A *periodic* or *closed* orbit is an orbit which closes up upon itself periodically after a given amount of time.

- A *quasi-periodic* orbit does not close up upon itself but resides on an invariant torus about the corresponding periodic orbit in phase space.

- A *stable* orbit is an orbit that, if its initial conditions are slightly modified, will remain (for infinite time) close to the original orbit rather than diverging away from it (if it diverges exponentially, it would be a *chaotic* orbit, Lyapunov 1992).

In an ideally unperturbed system, only a few families of periodic orbits exist. However, as a perturbation increases, new orbits are produced by bifurcations from the orbits of the unperturbed system and are called regular orbits. Stable periodic orbits trap nearby regular non-closed orbits, meaning that an orbit sufficiently close to a stable periodic orbit in phase space (i.e. in position and velocity) will tend to stay near it indefinitely. Consequently, stable periodic orbits can be seen as the fundamental building blocks of galaxies. They capture stars and gas in stable, non-closed orbits, contributing to the formation of various galactic structures.

In Cartesian coordinates, the position x_i does not increase limitless as the angle θ_i does. However, we can infer that the position is a periodic function of the angle. We can scale θ_i so that x_i returns to its original value after θ_i has increased by 2π. The positions can therefore be expanded in a Fourier series:

$$\boldsymbol{x}(\boldsymbol{\theta}, \mathbf{J}) = \sum_{\boldsymbol{n}} \boldsymbol{X}_{\boldsymbol{n}}(\mathbf{J}) e^{i\boldsymbol{n}\cdot\boldsymbol{\theta}} \tag{5.4}$$

with $\boldsymbol{n}$: a vector of three non-zero integers.
As shown in Equation 5.3, the angles increase linearly with time with rates set by three constant fundamental frequencies $\boldsymbol{\Omega} = (\Omega_1, \Omega_2, \Omega_3)$, i.e. a star oscillates at a certain frequency Ω_i in each dimension. We can then replace $\boldsymbol{\theta}$ in Eq. 5.4 using Eq. 5.3.

The fundamental frequencies of a generic orbit are incommensurable, i.e. $\boldsymbol{n} \cdot \boldsymbol{\Omega} \neq 0$. However, if they are commensurable ($\boldsymbol{n} \cdot \boldsymbol{\Omega} = 0$), the orbit is considered *resonant*. The latter is then confined to a surface with dimensionality depending on the number of resonance and which is lower than that of the orbital torus.

For a more detailed review, see J. Binney and Tremaine (2008).

Orbital parameters

Orbits can be characterised by several orbital parameters, which are essential for quantifying the spatial extent of the trajectory of a star in the Galaxy:

- The *pericentric* R_{min} or R_{peri} and *apocentric radius* R_{max} or R_{apo} determine the minimum and maximum distances from the Galactic centre that a star can reach according to its orbit.

- The maximal height z_{max} corresponds to the maximal vertical extent from the Galactic plane that the star can reach.

- The orbital *eccentricity* e is a convenient measure for quantifying the circularity of an orbit. For a circular orbit, $e = 0$ while for very elliptical orbits close to be unbound $e \to 1$. Based on a generalisation of the Keplerian case, the formula of the eccentricity can be approximated to a function of the pericentric and apocentric radius: $e = \dfrac{R_{apo} - R_{peri}}{R_{apo} + R_{peri}}$

In the case of regular (non-closed) orbits, these parameters can only be estimated.

5.1.2 Gravitational potentials

The motions of stars are governed by the distribution of mass of the galaxy. Given the current phase-space position of a star, we can determine its orbit if the mass density is known. Therefore, the mass profile of the Milky Way is essential to be able to study the dynamics in our Galaxy. However, it is very challenging to measure it and we need to resort to luminous dynamical tracers (bright stars, satellite galaxies, globular clusters, maser sources, HI gas clouds and tidal streams) to infer its properties. Extensive efforts

have been made to constrain the mass of the Galaxy as accurately as possible using a variety of methods. For an extensive review, see Jeff Shen et al., 2022.

The Poisson equation links the gravitational potential $\Phi(\boldsymbol{x})$ to the density $\rho(\boldsymbol{x})$:

$$\nabla^2\Phi(\boldsymbol{x}) = 4\pi\, G\, \rho(\boldsymbol{x}) \tag{5.5}$$

with G the gravitational constant.

Gravitational potential models are only estimates of the highly complex current Galactic potential, employing specific functional forms characterised by a particular set of parameters. To condense the description of the Galactic potential to just a few parameters, assumptions and simplifications are obviously necessary. These models are generally made up of several components to describe the distinct structures in the Milky Way, such as the disc, the dark matter halo and the bulge. Axisymmetric descriptions are often used to model the potential of the Milky Way and can be a good first approximation, notably for the Galactic disc and the dark matter halo. However, most disc galaxies also exhibit non-axisymmetric structures, such as giant molecular clouds, spiral arms and galactic bars, which interact with the material in the disc. These interactions distort orbits and often lead to resonances due to the coupling between the motion of stellar material and the non-axisymmetric structures. They play a crucial role in redistributing angular momentum and material within the galaxy, moving gas and stars either toward the galactic centre or to the outer regions (for more details, see the review Sellwood, 2014).
As I study stars located in the inner regions of the Galaxy, non-axisymmetric or triaxial potentials that account for the Galactic bar are necessary. This is why I will now focus on barred potentials.

For a star orbiting in a disc, the radial θ_R and azimuthal θ_ϕ orbital angles (see Section 5.1.1) are linear function of time with a frequency κ and Ω respectively. The former describes the radial oscillations[1] and the latter the rotation. Resonance occurs when the orbital period of a star matches a multiple of the period of another perturbing gravitational influence. In the case of a potential that rotates with a pattern speed Ω_b, the main resonances are:

- *Corotation* resonance (CR): $\Omega = \Omega_b$.

- *Lindblad* resonances: $m(\Omega - \Omega_b) = \pm\kappa$ where $+\kappa$ corresponds to the inner Lindblad resonance (ILR): the star overtakes the potential and $-\kappa$ to the contrary with the outer Lindblad resonance (OLR). In the case of a bar, the potential is bisymmetric and thus the integer m[2] is 2. Depending on the shape of the rotation curve (i.e. Ω_b

[1] Small radial deviations from the circular motion of the stars are called epicycles.
[2] Galaxies may have multiple Lindblad resonances, corresponding to different values of m.

as a function of galactocentric radius), a galaxy may have zero, one, or two ILRs (see Fig. 5.2).

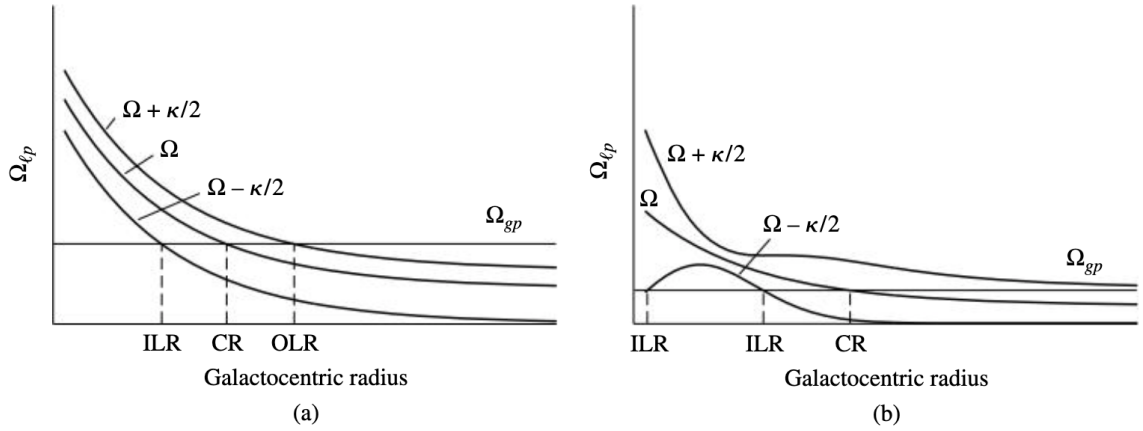

Figure 5.2: *Rotation curve of (a) a galaxy with a single ILR and (b) a galaxy with two ILR. (Carroll and Ostlie 2017)*

Triaxial potentials typically contain two primary types of orbits: **tube** orbits and **box** orbits. They also support various higher-order resonant orbits and **chaotic** orbits. Stars in tube orbits rotate around the galaxy while oscillating in both the radial and vertical directions and are confined within these two dimensions. They are divided into two categories: *short-axis* tubes and *long-axis* tubes depending on their symmetry axis. On the contrary, stars in box orbits undergo a reversal in their direction and never rotate completely around the galaxy. They are confined in azimuthal, radial and vertical directions. The type of an orbit can be determined by looking at the three components of the angular momentum along the orbit. If all components change sign, the orbit has not a sense of circulation and is classified as a box orbit. Conversely, if a component of the angular momentum keeps the same sign, the orbit is a tube around the corresponding axis (Carpintero and Aguilar 1998).

Stable periodic orbits are associated with groups of regular non-closed orbits that are called **orbital families**. Orbits within the same family exhibit qualitative similarities and share many fundamental characteristics. Each orbit family is typically said to be parented by one specific stable periodic orbit. A star on a non-closed orbit may undergo stable oscillations around one of the fundamental closed orbits. The amplitude of these oscillations depends on the initial conditions of the orbit and their proximity in phase space to the parent orbit.

As the shape of a galaxy is partly constrained by the available orbital families, their study is of great interest to identify the stellar populations present in the different structures of the galaxy. A particularly effective method of visualising the various orbit families in a potential involves the use of frequency maps. In Chapter 6, I will present a detailed frequency analysis.

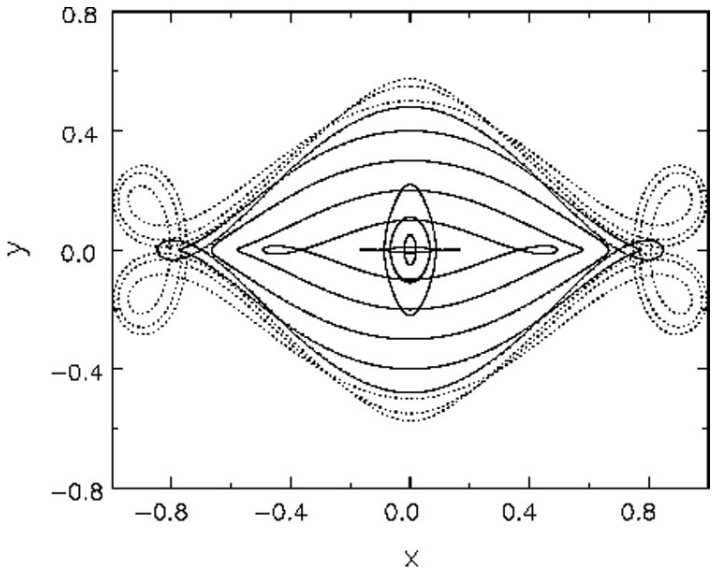

Figure 5.3: *Examples of x_1 (horizontal solid lines) and x_2 (vertical solid lines) orbits in the (x,y) plane of a rotating barred potential. The bar major axis is horizontal. The dotted lines show three 4:1 resonant orbits (which close after four radial oscillations for every turn about the centre).(Sellwood, 2014)*

Periodic orbits are numerous but the most important ones in barred potentials are:

- The x_1 family is the main supporting orbital family of the bar. These orbits are elongated along the bar (i.e. parallel to the bar major axis, see Fig. 5.3), look like ellipses and can feature loops at each both ends. They do not extend beyond the corotation resonance (Contopoulos, 1980).

- The x_2 (stable) and x_3 (unstable) families, in contrast to x_1 family, have rounder orbits perpendicular to the bar (see Fig. 5.3). The presence of x_2 orbits signals the existence of an ILR in the galaxy (Athanassoula, 1992a). They tend to weaken the bar and could even destroy it for small Ω_b.

- The x_4 family has circular retrograde orbits (i.e. they do not rotate in the same direction as the bar) that extend from the central regions to the outer parts of galaxies.

Using firstly 2D potentials, bars were found to be largely made out of regular orbit families trapped around stable periodic orbits (Contopoulos and Grosbol 1989). It was shown later in 3D barred potentials, that the third dimension introduces dynamical instabilities forcing the stable planar periodic orbits to bifurcate. For instance, the x_1 orbits can become vertically unstable in certain regions and bifurcate into various regular orbit families belonging to the so called x_1-tree (Skokos et al. 2002, Athanassoula 2005a). In the same way, the x_2 family parent a large variety of orbits that I will talk about in Chapter 6.

6

Orbital analysis of stars in the nuclear stellar disc of the Milky Way

Published in Astronomy & Astrophysics | A&A 685, A93 (2024)
Authors: N. Nieuwmunster, M. Schultheis, M. Sormani, F. Fragkoudi, F. Nogueras-Lara, R. Schödel, P. McMillan, L. C. Smith, J. L. Sanders

As presented in Chapter 1, the nuclear stellar disc (NSD) is a dense stellar structure in the centre of the Milky Way and surrounds the massive nuclear star cluster (NSC) with its central massive black hole (Launhardt et al. 2002a). The NSD is a flattened disc with a radius of ~ 200 pc and a scale height of ~ 50 pc (Launhardt et al. 2002a; Shogo Nishiyama et al. 2013, Gallego-Cano et al. 2020b). Increasing evidence is reported that the NSD is a distinct structure from the NSC and the nuclear bulge: Francisco Nogueras-Lara et al. (2020b) determined the SFH in the NSD using the GALACTICNUCLEUS data (F. Nogueras-Lara et al. 2018b) and analysing the luminosity function together with stellar evolutionary models. They found that $\sim 80\%$ of the stars formed more than 8 Gyr ago, followed by a quenching phase and then by a recent star formation activity, about 1 Gyr ago, in which about 5% of the NSD mass was formed. While most of studies agree that the NSD has a relatively early formation time, the detailed SFH is still under discussion (see e.g. F. Nogueras-Lara et al. 2023b, Sanders et al. 2024), and much more work is clearly needed.

By using a large sample of KMOS observations in the NSD (Fritz et al. 2021), Schultheis et al. (2021) found a difference in the chemistry, that is, in the metallicity distribution function, between the NSC, NSD, and the nuclear bulge that reinforces a different formation scenario of the NSD. Furthermore, they found some evidence that metal-rich stars may have formed in the central molecular zone, while metal-poor stars show more similarities to the surrounding Galactic bulge.

Kinematic studies relying on radial velocity measurements or proper motion studies show evidence that the NSD is rotating (see e.g. Lindqvist et al. 1992a, Schönrich et al. 2015a, Fritz et al. 2021, Shahzamanian et al. 2022). Linking the rotation to the chemistry,

Schultheis et al. (2021) found that metal-rich stars rotate faster than metal-poor stars, with some hints of counter-rotation for the most metal-poor stars.
Extragalactic studies showed that many barred galaxies host nuclear discs or rings (Gadotti et al., 2019b; Gadotti et al., 2020). So far, the most likely formation scenario of a nuclear disc, called inside-out formation, is linked to the galactic bar (Bittner et al., 2020). According to this scenario, a nuclear disc is a built up from a series of gaseous rings (i.e. nuclear rings) that grow in radius over time. The growth is caused by the gas that is moved towards the galactic centre by the bar.

Based on the 3D velocities, Sormani et al. (2022) constructed axisymmetric self-consistent equilibrium dynamical models of the NSD providing the full 6D distribution function (position and velocity) of the NSD. These models provide the best description of the rotation curve in the innermost few hundred parsecs of the Milky Way, and they are implemented in the *AGAMA* (Vasiliev 2019) software package.
A powerful method for obtaining a complete picture of the properties of the individual orbits is the so-called frequency analysis (Laskar 1993, Valluri et al. 1998, Vasiliev 2013) where the three fundamental frequencies of the orbit oscillation can be extracted accurately. This frequency analysis can be used to distinguish between regular and chaotic orbits and to classify the main orbital families. So far, this technique has mainly been used for studies in the Galactic halo and disc. Amarante et al. (2020) used frequency maps to show that the proposed wedges in the $R_{apo} - z_{max}$ plane, shown Fig. 6.1, identified by M. Haywood et al. (2018) as possible signs of accretion can be explained by the existence of different orbital families. Koppelman et al. (2021) revealed the prominent presence of resonances (see Fig. 6.1). According to this, $\sim$ 30% of the halo stars are associated with resonant families.

In this chapter, I calculate the orbital parameters of a representative sample of stars belonging to the NSD and I use frequency analysis to classify the different types of orbits present in the NSD.

6.1 Observations

6.1.1 Data sample

I used the NSD data obtained with the KMOS (Sharples et al., 2013) spectrometer at the ESO VLT. The detailed survey strategy and data reduction procedures are described by Fritz et al. (2021). As well as their radial velocities, I used the proper motions derived from the preliminary VIRAC2 (L. C. Smith et al., 2018) photometric and astrometric reduction of the VVV data (Minniti et al. 2010). I refer to Sormani et al. (2022) for a more thorough description of the data. The sample includes only stars that are primary sources of the survey leaving us a total of 2501 stars. It is shown in Fig. 6.2.

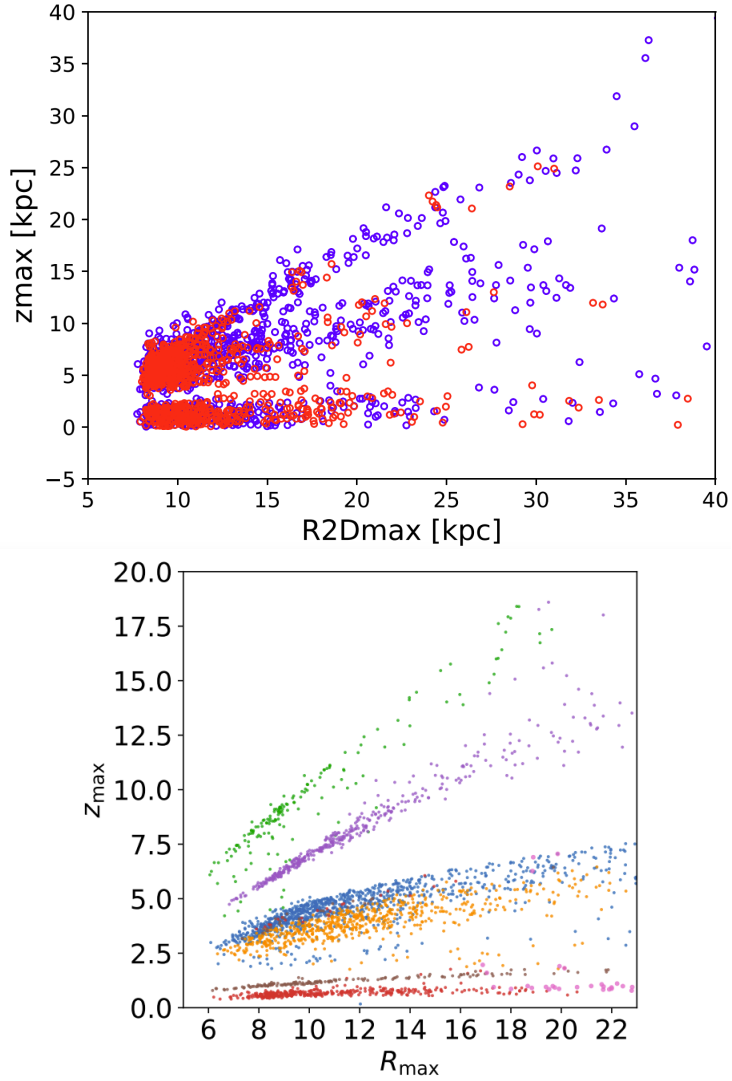

Figure 6.1: *R_{max} vs. z_{max} diagrams from literature showing wedges. Upper panel: Figure 5 from M. Haywood et al., 2018. Lower panel: Figure 10 from Koppelman et al., 2021 where each colour corresponds to an identified orbital resonance.*

6.1.2 Catalogue selection

Sormani et al. (2022) pointed out that stars belonging to the Galactic bar contribute significantly in the outermost fields of the NSD sample of Fritz et al. (2021). In their Tab. 10, they quantified the contamination of the bar: It ranges from 20–30% in the inner fields to up to 75% in the outermost fields. For this reason, I decided to use only the innermost fields, that is, $|l| < 1.5^o$ and $|b| < 0.3^o$, where the probability of NSD membership is higher than 70% (see Tab. 2 of Sormani et al. 2022). In addition, I used the same colour cut $(H - Ks) > \max(1.3, -0.0233\,K + 1.63)$ as in Schultheis et al. (2021) to remove foreground stars.

In order to obtain highly reliable orbital parameters, I constructed a golden sample and chose to keep stars with small proper motion uncertainties: $\mu_{l,err} < 0.6\,\mathrm{mas\,yr^{-1}}$

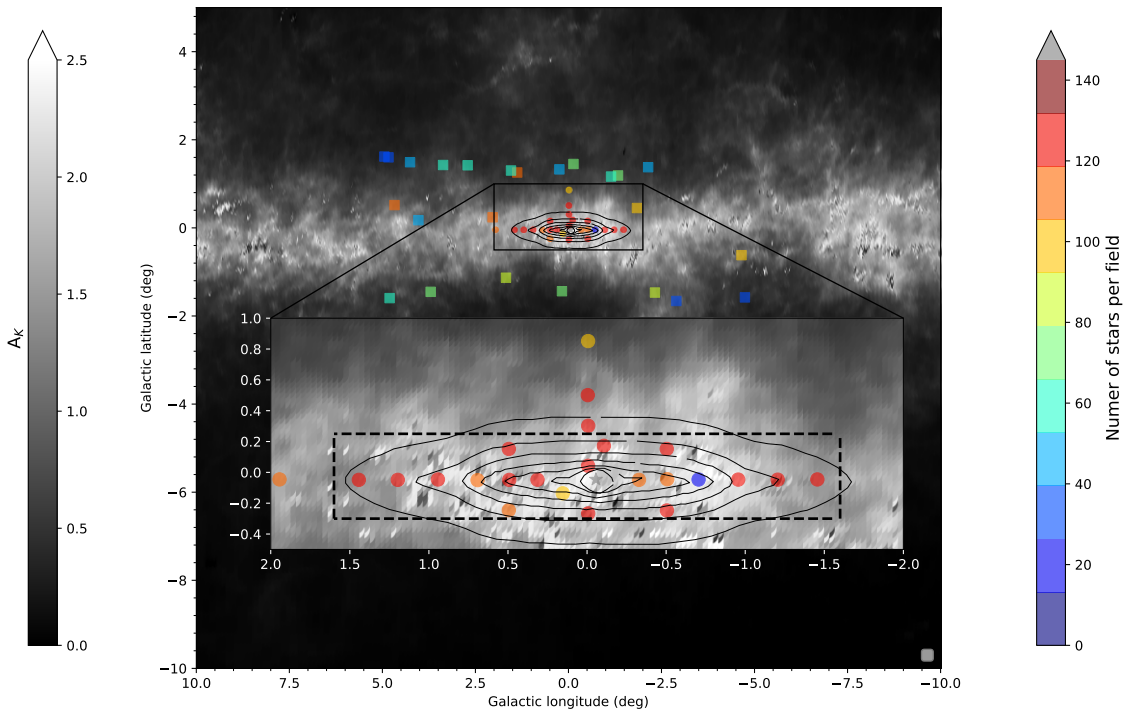

Figure 6.2: *Figure 1 from Schultheis et al., 2021 showing the location of the different KMOS fields of the sample (filled circles) superimposed on the extinction map of Gonzalez et al., 2012. The filled squares indicate the APOGEE DR16 comparison sample. The colour scale represents the number of objects, while the grey scale the AKs value of the extinction map. The black contours show the surface brightness map of the best-fit model of the nuclear bulge component by Launhardt et al., 2002a.*

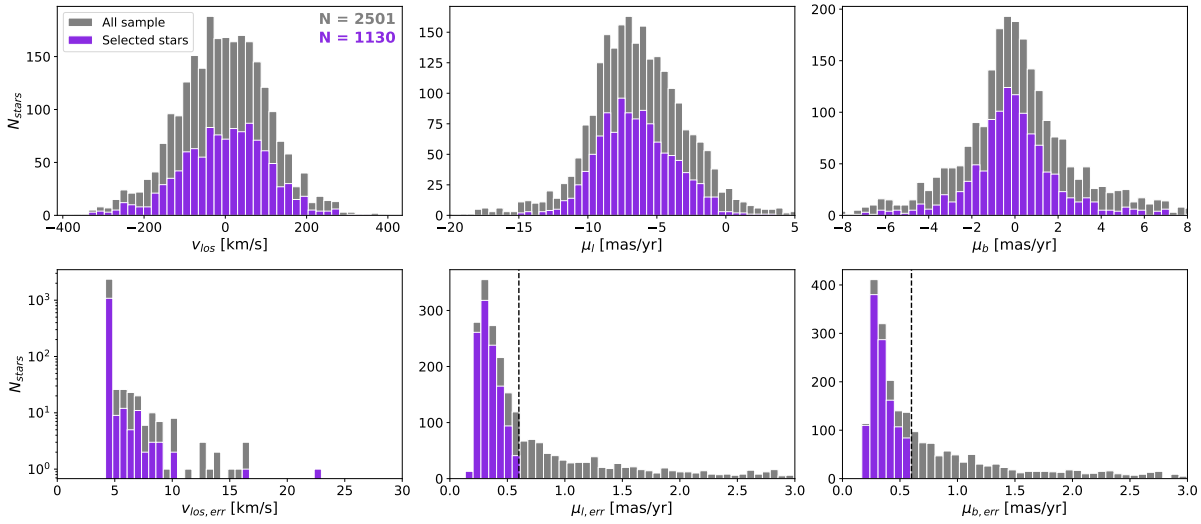

Figure 6.3: *Upper panel: Histograms of the radial velocities and proper motions in μ_l and μ_b, respectively. Lower panel: Same, but for the uncertainties. The grey sample is the full sample, and our final sample, used for the analysis, is shown in magenta.*

and $\mu_{b,err} < 0.6\,\mathrm{mas\,yr^{-1}}$ (corresponding to the 98^{th} percentile; see the vertical dashed line in Fig. 6.3), leading to a total sample of 1130 stars. As pointed out by Sormani et al. (2022), this proper motion cut also removes very bright stars (K < 10), for which

the proper motion errors become large due to saturation effects. Figure 6.4 shows the corresponding HK colour-magnitude diagram after removing the bright stars. The final sample contains stars in the interval $6.6575 < K - 1.37\,(H - K) < 9.1575$, corresponding to a dereddened magnitude of $7.0 < K_0 < 9.5$. The main purpose of this selection criteria was to obtain an unbiased sample in the metallicity distribution as discussed in Schultheis et al. (2021). I caution that the sample is far from complete, which affects the fraction of the different orbital families (see Section 8.3). To overcome this, I carried out in Appendices of Chapter 8 the same analysis using an hydrodynamic N-body simulation of an isolated Milky-Way like disc galaxy that contains a nuclear disc.

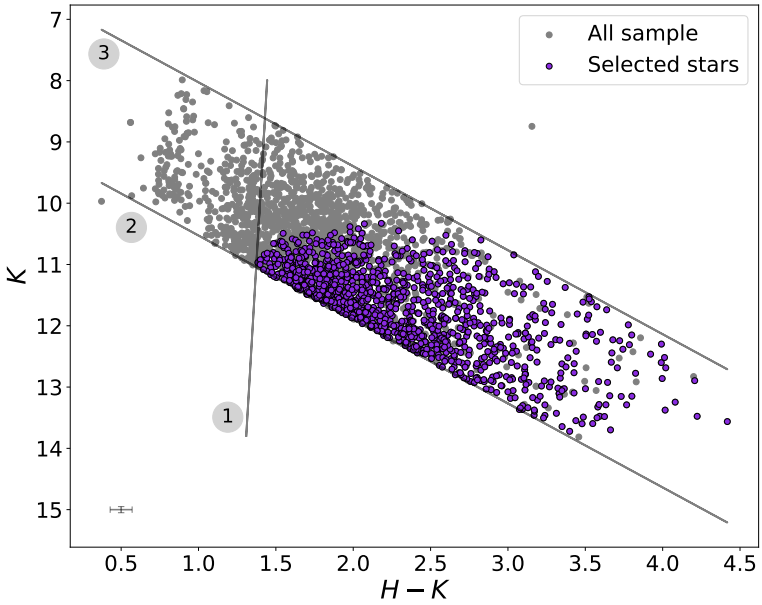

Figure 6.4: *K vs. H–K colour magnitude diagram of the total Fritz et al. (2021) sample in grey. My sample after application of the proper motion cuts is shown in magenta. Colour cut 1:* $(H - K) > max(1.3, -0.0233K + 1.63)$. *Colour cuts 2 and 3:* $6.6575 < K - 1.37(H - K) < 9.1575$. *The typical error for each axis is indicated in the lower left corner of the figure.*

6.2 Analysis

6.2.1 Orbit integration

I used the software package *AGAMA* (Vasiliev, 2019) to determine the orbital parameters. It is both fast in terms of computation time and provides methods for the easy handling of the computation of different potentials. This gives me the flexibility to test different potentials (e.g. axisymmetric, non-axisymmetric, or different bar pattern speeds).

One main source of uncertainties when calculating the orbital parameters is the distance uncertainty. While previous studies of the GC used a constant distance (e.g. 8.25 kpc GRAVITY Collaboration et al. 2020), I implemented a distance distribution in my analysis. As the NSD is an extended stellar feature with a scale length of ~ 100 pc (e.g.

Gallego-Cano et al. 2020b, Sormani et al. 2022, F. Nogueras-Lara 2022a), I assumed this typical scale length and integrated the orbits 100 times by using different distances chosen from a Gaussian distribution (μ = 8.2 kpc, σ = 50 pc) between 8.1 kpc and 8.3 kpc (Launhardt et al. 2002a, F. Nogueras-Lara 2022a).
In addition, I carried out two other tests in which I assigned the distances of the stars in two different ways: (i) I used the colour cuts made by F. Nogueras-Lara et al., 2023b to identify, the stars in the sample that belong to the close edge (i.e. bluer in H–K) and those that belong to the inner region of the NSD (i.e. redder in H–K). Typical distances of 8.05 kpc and 8.2 kpc with a standard deviation of 50 pc were used for the closest edge and the inner population, respectively. (ii) I computed the most likely distances for each star, by using their probability to belonging to the NSD. The probabilities were derived from the distribution function provided by the self-consistent model from Sormani et al., 2022. The results obtained with these different distance values are discussed in Sections 8.2 and 8.3.

For the purpose of this paper, I constructed a non-axisymmetric potential by combining the potentials that correspond to the main components of the Galaxy that affect the dynamics of stars in the NSD: the inner bulge/bar, NSD, and NSC. The total density is $\rho_{\rm tot} = \rho_{\rm bar} + \rho_{\rm NSD} + \rho_{\rm NSC}$ where (i) the bar/bulge density is taken from Launhardt et al., 2002a; (ii) I adopted the NSD density from Sormani et al., 2020 (see their Equation 27); (iii) I used the NSC density from Chatzopoulos et al., 2015a (see their Equation 17). I show a comparison with other potentials in Appendix 6.B. I took into account a typical (clock-wise) rotation pattern speed of Ω_b = 40 km s^{-1} kpc^{-1} (Portail et al., 2017a) for the bar component of the potential which is at an angle of α = 25° from the line of sight towards the Galactic centre (GC).

For the purpose of this study, it is not necessary to set a long integration time because stars located near the GC rotate quickly around it. As explained in Valluri et al., 2016, an accurate determination of the fundamental orbital frequencies requires that orbits are integrated for at least 20 orbital periods. During 500 Myr, most of the stars of the sample have therefore made hundreds to thousands of periods, which is enough to estimate orbital frequencies (see Section 6.2.2). I chose a short timestep of 4000 yr for a good sampling of the orbits.

6.2.2 Orbital frequency determination

Bounded regular orbits in a triaxial potential have three fundamental frequencies, Ω, that determine the periodic behaviour of motion (J. Binney et al. 2008). This motion can be decomposed as a Fourier sum, where the Fourier frequencies are linear combinations of the fundamental frequencies. These fundamental frequencies can be recovered, as shown by Laskar, 1993, using the so-called numerical approximation of fundamental frequencies (NAFF), which has been applied in planetary dynamics. Price-Whelan (2015)

developed an open-source code called *SuperFreq*, which is a Python implementation similar to the NAFF code. This code finds the fundamental frequencies (starting with the highest amplitude) by computing the Fourier spectra for the phase-space coordinates used to describe the orbit. A plot of these fundamental frequencies of a set of orbits gives then a frequency map that allows identifying resonances. As explained in Chapter 5, resonant orbits are those for which the fundamental frequencies $\Omega = \Omega_x, \Omega_y, \Omega_z$ (or $\Omega_R, \Omega_\Phi, \Omega_z$ depending on the selected coordinate system) can be measured and where $n \cdot \Omega = 0$ for $n = (n_x, n_y, n_z)$, where the vector n only contains integer numbers and at most one zero (Koppelman et al. 2021). For example, in Cartesian coordinates, $n_x\Omega_x + n_y\Omega_y + n_z\Omega_z = 0$, and the resonance is then called $n_x : n_y : n_z$. Moreover, boxlets are special cases of resonant orbits in which one of the integers n_x, n_y, n_z is zero.
Frequency maps are a powerful tool for obtaining an automatic classification of the different orbital families with a much clearer separation when plotting the fundamental frequencies in Cartesian coordinates (Valluri et al. 2016).
We can classify orbits into two main categories: tubes (short-axis or long-axis)[1], and box orbits (chaotic orbits correspond to orbits that cannot be identified with one of these categories, see Section 6.2.3). Based on the frequencies in Cartesian coordinates $(\Omega_x, \Omega_y, \Omega_z)$, we can identify most of the orbital families corresponding to the different resonances. However, since the chosen coordinate system only allows us to trace symmetries within the system, short-axis and long-axis tube orbits in the Cartesian case are clustered to a trivial resonance (e.g. 1:-1:0 resonance for short-axis tube orbits). It is then more effective to study orbital frequencies in several coordinate systems even though the Cartesian frequencies give us a general picture of the orbital families. To study tube orbits more precisely and identify their true resonances, it can be better to examine the frequencies in cylindrical coordinates $(\Omega_R, \Omega_\Phi, \Omega_z)$. However, Valluri et al., 2016 showed that Cartesian orbital frequencies are more reliable for bar orbit classification.

6.2.3 Chaoticity

To study chaoticity and particularly identify chaotic orbits, I used two different methods that I introduce in this section.

Lyapunov exponent

The Lyapunov exponent (Lyapunov, 1992) is a fundamental concept in the field of non-linear dynamics and chaos theory. It quantifies the sensitivity of a dynamical system to initial conditions. In a global context, the Lyapunov exponent characterizes how the trajectories in a system diverge or converge as time progresses, providing insights into the long-term behaviour of complex systems.

[1] Tube orbits circulate around a certain axis: z for short-axis tubes and x for long-axis tubes.

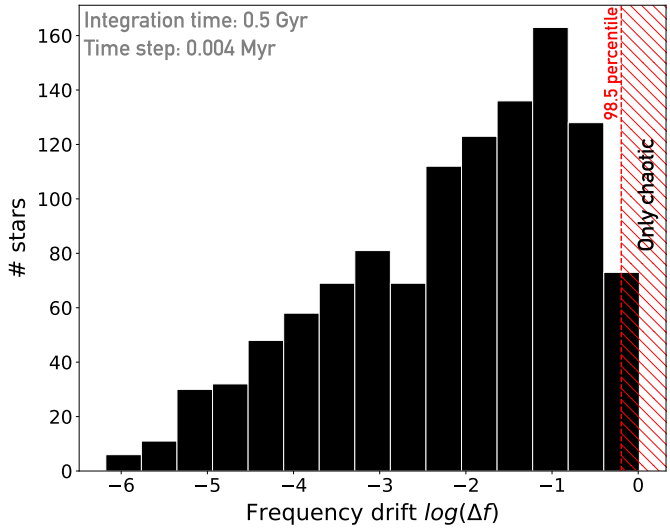

Figure 6.5: *Histogram of the frequency drift. The dashed red area denotes the 98.5 percentile limit above which all orbits are classified as chaotic orbits.*

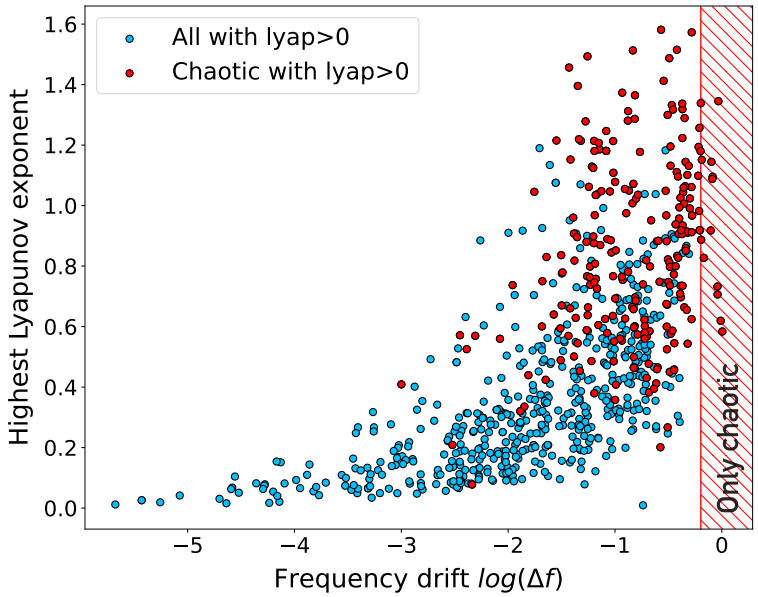

Figure 6.6: *Comparison between highest Lyapunov exponent and frequency drift. The red points show the chaotic orbits identified with the visual classification (see Sect. 6.3.2) while the red shaded area indicates the zone containing only chaotic orbits according to the frequency drift method (see Sect. 6.2.3). Only orbits with a highest Lyapunov exponent greater than 0 are shown in this diagram.*

When considering a dynamical system, even tiny differences in initial conditions can lead to drastically different trajectories over time. The Lyapunov exponent captures this phenomenon by measuring the rate of exponential separation between initially close trajectories. A high Lyapunov exponent indicates chaotic behaviour, where trajectories diverge exponentially over time, making long-term predictions inherently uncertain. Conversely, a low Lyapunov exponent indicates convergence towards a stable equilibrium or periodic behaviour.

I used the highest Lyapunov exponent estimation method provided by *AGAMA* (Vasiliev, 2019). For more details about the method, see Section 4.3 of Vasiliev, 2013.

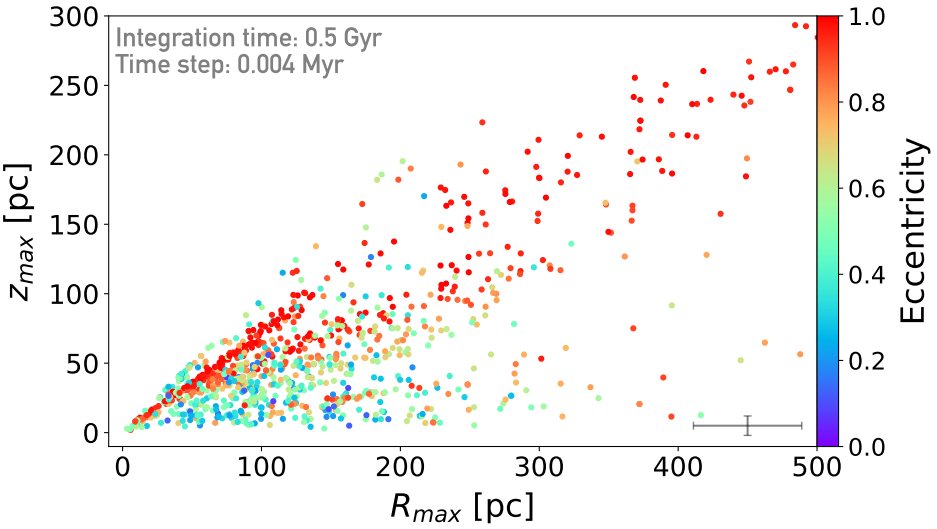

Figure 6.7: *R_{max} vs. z_{max} diagram colour-coded with eccentricity. The typical error on both parameters arising from the propagation of the observational uncertainties and the distance uncertainty is indicated in the lower right corner.*

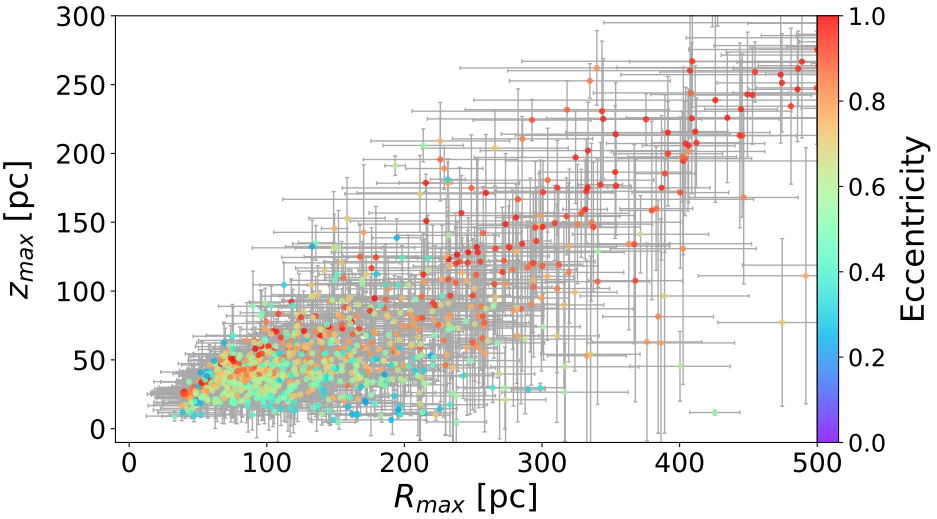

Figure 6.8: *Average R_{max} vs. z_{max} diagram (colour-coded with eccentricity) by using 100 MCMC distances. The standard deviation for each star is indicated with the error bars.*

Frequency drift

Another way to study chaoticity is to directly use the orbital frequencies. Valluri et al., 2010 (see their Section 3.1) showed that it is possible to measure the stochasticity of an orbit based on the change in the fundamental frequencies over two consecutive

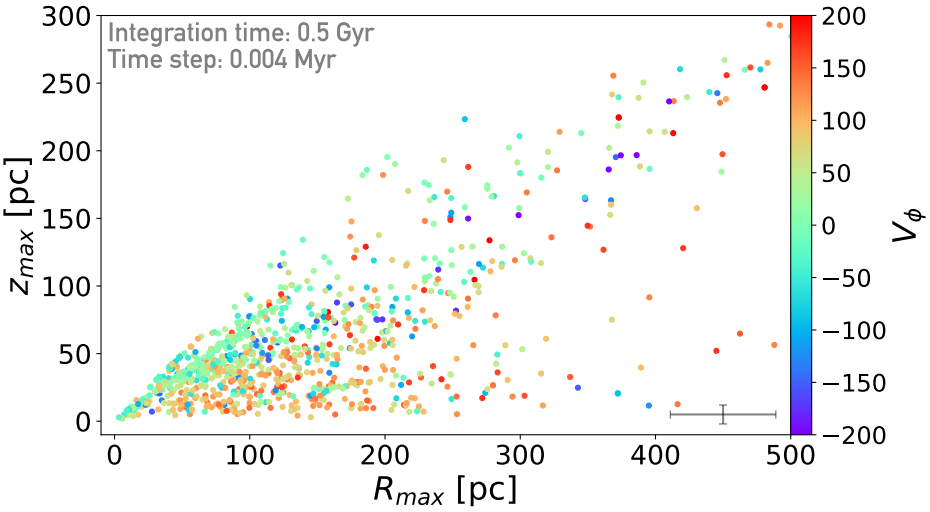

Figure 6.9: *R_{max} vs. z_{max} diagram colour-coded with the rotational velocity. $V_\phi > 0$ means clockwise (i.e. the same direction as the bar). The typical error on both parameters arising from the propagation of the observational uncertainties and the distance uncertainty is indicated in the lower right corner.*

time intervals. For each frequency component f_i, they computed what they called the frequency drift:

$$\log(\Delta f_i) = \log \left| \frac{\Omega_i(t_1) - \Omega_i(t_2)}{\Omega_i(t_1)} \right| \tag{6.1}$$

where i defines the frequency component in Cartesian coordinates (i.e. $\log(\Delta f_x)$, $\log(\Delta f_y)$ and $\log(\Delta f_z)$). The highest value of the three frequency drift parameters $\log(\Delta f_i)$ is then associated with the frequency drift parameter $\log(\Delta f)$. The higher the value of $\log(\Delta f)$, the more chaotic the orbit. However, as shown by Valluri et al. (2010), the accuracy of the frequency analysis requires at least 20 oscillation periods in order to avoid a misclassification of the orbits as chaotic. Figure 6.5 shows the distribution of the frequency drift parameter $\log(\Delta f)$. In order to define a threshold value of $\log(\Delta f)$ at which orbits are classified as chaotic, I followed a similar approach as in Valluri et al. (2010). 1.5 % of the orbits have $\log(\Delta f) > -0.2$ which I consider as the threshold of being chaotic orbits. In total, I obtained 18 chaotic orbits in the sample. Figure 6.6 shows the comparison between the frequency drift parameter and the highest Lyapunov exponent. These two measurements of the chaoticity are generally correlated but the dispersion is high. The visual classification of chaotic orbits (see Sect. 6.3.2, red points in Fig. 6.6) nicely shows that chaotic orbits can indeed be identified based on their large Lyapunov exponent and high frequency drift parameter.

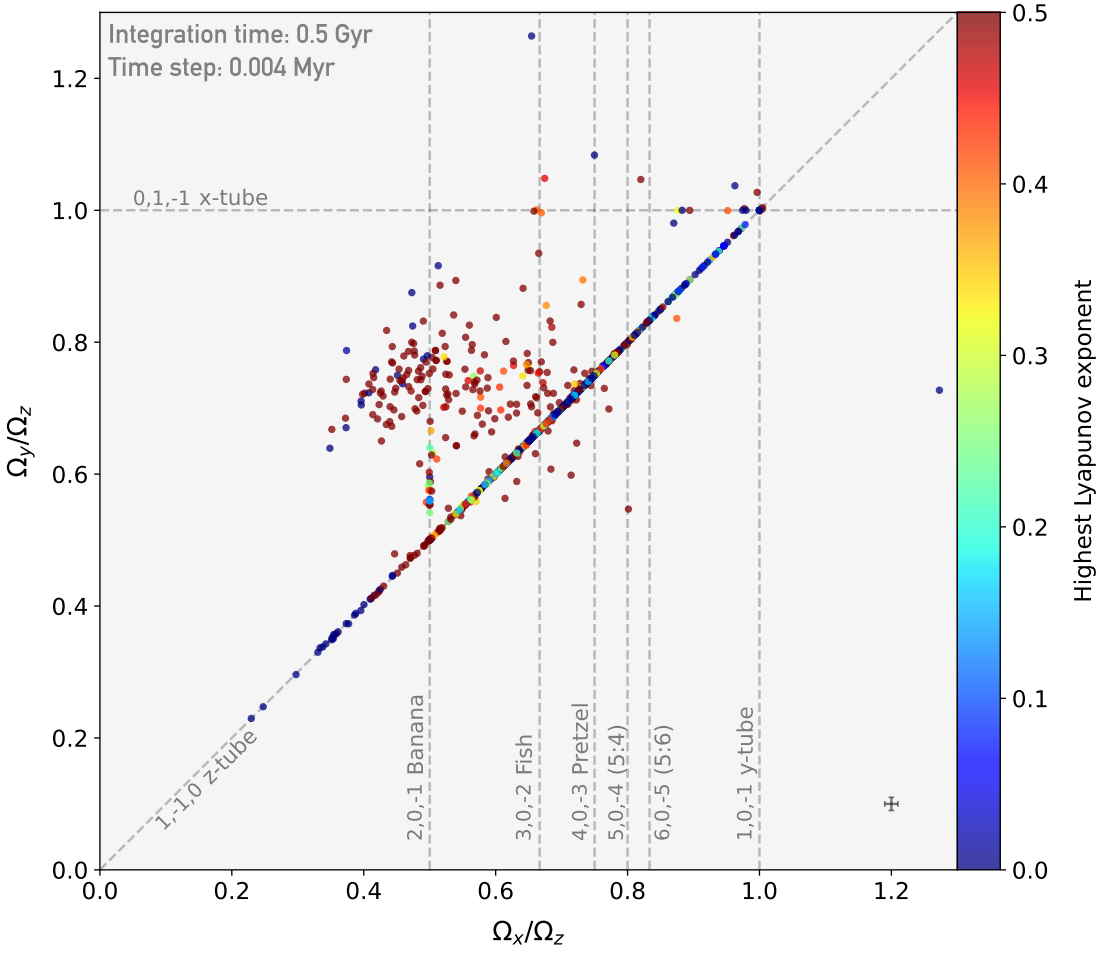

Figure 6.10: *Frequency map in Cartesian coordinates vs. highest Lyapunov exponent. For reasons of legibility, the banana, fish, pretzel, 5:4 and 5:6 resonances are only shown here for the (x, z) plane case. The typical error on both frequency ratios arising from the propagation of the observational uncertainties and the distance uncertainty is indicated in the lower right corner.*

6.3 Results

6.3.1 R_{max} vs. z_{max} diagram

Figure 6.7 shows the apocentric radius (R_{max}) versus the maximum height (z_{max}) of our NSD sample colour-coded by the eccentricity. This diagram shows several features: (i) One striking feature is that the stars are not homogeneously distributed, but congregate in distinct diagonal wedges in which z_{max} increases with R_{max}. (ii) Highly eccentric orbits are confined to one wedge. (iii) Some of these highly eccentric orbits extend beyond the typical radius of the NSD and are likely stars related to the Galactic bar. Figure 6.8 shows the impact for a relaxed assumption of a constant distance and when the distances of the stars are instead allowed to vary within a spread of 100 pc for the NSD, using MCMC simulations (as detailed in Section 3). The key characteristics mentioned earlier clearly persist. This indicates that the uncertainty in the distances of NSD stars can safely be disregarded.

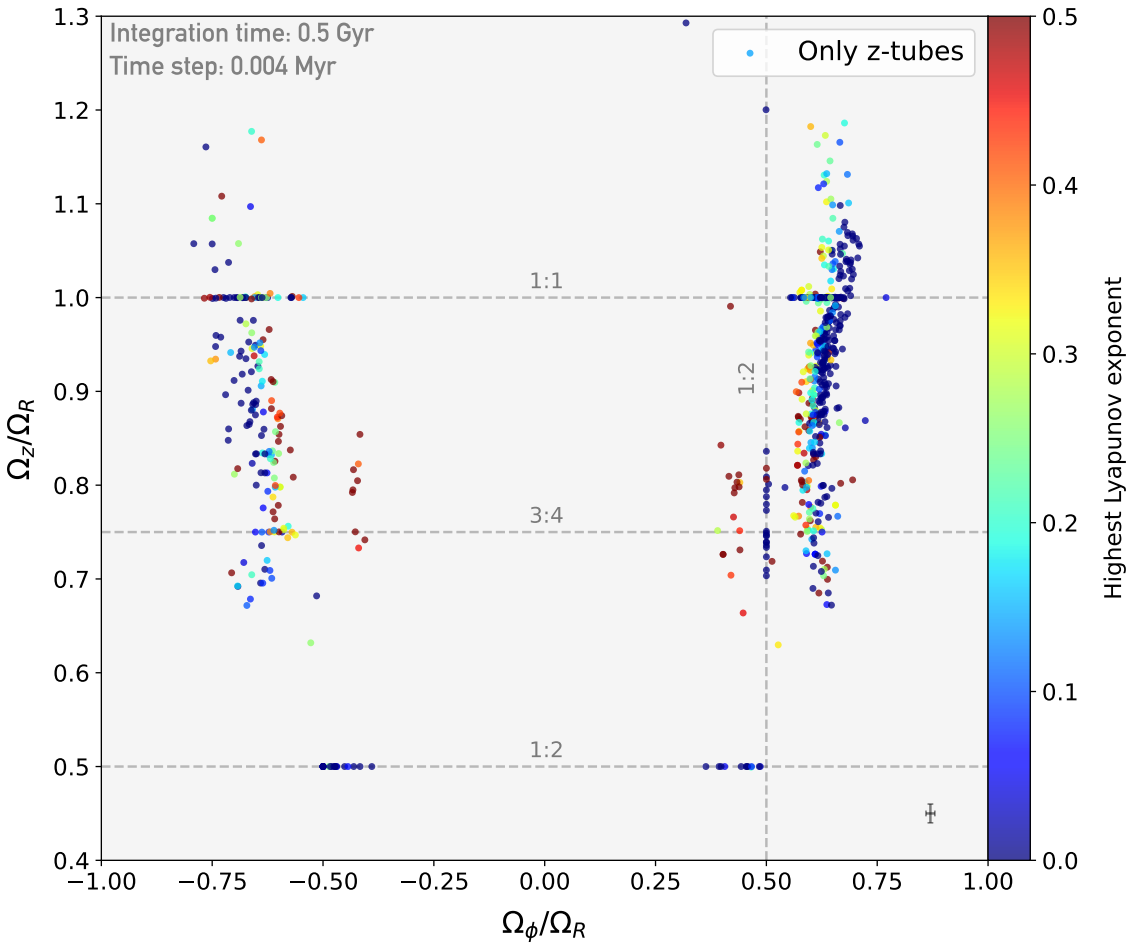

Figure 6.11: *Frequency map in cylindrical coordinates for z-tubes alone (orbits for which a circulation around the z-axis has been detected), i.e. orbits from the resonance (1:-1:0) in Cartesian coordinates (see Fig.6.10). The horizontal and vertical lines correspond to resonances between Ω_z and Ω_R and between Ω_ϕ and Ω_R respectively. The typical error on both frequency ratios arising from the propagation of the observational uncertainties and the distance uncertainty is indicated in the lower right corner.*

Figure 6.9 shows the same feature, but as a function of rotational velocity V_ϕ. The NSD clearly rotates with typical velocities of 80 km/s, which agrees with the works of Lindqvist et al. (1992a), Schönrich et al. (2015a), Schultheis et al. (2021), Shahzamanian et al. (2022), and Sormani et al. (2022). The figure also shows stars with slower rotation and even counter-rotating stars, which have been identified previously by Schultheis et al. (2021).

6.3.2 Orbit classification

I discuss and compare the two methods I used to classify orbits in various orbital families.

Automatic method

I call this method "automatic" because no visual inspection of the orbits is used to classify them (compared to the other classification method presented in Section 6.3.2). Firstly, to differentiate tube orbits from chaotic/box orbits, I determined whether the orbit circulates around a specific axis (e.g. a circulation around the x-axis results in an x-tube) or not (box orbit or chaotic orbit). To do this, I verified whether there was a change in the sign of the angular momentum about an axis. I find 34% box orbits and 66% tube orbits among the 1130 stars. Secondly, to identify the different orbital families, I studied the resonances on the frequency map as explained in Section 6.2.2. In the Cartesian version of the frequency map, Fig.6.10, I observe two main structures: (i) a diagonal line called the 1:-1:0 resonance, where short-axis tubes (called here after "z-tubes") lie, and (ii) a cloud located above the latter resonance and below the 0:1:-1 resonance that is thought to contain mainly box and chaotic orbits. In addition to these two large structures that clearly dominate the frequency map, a few orbits lie close to the 0:1:-1 resonance where long-axis tubes, called here after x-tubes, are located. An example of the morphology of an x-tube is given in Fig.6.A.2.
Based on the three main types of orbits (box/chaotic, z-tube, x-tube), I proceeded with the classification in order to distinguish the resonant orbits that populate the two large structures of the map.
Classical tube orbits are simply orbits with a resonance 1:1 between two of the three frequency ratios. In the same way, I obtained banana orbits with a 2:1 resonance (see Fig.6.A.3), fish orbits with 3:2 (see Fig.6.A.4), pretzel orbits with 4:3 (see Fig.6.A.6), and so on. By plotting lines that correspond to resonances on the frequency map, we gained a first idea of the orbital families that populate the sample. For the same global resonance, for instance, 4:3, this kind of orbit can be observed in different planes (x,y), (x,z), or (y,z), that match the resonances 4:-3:0, 4:0:-3, and 0:4:-3, respectively. In addition to the previously introduced families, I also searched for other pretzel varieties: 5:4 orbits (see Fig.6.A.7) and 5:6 orbits (see Fig.6.A.8).
As explained Section 6.2.2, I also considered the frequencies in cylindrical coordinates (see Fig.6.11), which were only computed for z-tubes (because our sample contains very few x-tubes, I did not consider it necessary to study the frequency map in their corresponding cylindrical coordinates). There is no bisymmetry around $\Omega_\phi/\Omega_R = 0$, which is another way of detecting the rotation of the NSD. More stars orbit in the positive than in the negative sense. The resonances also appear as straight lines here (horizontal lines for a resonance between the vertical oscillation frequency Ω_z and the radial oscillation frequency Ω_R and vertical lines between the azimuthal oscillation frequency Ω_ϕ and the radial oscillation frequency Ω_R). I discern then some resonances, $\Omega_z : \Omega_R = 1:1,\ 3:4,\ 1:2$, and $\Omega_\phi : \Omega_R = 1:2$. Saucer orbits (Sambhus et al. 2000;Vasiliev 2014) (see an example Fig.6.A.5) were found via the resonance $\Omega_z : \Omega_R = 1:1$ (Yavetz et al., 2023), and I therefore have an estimate of their number.
We call a chaotic orbit a weakly chaotic or sticky orbit when it lies near a resonance

Table 6.1: *Family membership results for the automatic and visual methods. NB: The "z-tube" family contains all orbits with a circulation around the z-axis and includes therefore fish, saucer, pretzel,* 5 : 4*,* 5 : 6 *orbits.*

		Chaotic/Box	x-tube	z-tube	Banana	Fish	Saucer	Pretzel	5 : 4	5 : 6
Automatic	**Total**	**34.0%**	**1.1%**	**64.9%**	**4.7%**	**9.0%**	**13.6%**	**3.5%**	**1.5%**	**1.6%**
	With identified chaotics	-	2.1%	-	-	11.2%	-	5.0%	1.9%	1.8%
Visual	**Total**	**24.7%**	**1.5%**	**68.2%**	**5.7%**	**11.2%**	**8.7%**	**4.5%**	**0.6%**	**1.1%**
	Centrophobic	-	-	-	4.0%	9.6%	-	1.8%	-	-
	Centrophilic	-	-	-	1.7%	1.6%	-	2.6%	-	-

(Valluri et al., 2016). It might appear regular for some time, but will finally exhibit chaotic behaviour. With this method, I selected (see Fig. 6.10 and 6.11) all orbits close enough to the resonances in the frequency maps. More precisely, I made the selection at ±0.01 (in frequency ratio), which is enough for contamination by sticky chaotic orbits. However, I limited this contamination by removing orbits from the selection of tubes, that were identified as box/chaotic orbits (without any circulation around an axis). I list in Table.6.1 the percentage for each family with and without these latter contaminants.

Visual method

To evaluate the validity of the automatic orbit classification, I carried out a visual classification by studying each of our 1130 orbits. I was able to identify orbits belonging to the families presented in Section 6.3.2 that are chaotic, x-tube, z-tube, saucer, banana, fish, pretzel, 5 : 4 and 5 : 6 orbits. In addition to this, unlike the automatic method, the visual identification allowed me to differentiate centrophobic and centrophilic orbits of the same family (i.e. of the same resonance). Therefore, I have an estimate of the quantity of anti-banana,-fish, and -pretzel orbits. It is also possible to identify precisely orbits whose own well-known resonance is lacking in the Cartesian/cylindrical frequency maps as for example saucer orbits. Because it was too difficult to visually identify box from chaotic orbits, I decided to class them in the same category for the rest of the orbital analysis as in Section.6.3.2.

As explained in Section 6.3.2, resonant orbits have specific ratios of frequencies that correspond to their resonance. This information is clearly visible in the orbital shape. Therefore, we can visually determine the resonance of an orbit by counting how many times the orbit crossed each of the axes and obtain ratio from this. I identified the different orbital families by using this method.

The results of this classification show in the frequency maps of the figures 6.A.1 to 6.A.8 that the stars belonging to the identified orbital families lie near the corresponding resonances with a larger scattering than the maximum distance from the resonance I took for the automatic method in Section 6.3.2. However, most of the stars for each family are still located very close to the resonance. The identified chaotic/box orbits populate the frequency map in a less regular manner, as expected.

The location of the stars belonging to the identified orbital families in the R_{max} vs. z_{max}

diagram shows that they are arranged in preferential zones:
(i) Chaotic orbits that are scattered all over the frequency map, are only located along the observed filament in the R_{max} vs. z_{max} diagram (see Fig.6.A.1).
(ii) x-tubes only populate the uppermost part of the R_{max} vs. z_{max} diagram, that is, they have the highest z_{max} values for a wide range of R_{max} (see Fig.6.A.2).
(iii) Banana (and anti-banana) orbits are found to occupy a few wedges, but seem to be mainly present in the upper part of the R_{max} vs. z_{max} diagram (see Fig.6.A.3).
(iv) Fish (and anti-fish) orbits are scattered and lack a strong tendency for any wedge (see Fig.6.A.4).
(v) Saucer orbits populate the middle part of the diagram and only appear to correspond to these R_{max}, z_{max} values (see Fig.6.A.5).
(vi) Pretzel (and anti-pretzel) orbits and their derivatives (5:4 and 5:6 orbits) are mainly located in the upper wedges (see Fig.6.A.6,6.A.7,6.A.8 respectively).

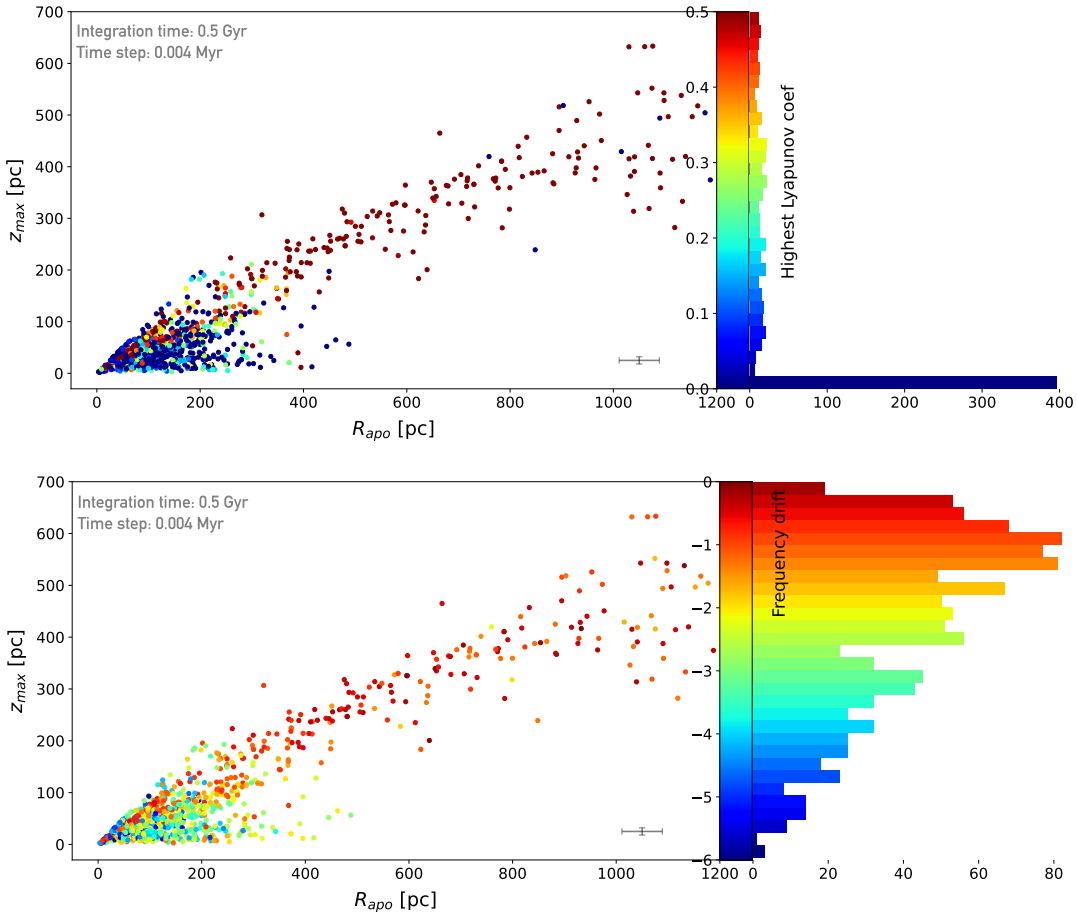

Figure 6.12: *Upper panel: R_{max} vs. z_{max} vs. Lyapunov. Lower panel: R_{max} vs. z_{max} vs. frequency drift. Red indicates the most chaotic orbits in both methods. The typical error on both parameters arising from the propagation of the observational uncertainties and the distance uncertainty is indicated in the lower right corner of each plot.*

6.4 Discussion

This project is the first orbital analysis of stars located in the NSD and also using a non-axisymmetric potential. The purpose of this study therefore is to obtain a general picture of the dynamical signatures in the NSD by studying the orbital resonances.
Wedges in the R_{max} vs. z_{max} diagram have been detected in the Galactic halo by M. Haywood et al. (2018), who attributed these substructures to some heating process related to the early phase of the Galactic disc. Koppelman et al. (2021) investigated these features in the halo in detail using orbital frequencies and axisymmetric potentials. They demonstrated that these structures are due to resonant families and that the depletion around these resonances is related to non-integrable potentials with some indication of chaotic orbits (Price-Whelan et al. 2016).

As explained Section 7.6, I integrated orbits using four different distance estimations: a case with a fixed distance value, another case with distances chosen from a Gaussian distribution, one case with two different distances depending on the estimated position of stars along the line of sight, that is, in front or behind, and a final case where the distance of each star was derived from its position probability along the line of sight. For all the cases, I found the similar R_{max} vs. z_{max} diagrams and frequency maps, showing a very similar orbit distribution. These wedges therefore do not depend on the assumed distance inputs. This confirms that the observed substructures are indeed real and that our frequency maps are reliable. Therefore, I clearly detect wedges in the NSD, as shown in Fig.6.7, where the resonances are visible as thin straight lines. In addition, I conducted many tests with different Galactic potentials, for instance, assuming a classical Milky Way potential with and without a rotating bar (non-axisymmetric and axisymmetric; see Fig. 6.B.1) with which the resonances still occur. This confirms that the conclusions of Koppelman et al. (2021) are relevant in this case as well.
The R_{max} vs. z_{max} diagrams Fig.6.12 and Fig.6.A.1 show a "filament" at high z_{max} that dives into the structure at low R_{max}. It is mainly composed of chaotic orbits, regardless of the method used to identify them (highest Lyapunov exponent Sect.6.2.3, frequency drift Sect.6.2.3 and visual classification Sect.6.3.2). Because this structure is only visible when the bar potential is used in the combination of potentials and because it becomes denser with increasing integration time, I can conclude that the bar disturbs orbits to the point of making them chaotic. With an axisymmetric potential (i.e. without a bar), this filament disappears. This supports the argument of a clear bar signature of this filament. In addition, a projection of these stars in the (l,b) plane shows that these stars are mostly located in the outer parts of the NSD ($|l| > 1.0^o$), where the contamination of the bulge/bar stars in the NSD increases significantly (see Fig. 10 of Sormani et al. 2022). The observed filament consists of $\sim$ 20% stars of the sample, which agrees with the predicted contamination rate from the NSD models of $\sim$ 25% (Sormani et al. 2022).

The distribution of orbits in the Cartesian frequency map Fig.6.10, shows a large majority

of z-tubes that is expected for stars forming a disc structure such as the NSD and a minority of x-tubes. In addition, I was able to identify a variety of families that mostly belong to z-tubes. I introduced in Sect.8.2 two orbital classification methods used in this study: an automatic (see Sect.6.3.2) and visual method (see Sect.6.3.2). Based on previous works about orbit classification (Valluri et al. 2010; Valluri et al. 2012; Valluri et al. 2016), I was able to search several orbital families. Therefore, the automatic and visual classifications contain the same families and I compare their number in Table.6.1. The results of the two methods agree very well for the different identified families. However, the automatic way seems to slightly overestimate chaotic, saucer, 5 : 4, and 5 : 6 orbits and underestimate z-tube, x-tube, banana, fish and pretzel orbits. Even though the visual method can lead to false positives, it still remains better than the automatic one because of the visual check that allowed me to identify every orbital family without any dependence on resonance knowledge. In the era of machine learning (ML) techniques, the visual classification might in future be performed using different algorithms. de los Rios et al. (2021) tested different ML techniques such as a random forest technique, which is a supervised decision tree algorithm, a support vector machine, or K-nearest neighbours to classify galaxies in, and around clusters according to their projected phase-space position. In order to obtain a precise classification, a large training set is necessary on which N-body simulations can be used.
Figure 6.13 shows that fish and saucer orbits dominate the middle and low part of the R_{max} vs. z_{max} diagram, unlike banana and pretzel (and 5:4, 5:6) orbits, which cover the high part. In addition, the few x-tubes are located at the highest z_{max}. Therefore, the results given by the visual classification confirm the link between the observed wedges in the R_{max} vs. z_{max} diagram and orbital resonances, and more precisely, orbital families.

One direct application of the orbital parameter is the determination of the radial and vertical extent of the NSD. Figure 6.14 shows the median apocentric radius R_{max} (left panel) and z_{max} for stars with a different minimum eccentricity threshold (ecc_{min}). For $\mathrm{ecc_{min}} < 0.25$, the truncation radius of the NSD (indicated by the grey area) is 138 ± 5 pc and the vertical extent is 53 ± 1 pc. Schönrich et al. (2015a) constructed a toy model based on APOGEE kinematic data assuming a disk in which the best fit suggest a truncation radius of 150 pc (see their Tab. 1). This is very consistent with the values found in this work but smaller than the radial scale of ~ 230 pc found by Launhardt et al. (2002a). This could be due to the heavy differential reddening as they used photometric data. The vertical extent is about 50 pc in Schönrich et al. (2015a), but they did not confine this parameter from their toy model.
I stress that my sample size is limited due to my selection cuts (see Section 6.1.2), leading to statistically small sample sizes for each derived family of orbits. A first rough estimate of the completeness of the sample by using luminosity functions (see e.g. F. Nogueras-Lara et al. 2023b) shows that my working sample is indeed highly incomplete ($\sim 15\%$ completeness at $\mathrm{K_S} \sim 11.5$ mag).

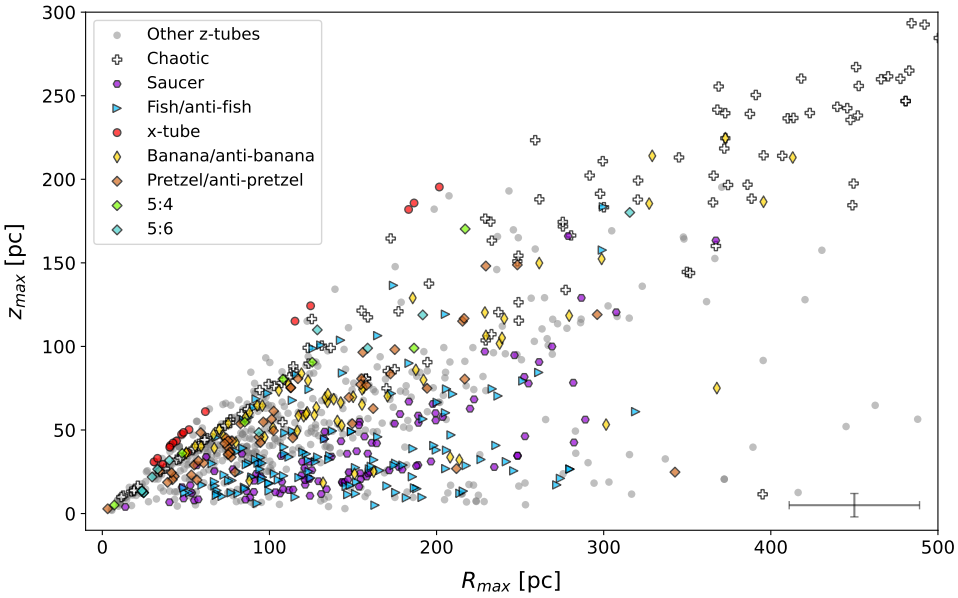

Figure 6.13: *R_{max} vs. z_{max} diagram with the different identified orbital families. Separate diagrams for each family are given in Appendix 6.A. The typical error on both parameters arising from the propagation of the observational uncertainties and the distance uncertainty is indicated in the lower right corner.*

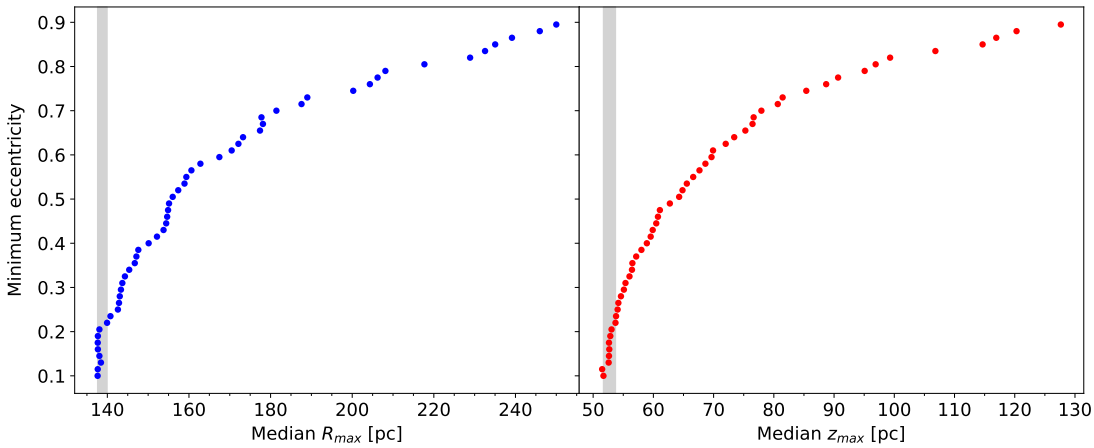

Figure 6.14: *Median apocentric radius R_{max} and maximum height z_{max} for stars with a different minimum eccentricity threshold. For instance, the median R_{max} for a minimum eccentricity of 0.5 means that we only computed the median of the R_{max} values of stars with an eccentricity above 0.5.*

Complementary high-resolution N-body simulations of the NSD are necessary to (i) extend my study to a much larger sample, (ii) compare simulations and the observed data set in detail, and (iii) study the effect of different Galactic potentials on the derived orbital families.

As explained in Chapter 5, in the vicinity of the Galactic bar, orbits perpendicular to the bar are called x_2-type, and orbits parallel to the bar are called x_1-type orbits. x_2-type orbits are parents of the z-tube family, occupying the 1:-1:0 main resonance line in the frequency map (see Fig. 6.10), where about two-thirds of our sample lies. The

formation of nuclear stellar discs is strongly connected to the properties of the galactic bar. Hydrodynamical simulations suggest that nuclear stellar discs form close to the inner Lindblad resonance of the main bar, where the x_2-type orbital family dominates (Athanassoula 1992a; Athanassoula 1992b, Z. Li et al. 2015, Sormani et al. 2018b, Sormani et al. 2023). After the Galactic bar was formed, gas was funnelled along the bar towards the GC, where it settled down to form a nuclear disc. The gas then formed stars, which keep their resulting x_2 orbits, and the resulting stellar population resembles a disc. Additional evidence comes from the spatial and kinematical overlap between the central molecular zone and the NSD (Schönrich et al. 2015a, Schultheis et al. 2021) in the Milky Way, which supports this scenario that the stars in the NSD should be more metal-rich and dynamically cooler than the surrounded bar/bulge populations. This feature can also be seen in external galaxies with NSDs (Bittner et al. 2020, Gadotti et al. 2019b).
Planar periodic orbits x_1, x_2, and x_4 share the $1:2$ resonance between the tangential oscillation frequency (Ω_ϕ) and the radial frequency (Ω_R). Unfortunately, they are not anticipated to be abundant in N-body simulations (Valluri et al., 2016) and it is a delicate task to identify these orbits visually. This prevented us from distinguishing them properly. However, I was able to detect bifurcations from the x_1-tree (Athanassoula, 2005a) with banana orbits that were called "x_1v_1" by Skokos et al., 2002. The presence of the latter would suggest the existence of an inner bar embedded in the NSD, as observed in others galaxies (Méndez-Abreu et al., 2019), but a more in-depth study is needed.

6.5 Conclusions

I presented a detailed orbital analysis of stars in the NSD by using orbital frequencies and a visual classification of the orbits obtained from the orbital integration. A comparison between these two methods shows very similar results in the classification of the different orbital families, such as chaotic/box, z-tube, x-tube, banana, fish, saucer, pretzel, 5:4, and 5:6 resonances. The large majority of sources are z-tubes, which is expected for stars located in an NSD. I used two different methods: the Lyapunov exponent, and the frequency drift. I estimated the chaoticity of the orbits with these methods and showed by using in addition a visual classification that chaotic orbits can be identified by their high Lyapunov exponent as well as by their high frequency drift parameter. They occupy in the R_{max} vs. z_{max} the filament at high z_{max} where the bar most likely causes the highly chaotic orbits. About 20% of our stars are contaminated by the bar/bulge population which is very close to the predicted 25% contamination from the most recent NSD models of Sormani et al. (2022). I emphasise that I performed here a statistical approach and that the orbits of the individual stars can be affected by the presence of molecular clouds as well as by the disruption of their trajectory by tidal forces (e.g Portegies Zwart et al. 2002, Kruijssen et al. 2014).
I detected clear substructures in the R_{max} vs. z_{max} diagram in the NSD that were identified as wedges that are related to different resonances and therefore different orbital families. 68.2% of our sample show z-tube orbits that are parented by the x_2-type

orbits. This is indeed expected if the formation of the NSD is coupled with the formation of the Galactic bar where x_2-type orbits are the dominant population. As a follow-up work, a comparison with self-consistent models of the NSD (e.g. Sormani et al. 2022) is necessary for a detailed comparison between the observations and the predictions from the models (e.g. fraction of different orbital families) and to improve our orbital classification.

I used the R_{max} vs. z_{max} diagram to constrain the radial and vertical extent of the NSD with 138 ± 5 pc and 53 ± 1 pc, respectively, which is consistent with the values found in Schönrich et al. (2015a). A first study of the chemistry of the stars presented here is shown in Chapter 7 and shows possible trends between the identified orbital families and metallicity. Future large surveys of the NSD, such as the upcoming MOONS survey (Gonzalez et al. 2020) will clearly benefit from the large number of stars to establish the strong connection between dynamics and chemistry.

Appendices

6.A Orbital families

I present here typical examples of orbits in the x, y, z plane as well as the location in the R_{max} vs. z_{max} diagram and in the frequency map in Cartesian coordinates. I also show in Fig.6.A.9 the location of certain families in the cylindrical frequency map.

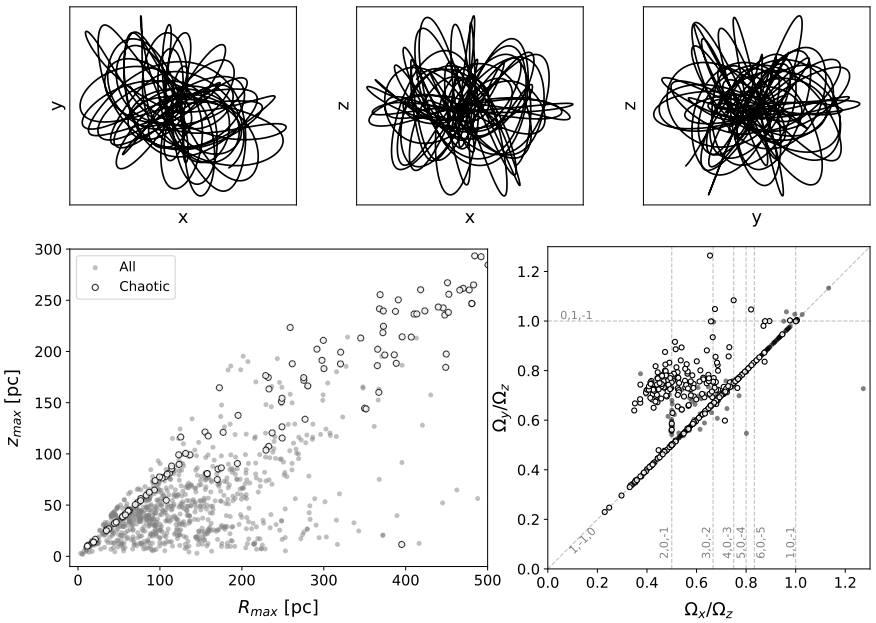

Figure 6.A.1: *Example of a chaotic orbit. Upper panel: Orbit plotted in the (x, y), (x, z) and (y, z) planes. Lower panel: R_{max} vs. z_{max} diagram (left) and Cartesian frequency map (right). The coloured markers correspond to the chaotic orbits identified with the visual method (see 6.3.2).*

6.B Comparison of potentials

To assess the sensitivity of the study outcomes to the selection of the mean potential, I integrated the orbits using an axisymmetric potential or slightly varied combinations of (non-axisymmetric) potentials. As detailed in section 7.6, my approach involves considering three components: the bulge/bar, the NSD, and the NSC. In the following figures (Fig. 6.B.1, Fig. 6.B.2, 6.B.3 and 6.B.4), I compare the R_{max} vs. z_{max} diagram

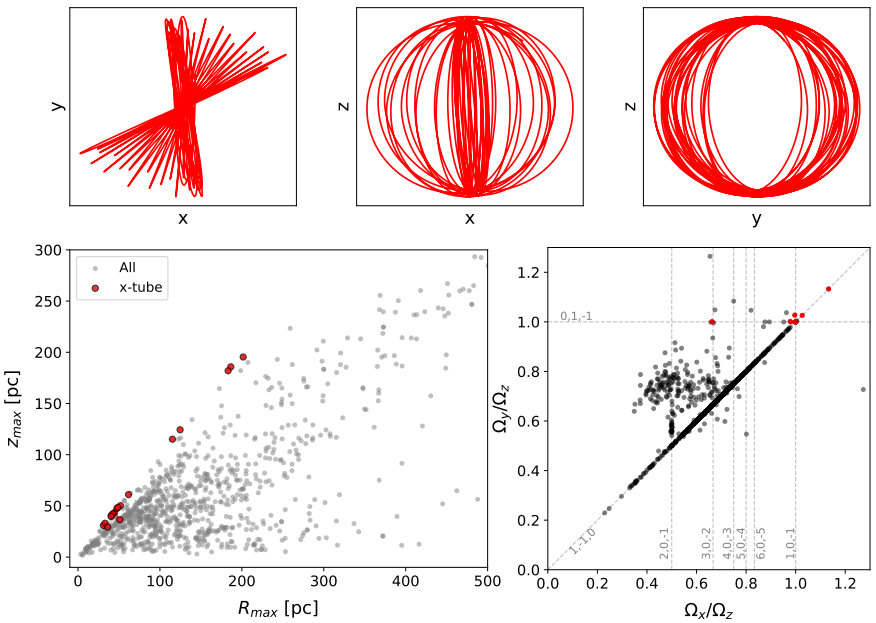

Figure 6.A.2: *Example of an x-tube, i.e.* $1:1$ *resonance between* Ω_y *and* Ω_z*, also called* $(0:1:-1)$*. Upper panel: Orbit plotted in the* (x,y)*,* (x,z)*, and* (y,z) *planes. Lower panel:* R_{max} *vs.* z_{max} *diagram (left) and Cartesian frequency map (right). The coloured markers correspond to the x-tube orbits identified with the visual method (see 6.3.2).*

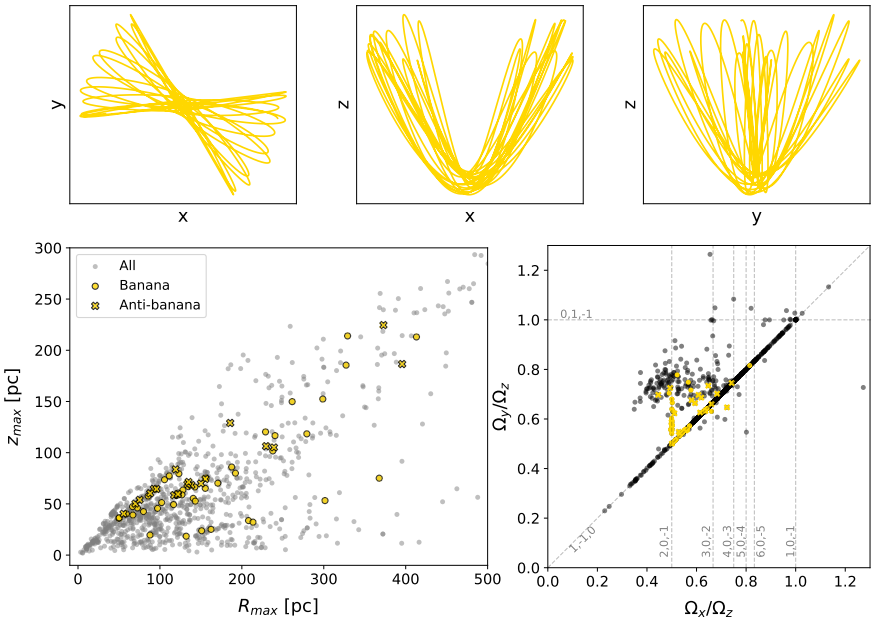

Figure 6.A.3: *Example of a banana orbit (here, a* (x,z) *banana), i.e.* $2:1$ *resonance between two orbital frequencies (here,* Ω_z *and* Ω_x*, also called* $(2:0:-1)$*). Upper panel: Orbit plotted in the* (x,y)*,* (x,z)*, and* (y,z) *planes. Lower panel:* R_{max} *vs.* z_{max} *diagram (left) and Cartesian frequency map (right). The coloured markers correspond to the banana and anti-banana orbits identified with the visual method (see 6.3.2).*

presented in this paper (Fig. 6.7) with those obtained with an axisymmetric potential

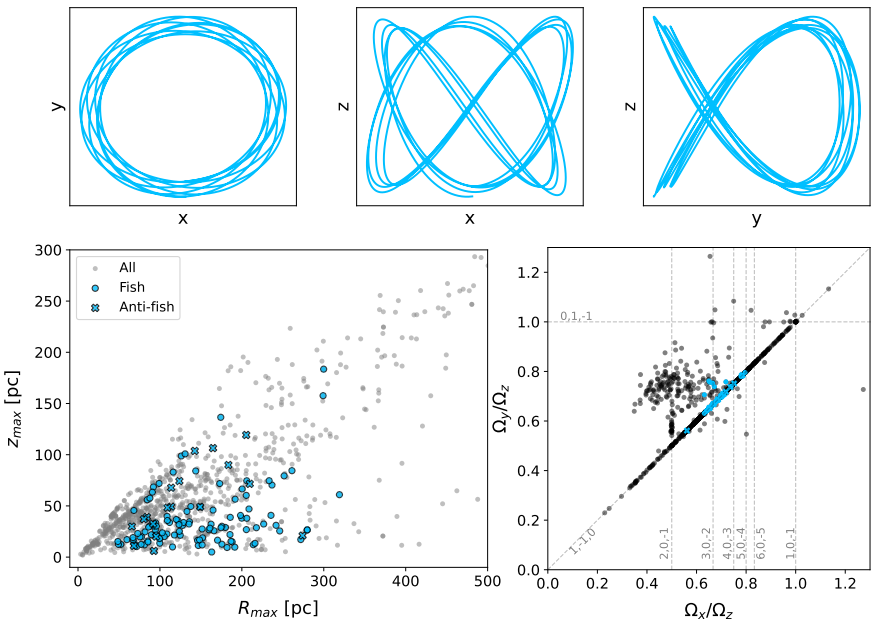

Figure 6.A.4: *Example of a fish orbit (here, a (y, z) fish), i.e. $3:2$ resonance between two orbital frequencies (here, Ω_z and Ω_y, also called $(0:3:-2)$). Upper panel: Orbit plotted in the (x, y), (x, z) and (y, z) planes. Lower panel: R_{max} vs. z_{max} diagram (left) and Cartesian frequency map (right). The coloured markers correspond to the fish and anti-fish orbits identified with the visual method (see 6.3.2).*

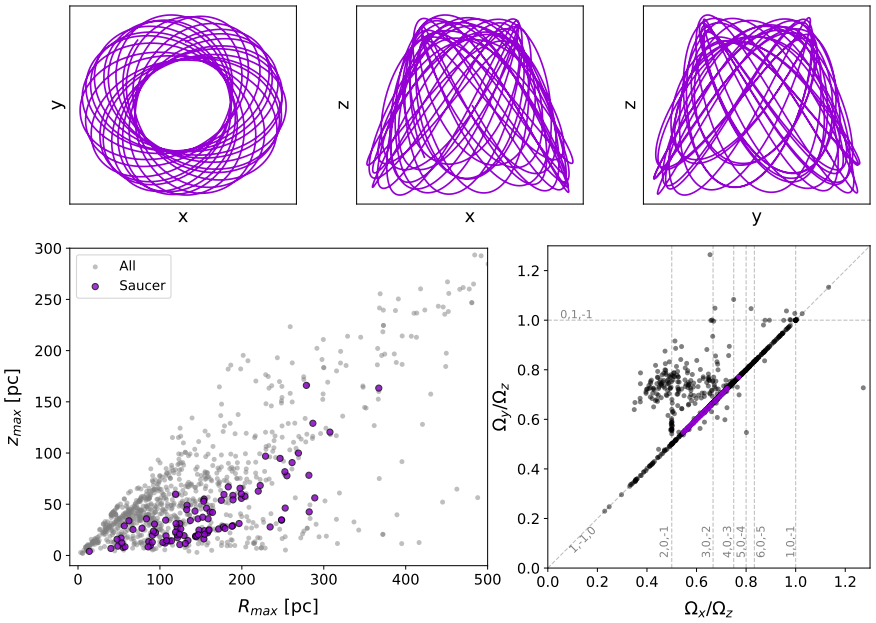

Figure 6.A.5: *Example of a saucer orbit, i.e. $1:1$ resonance between Ω_z and Ω_R. Upper panel: Orbit plotted in the (x, y), (x, z), and (y, z) planes. Lower panel: R_{max} vs. z_{max} diagram (left) and Cartesian frequency map (right). The coloured markers correspond to the saucer orbits identified with the visual method (see 6.3.2).*

(MWPotential14 from Bovy 2015) or by changing the NSD potential (Sormani et al. 2022 and Launhardt et al. 2002a), the bar potential (Portail et al. 2017a), or the bar angle.

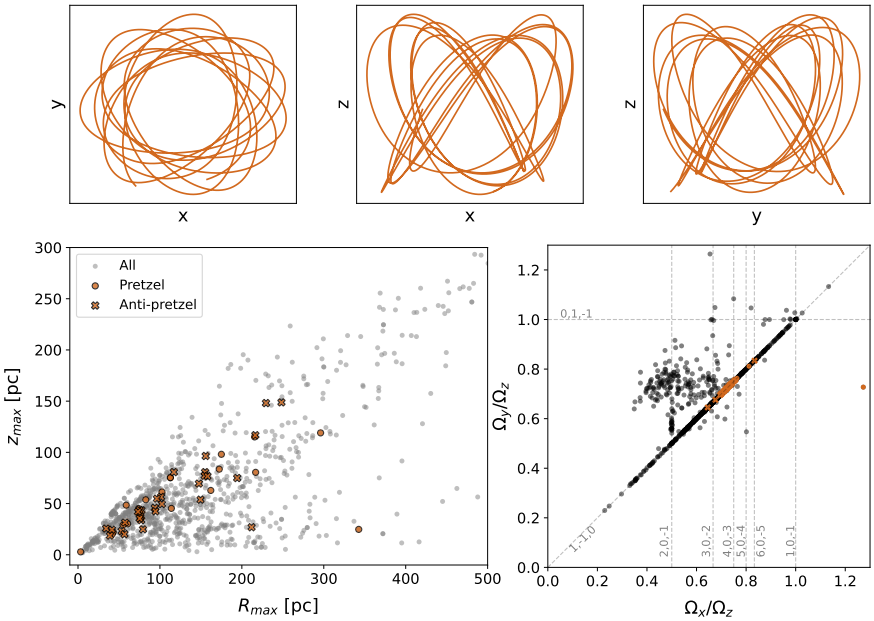

Figure 6.A.6: *Example of a pretzel orbit, i.e.* $4:3$ *resonance between two orbital frequencies (here,* Ω_z *and* Ω_y*, also called* $(0:4:-3)$*). Upper panel: Orbit plotted in the* (x,y)*,* (x,z) *and* (y,z) *planes. Lower panel:* R_{max} *vs.* z_{max} *diagram (left) and Cartesian frequency map (right). The coloured markers correspond to the pretzel and anti-pretzel orbits identified with the visual method (see 6.3.2).*

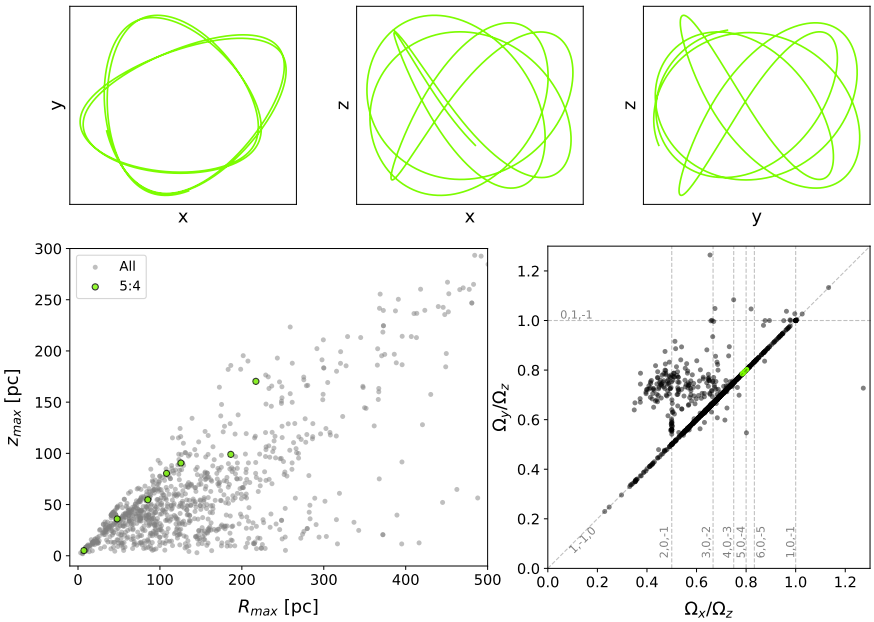

Figure 6.A.7: *Example of a 5:4 orbit, i.e.* $5:4$ *resonance between two orbital frequencies (here* Ω_z*, and* Ω_y*, also called* $(0:5:-4)$*). Upper panel: Orbit plotted in the* (x,y)*,* (x,z)*, and* (y,z) *planes. Lower panel:* R_{max} *vs.* z_{max} *diagram (left) and Cartesian frequency map (right). The coloured markers correspond to the 5:4 orbits identified with the visual method (see 6.3.2).*

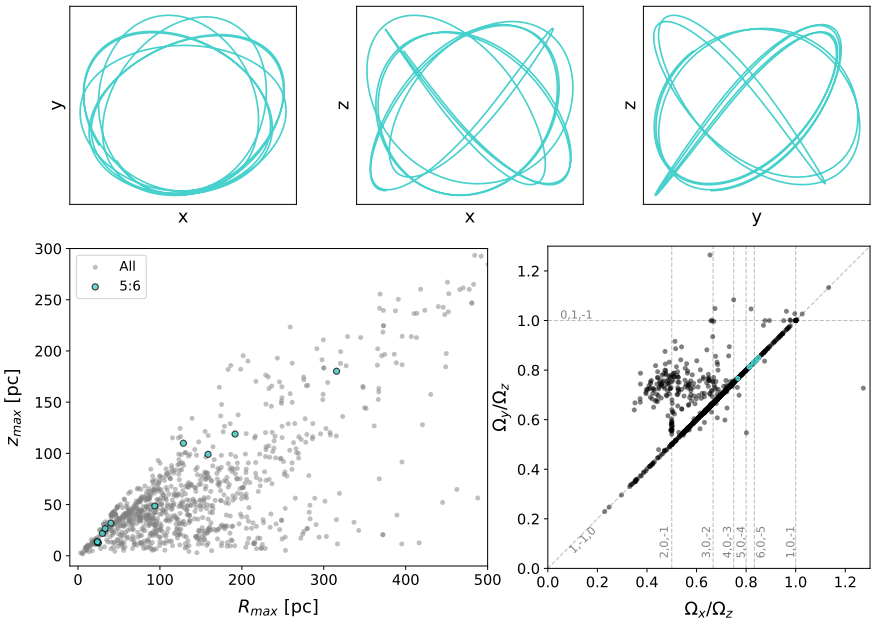

Figure 6.A.8: *Example of a 5:6 orbit, i.e.* $5:6$ *resonance between two orbital frequencies (here,* Ω_y *and* Ω_z*, also called* $(0:6:-5)$*). Upper panel: Orbit plotted in the* (x,y)*,* (x,z)*, and* (y,z) *planes. Lower panel:* R_{max} *vs.* z_{max} *diagram (left) and Cartesian frequency map (right). The coloured markers correspond to the 5:6 orbits identified with the visual method (see 6.3.2).*

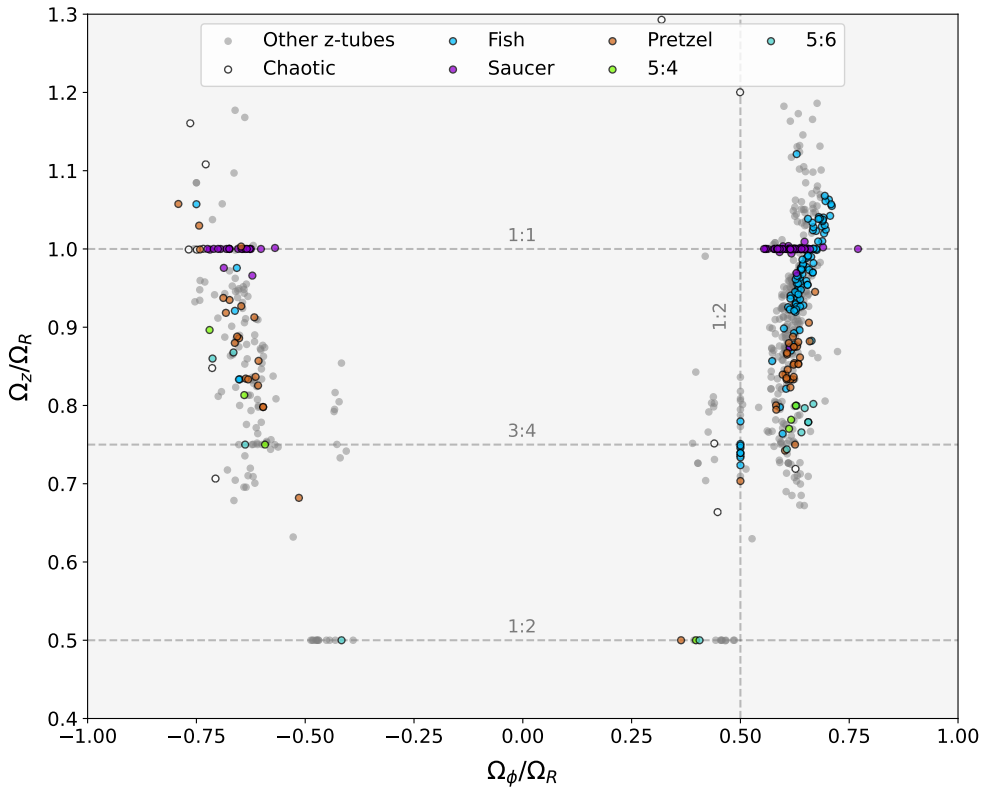

Figure 6.A.9: *Frequency map in cylindrical coordinates for different families (identified with the visual method; see Section.6.3.2) with computable cylindrical frequencies.*

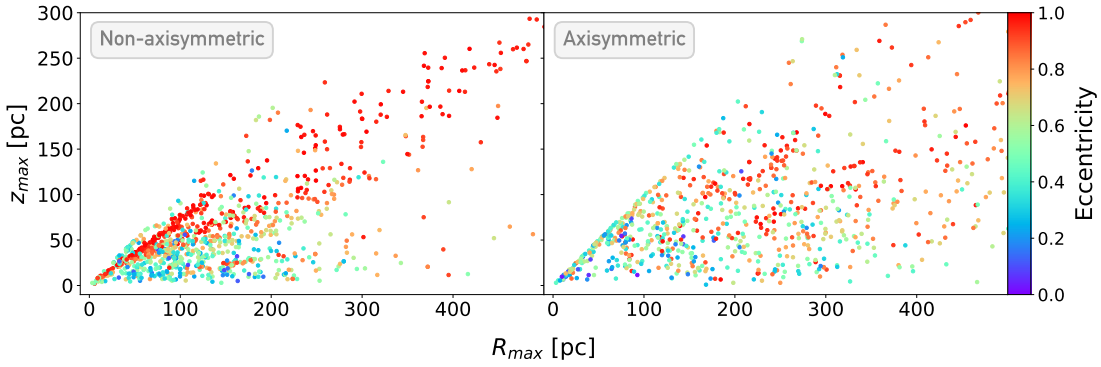

Figure 6.B.1: *R_{max} vs. z_{max} diagram comparison for the axisymmetric and non-axisymmetric cases. Left: Reference diagram, with the non-axisymmetric combination of potentials presented in Section 7.6. Right: Using the axisymmetric potential MWPotential14 from Bovy, 2015.*

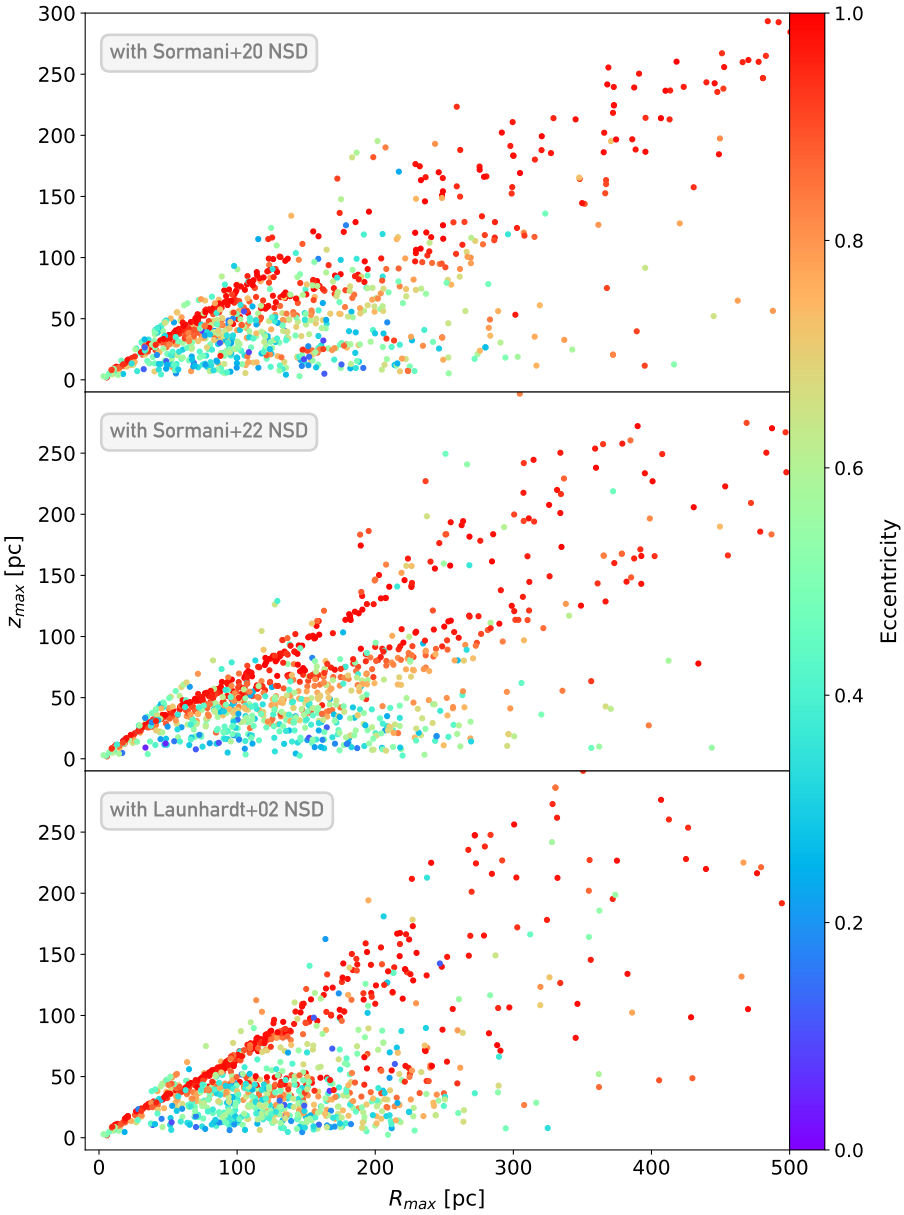

Figure 6.B.2: *R_{max} vs. z_{max} diagram comparison with different NSD potentials. Upper panel: Reference diagram, with the NSD potential from Sormani et al., 2020 (model 3) used in our study. Middle panel: Using the NSD potential from Sormani et al., 2022. Lower panel: Using the NSD potential from Launhardt et al., 2002a. In the three cases, the bar and the NSC potentials are not changed.*

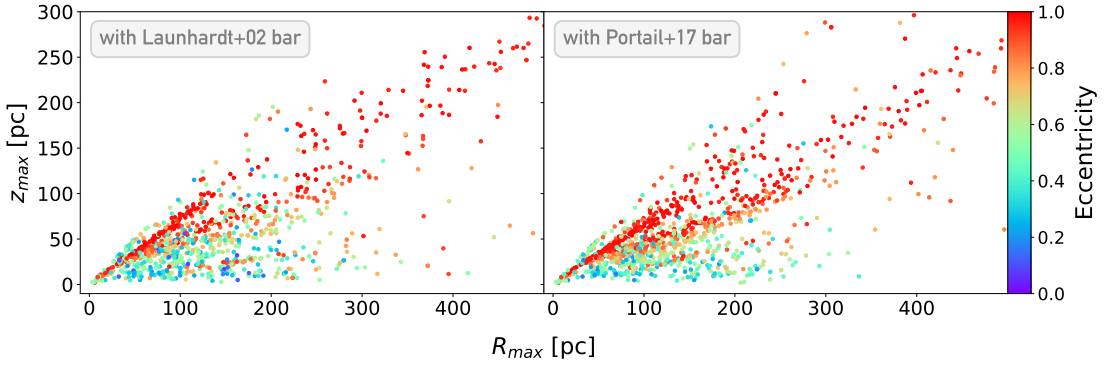

Figure 6.B.3: *R_{max} vs. z_{max} diagram comparison with different bar potentials. Left: Reference diagram, with the bar potential from Launhardt et al., 2002a. Right: Using the bar potential from Portail et al., 2017a. In both cases, the NSD and NSC potentials are not changed.*

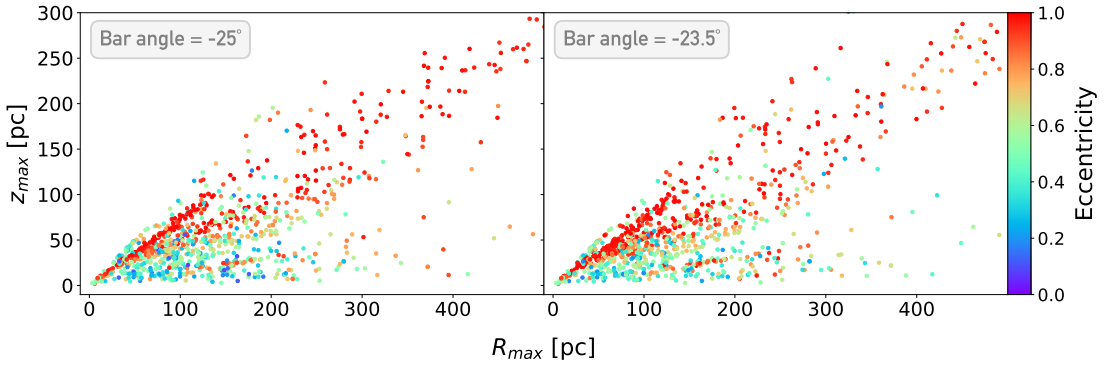

Figure 6.B.4: *R_{max} vs. z_{max} diagram comparison with a different bar angle with respect to the line of sight towards the GC. Left: Reference diagram as presented in Section 7.6. Right: Case with a 10% variation of the angle.*

7

Metallicity-dependent kinematics and orbits in the Milky Way's nuclear stellar disc

Submitted to Astronomy & Astrophysics
Authors: F. Nogueras-Lara, **N. Nieuwmunster**, M. Schultheis, M. C. Sormani, F. Fragkoudi, B. Thorsbro, R. M. Rich, N. Ryde, J. L. Sanders, L. C. Smith

This chapter contains the copied version of the forthcoming paper from Nogueras-Lara et al. It is a direct follow-up to the previous paper presented in Chapter 6 and discusses the metallicity of the different orbital families that I identified in the NSD of the Milky Way.

7.1 Introduction

The heart of the Milky Way stands out as our closest galaxy centre and the only one where we can study stars down to milli-parsec scales (e.g. Dong et al., 2011; F. Nogueras-Lara et al., 2019a; GRAVITY Collaboration et al., 2020). Therefore, it constitutes a unique template for analysing the stellar population of a galaxy nucleus, providing a better understanding of galactic nuclei and their role in galaxy formation and evolution. Nevertheless, the high extinction and extreme source crowding hamper the analysis of the Galactic centre stellar population and primarily limit it to the near infrared regime (e.g. Shogo Nishiyama et al., 2006; Shogo Nishiyama et al., 2008; Schultheis et al., 2009; Alonso-García et al., 2017; Thorsbro et al., 2020; F. Nogueras-Lara et al., 2021b; Sanders et al., 2022b).

The Galactic centre is roughly outlined by the nuclear stellar disc (NSD), a flat, likely axisymmetric, stellar structure with a scale length of $\sim 100\,\mathrm{pc}$ and a scale height of $\sim 40\,\mathrm{pc}$ (e.g. Gallego-Cano et al., 2020a; F. Nogueras-Lara, 2022c; Sormani et al., 2022). It contains a total stellar mass of $\sim 10^9\,\mathrm{M}_\odot$ (Launhardt et al., 2002a; Sormani et al., 2022) and is characterised by a predominantly old stellar population and a bursty star

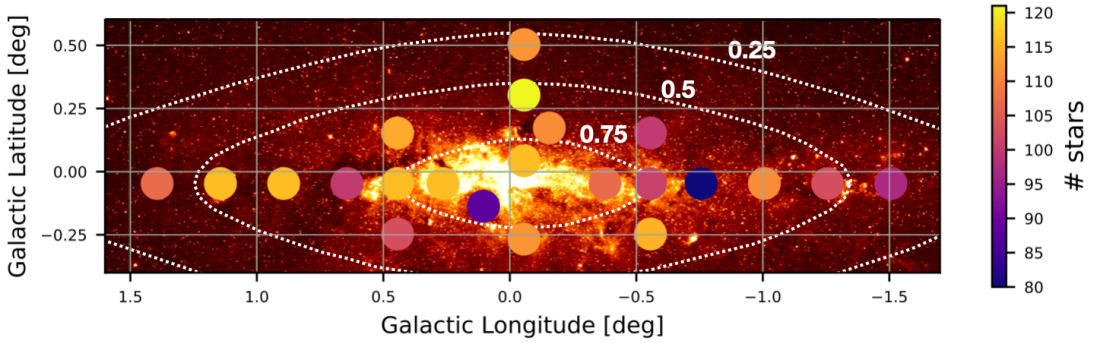

Figure 7.1: *Scheme of the observed region over plotted on an Spitzer/IRAC image at 8 µm. (Stolovy et al., 2006). Coloured circles correspond to the KMOS fields in which the colour scale indicates the number of stars. The dotted contours show the 25 %, 50 %, and 75 % levels of the NSD self-consistent model obtained by Sormani et al. (2022).*

formation history (e.g. Francisco Nogueras-Lara et al., 2020c; Sanders et al., 2022a; Schödel et al., 2023), which makes it different from the surrounding and much larger Galactic bar/bulge (e.g. Zoccali et al., 2003; E. Valenti et al., 2013; Christopher Wegg et al., 2013; Christopher Wegg et al., 2015; Portail et al., 2017b; Surot et al., 2019). Additionally, the NSD contains $\sim 10^6\,M_\odot$ of young stars that formed in-situ in the last 30 Myr (e.g. Matsunaga et al., 2013; Francisco Nogueras-Lara et al., 2020c; Francisco Nogueras-Lara et al., 2022; F. Nogueras-Lara, 2024), and has contributed to up to 10 % of the star forming activity observed throughout the entire Milky Way over the past $\sim$ 100 Myr (e.g. Mezger et al., 1996; Mauerhan et al., 2010; Matsunaga et al., 2011; Crocker et al., 2011; Francisco Nogueras-Lara et al., 2020c).

The NSD is a rotating structure (Lindqvist et al., 1992a; Schönrich et al., 2015a; Fritz et al., 2021; Shahzamanian et al., 2022) that appears to be kinematically distinct from the Galactic bar/bulge (Schönrich et al., 2015a; Schultheis et al., 2021). However, Zoccali et al. (2024) recently reported that they were unable to definitively identify the NSD as a distinct kinematic feature when compared to nearby control fields in the Galactic bar/bulge, contradicting precious work. This analysis used proper motions derived from the VISTA Variables in the Vía Láctea survey (Minniti et al., 2010) and APOGEE DR17 data (Steven R. Majewski et al., 2017; Abdurro'uf et al., 2022b).

The NSD stellar population exhibits a broad metallicity distribution that has been previously fitted using two Gaussian models accounting for the metal-rich and metal-poor stars, respectively (Schultheis et al., 2021; F. Nogueras-Lara et al., 2023a). The metal-rich component (mean metallicity $[M/H] = 0.12$, Schultheis et al. 2021) constitutes approximately 70-80 % of its stars and shows a lower line-of-sight velocity dispersion in comparison with the metal-poor one (mean metallicity $[M/H] = -0.22$, Schultheis et al. 2021). This suggests that metal-rich stars have a different origin and probably formed in situ (Schultheis et al., 2021) from the dense

accumulation of gas and dust that comprises the central molecular zone (CMZ, e.g. Henshaw et al., 2023). This is further supported by indications that stars in the NSD and the gas in the CMZ appear to be corotating (Schönrich et al., 2015a; Schultheis et al., 2021).

In this paper, we aim to study the proper motion distribution of NSD stars with different metallicities to assess previous analysis using line-of-sight velocities and confirm whether they have different kinematics and origin. Additionally, we utilise the recent orbital analysis of NSD stars by Nieuwmunster et al. (2024) (see Chapter 6) to determine whether stars with different metallicities have different orbits. Analysing stars with different kinematics and orbits also helps us shed light on the potential kinematic difference between the NSD and the Galactic bar/bulge, and is crucial to understand their relation and the NSD formation mechanism.

7.2 Data

7.2.1 Metallicity and proper motions

We used the spectroscopic survey of the NSD (Fritz et al., 2021) obtained with the KMOS instrument at the VLT (Sharples et al., 2013). The chosen sample includes the primary targets of the survey contained within the self-consistent model of the NSD by Sormani et al. (2022), 2303 stars, whose metallicity was derived with a mean uncertainty of ~ 0.1 dex. Figure 7.1 shows the target fields.

For the kinematical analysis, we used proper motions from a preliminary version of the second version of VIRAC (VIRAC2, Smith et al. in prep). This dataset is the same as was used previously by Sormani et al. (2022) and Nieuwmunster et al. (2024). It contains absolute proper motions of stars in the spectroscopic survey, using Gaia as an astrometric reference. Sormani et al. (2022) describes the data set in more detail.

We reduced the contamination from foreground stars (mainly from the spiral arms along the line-of-sight towards the Galactic centre and, up to certain extend, to the Galactic bar/bulge), by using their significantly different extinction (e.g. F. Nogueras-Lara et al., 2021a). We removed them by applying a colour cut $(H - K_s) > \max(1.3, -0.0233\ K_s + 1.63)$ as done in Schultheis et al., 2021, and ended up with a total of 2152 stars for the subsequent analysis.

7.2.2 Orbits catalogue

We utilised the orbital catalogue obtained by Nieuwmunster et al. (2024) (see Chapter 6), which was derived from the previously described KMOS spectroscopic survey of the NSD (Fritz et al., 2021), and the preliminary proper motions from VIRAC2 (Smith et al., in prep.). The orbits catalogue also implemented the previously mentioned

colour cut to mitigate potential contamination from foreground sources, and applied a strict proper motion uncertainty cut, $d\mu_{l,b} < 0.6$ mas/yr, resulting in a sample of 1130 stars (for further details, see Nieuwmunster et al., 2024). The orbits of the stars were integrated in a non-axisymmetric potential combining the potentials corresponding to the Galactic bulge/bar density (Launhardt et al., 2002a), the NSD (Sormani et al., 2022), and the nuclear star cluster (Chatzopoulos et al., 2015a). They also assumed a distance distribution considering a mean Galactic centre distance of 8.2 kpc and a NSD scale length of $\sim$ 100 pc (e.g. Gallego-Cano et al., 2020a; Sormani et al., 2022; F. Nogueras-Lara, 2022c). The final catalogue comprises several orbital families (i.e. chaotic, z-tube, x-tube, banana, fish, saucer, pretzel, 5:4, and 5:6 orbits), which are present in the NSD region.

7.3 Metallicity distribution and proper motions

To investigate the proper motion distribution of stars with different metallicities, we first analysed the metallicity distribution of the target stars by repeating the analysis in Schultheis et al. (2021). Namely, we applied a Gaussian mixture model (GMM, Pedregosa et al., 2011) to obtain the number of Gaussians that best reproduce the metallicity distribution. We distinguished between a single-Gaussian and a two-Gaussian models by applying the Bayesian information criterion (Schwarz, 1978) and the Akaike information criterion (Akaike, 1974). We found that the data is best represented by a two-Gaussian model. Figure 7.2 shows the obtained results. To estimate the mean metallicity and the associated uncertainty for each component, we resorted to MonteCarlo (MC) simulations and generated 1000 MC samples by randomly varying the metallicity of each star assuming Gaussian uncertainties. We performed the GMM analysis on each of the 1000 samples, assuming a two-Gaussian distribution, and computed the final values along with their associated uncertainties as the mean and standard deviation. The results, shown in Table 7.1, are in perfect agreement with those reported by Schultheis et al. (2021).

Table 7.1: *Characterisation of the two-Gaussian decomposition of NSD metallicity distribution.*

	W	$[M/H]$	$\sigma_{[M/H]}$	μ_l	σ_{μ_l}	μ_b	σ_{μ_b}	$H-K_s$
Metal rich	0.79 ± 0.02	0.11 ± 0.01	0.26 ± 0.01	-1.12 ± 0.08	2.70 ± 0.05	0.17 ± 0.05	1.89 ± 0.05	2.24 ± 0.02
Metal poor	0.21 ± 0.02	-0.20 ± 0.04	0.71 ± 0.04	-1.34 ± 0.29	3.07 ± 0.21	0.02 ± 0.32	3.33 ± 0.26	2.21 ± 0.05

Notes. W, $[M/H]$, and $\sigma_{[M/H]}$ correspond to the results from the GMM analysis of the two-Gaussian distribution, where W indicates the relative weight of each of the Gaussian components. μ_l, σ_{μ_l}, μ_b, and σ_{μ_b} are in mas/yr. $H-K_s$ are in Vega magnitudes.

We also employed the GMM approach to calculate the likelihood of each star being associated with each of the Gaussian distributions. To analyse the proper motion distribution of stars belonging to each metallicity component, we assumed that a star belongs to either the metal-rich or the metal-poor one if its likelihood of being associated

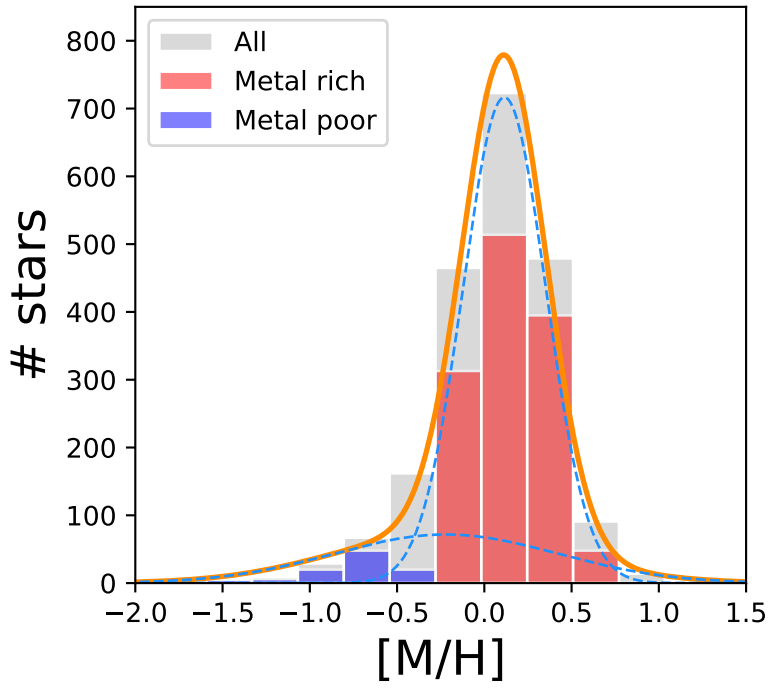

Figure 7.2: *Two-Gaussian decomposition of the NSD metallicity distribution. The orange line shows the result of the GMM analysis, whereas the blue dashed lines depict each of the Gaussian components. Red and blue bars correspond to stars with more than 70 % probability of belonging to each of the components.*

to that component is larger than 70 %. Given that the stellar metallicity of the KMOS catalogue was calibrated using empirical spectra with $[M/H] < 0.6$ dex, we excluded stars with higher metallicities from the subsequent analysis. Additionally, for the proper motion analysis, we removed stars with high proper motion uncertainties (> 1 mas/yr). Figure 7.2 shows the final selection of stars. We ended up with 1263 metal-rich and 111 metal-poor stars.

We built histograms for the proper motion component parallel (μ_l) and perpendicular (μ_b) to the Galactic plane. To estimate the mean and the standard deviation of each distribution and their corresponding uncertainties, we applied a 3σ clipping algorithm to remove potential outliers, and used a bootstrap resampling method with 5000 iterations. Table 7.1 and Fig. 7.3 show the obtained results. To assess potential sources of systematic uncertainties, we repeated the calculation considering stars with uncertainties below 1.2 mas/yr and 0.8 mas/yr, and also changing the cut to remove the foreground population (i.e. $H - K_s \sim 1.1$ mag). We did not find any significant variation within the obtained uncertainties.

We concluded that although the mean proper motions are similar for both stellar populations, there is a significant difference in the velocity dispersion of the μ_b component. Namely, the metal-poor component exhibits a μ_b standard deviation that is

approximately a factor 2 larger than that of the metal-rich group. Regarding the μ_l component, we found that the velocity dispersion is slightly larger for the metal-poor stellar population, although there is not a clear significant difference. This is not surprising because the proper motion component parallel to the Galactic plane is much more affected by the extinction along the line of sight and the fact that the NSD is a rotating structure. Therefore, the presence of stars moving eastwards and westwards will depend on the completeness of the data and will be different for the different regions analysed (e.g. Schönrich et al. 2015a; Martínez-Arranz et al. 2022; F. Nogueras-Lara 2022c, and Figs. A1-A4 in Sormani et al. 2022, which show the μ_l and μ_b decomposition between Bar and NSD).

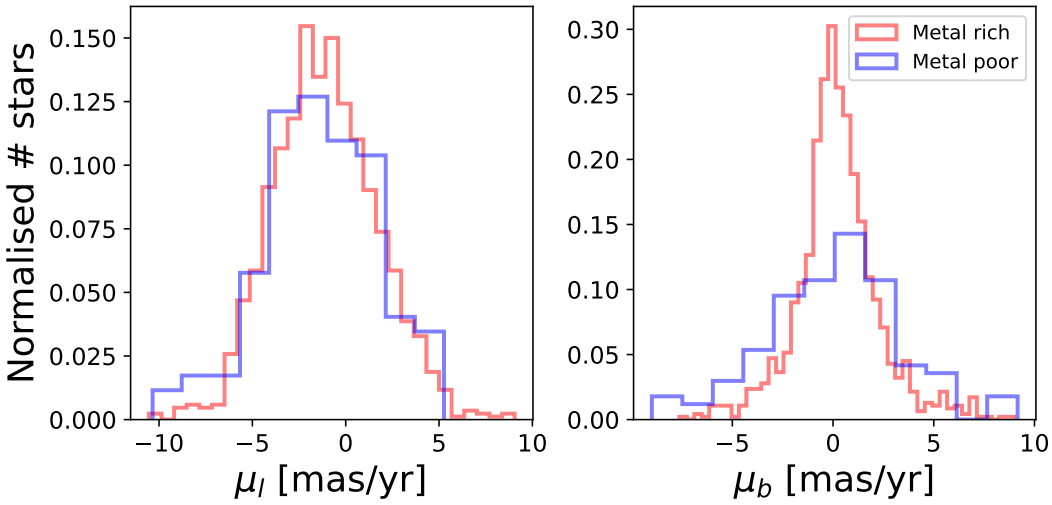

Figure 7.3: *Proper motion distribution of metal-rich and metal-poor stars in the NSD following the GMM analysis (see Sect. 7.3).*

We also explored the proper motion orientation, $\alpha = \text{atan}(\mu_b/\mu_l)$, of metal-rich and metal-poor stars. We subtracted the proper motion velocity of Sgr A* ($\mu_l = -6.396 \pm 0.071$ mas/yr and $\mu_b = -0.239 \pm 0.045$ mas/yr, see Gordon et al., 2023) to obtain Galactic proper motions relative to the Galactic centre. To ensure $\alpha \in [-180, 180]$ degrees, we adjusted the output based on the orientation of the proper motions and adopted the origin pointing East. Figure 7.4 shows the obtained results. We computed the mean orientation values, their standard deviations, and the associated uncertainties by applying a bootstrap resampling method with 5000 iterations. We obtained $\alpha_{rich} = 5 \pm 1°$, $\sigma_{\alpha_{rich}} = 30 \pm 1°$, and $\alpha_{poor} = 4 \pm 4°$, $\sigma_{\alpha_{poor}} = 45 \pm 5°$, for the metal-rich and the metal-poor component, respectively. Although the orientation values for both populations are compatible, the metal-poor stellar population shows a significantly larger standard deviation.

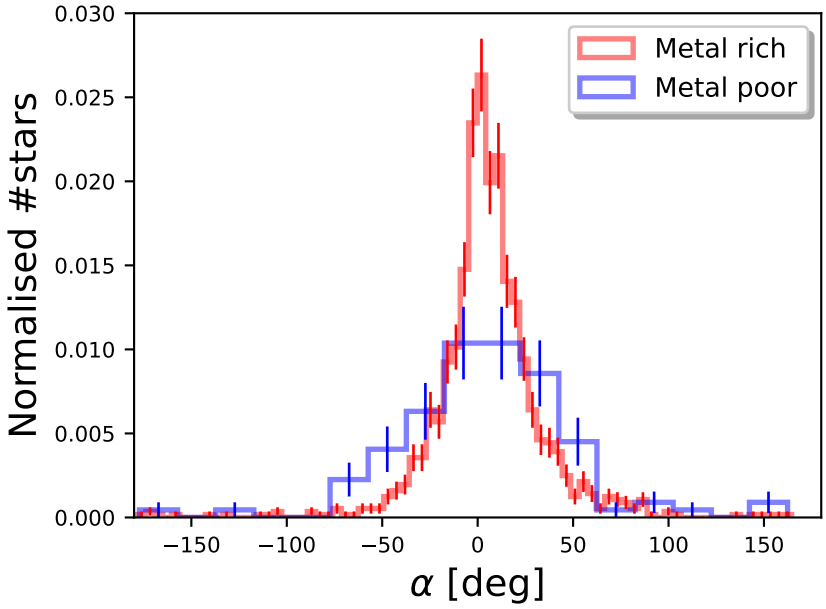

Figure 7.4: *Proper motion orientation of metal-rich and metal-poor stars. The uncertainties correspond to Poisson errors (i.e. $\sqrt{\#stars/bin}$) scaled to the normalised number of stars in each bin.*

7.4 Metallicity distribution and orbits

7.4.1 Orbits for each metallicity group

We used the orbital catalogue obtained by Nieuwmunster et al. (2024) (see Chapter 6) to explore whether stars with different metallicities and kinematics undergo different orbits. Nieuwmunster et al. (2024) found that z-tube orbits (including all orbital families with a circulation around the z-axis –i.e. z-tube, fish, saucer, pretzel, 5:4, and 5:6 orbits) dominate the orbital families, comprising approximately 70 % of the stars in the catalogue, and are directly associated with the NSD. Conversely, chaotic/box orbits constitute about 25 % of the sample and are likely related to Galactic bar orbits. We analysed the fraction of stars with these orbits belonging to the previously defined metal-rich and metal-poor stellar populations. We obtained that the orbits are different for the different metallicity components, as shown in Fig. 7.5. We concluded that z-tube orbits dominate the metal-rich component ($\sim$ 70 % of the metal-rich stars belong to this orbital family) and are less frequent in the metal-poor stellar population, in which the chaotic/box orbits dominate and correspond to $\gtrsim$ 50 % of the stars with defined orbits in the metal-poor component.

7.4.2 Metallicity for z-tube and chaotic/box orbits

We also explored the metallicity distribution of all the stars in the orbits catalogue with z-tube and chaotic/box orbits. First of all, we analysed the spatial distribution of z-tube and chaotic/box orbits. Figure 7.6 shows the obtained results. We found that

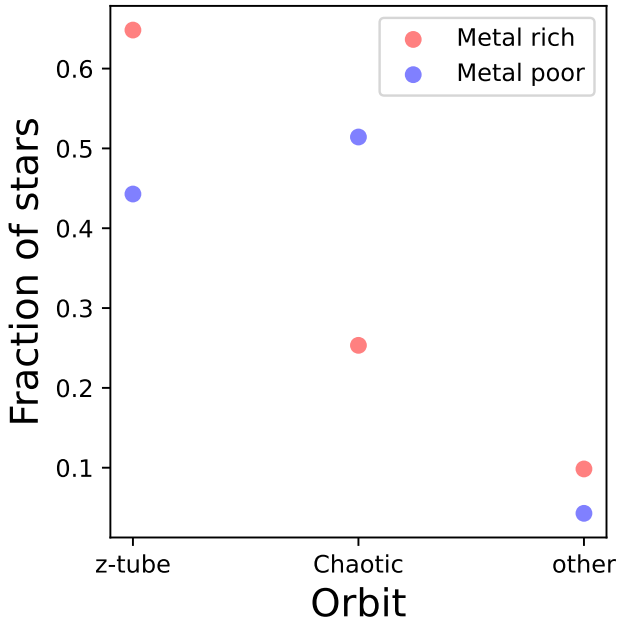

Figure 7.5: *Relative fraction of stars with z-tube and chaotic/box orbits for the metal-rich and metal-poor stellar populations defined in Sect. 7.3. The label "other" corresponds to stars following banana and x-tube orbits (see Nieuwmunster et al. (2024) for further details).*

the relative fraction of stars undergoing chaotic orbits are more common towards the edge of the NSD, as was also discussed by Nieuwmunster et al. (2024) (see Chapter 6), supporting their relation with potential contaminants from the bar. On the contrary, stars with z-tube orbits and, in general, stars without chaotic orbits, are more centrally concentrated and seem to better trace the NSD.

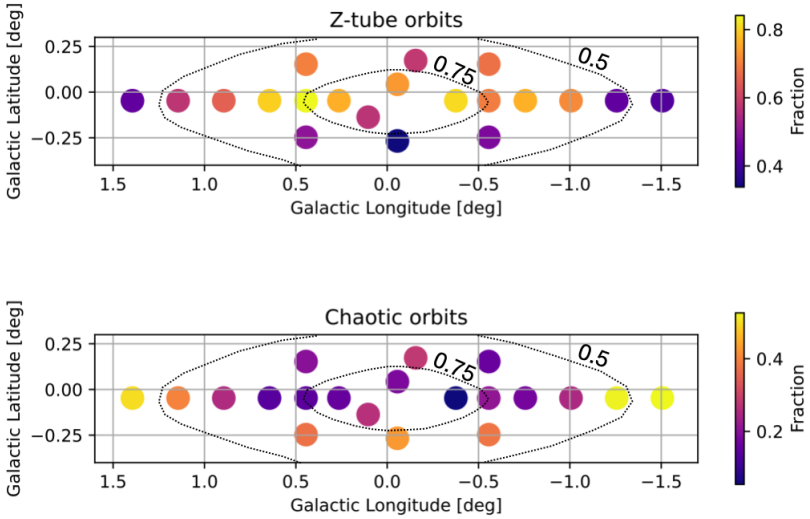

Figure 7.6: *Relative fraction of stars with z-tube and chaotic. The contours show the 50 % and 75 % levels of the NSD self-consistent model obtained by Sormani et al. (2022).*

We computed the metallicity distribution for stars with z-tube and chaotic/box orbits and observed that they are different, being z-tube stars more metal-rich on average (Fig. 7.7). We also applied the previously described GMM approach (see Sect. 7.3) to compare a single- and a two-Gaussian model. In all the cases, we found that a two-Gaussian model is preferred. Figure 7.7 shows the results for each of the orbital families. We also computed the parameters associated to the metal-rich and metal-poor stellar populations by resorting to MC simulations with 1000 iterations, as explained in Sect. 7.3. The results are presented in Table 7.2.

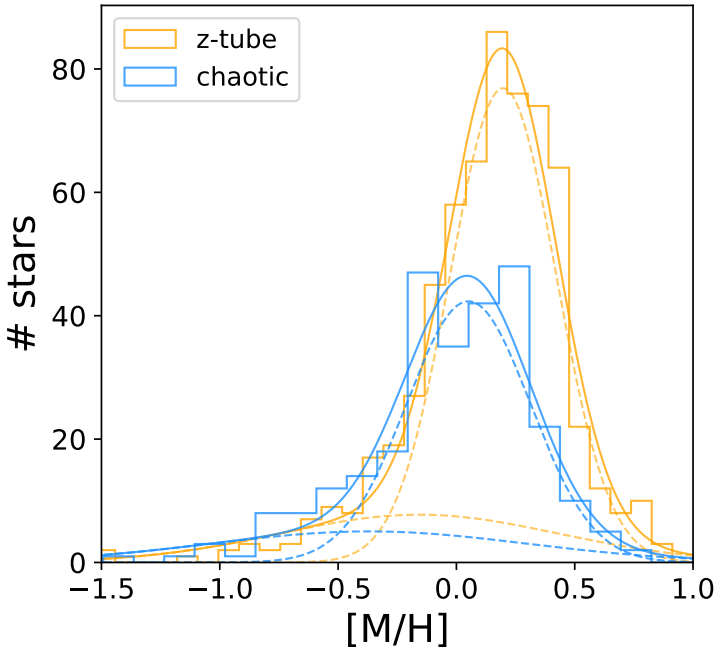

Figure 7.7: *Metallicity distribution of all stars in the orbits catalogue (Nieuwmunster et al., 2024) following z-tube orbits (including all orbital families with a circulation around the z-axis), and chaotic/box orbits. The solid lines show the result of the GMM analysis, whereas the dashed lines correspond to each Gaussian model.*

We observed that stars exhibiting chaotic/box orbits, regardless of their metallicity, are generally more metal-poor compared to those following z-tube orbits (Fig. 7.7). The mean metallicity values obtained for both metallicity components with chaotic/box orbits align well with the results from Schultheis et al. (2021) for the inner regions of the Galactic bulge/bar by analysing APOGEE data (Ahumada et al., 2020; Alvaro Rojas-Arriagada et al., 2020b). Similarly, the metallicity values obtained for stars undergoing z-tube orbits closely match our results for the NSD (see Table 7.1).

Given the statistical approach used to obtain the orbits in Nieuwmunster et al. (2024) (see Chapter 6), our results should be interpreted statistically and may not be valid on

Table 7.2: *Characterisation of the two-Gaussian metallicity decomposition of stars with different orbits.*

Orbit	Metallicity	W	$[M/H]$	$\sigma_{[M/H]}$
z-tube	Rich	0.79 ± 0.05	0.19 ± 0.01	0.26 ± 0.01
	Poor	0.21 ± 0.05	-0.15 ± 0.17	0.67 ± 0.09
Chaotic	Rich	0.78 ± 0.07	0.05 ± 0.02	0.30 ± 0.03
	Poor	0.22 ± 0.07	-0.47 ± 0.41	0.73 ± 0.11

Notes. W, $[M/H]$, and $\sigma_{[M/H]}$ correspond to the results from the GMM analysis of the two-Gaussian distribution, where W indicates the relative weight of each of the Gaussian components.

an individual star basis. However, this does not pose any problem because our objective is to understand the mean behavior of stars with different metallicities.

7.5 Extinction of stars with different metallicities

The NSD formed $\gtrsim 8$ Gyr ago and appears to be dominated by an old stellar population (> 80 % of the stellar mass is older than $\gtrsim 7$ Gyr, e.g. Francisco Nogueras-Lara et al., 2020c; Francisco Nogueras-Lara et al., 2022; Sanders et al., 2022a; Schödel et al., 2023). Assuming that metal-rich and metal-poor stars have a similar age, allows us to use the $H - K_s$ colour as a proxy for the extinction towards these stars (e.g. F. Nogueras-Lara et al., 2018a; F. Nogueras-Lara et al., 2021b). Moreover, there is a statistical correlation between distance along the line of sight and extinction in the NSD (e.g. F. Nogueras-Lara, 2022c; F. Nogueras-Lara et al., 2023c), which makes it possible to estimate whether the spatial distribution is similar for both stellar populations by analysing their extinction.

We built a colour-magnitude diagram K_s vs. $H - K_s$ to analyse the colour distribution (Fig. 7.8) of the stars belonging to each stellar population whose proper motions were previously analysed. We computed the mean colour and its associated uncertainty for the metal-rich and the metal-poor stars by applying a bootstrap resampling method with 5000 iterations. Table 7.1 shows the obtained results. We found that the metal-poor stars show a somewhat smaller $H - K_s$ colour, which might indicate that they are more abundant close to the NSD edge. Nevertheless, the colours for both stellar populations are similar within the uncertainties, so there is not a clear difference in the spatial distribution along the line of sight. In any case, we detect metal poor and metal rich stars with both, large and small extinction indicating that they are present all over the NSD.

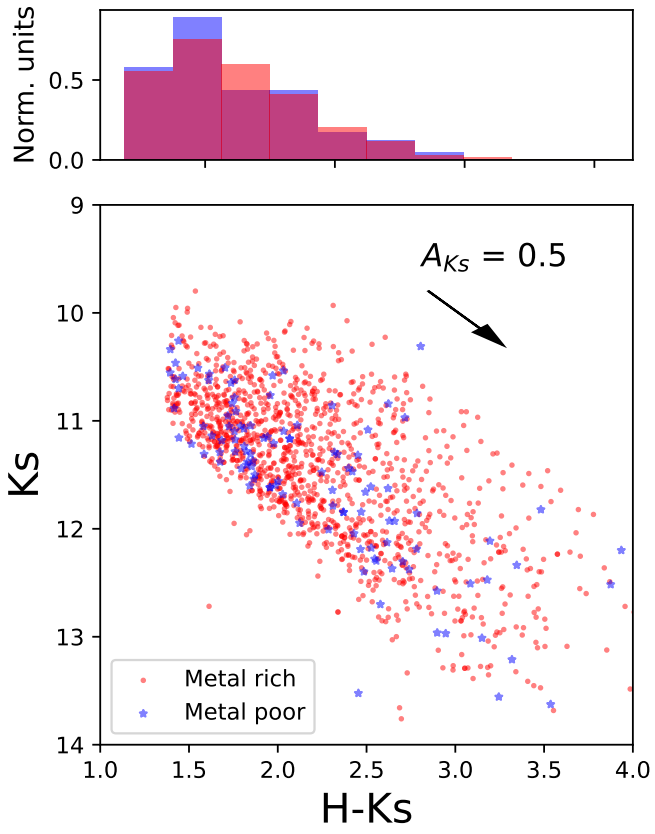

Figure 7.8: *Colour-magnitude diagram of the metal-rich and metal-poor stars used in Sect. 7.3. The black arrow shows the direction of the reddening vector.*

7.6 Spatial analysis of stars with different metallicities

We studied the metallicity distribution of KMOS stars at different longitudes from the Galactic centre. In this way, we investigated whether the two-Gaussian metallicity distribution is homogeneously distributed across the field or whether metal-rich and metal-poor stars have different spatial distributions.

To avoid mixing stellar populations at significantly different latitudes, whose metallicity might also vary vertically, we restricted our analysis to stars within $|b| \lesssim 20\,\mathrm{pc}$. For our analysis, we defined five regions with different longitudes, as colour-coded in the upper panel of Fig. 7.9

We applied the GMM approach described in Sect. 7.3 to check whether the metallicity distribution of each of the defined regions is best represented by one or two Gaussian models. We found that a two-Gaussian distribution is preferred for all the cases. To estimate the mean metallicity and the associated uncertainty for each component and

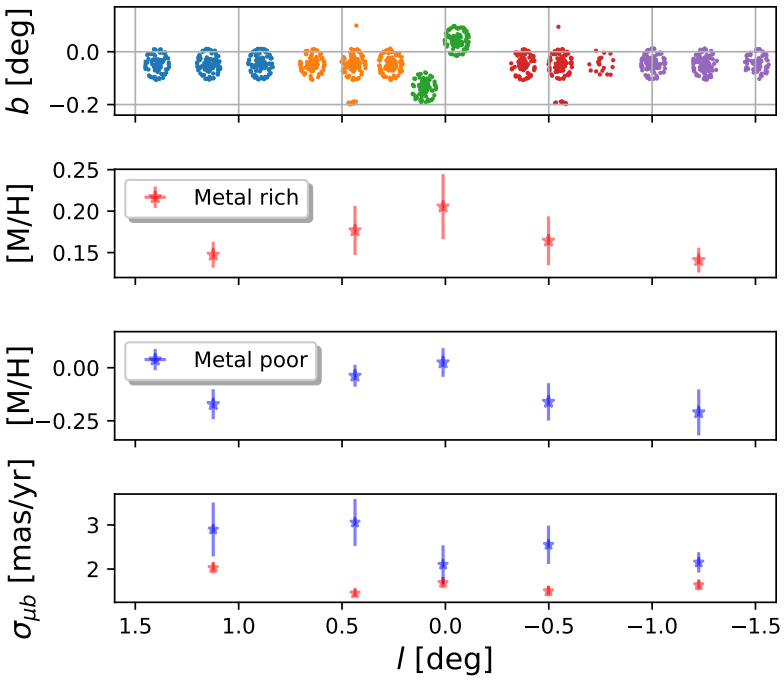

Figure 7.9: *Line of sight analysis of the NSD metallicity and kinematics. Top panel: target KMOS stars divided into five colour-coded regions at different longitudes. Middle panels: mean metallicity obtained for the metal-rich (top) and the metal-poor (bottom) components of the two-Gaussian distribution. We plot metal-rich and metal-poor stars separately to highlight the detected gradients more effectively. Bottom panel: μ_b velocity dispersion for the metal-rich and metal-poor components.*

region, we followed the previously described method and employed MC simulations building 1000 samples randomly varying the metallicity of each star assuming Gaussian uncertainties. Figure 7.A.1 and Table 7.A.1 in the appendix show the obtained results. We measured a metallicity gradient with increasing metallicities towards the centre of the NSD that is present in both, the metal-rich and the metal-poor components. Figure 7.9 shows the detected gradient. This result aligns with previous work finding a global metallicity gradient (without distinguishing between metal-rich and metal poor stars) towards the innermost regions of the NSD (Feldmeier-Krause, 2022).

We also found that the relative weight of the components does not change spatially within the uncertainties. The relative weight of the metal-rich component is slightly larger than the one obtained when combining all the stars without defining different regions at different latitudes. This is probably due to the metallicity gradient that shifted the mean metallicity of the metal-rich component towards lower metallicities when combining all the stars. Therefore, the metal-rich component encompasses more stars and its relative weight is somewhat higher.

We also repeated the previous analysis on proper motions and $H - K_s$ colour for the

metal-rich and metal-poor stellar populations in each region. We kept stars whose likelihood to belong to either of the groups is larger than 70 %, restricted the sample to targets whose proper motion uncertainty is below 1 mas/yr, and restricted the selection to stars with $[M/H] < 0.6$ dex, as previously explained. Figure 7.A.2 and Table 7.A.1 in the appendix show the results. In spite of the relatively low number of stars for the metal-poor population ($\sim 15 - 25$ stars for each spatial group), we found a good agreement with the results obtained when analysing all the stars in Sect. 7.3. Although there is not a significant difference between the mean proper motions for each stellar population (only in some cases we found a difference of $\gtrsim 1$ sigma), we detected that the velocity dispersion of the μ_b component of the metal-poor stellar population is $\gtrsim 2$ sigma larger than that of the metal-rich stellar population in all cases, except at $l = 0°$, in which it is ~ 1 sigma larger. This supports that the metal-poor component is kinematically hotter than the metal-rich one regardless of the spatial distribution. The bottom panel of Fig. 7.9 shows the obtained results.

Finally, the colour analysis is also consistent with the previous results (Sect. 7.5) and shows no significant difference between the metal-rich and the metal-poor stellar populations with longitude. The only exception is the central-most field for which the metal-rich population exhibits a somewhat larger $H - K_s$ value, which is associated to a larger extinction for this region. This is not strange given some potential contamination from the nuclear star cluster (e.g. Launhardt et al., 2002a; Schödel et al., 2014a; Feldmeier et al., 2014), whose extinction is higher and which is arguably the most metal-rich region of the Galaxy (e.g. Schödel et al., 2010; Feldmeier-Krause et al., 2017a; Schultheis et al., 2021; Francisco Nogueras-Lara et al., 2021a; F. Nogueras-Lara, 2022b).

7.7 Discussion

7.7.1 Correlation between metallicity, velocity dispersion, and orbits

We distinguished between metal-rich and metal-poor stars by applying a GMM approach and obtained that a two-Gaussian model best reproduces the data, as found in previous work (e.g. Schultheis et al., 2021; F. Nogueras-Lara, 2022b; F. Nogueras-Lara et al., 2023a). In principle, the presence of these two Gaussian components is just a mathematical description of the underlying metallicity distribution and is not necessarily related with the origin of metal-poor and metal-rich stars in the NSD. Actually, the metallicity distribution might be also explained by chemical evolution models (e.g. Grieco et al., 2015; Friske et al., 2023), and thus the presence of metal-rich and metal-poor stars would be a consequence of the natural star formation process in the NSD. However, the obtained correlation between metal-poor stars, high velocity dispersion, and chaotic/box orbits indicates a different origin for a significant fraction of metal-poor stars in comparison to the metal-rich ones. Our results suggest that the metal-poor stars are related to the innermost regions of the Galactic bulge/bar, which overlaps with the NSD. In this way,

these stars are probably interlopers from the Galactic bulge/bar, which is in agreement with the Galactic bar/bulge contamination estimated in Sormani et al. (2022). Moreover, the metallicity distribution obtained for stars following chaotic orbits (likely associated to the Galactic bar/bulge) matches previous results for the innermost regions of the Galactic bulge/bar (e.g. Schultheis et al., 2021).

Another possibility is that a fraction of the metal-poor stars might correspond to dispersed clusters that were accreted by the NSD (e.g. van Donkelaar et al., 2024). The accretion of stellar clusters, combined with in-situ star formation, has been proposed as one of the formation channels of the nuclear star cluster at the centre of the Galaxy (e.g. Tremaine et al., 1975; Capuzzo-Dolcetta, 1993; Antonini et al., 2012; Antonini, 2013; Perets et al., 2014; Gnedin et al., 2014; Arca-Sedda et al., 2015; Tsatsi et al., 2017a; Arca Sedda et al., 2020b). In this way, van Donkelaar et al. (2024) used hydro-dynamical simulations to show that the infalling clusters can be also accreted by the NSD contributing to its growth.

Additionally, we found that the proper motion orientation of both metallicity components show a different standard deviation, being the distribution of metal-poor stars more scattered in comparison to the metal rich component. This is compatible with a more chaotic motion that is expected under the influence of the Galactic bulge/bar. On the contrary, metal-rich stars are kinematically cooler and show orbits tracing the NSD (e.g. Schultheis et al., 2021; Nieuwmunster et al., 2024).

The similar extinction observed for both the metal-poor and metal-rich components suggests a widespread distribution of both types of stars across the region. Hence, there is not a specific region in which either metal-rich or metal-poor stars are concentrated. This observation is also supported by the spatial analysis in Sect. 7.5, given that we found metal-rich and metal-poor stars distributed all over the field and with similar relative weights within the uncertainties.

7.7.2 The NSD as a distinct kinematic structure

Recently, Zoccali et al. (2024) analysed the proper motion distribution of the NSD compared to control fields in the innermost region of the Galactic bulge/bar. Their findings did not reveal any clear distinct kinematical signature of the NSD. This result challenges previous studies that identified the NSD as kinematically different from its surroundings based on line-of-sight velocities (Schönrich et al., 2015a) and velocity dispersions (Schultheis et al., 2021).

In this paper we limited our analysis to the NSD without any comparison with the surrounding region. Nevertheless, we found the presence of two kinematically distinct components with different metallicities and orbits. We detected that the metal-poor

component is dominated by chaotic/box orbits that are likely associated to the Galactic bar and has a metallicity distribution also in agreement with previous work on the inner bulge/bar (carried out in fields without contamination from the NSD, e.g. Schultheis et al., 2021). On the other hand, the dominant metal-rich component is kinematically cooler, given its lower velocity dispersion, and undergo z-tube orbits, better tracing the NSD (e.g. Nieuwmunster et al., 2024, see Chapter 6). The fact that we observe these two different stellar populations with different orbits and kinematics, being one of them more related to the Galactic bulge/bar, suggests that the NSD is a different kinematic structure, and agrees with previous work (Schönrich et al., 2015a; Schultheis et al., 2021), showing that it is possible to kinematically distinguish the NSD. Additionally, having a metal-rich, and kinematically cool NSD different from the surrounding Galactic bulge/bar, also agrees with previous results on external Milky Way-like galaxies, in which these structures have been identified via their different kinematics and metallicity (e.g. Gadotti et al., 2019a; Bittner et al., 2020; Gadotti et al., 2020).

7.7.3 The metallicity gradient and the NSD formation

Stellar population analyses along and across the line of sight towards the NSD have suggested the presence of radial age and metallicity gradients towards the centre of the NSD (e.g. Francisco Nogueras-Lara et al., 2020c; Francisco Nogueras-Lara et al., 2022; Feldmeier-Krause, 2022; F. Nogueras-Lara et al., 2023c; F. Nogueras-Lara et al., 2023a; F. Nogueras-Lara, 2024). In this way, the innermost regions of the NSD contain a predominantly old ($\gtrsim 7$ Gyr) and metal-rich stellar population, while a significant intermediate-age stellar population (~40 % of the stellar mass with ages between 2-7 Gyr) is found towards the outer edge of the NSD, where the metallicity is lower. Conversely, Sanders et al. (2024) analysed the period-age relation of Mira variables in the NSD and found only a weak indication of inside-out formation. They attributed this to potential dynamical mixing and/or the smoothing effect of their spline model, which might hide a significant population of Mira variables with ages around $5 - 6$ Gyr (periods $\sim$ 400,days). In this way, these variables could potentially trace the gradient but have large uncertainties.

We observed that the metal-rich and metal-poor components of the NSD are uniformly distributed across the field, both exhibiting a metallicity gradient with a higher metallicity towards the center of the NSD. These metallicity gradients correspond to an increase of approximately 3×10^{-4} dex/pc and 1×10^{-3} dex/pc for the metal-rich and metal-poor stellar populations, respectively, assuming a Galactic center distance of 8.25 kpc (GRAVITY Collaboration et al., 2020). To compare our results with the metallicity gradient obtained by Feldmeier-Krause (2022), which does not distinguish between metal-rich and metal-poor stars, we estimated the metallicity increase per parsec using the metallicity values at the edge and center for a region with a Galactic latitude $b < 19°$, as specified in their Fig. 11. We obtained a metallicity gradient of

approximately 5×10^{-4} dex/pc, which roughly corresponds to the mean of the gradients we found for the metal-rich and metal-poor stars.

The detected gradients align with the currently accepted inside-out formation scenario of the NSD through bar-driven mechanisms (e.g. Bittner et al., 2020; F. Nogueras-Lara et al., 2023c). Similar gradients have been found in Milky Way-like galaxies analysed in the TIMER survey (e.g. Gadotti et al., 2019a; Bittner et al., 2020), and can be attributed to the growth of the galaxy bar that funnels gas from different galactic radii towards the center as it evolves (the more internal, the more metal-rich). Furthermore, in evolved systems, it is anticipated that metallicity will rise towards the center due to the enhanced difficulty of stellar feedback processes in expelling gas as it becomes more tightly bound within the galaxy's potential well. This is compounded by the potential rapid increase in metallicity in star-forming systems.

Additionally, the metal-rich stellar population follows a rotation pattern similar to that of the gas in the central molecular zone (Schultheis et al., 2021). Thus, it is likely that the metal-rich stars formed in-situ from gas funneled toward the Galactic center via bar-driven processes, contributing to the inside-out growth of the NSD. This also justifies why these stars undergo z-tube orbits and have a lower velocity dispersion in comparison to the metal-poor component. Conversely, the metallicity gradient observed for metal-poor stars, which are kinematically hotter and follow Galactic bar-related orbits, may be caused by the combination of Galactic bar interlopers and/or stars accreted from clusters within a radius of 1.5 kpc at $z > 4$ (van Donkelaar et al., 2024).

7.8 Conclusion

In this paper, we investigated the proper motion and orbits distribution of stars with different metallicities in the NSD. We obtained that metal-rich stars show a lower velocity dispersion in comparison with metal-poor ones, and are dominated by stars following z-tube orbits that are representative of the NSD (Nieuwmunster et al., 2024, see Chapter 6). Conversely, metal-poor stars are kinematically hotter and a significant fraction of them undergo chaotic/bar orbits that are likely related to the Galactic bar. We also found that the proper motion orientation of metal-rich stars shows a sharper profile parallel to the Galactic plane in comparison with the metal-poor ones.

We used the statistical correlation between distance and extinction in the NSD (F. Nogueras-Lara, 2022c) to explore whether stars with different metallicities show a special location along the line of sight. We concluded that the average near infrared colour of both stellar population is similar within the uncertainties and there is not any significant difference in extinction. Therefore, we did not detect any preferred location for stars with different metallicities, and they seem to be present all over the observed regions.

Finally, we analysed the metallicity distribution of stars at different longitudes and found that metal rich and metal-poor stars are present throughout the NSD. We also detected the presence of metallicity gradients for both stellar populations with increasing metallicities towards the central regions of the NSD. Our results support an inside-out formation of the nuclear stellar disc, as inferred from studies of external Milky Way-like galaxies (e.g. Gadotti et al., 2019a; Bittner et al., 2020). We interpret the gradient in the metal rich population as a consequence of in-situ formation from gas funneled towards the Galactic centre through bar-driven mechanisms (e.g. Sormani et al., 2019). This justifies the dominant z-tube orbits and the lower velocity dispersion and kinematics that align with the rotation velocity of gas from the central molecular zone (Schultheis et al., 2021).

Appendices

7.A Parameters of the spatial analysis of the two-Gaussian metallicity distribution

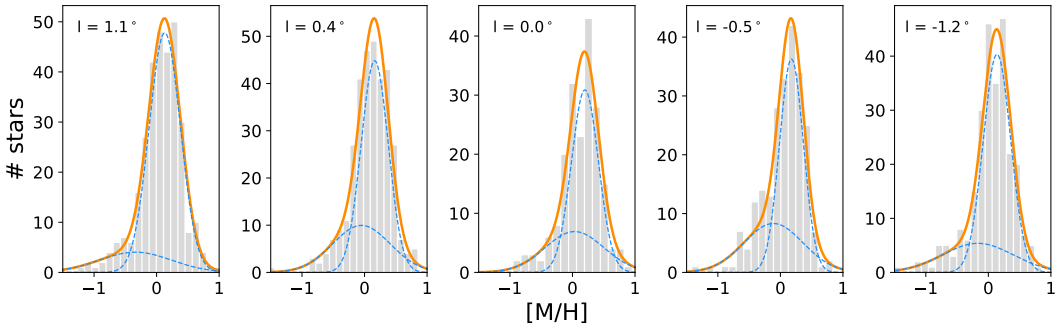

Figure 7.A.1: *Two-Gaussian decomposition of the NSD metallicity distribution for different longitudes. The orange line shows the result of the GMM analysis, whereas the blue dashed lines depict each of the Gaussian components.*

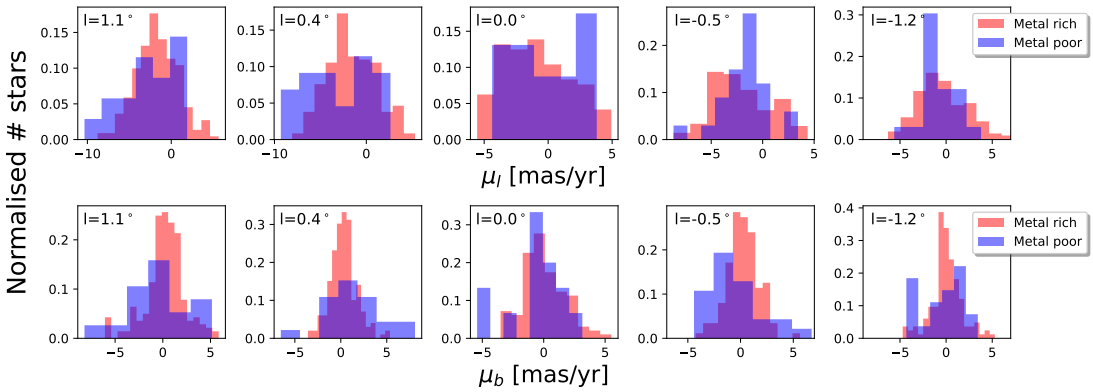

Figure 7.A.2: *Proper motion distribution of metal-rich and metal-poor stars in the NSD for different longitudes following the GMM analysis in Sect. 7.6.*

Table 7.A.1: *Characterisation of the two-Gaussian decomposition of the NSD metallicity distribution at different longitudes.*

l	W	$[M/H]$	$\sigma_{[M/H]}$	μ_l	σ_{μ_l}	μ_b	σ_{μ_b}	$H-K_s$
1.1	0.72 ± 0.05	0.15 ± 0.02	0.25 ± 0.01	-1.67 ± 0.17	2.49 ± 0.12	0.22 ± 0.14	2.03 ± 0.13	2.53 ± 0.04
	0.28 ± 0.05	-0.17 ± 0.07	0.52 ± 0.05	-2.54 ± 0.83	3.34 ± 0.52	-0.33 ± 0.74	2.90 ± 0.61	2.31 ± 0.18
0.4	0.64 ± 0.06	0.18 ± 0.03	0.25 ± 0.01	-1.67 ± 0.19	2.64 ± 0.12	0.31 ± 0.10	1.45 ± 0.09	2.43 ± 0.04
	0.36 ± 0.06	-0.04 ± 0.05	0.44 ± 0.06	-3.06 ± 0.69	3.18 ± 0.35	1.35 ± 0.697	3.06 ± 0.53	2.56 ± 0.12
0.0	0.65 ± 0.07	0.21 ± 0.04	0.26 ± 0.02	-0.83 ± 0.25	2.59 ± 0.14	0.05 ±0.16	1.69 ± 0.13	2.38 ± 0.04
	0.35 ± 0.07	0.02 ± 0.07	0.50 ± 0.09	-0.28 ± 0.70	2.52 ± 0.33	-0.67 ± 0.60	2.10 ± 0.44	2.14 ± 0.11
-0.5	0.69 ± 0.05	0.16 ± 0.03	0.25 ± 0.02	-2.07 ± 0.24	2.74 ± 0.15	0.23 ± 0.13	1.50 ± 0.12	2.55 ± 0.05
	0.31 ± 0.05	-0.16 ± 0.09	0.49 ± 0.07	-1.74 ± 0.48	2.32 ± 0.46	-0.51 ± 0.53	2.55 ± 0.44	2.47 ± 0.08
-1.2	0.75 ± 0.06	0.14 ± 0.02	0.25 ± 0.01	-0.41 ± 0.22	2.65 ± 0.15	0.05 ± 0.13	1.64 ± 0.12	1.96 ± 0.04
	0.25 ± 0.06	-0.21 ± 0.11	0.55 ± 0.06	-0.74 ± 0.45	1.99 ± 0.33	-0.31 ± 0.49	2.15 ± 0.23	2.13 ± 0.12

Notes. W, $[M/H]$, and $\sigma_{[M/H]}$ correspond to the results from the GMM analysis of the two-Gaussian distribution, where W indicates the relative weight of each of the Gaussian components. μ_l, σ_{μ_l}, μ_b, and σ_{μ_b} are in mas/yr. $H-K_s$ are in Vega magnitudes.

Part III

Galaxy simulation

8

A common in situ formation pathway for nuclear discs and nuclear star clusters

Authors/contributors: N. Nieuwmunster, F. Fragkoudi, M. Schultheis

In this chapter, I present the analysis of the inner regions of a barred disc galaxy in a hydrodynamical simulation. This project is in preparation for submission. In addition, in appendices at the end of the chapter, I carried out the same orbital analysis as in Chapter 6 using the data from this simulation.

Nuclear stellar discs (NSDs) are dense flattened rotating stellar systems found in the central hundred parsecs in many galaxies. They are kinematically cold stellar structures and show a wide range in sizes from 100 pc to about 1 kpc (Gadotti et al. 2020, de Sá-Freitas et al. 2023a). They are supposed to be formed from gas that is brought to the centre and which forms stars, thus building an in-situ NSD. The formation of NSDs is therefore strongly connected to the formation of the bar for barred galaxies. However, NSDs are also seen in elliptical galaxies where other mechanisms have been proposed such as the transport of gas to the centre via minor mergers and stellar mass loss.

Nuclear star clusters (NSCs) are compact and massive clusters located at the dynamical centres of their many host galaxies. Their effective radii, within which half of the cluster light is contained, are found to span a wide range from 0.4 to 44 pc (Neumayer et al., 2020). While the two proposed formation mechanisms are the inspiral and mergers of massive star clusters, and in situ formation, both scenarios could possibly contribute to the growth of NSCs (Böker, 2010). Moreover, the in situ formation can be caused by several secular mechanisms such as bar-driven gas infall (Shlosman et al., 1990), dissipative nucleation (Kenji Bekki et al., 2006; K. Bekki, 2007), tidal compression (Emsellem et al., 2008) or magneto-rotational instability (Milosavljević, 2004).

The Milky Way shows a clear structure of the NSD with a radius of $\sim 120\,pc$ and a scale height of $\sim 50\,pc$ (Launhardt et al. 2002a, S. Nishiyama et al. 2013). Kinematic studies revealed that the Milky Way NSD (MWNSD) is rotating (e.g. Lindqvist et al.

1992b, Schönrich et al. 2015b,Shahzamanian et al. 2022). Combining the chemistry with the kinematics, Schultheis et al. (2021) found a metal-rich, dynamical cool population which might have formed in-situ from the overlapping central molecular zone, and a metal-poorer population with similar kinematics as the Galactic bulge.

The Milky Way also features a NSC (hereafter called MWNSC) in its centre with an effective radius between $4.2 \pm 0.4\ pc$ and $7.2 \pm 2.0\ pc$ (Schödel et al. 2014b, Fritz et al. 2016) and a mass between $2.1 \pm 0.7 \times 10^7$ and $4.2 \pm 1.1 \times 10^7\ M_\odot$ (Schödel et al. 2014b; Schödel et al. 2020b, Chatzopoulos et al. 2015b, Feldmeier et al. 2014,Feldmeier-Krause et al. 2017c).

While several photometric studies suggest that the MWNSD and MWNSC may have undergone distinct formation histories (Francisco Nogueras-Lara et al., 2020a; Francisco Nogueras-Lara et al., 2021b), F. Nogueras-Lara et al., 2023c found kinematic and metallicity gradients that would suggest a smooth transition between both components. They propose that the MWNSD and MWNSC might be part of the same structure. Also, Seth et al., 2006 found discs or rings superimposed onto the observed NSCs in the nuclear regions of 14 nearby galaxies. They suggest that their observations strongly support an in situ formation where NSCs are formed from stars losing angular momentum from the NSDs in which NSCs are embedded. The links between NSDs and NSCs are however still under discussion and much more work is needed.

Due to their non-axisymmetric potential, galactic bars are responsible for redistributing angular momentum, gas and stars into their host galaxies. They exert gravitational torques and force the gas to shock and funnel towards the galactic centres. Higher metallicities and star formation rates are observed in the inner regions of barred galaxies (Ellison et al., 2011). Gaseous nuclear rings and NSDs are expected to form inside-out from the gas infall and thus to be directly linked to the evolution of galactic bars. Their formation processes have been extensively examined in the literature using analytical calculations and numerical techniques such as hydrodynamic simulations (Athanassoula, 1992c; Kim et al., 2012; Fragkoudi et al., 2016; Fragkoudi et al., 2017; Seo et al., 2019; Sormani et al., 2018a; Sormani et al., 2024). The resonant theory (Buta et al., 1996) that states that nuclear rings form from the accumulation of gas at the inner Lindblad resonance (ILR) is challenged by a new theory proposed by Sormani et al., 2024 according to which the gas accumulates at the inner edge of an extensive gap that forms around the ILR (and see also Athanassoula 1992c). This would explain why the nuclear rings and NSDs are found inside the ILR in simulations and in observations as with the MWNSD. Moreover, in simulations, the residual angular momentum of the infalling gas, the resolution, the gas viscosity and gas sound speed play important roles in the formation of nuclear rings and their sizes (Fragkoudi et al., 2017; Sormani et al., 2018a; Kim et al., 2012; Seo et al., 2019)

In the case of NSCs, most simulations studying their formation processes focused on testing the infall and merger of globular clusters scenario (Antonini et al., 2012; Tsatsi et al., 2017b). Given the demanding resolution requirements, numerically simulating the NSCs in situ formation is challenging, with few studies having been carried out so far (see for example Brown et al. 2018).

In this project, I use a hydrodynamic simulation to characterise the inner structures of an isolated barred disc galaxy and to understand their formation processes.

8.1 Simulation

In this study I use an N-body hydrodynamic simulation of an isolated Milky Way-like disc galaxy which evolves self-consistently to form a bar, a nuclear stellar disc, and a structure akin to a nuclear star cluster. The model is part of a suite of hydrodynamic N-body simulations first presented in de Sá-Freitas et al., 2023b, and which will be described in detail in Fragkoudi et al. (in prep.). Here I provide some basic information about the model and refer the reader to de Sá-Freitas et al., 2023b for more details.

The initial conditions of the simulation contain a stellar disc, a dark matter halo as well as a gaseous disc, and are setup using the code DICE (see V. Perret et al. 2014; Valentin Perret 2016). The simulation uses the adaptive mesh refinement code RAMSES (Teyssier 2002) and has a resolution of 10 pc and is evolved for 3.33 Gyr. The total mass of the simulated galaxy is $M = 2 \times 10^{12} \mathrm{M}_{\odot}$ with a dark matter halo $M_{\mathrm{DM}} = 1.97 \times 10^{12} M_{\odot}$, a stellar component $M_{\star} = 2.85 \times 10^{10} \mathrm{M}_{\odot}$ and a gaseous component $M_g = 1.5 \times 10^{9} \mathrm{M}_{\odot}$. The masses of the stellar and dark matter particles are $3.7 \times 10^{4} \mathrm{M}_{\odot}$ and $4.3 \times 10^{5} \mathrm{M}_{\odot}$ respectively. The stellar and gaseous content initially follow a simple exponential disc with a scale-length of 3 kpc and 4 kpc and a scale-height of 150 pc and 50 pc, respectively. The dark matter halo follows the typical Navarro-Frenk-White profile (Navarro et al. 1997) with a scale-length of 3 kpc.

Star formation in the simulation follows the Kennicutt-Schmidt law assuming a star forming efficiency of 1%. Star formation occurs when the gas density is larger than $1\,\mathrm{cm}^{-3}$ and the temperature is below 100 K. It is assumed that 20% of the population will explode as a core-collapse supernova, and redistributes metals into the surrounding ISM, thus enriching it and increasing its metallicity. The stellar and gaseous components of the simulation are initialised with metallicity $Z_{\mathrm{in}} = 0.02$ which is close to solar metallicity, $\sim Z_{\odot}$. As the metallicity starting point in the simulation is somewhat arbitrary, I rescaled the metallicity to match that of the inner regions of the Milky Way. The conversion from absolute to relative metallicity is given by,

$$[M/H] = \log_{10}(Z) - \log_{10}(Z_{\odot}), \tag{8.1}$$

where $Z_{\odot} = 0.02$.

At the beginning of the simulation the stellar disc is already in place and becomes unstable to the formation of a bar, which begins to form after $\sim 0.3\,\mathrm{Gyr}$. During the formation of the bar, gas is funnelled to the centre where it forms a rotating NSD and a more concentrated central structure – see Fig 8.1.

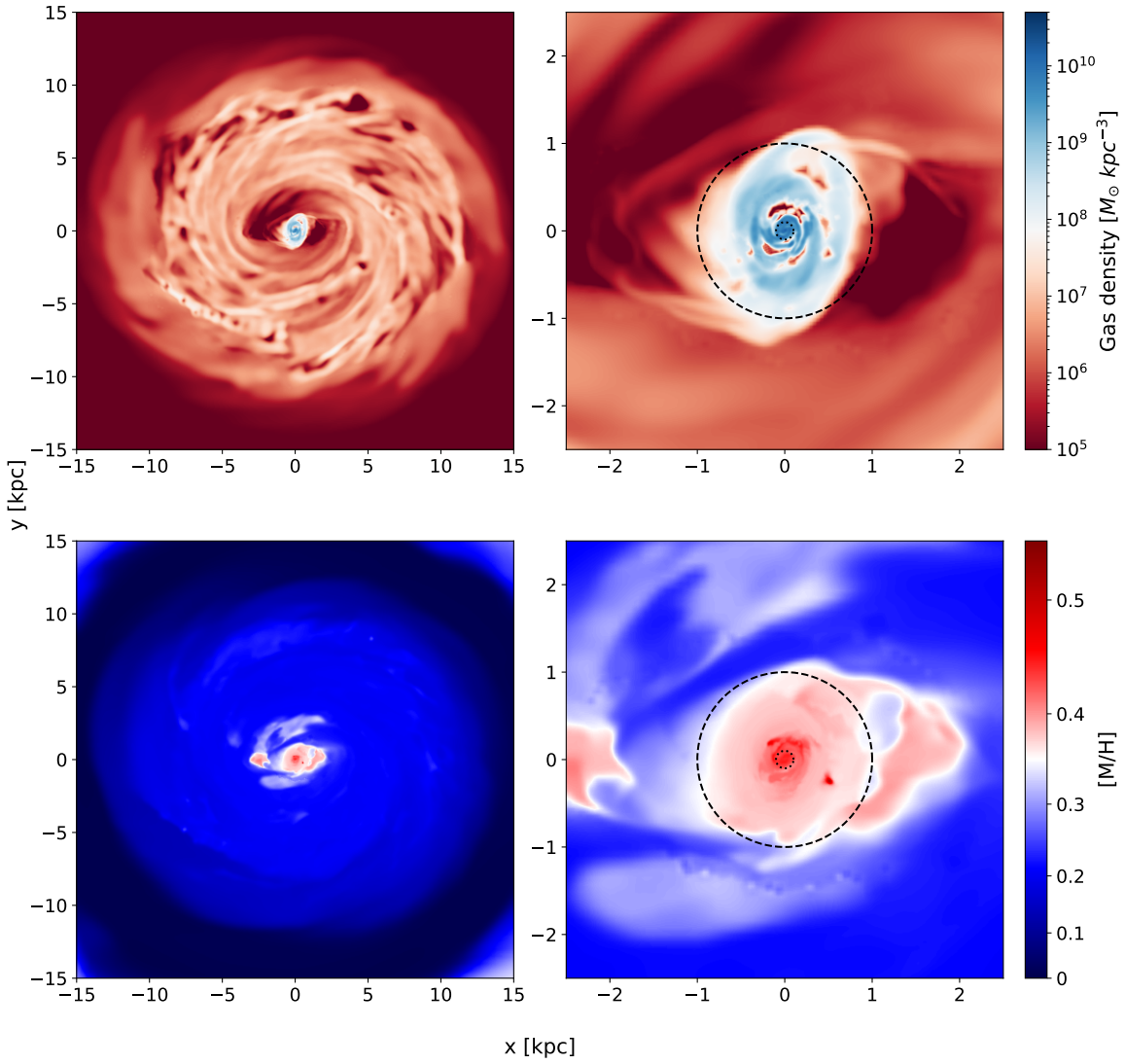

Figure 8.1: *(x,y) plane showing the gas density (upper panels) and gas metallicity (lower panels) in the whole simulated galaxy (left panels) and in the inner regions (right panels). The black dashed and dotted circles indicate the region with a radius below* 1 kpc *and* 100 pc *respectively.*

8.2 Results

To visualise the enrichment history of the inner regions of our simulated galaxy, I show in Fig. 8.2 the stellar metallicity [M/H] as a function of time and age for all stars formed from gas during the simulation (hereafter referred to as "all young stars"). In the upper

panel, the plot is colour coded with the galactocentric radius using a colour bar scaled for $R \leq 1\ kpc$ in order to focus our study on the inner regions. The main disc stars, i.e. for $R >> 1\ kpc$, are shown in brown and correspond to the metal poorest young population ([M/H]$\leq$ 0.15 dex) of the galaxy. From 0.3 Gyr after the start of the simulation to 0.8 Gyr, gas is very turbulent, the main disc rapidly forms the bar and we see that a large number of stars is formed with intermediate and high metallicities in the central regions of the galaxy. From 0.8 Gyr to 1.0 Gyr we still observe newly formed stars at high metallicities close to the centre. However, after 1.0 Gyr, this distribution of stars initially whole is divided through time into two distinct sequences: (i) one composed of very metal rich stars located at the very centre and (ii) another one containing less metal rich stars located at larger radii until 1 kpc. I made three selections in the lower panel of Fig. 8.2 colour coded in green for the old structure and red and blue for both newly formed structures, to study these different structures more below.
In the upper left panel of Fig. 8.3, I show the 2D density plot of stellar age as a function of galactocentric radius for all young stars. We observe two successive star formation bursts for 2.1 < age < 3.0 Gyr followed by a more quiescent phase until the end of the simulation where stars keep forming at a lower rate. This last phase shows two different distributions: a vertical one in the galactic centre and a diagonal one at larger radii. In the upper right panel of Fig. 8.3, I show the same plot with the colour code introduced previously. While the red selection is restricted to the very central region, we observe that the blue selection expands from the centre to larger radii until $R \simeq 1\ kpc$. From now on, I will refer to the red and blue structures as the NSC and NSD of the galaxy while the green structure will be considered as the progenitor of both latter components.

In the same way, we can look at the 2D density plot of stellar metallicity as a function of galactocentric radius for all young stars shown in the lower left panel of Fig. 8.3. We observe that stars with low and intermediate metallicities ([M/H]< 0.2) are located at various radii while the very metal rich stars ([M/H]> 0.3) are only located at low radii and in a large number. We can also distinguish an horizontal overdensity for $0.25 < R_{GC} < 1.0\ kpc$ and 0.27 < [M/H] < 0.32. When plotting only stars with an age below 2.53 Gyr (see lower middle panel of Fig. 8.3), only the overdensity at very high metallicities and the horizontal one remain. Finally, by using the colour code, in the lower left panel of Fig. 8.3, we observe that the very high metallicity distribution corresponds to both the progenitor and NSC while the horizontal overdensity corresponds to the NSD. It is worth noting that the latter has an almost uniform metallicity distribution 0.27 < [M/H] < 0.32.
As the spatial resolution of the simulation is 10 pc, I have to ensure that we resolve the three observed inner components and most importantly the smallest one: the NSC. To do so, I determined their effective radius by fitting a Sérsic profile to their stellar surface density. I used the equation 1 from Graham, 2001 and performed bootstrapping to account for the uncertainties in stellar density in the fitting procedure. The fitted stellar surface densities for each structure or combination of structures are plotted as a

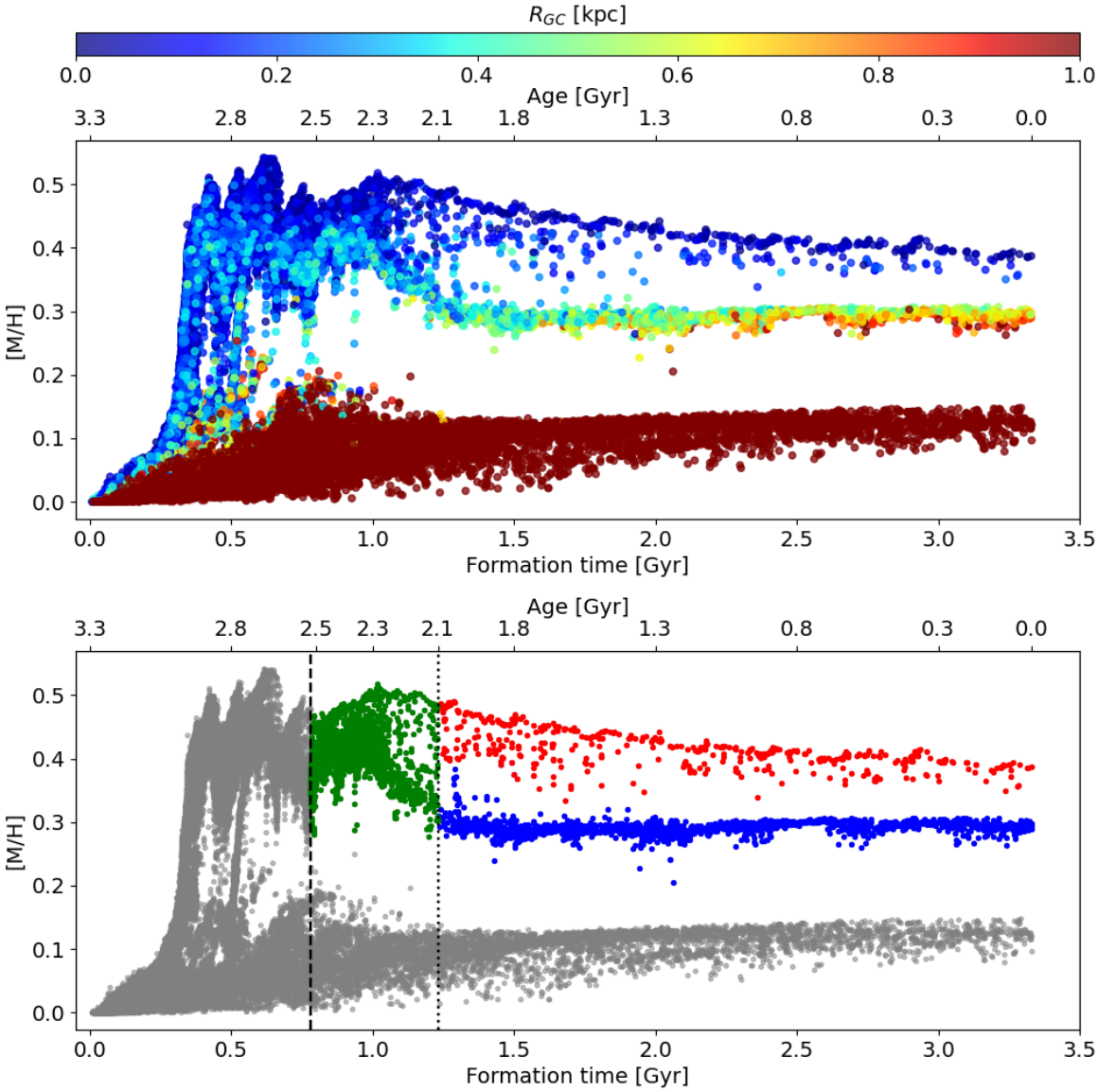

Figure 8.2: *Upper panel: metallicity vs. time (and age) colour coded by radius for all stars formed during the simulation. Lower panel: metallicity vs. time (and age) with the three selections corresponding to the progenitor (green), NSC (red) and NSD (blue).*

function of radius with a 25 pc step slightly higher than our spatial resolution (see Fig. 8.4). The estimated effective radii can be found in Table 8.1. Since the effective radius of the NSC is estimated to be 61 pc, it is above our resolution limit and therefore I can say that this component is resolved. The progenitor component (R_{eff} = 145 pc) extends at larger radii as observed visually in the previous Figures 8.2, 8.3. By combining the stellar surface density of the progenitor and the NSD, I get the larger effective radius of all the selections R_{eff} = 201 pc, which is expected since the NSD extends to larger radii as shown previously.

I can also estimate the dimensions of the three identified inner components of the galaxy by plotting the 2D stellar density face-on (x,y plane) and edge-one (x,z plane) as shown

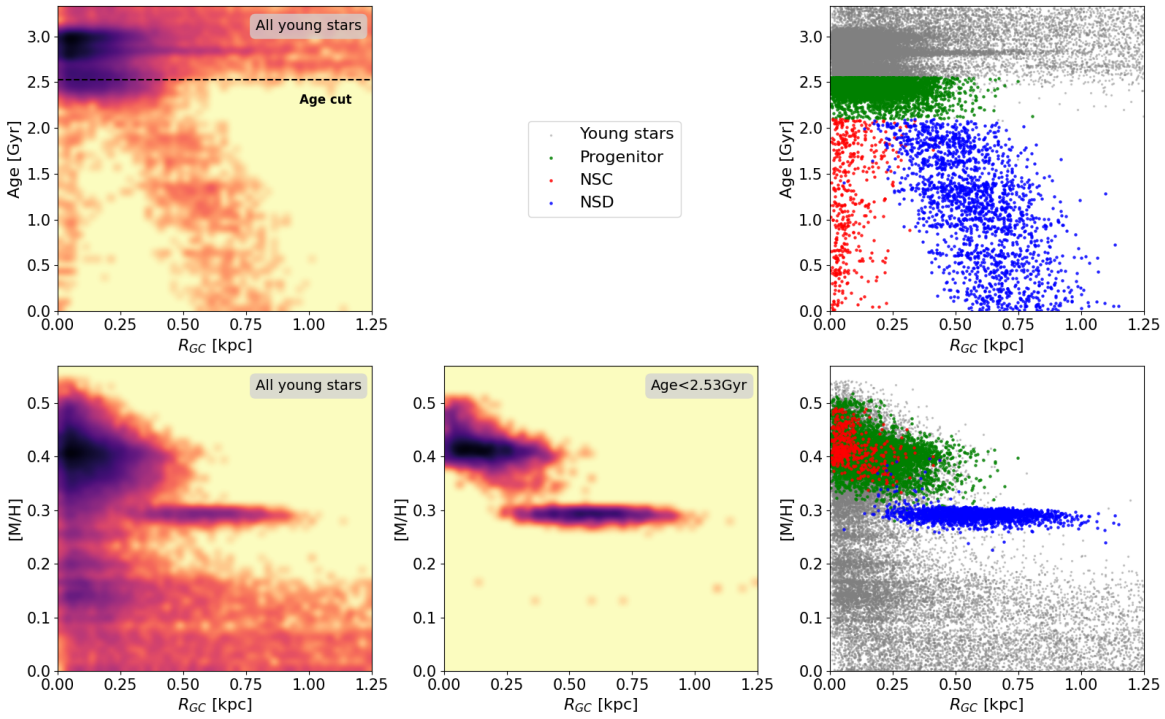

Figure 8.3: *Upper left and right panels: 2D density plot and scatter plot of stellar age vs. galactocentric radius respectively. Lower left and middle panels: 2D density plots of stellar metallicity vs. galactocentric radius for all young stars and stars with age below* 2.53 Gyr. *Lower right panel: scatter plot of stellar metallicity vs. galactocentric radius for all young stars. Green, red and blue markers correspond to the progenitor, NSC and NSD respectively.*

in Fig. 8.5. We clearly see the spherical shapes of the progenitor and the NSC, and the discy/ring shape of the NSD.

We can also look for the presence of any age or metallicity gradient in the identified components. In Fig. 8.6 and 8.7, I show the 2D histograms weighted by stellar age and metallicity in the (x,y) plane for different selections. We see that neither the progenitor nor the NSC show a specific age gradient and none of the three structures show a metallicity gradient. However, in the case of the NSD, we distinguish easily a positive age gradient: stars are younger as radius increases.

	Effective radius [pc]	Stellar mass [$M_\odot$]
Progenitor	145	1.1×10^8
NSC	61	1.2×10^7
NSD	201	4.6×10^7
MWNSC	4.2 to 7.2 (a)	2.1×10^7 to 4.2×10^7 (a)
MWNSD	74 (b)	10.5×10^8 (b)

Table 8.1: *Comparison between the simulation and observations in the Milky Way. (a): Neumayer et al., 2020, (b): Sormani et al., 2022.*

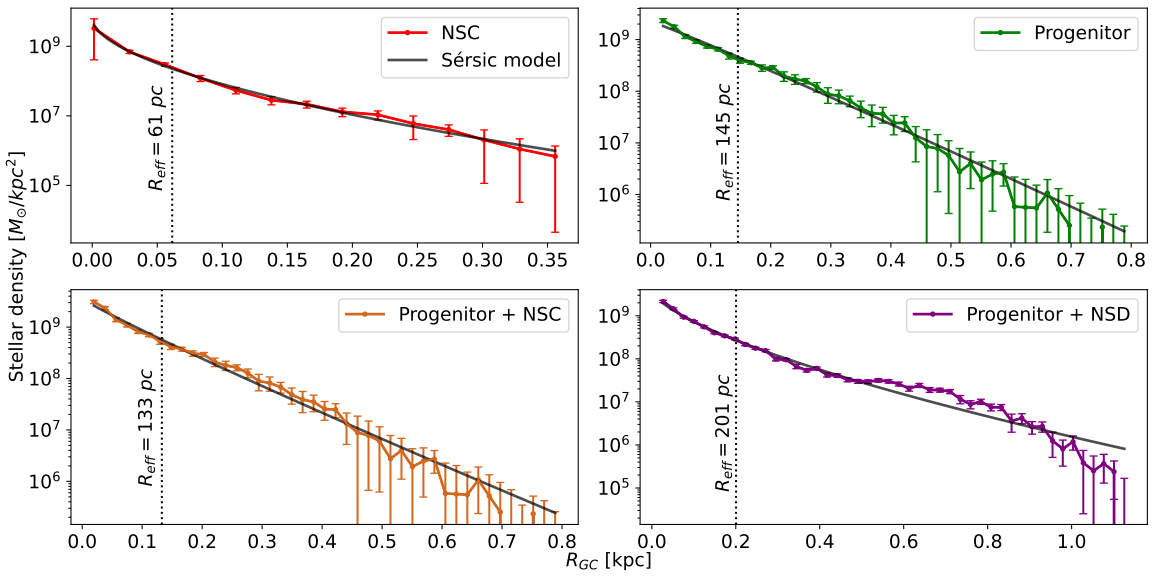

Figure 8.4: *Stellar surface density of the each or combination of the identified inner components are fitted with a Sérsic profile.*

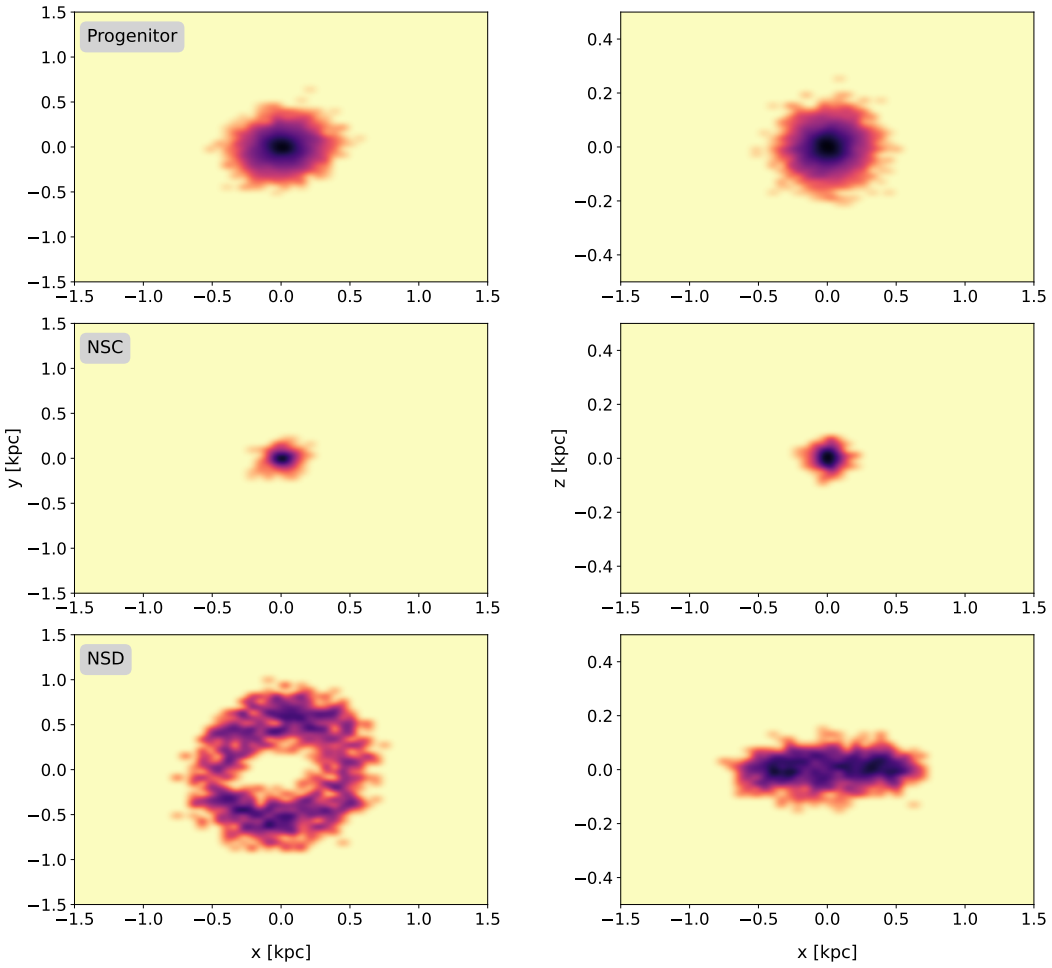

Figure 8.5: *2D density plots in (x,y) and (x,z) planes for the three identified structures: progenitor (upper panel), NSC (middle panel), NSD (lower panel).*

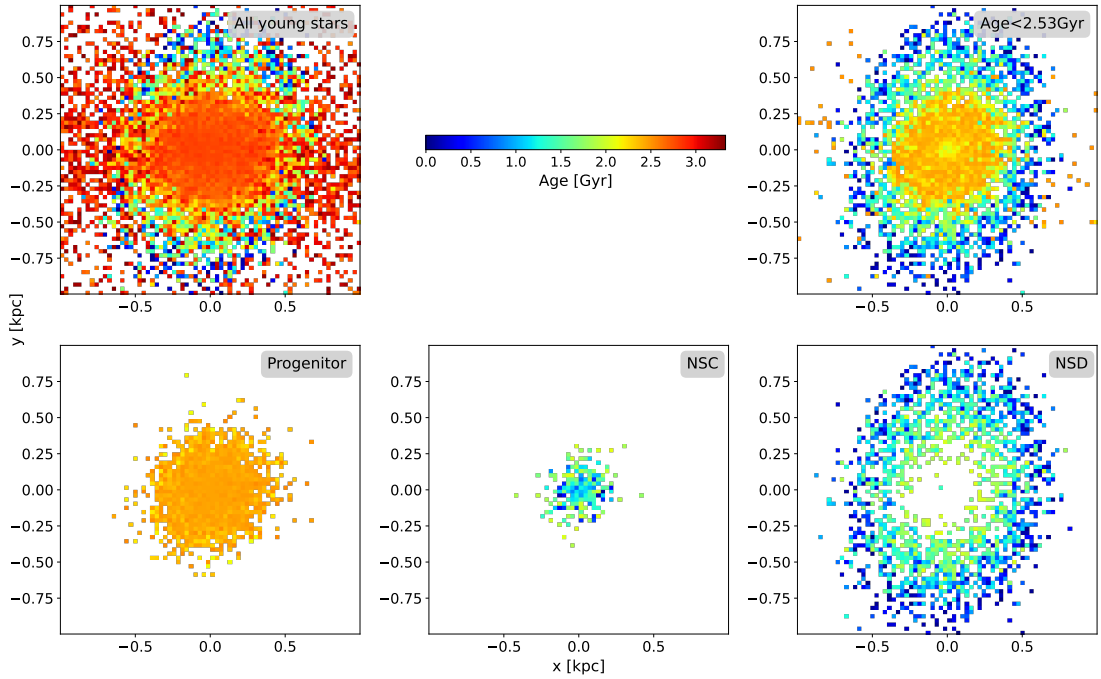

Figure 8.6: *2D histograms weighted by stellar age in the (x,y) plane of all young stars (upper left panel), stars with* age $< 2.53\ Gyr$ *(upper right panel), progenitor (lower left panel), NSC (middle lower panel) and NSD (lower right panel).*

Finally, I show in Fig. 8.8 the histogram of the rotation velocity for each structures. The NSD shows a very clear rotation with all its stars at positive velocities distributed around 150 $km\ s^{-1}$ with small scatter. The stars of the progenitor structure have a wider range of rotation velocities and the majority rotates at a lower speed. In the case of the NSC, we almost see no rotation signature.

To summarise this section, by analysing the galactocentric radius, age, metallicity of stars, and the stellar surface density, I have been able to identify three distinct structures in the inner regions of the galaxy. The NSD and the NSC are formed from the same older progenitor structure through different formation processes that I will discuss in the next section.

8.3 Discussion and early conclusions

NSDs are believed to be formed when the galactic bar brings gas to the centre of the galaxy and where the resulting gas disc form new stars building up an in-situ nuclear stellar disc. The gas inflow rates generate disc or ring like structures, such as the central molecular zone in the Milky Way (Morris et al. 1996). The current idea is that star formation occurs in these gaseous rings which build up nuclear stellar discs over time. Some evidence for this scenario comes from the fact that the rotational velocities of the gas and stars are similar (see e.g. Bittner et al. 2020, Gadotti et al. 2020

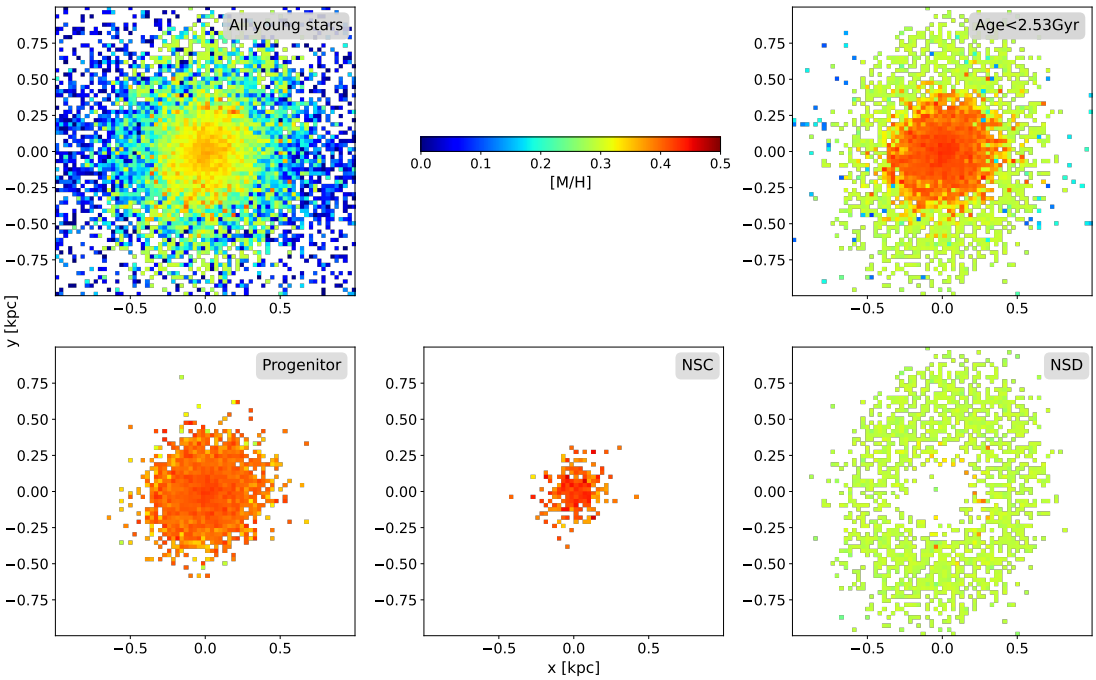

Figure 8.7: *2D histograms weighted by stellar metallicity in the (x,y) plane of all young stars (upper left panel), stars with* age $< 2.53\ Gyr$ *(upper right panel), progenitor (lower left panel), NSC (middle lower panel) and NSD (lower right panel).*

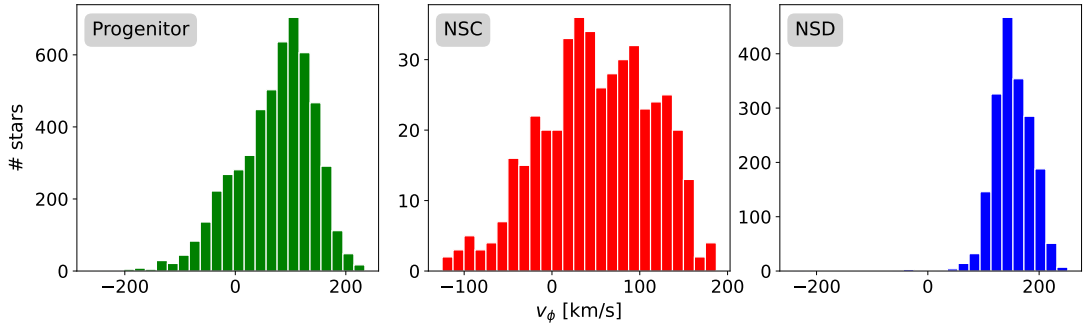

Figure 8.8: *Rotation velocity V_ϕ histogram of the selected structures.*

in extragalactic systems or Schönrich et al. 2015b, Schultheis et al. 2021 in the Milky Way). If NSDs indeed form from bar-driven gas inflows, one would expect that NSDs are typically younger and more metal-rich than their surroundings. Concerning NSCs, several possible formation scenarios for in-situ formation have been proposed such as bar-driven gas infall, dissipative nucleation, tidal compression or magneto-rotational instability (see Neumayer et al. 2020 for more details). The presence of a young stellar population concentrated at small radii (e.g < 0.5 pc in the Milky Way, Feldmeier-Krause et al. 2015) favours the scenario of an in-situ formation of the NSC which has been also detected in other NSCs such as M31 (Carson et al. 2015).

The hydrodynamic simulation employed in this paper is a self-consistent simulation of a barred disc galaxy in which a bar forms and affects the gas flows in the galaxy. In this model, I distinguished three distinct structures in the inner regions of the galaxy by looking exclusively to the stars formed from the gas (see Section 8.2). I identified a group of very metal rich stars ($[M/H]_{mean} \simeq 0.42$ dex) distributed spherically in the very central regions ($R_{GC} \leq 250$ pc). In addition, I measured an effective radius about $R_{eff} \simeq 61$ pc which is compatible with measurements of NSCs from the literature (e.g. Neumayer et al., 2020 for extragalactic NSCs and Schödel et al., 2014b for the MWNSC). Thus, this structure can be thought of as being analogous to a NSC. It shows a continuous star formation close to the centre and as the galaxy is isolated, this NSC cannot have formed through the inspiral and merger of star clusters (Böker, 2010) and therefore only the in-situ scenario can occur in our simulation.
I also found a more extended and flattened distribution of stars from $R_{GC} \simeq 250$ pc to $R_{GC} \simeq 1$ kpc that features a disc or ring shape and which shows a significant rotation (see Fig. 8.8). Thanks to all these characteristics, we see that this structure corresponds to the description of a NSD. Moreover, its stars are metal richer from the outer surroundings (i.e. stars from the main disc and bar) ($[M/H]_{mean} \simeq 0.29$ dex) and are metal poorer than those of the NSC. No metallicity gradient is however observed in the NSD (see Fig. 8.7). Also, I found an age gradient showing that the inner part of the NSD is composed of older stars (see Fig. 8.6). These results are consistent with observations in extragalactic systems and in the Milky Way. The MWNSC is measured to be metal richer than the MWNSD (Schultheis et al. 2021) and age gradients (and also metallicity gradients) have been measured in the MWNSD (F. Nogueras-Lara et al., 2023a) and in extragalactic NSDs (Bittner et al., 2020). My results are therefore a clear evidence that the NSD of the simulation formed from inside out. This process - the inside out formation - has already been well studied in hydrodynamic simulations (Athanassoula 1992c, Fragkoudi et al. 2016, Kim et al., 2012, Seo et al., 2019 among others) and observed in extragalactic systems (Bittner et al. 2020).

Both these structures are built by gas inflow due to the bar and have a common progenitor, which is also a spheroidal-like component in the central region (for $R_{GC} \leq 500$ pc, see green selection in Fig. 8.2) and composed of very metal rich stars ($[M/H]_{mean} \simeq 0.40$

dex) like the NSC. Both these structures (NSD and NSC) "emerge" from the initial gas inflow via the bar into two separate sequences in the metallicity versus age plot shown in Fig. 8.2. They form at the same time ($\simeq$ 2.1 Gyr), but have different chemical evolutionary tracks, likely due to the different gas surface densities. Therefore, this model offers a formation scenario for the NSC which is concurrent with the NSD, and which emerges from the same progenitor, and effectively due to the gas inflow via the bar.
I emphasise that this does not imply the MWNSC formed through the same process but rather illustrates how a NSC could form in situ. Additionally, it is possible that a NSC could have already been in place before the bar-induced gas inflow. However, the bar can still contribute to the accumulation of gas in the central regions through gas inflow and resonances.

The objective of this paper is not to make a strict comparison with the Milky Way, as the galaxy in the simulation is not analogous to it. However, for reference, the mass and effective radius ratios between the NSD and the NSC in our simulation are $M_{NSD}/M_{NSC} \simeq 3.8$ and $R_{NSD}/R_{NSC} \simeq 3.3$ while the one of the Milky Way are $M_{MWNSD}/M_{MWNSC} \simeq 42$ and $R_{MWNSD}/R_{MWNSC} \simeq 13.5$. The respective masses and effective radii can be found in Table 8.1.

Appendices

In Chapter 6, I presented an orbital analysis of stars observed in the Milky Way's NSD (MWNSD) and I identified several orbital families. In this current chapter, as I used a hydrodynamic N-body simulation of a barred disc galaxy containing a nuclear disc, I took this opportunity to carry out the same analysis with stars from the inner regions of this simulated galaxy. The purpose is to make a first comparison between observations and simulation of the orbital families located in a NSD.

8.A Orbit integration

The simulation previously presented in Section 8.1 is composed of 438 snapshots and is evolved for 3.33 Gyr. Unfortunately, as the frequency analysis needs a short time step to have a good sampling of the orbits, there are too few snapshots to provide a sufficiently short time step in order to determine accurate orbital frequencies for the majority of the orbits. For this reason, this additional project is incomplete and increasing the number of snapshots is necessary to study the orbits provided by the simulation.

A way to get an estimation of the orbits of the stars in the simulation is to compute the orbits with AGAMA (Vasiliev, 2019) as in Chapter 6. To do so, I extracted the gravitational potential (stars, gas and dark matter) from the last snapshot using routines provided by AGAMA. In order to study only the orbits of stars located in the inner regions of the galaxy, I selected stars with a galactocentric radius below 1 kpc and younger than 2.53 Gyr (see Fig. 8.3). In the same way as in Chapter 6, I computed the orbits of these stars using their phase space coordinates in the last snapshot as initial conditions and by using the extracted potential of the snapshot and accounting for the rotation of the bar (measured to be $\sim 40\ km\ s^{-1}\ kpc^{-1}$ at this snapshot and anticlockwise). I also computed the highest Lyapunov exponent as in Chapter 6 to measure the chaoticity of orbits.

8.B First results

In this section, I present the first results obtained for the orbits (computed with AGAMA) of the stars located in the inner regions of the simulated galaxy.

Firstly, I show in Figure 8.B.1 the R_{max} vs z_{max} diagram of the orbits as a function of eccentricity, metallicity and age. An interesting observation is that there are no discernible structures analogous to the "wedges" discussed in Chapter 6. We can however observe a filament structure as in Chapter 6 which corresponds to bar contaminants. Additionally, as seen previously in this chapter, we observe high metallicities close to the centre and we distinguish the young stars from the NSD. The selection used here contains the three identified structures: the progenitor, NSC and NSD. Since these parameters (age and metallicity) have already been well discussed before these appendices, I will not comment more these plots.

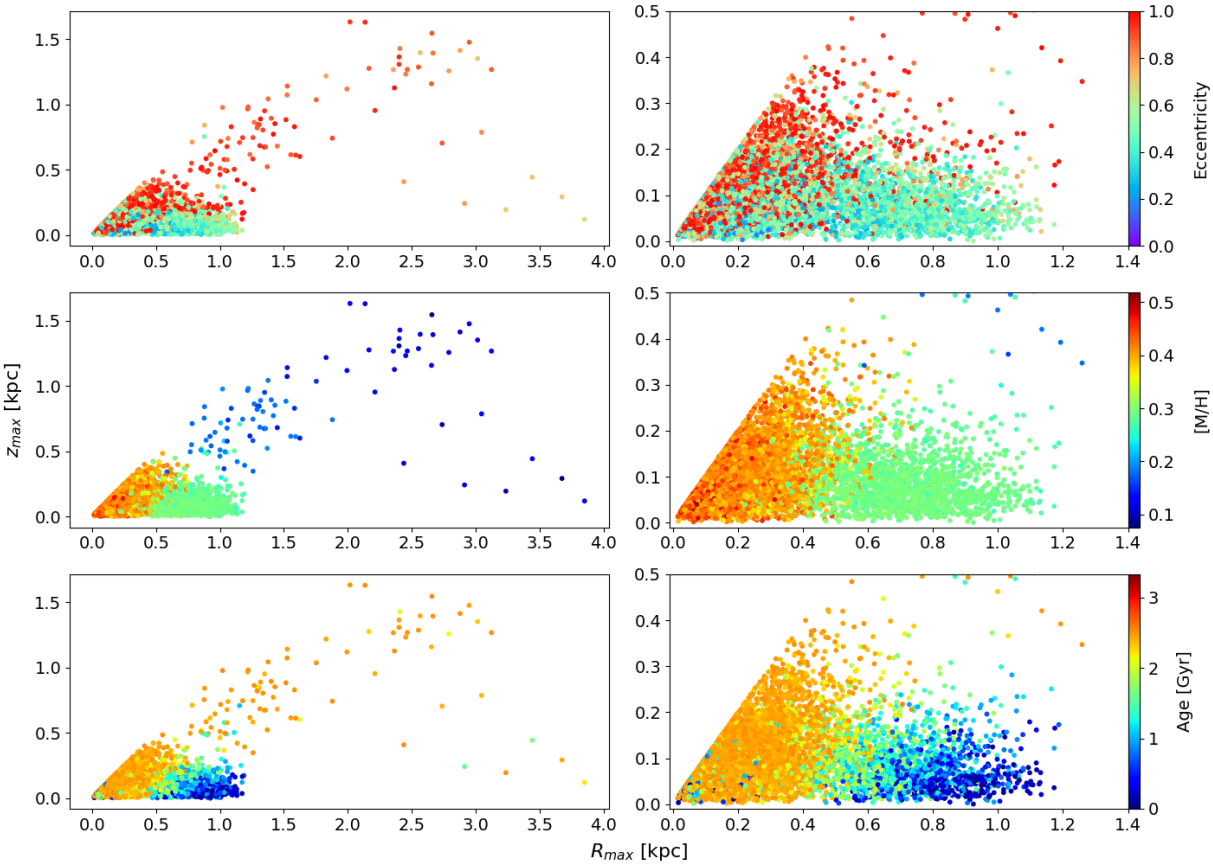

Figure 8.B.1: *R_{max} vs z_{max} diagram of the orbits of inner regions stars. Right panels are zoomed-in versions of left panels. The plot is colour coded with eccentricity (upper panels), metallicity (middle panels) and age (lower panels).*

In Figure 8.B.2, I show the Cartesian frequency map colour coded with the highest Lyapunov exponent. We observe similar distributions of stars as for the MWNSD (see Figure 6.10): a large concentration stars on the z-tube resonance (i.e. 1:-1:0 resonance) and a cloud located above the latter resonance and below the 0:1:-1 resonance containing mainly box and chaotic orbits. We also observe a few x-tubes located at the 0:1:-1 resonance. Regarding the highest Lyapunov exponent, as initial conditions are known exactly from the simulation, these coefficients are much smaller for the majority of the

orbits than for those computed for the MWNSD.

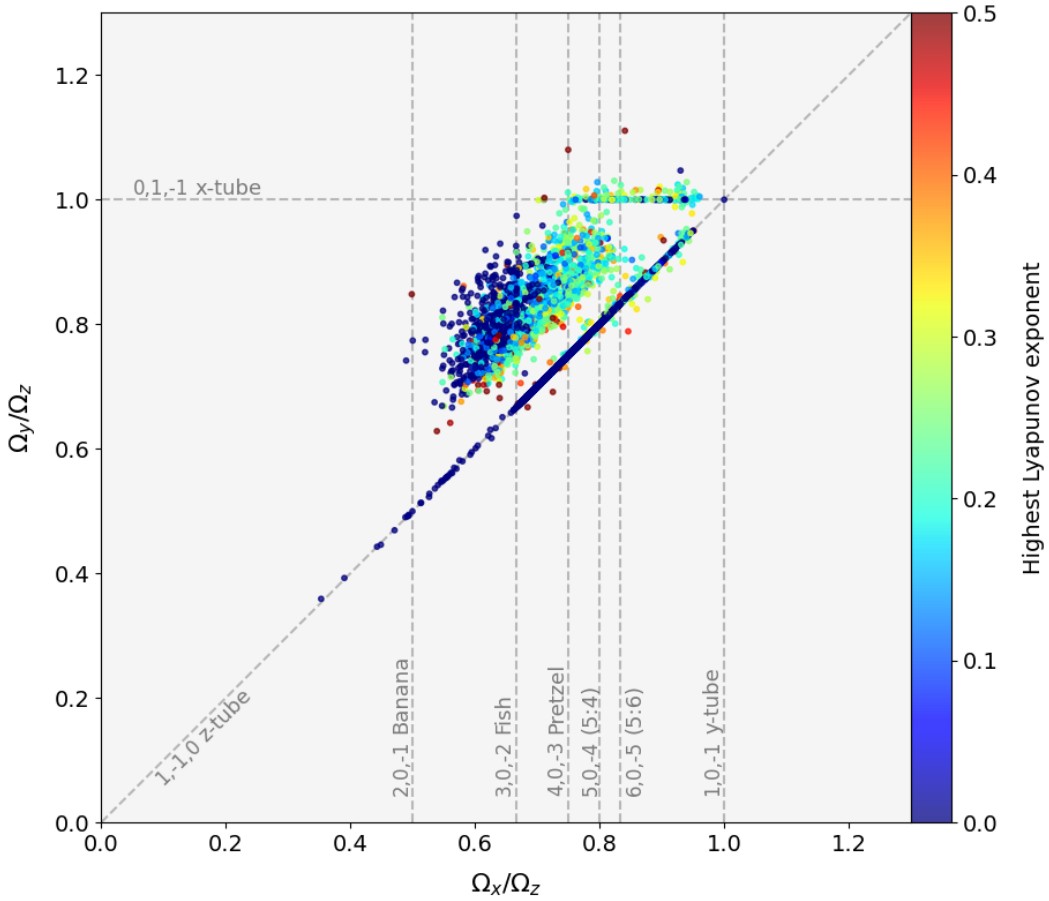

Figure 8.B.2: *Frequency map in Cartesian coordinates vs. highest Lyapunov exponent.*

To identify the different orbital families, I only used the automatic method presented in Chapter 6 and therefore I have not been able to estimate the number of saucer orbits. The comparison of the percentages for each family found in the MWNSD and in the inner regions of the simulation is shown in Table 8.B.1. I found almost the same amount of chaotic/box and x- and z-tube orbits. However, I have almost detected no banana and fish orbits. In the contrary, I found more pretzel, 5:4 and 5:6 orbits than in the MWNSD. As no inner bar has been detected in the simulation and almost no contaminants of the bar are present, the lack of banana orbits is expected. A more in-depth study would be however needed to understand the various amounts of fish, pretzel, 5:4 and 5:6 orbits.

Table 8.B.1: *Comparison of the family membership results obtained with the automatic method for orbits of the MWNSD from Chapter 6 and orbits from the inner regions of the simulation.*

	Chaotic/Box	x-tube	z-tube	Banana	Fish	Saucer	Pretzel	5 : 4	5 : 6
Observations	**34.0%**	**1.1%**	**64.9%**	**4.7%**	**9.0%**	**13.6%**	**3.5%**	**1.5%**	**1.6%**
Simulation	**32.0%**	**1.5%**	**66.5%**	**0.1%**	**0.9%**	**None**	**9.7%**	**7.5%**	**3.8%**

Finally, I show in Figure 8.B.3, the R_{max} vs z_{max} diagram with the different identified orbital families superimposed. We distinguish very clearly the different families. They

are clustered in separated regions of the diagram and almost never overlap. Even if we do not find wedges visually on the classical R_{max} vs z_{max} diagram Fig. 8.B.1, we observe that when plotting the orbital resonances (i.e. families), they construct very distinct "wedges"-like structures.

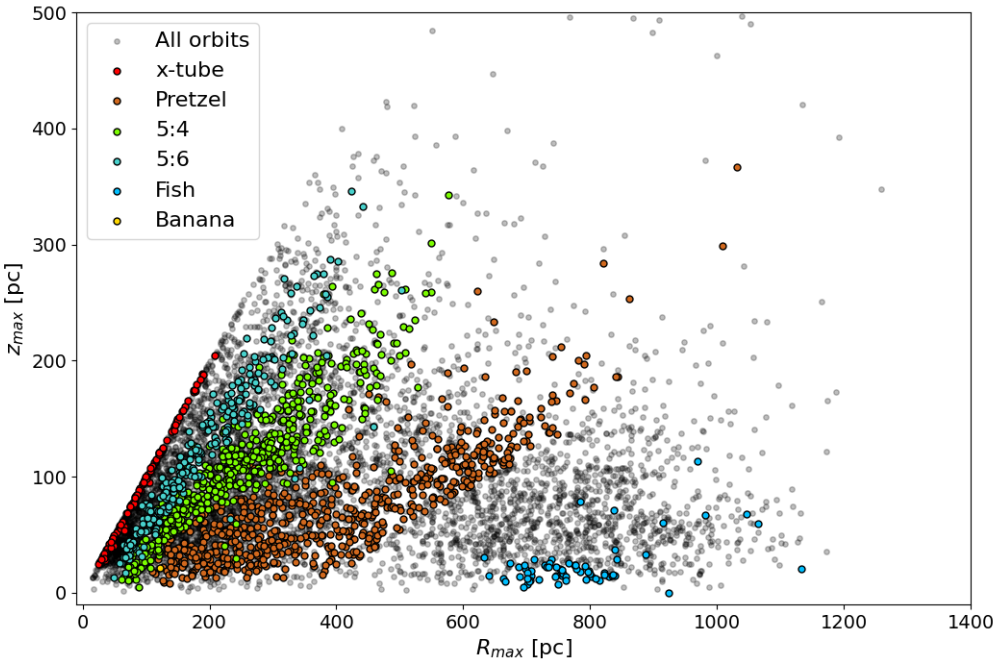

Figure 8.B.3: *R_{max} vs. z_{max} diagram with the different identified orbital families.*

8.C Early conclusions

This first orbital analysis of stars from a hydrodynamic simulation confirms even more the benefits of this method for our understanding of stellar populations and galactic structures. Also, it shows again that wedges which can be observed in the R_{max} vs. z_{max} diagram are related to the orbital resonances. The reason why these wedges are not always observed visually in the classical R_{max} vs. z_{max} diagram still has to be determined.

This early study can however be improved using a simulation with a sufficient number of snapshots allowing to get the orbits directly from the simulation and by studying each inner structure separately. The automatic method to identify orbital families can also be improved as discussed in Chapter 6.

9

Conclusions and outlook

The most incomprehensible fact about the Universe is that it is comprehensible.
Albert Einstein (rephrased quote)

During this thesis, I aimed at unveiling the physical processes which led to the formation of the NSD and its links with the other components of the Milky Way. I had the chance to employ a great variety of methodologies and techniques in order to study directly or indirectly the evolution of the inner regions of galaxies.

9.1 Summary

In Part I, I took advantage of high resolution near infrared spectroscopy to carry out two distinct projects. In Chapter 3, I performed a detailed chemical analysis of M-giant stars located in the inner Galactic bulge. I used CRIRES spectra combined with an updated line list, precise broadening parameters and accounting for NLTE corrections in order to derive the most precise α-abundances as possible in this region. I found that the α-abundance trends have a typical thick disc α-element behaviour. Moreover, these abundances were modelled by a chemical evolution model with two distinct gas-infall episodes. In Chapter 4, I used IGRINS spectra of K-giants located in the solar neighbourhood to measure their isotopic carbon ratio $^{12}C/^{13}C$. Thanks to these measurements, I aimed to establish a relation between the carbon ratio and asteroseismic stellar mass.

In Part II, I studied the dynamics of stars located in the NSD. In Chapter 6, I computed their orbits using a non-axisymmetric potential accounting for the rotating potential of the Galactic bar and I derived their respective orbital frequencies. This allowed me to identify a variety of orbit families present in the NSD. I found out that most of these families are z-tubes and therefore are parented by x_2 orbits which are dominant in the inner part of the bar. These results support the contribution of the bar in the formation of the NSD. In Chapter 7, I presented a co-author paper that can be considered as a

follow-up to the previous chapter. This study explored the metallicity of the different orbital families identified previously and found that z-tube orbits are predominant among metal-rich stars while chaotic/box orbits are more common among metal-poor ones. This would suggest that metal-rich stars trace the NSD and metal-poor stars are related to the Galactic bar and probably constitute Galactic bar interlopers or originated from accreted clusters.

Finally in Part III and Chapter 8, I used a N-body hydrodynamic simulation of a barred disc galaxy to study the formation processes of its inner components. I identified three structures: a nuclear disc and a nuclear cluster that are built by gas inflow due to the bar and have a common progenitor which is a central spheroidal-like component in the central region. The model offers an in situ formation scenario for the nuclear cluster which is concurrent with the nuclear disc. Moreover, I carried out the same orbital analysis as in Chapter 6 for the nuclear disc and inner stars of the simulated galaxy in order to compare with the results from observations.

9.2 Perspectives

The existence of the NSD has only been known for a very short time and remains underexplored due to the significant observational challenges. However, in this thesis, I showed that our comprehension of this structure has significantly advanced these last years.

The α-abundance analysis carried out in Chapter 3 for inner bulge stars can be used as a benchmark study for the future spectroscopic surveys. For instance, it could serve for the MOONS survey (Cirasuolo et al., 2014) that will soon cover the inner regions of the Milky Way in the near infrared wavelength range. The latter will allow us to measure the metallicity and chemical abundances of inner bulge and NSD stars thanks to high resolution H-band spectra ($R \simeq 20000$).

The isotopic carbon ratio $^{12}C/^{13}C$ can be easily measured with high resolution near infrared spectroscopy for K-giants as shown in Chapter 4. Although I established an early relation between this ratio and asteroseismic mass, more work is necessary to validate and apply it to inner regions stars. This relation combined with spectra from the coming spectroscopic surveys will be useful for estimating stellar ages in the nuclear bulge of the Milky Way and in particular in the NSD. Such precise age measurements would allow us to better understand the history of this structure.

The frequency analysis presented in Chapter 6 has been until now very poorly employed in Galactic archaeology. However, the findings for NSD stars show that it can provide valuable insights into the formation scenario of a structure. Therefore, applying this

method combined with chemical studies for the various components of the Milky Way would be of great interest. Moreover, the automatic classification of orbital families has significant potential for improvement, for example, through the application of machine learning techniques.

Chapter 8 demonstrates that observations alone are insufficient for understanding the evolution of galaxies. Simulations are also essential for comparing results and decipher the physical processes that lead to the diverse morphologies and structures within a galaxy. In my case, increasing the number of snapshots in the simulation would allow to better sample the orbits and thus be able to compute more precise frequencies. Moreover, it would be very interesting to explore the impact of the input parameters of the simulation - such as the spatial resolution, the viscosity, the gravitational barred potential - on the formation processes and characteristics of the nuclear disc and nuclear cluster.

The most obscured regions of the Milky Way are on the verge of being revealed thanks to upcoming observational surveys. Additionally, ongoing projects like TIMER (Gadotti et al., 2019a) and PHANGS (`www.phangs.org`) are focusing on extra galactic systems with the same interest in unravelling the evolution of galaxies. With all these recent technological advancements, we have reached a pivotal moment where it is crucial to integrate findings from various fields to achieve a comprehensive understanding of galaxy formation and evolution. This aligns with the consistent use of definitions, as discussed in Chapter 1 for instance regarding pseudo-bulges and nuclear discs.

Bibliography

Abdurro'uf et al. (Apr. 2022a). "The Seventeenth Data Release of the Sloan Digital Sky Surveys: Complete Release of MaNGA, MaStar, and APOGEE-2 Data". In: 259.2, 35, p. 35. DOI: 10.3847/1538-4365/ac4414. arXiv: 2112.02026 [astro-ph.GA].

— (Apr. 2022b). "The Seventeenth Data Release of the Sloan Digital Sky Surveys: Complete Release of MaNGA, MaStar, and APOGEE-2 Data". In: 259.2, 35, p. 35. DOI: 10.3847/1538-4365/ac4414. arXiv: 2112.02026 [astro-ph.GA].

Agertz, Oscar et al. (June 2021). "VINTERGATAN - I. The origins of chemically, kinematically, and structurally distinct discs in a simulated Milky Way-mass galaxy". In: 503.4, pp. 5826–5845. DOI: 10.1093/mnras/stab322. arXiv: 2006.06008 [astro-ph.GA].

Aguerri, J. A. L., M. Balcells, and R. F. Peletier (Feb. 2001). "Growth of galactic bulges by mergers. I. Dense satellites". In: 367, pp. 428–442. DOI: 10.1051/0004-6361:20000441. arXiv: astro-ph/0012156 [astro-ph].

Ahumada, Romina et al. (July 2020). "The 16th Data Release of the Sloan Digital Sky Surveys: First Release from the APOGEE-2 Southern Survey and Full Release of eBOSS Spectra". In: 249.1, 3, p. 3. DOI: 10.3847/1538-4365/ab929e. arXiv: 1912.02905 [astro-ph.GA].

Akaike, H. (Jan. 1974). "A New Look at the Statistical Model Identification". In: *IEEE Transactions on Automatic Control* 19, pp. 716–723.

Alonso, Sol et al. (Oct. 2018). "The impact of bars and interactions on optically selected AGNs in spiral galaxies". In: 618, A149, A149. DOI: 10.1051/0004-6361/201832796. arXiv: 1808.05536 [astro-ph.GA].

Alonso-García, Javier et al. (Nov. 2017). "Extinction Ratios in the Inner Galaxy as Revealed by the VVV Survey". In: 849.1, L13, p. L13. DOI: 10.3847/2041-8213/aa92c3. arXiv: 1710.04854 [astro-ph.GA].

Amarante, João A. S., Martin C. Smith, and Corrado Boeche (Jan. 2020). "The tale of the tail - disentangling the high transverse velocity stars in Gaia DR2". In: 492.3, pp. 3816–3828. DOI: 10.1093/mnras/staa077.

Amarsi, A. M. et al. (Dec. 2016). "Non-LTE line formation of Fe in late-type stars - III. 3D non-LTE analysis of metal-poor stars". In: 463.2, pp. 1518–1533. DOI: 10.1093/mnras/stw2077. arXiv: 1608.06390 [astro-ph.SR].

Amarsi, A. M. et al. (Oct. 2020). "The GALAH Survey: non-LTE departure coefficients for large spectroscopic surveys". In: 642, A62, A62. DOI: 10.1051/0004-6361/202038650. arXiv: 2008.09582 [astro-ph.SR].

Anstee, S. D. and B J O'Mara (1995). "Width Cross-Sections for Collisional Broadening of s-p and p-s Transitions by Atomic Hydrogen". In: *MNRAS* 276.3, pp. 859–866.

— (Dec. 1991). "An Investigation of Brueckner's Theory of Line Broadening with Application to the Sodium D Lines". In: *MNRAS* 253, pp. 549–560. ISSN: 0035-8711.

Antoja, T. et al. (Mar. 2020). "An all-sky proper-motion map of the Sagittarius stream using Gaia DR2". In: 635, L3, p. L3. DOI: 10.1051/0004-6361/201937145. arXiv: 2001.10012 [astro-ph.GA].

Antonini, Fabio (Jan. 2013). "Origin and Growth of Nuclear Star Clusters around Massive Black Holes". In: 763.1, 62, p. 62. DOI: 10.1088/0004-637X/763/1/62. arXiv: 1207.6589 [astro-ph.GA].

— (Oct. 2014). "On the Distribution of Stellar Remnants around Massive Black Holes: Slow Mass Segregation, Star Cluster Inspirals, and Correlated Orbits". In: 794.2, 106, p. 106. DOI: 10.1088/0004-637X/794/2/106. arXiv: 1402.4865 [astro-ph.GA].

Antonini, Fabio et al. (May 2012). "Dissipationless Formation and Evolution of the Milky Way Nuclear Star Cluster". In: 750.2, 111, p. 111. DOI: 10.1088/0004-637X/750/2/111. arXiv: 1110.5937 [astro-ph.GA].

Arca Sedda, Manuel et al. (Oct. 2020a). "On the Origin of a Rotating Metal-poor Stellar Population in the Milky Way Nuclear Cluster". In: 901.2, L29, p. L29. DOI: 10.3847/2041-8213/abb245. arXiv: 2009.02328 [astro-ph.GA].

— (Oct. 2020b). "On the Origin of a Rotating Metal-poor Stellar Population in the Milky Way Nuclear Cluster". In: 901.2, L29, p. L29. DOI: 10.3847/2041-8213/abb245. arXiv: 2009.02328 [astro-ph.GA].

Arca-Sedda, M. and R. Capuzzo-Dolcetta (Nov. 2014). "The globular cluster migratory origin of nuclear star clusters". In: 444.4, pp. 3738–3755. DOI: 10.1093/mnras/stu1683. arXiv: 1405.7593 [astro-ph.GA].

Arca-Sedda, M. et al. (June 2015). "Henize 2-10: The Ongoing Formation of a Nuclear Star Cluster around a Massive Black Hole". In: 806.2, 220, p. 220. DOI: 10.1088/0004-637X/806/2/220. arXiv: 1501.04567 [astro-ph.GA].

Asplund, Martin et al. (Sept. 2009). "The Chemical Composition of the Sun". In: 47.1, pp. 481–522. DOI: 10.1146/annurev.astro.46.060407.145222. arXiv: 0909.0948 [astro-ph.SR].

Athanassoula, E. (Nov. 1992a). "Morphology of bar orbits." In: 259, pp. 328–344. DOI: 10.1093/mnras/259.2.328.

— (Nov. 1992b). "The existence and shapes of dust lanes in galactic bars." In: 259, pp. 345–364. DOI: 10.1093/mnras/259.2.345.

— (Nov. 1992c). "The existence and shapes of dust lanes in galactic bars." In: 259, pp. 345–364. DOI: 10.1093/mnras/259.2.345.

— (June 2003). "What determines the strength and the slowdown rate of bars?" In: 341.4, pp. 1179–1198. DOI: 10.1046/j.1365-8711.2003.06473.x. arXiv: astro-ph/0302519 [astro-ph].

Athanassoula, E. (Apr. 2005a). "On the nature of bulges in general and of box/peanut bulges in particular: input from N-body simulations". In: 358.4, pp. 1477–1488. DOI: 10.1111/j.1365-2966.2005.08872.x. arXiv: astro-ph/0502316 [astro-ph].

— (Apr. 2005b). "On the nature of bulges in general and of box/peanut bulges in particular: input from N-body simulations". In: 358.4, pp. 1477–1488. DOI: 10.1111/j.1365-2966.2005.08872.x. arXiv: astro-ph/0502316 [astro-ph].

— (July 2008). "Boxy/peanut and discy bulges: formation, evolution and properties". In: *Formation and Evolution of Galaxy Bulges*. Ed. by Martin Bureau, E. Athanassoula, and Beatriz Barbuy. Vol. 245, pp. 93–102. DOI: 10.1017/S1743921308017389.

— (Jan. 2016). "Boxy/Peanut/X Bulges, Barlenses and the Thick Part of Galactic Bars: What Are They and How Did They Form?" In: *Galactic Bulges*. Ed. by Eija Laurikainen, Reynier Peletier, and Dimitri Gadotti. Vol. 418. Astrophysics and Space Science Library, p. 391. DOI: 10.1007/978-3-319-19378-6_14. arXiv: 1503.04804 [astro-ph.GA].

Athanassoula, E. and M. Bureau (Sept. 1999). "Bar Diagnostics in Edge-on Spiral Galaxies. II. Hydrodynamical Simulations". In: 522.2, pp. 699–717. DOI: 10.1086/307677. arXiv: astro-ph/9904206 [astro-ph].

Athanassoula, E. and A. Misiriotis (Feb. 2002). "Morphology, photometry and kinematics of N -body bars - I. Three models with different halo central concentrations". In: 330.1, pp. 35–52. DOI: 10.1046/j.1365-8711.2002.05028.x. arXiv: astro-ph/0111449 [astro-ph].

Baade, W. (Aug. 1946). "A Search For the Nucleus of Our Galaxy". In: 58.343, pp. 249–252. DOI: 10.1086/125835.

Babusiaux, C. et al. (Sept. 2010). "Insights on the Milky Way bulge formation from the correlations between kinematics and metallicity". In: 519, A77, A77. DOI: 10.1051/0004-6361/201014353. arXiv: 1005.3919.

Baglin, Annie (Jan. 2003). "COROT: A minisat for pionnier science, asteroseismology and planets finding". In: *Advances in Space Research* 31.2, pp. 345–349. DOI: 10.1016/S0273-1177(02)00624-5.

Barbuy, Beatriz, Cristina Chiappini, and Ortwin Gerhard (Sept. 2018a). "Chemodynamical History of the Galactic Bulge". In: 56, pp. 223–276. DOI: 10.1146/annurev-astro-081817-051826. arXiv: 1805.01142 [astro-ph.GA].

— (Sept. 2018b). "Chemodynamical History of the Galactic Bulge". In: 56, pp. 223–276. DOI: 10.1146/annurev-astro-081817-051826. arXiv: 1805.01142 [astro-ph.GA].

Barklem, P S and B J O'Mara (1997). "The Broadening of P-d and d-p Transitions by Collisions with Neutral Hydrogen Atoms". In: *MNRAS* 290.1, pp. 102–106.

Barklem, P S, B J O'Mara, and J. E. Ross (1998). "The Broadening of D-f and f-d Transitions by Collisions with Neutral Hydrogen Atoms". In: *MNRAS* 296.4, pp. 1057–1060. DOI: 10.1046/j.1365-8711.1998.01484.x.

Barklem, P. S. (2015). *MSWAVEF: Momentum-Space Wavefunctions, https://github.com/barklem/mswavef DOI 10.5281/Zenodo.50218*.

Barnes, A. T. et al. (Aug. 2017). "Star formation rates and efficiencies in the Galactic Centre". In: 469.2, pp. 2263–2285. DOI: 10.1093/mnras/stx941. arXiv: 1704.03572 [astro-ph.GA].

Barnes, Joshua E. and Lars Hernquist (Jan. 1992). "Dynamics of interacting galaxies." In: 30, pp. 705–742. DOI: 10.1146/annurev.aa.30.090192.003421.

Becklin, E. E. and G. Neugebauer (Jan. 1968). "Infrared Observations of the Galactic Center". In: 151, p. 145. DOI: 10.1086/149425.

Bekki, K. (July 2007). "The Formation of Stellar Galactic Nuclei through Dissipative Gas Dynamics". In: 24.2, pp. 77–94. DOI: 10.1071/AS07008.

Bekki, Kenji, Warrick J. Couch, and Yasuhiro Shioya (May 2006). "Dissipative Transformation of Nonnucleated Dwarf Galaxies into Nucleated Systems". In: 642.2, pp. L133–L136. DOI: 10.1086/504588. arXiv: astro-ph/0604340 [astro-ph].

Bell, Eric F. et al. (June 2008). "The Accretion Origin of the Milky Way's Stellar Halo". In: 680.1, pp. 295–311. DOI: 10.1086/588032. arXiv: 0706.0004 [astro-ph].

Belokurov, Vasily and Andrey Kravtsov (July 2022). "From dawn till disc: Milky Way's turbulent youth revealed by the APOGEE+Gaia data". In: 514.1, pp. 689–714. DOI: 10.1093/mnras/stac1267. arXiv: 2203.04980 [astro-ph.GA].

Bensby, T., S. Feltzing, and M. S. Oey (Feb. 2014). "Exploring the Milky Way stellar disk. A detailed elemental abundance study of 714 F and G dwarf stars in the solar neighbourhood". In: 562, A71, A71. DOI: 10.1051/0004-6361/201322631. arXiv: 1309.2631 [astro-ph.GA].

Bensby, T. et al. (Sept. 2011). "Chemical evolution of the Galactic bulge as traced by microlensed dwarf and subgiant stars. IV. Two bulge populations". In: 533, A134, A134. DOI: 10.1051/0004-6361/201117059. arXiv: 1107.5606 [astro-ph.GA].

Bensby, T. et al. (Jan. 2013). "Chemical evolution of the Galactic bulge as traced by microlensed dwarf and subgiant stars. V. Evidence for a wide age distribution and a complex MDF". In: 549, A147, A147. DOI: 10.1051/0004-6361/201220678. arXiv: 1211.6848 [astro-ph.GA].

Bensby, T. et al. (Sept. 2017). "Chemical evolution of the Galactic bulge as traced by microlensed dwarf and subgiant stars. VI. Age and abundance structure of the stellar populations in the central sub-kpc of the Milky Way". In: 605, A89, A89. DOI: 10.1051/0004-6361/201730560. arXiv: 1702.02971 [astro-ph.GA].

Berendzen, Richard (Jan. 1975). "Geocentric to heliocentric to galactocentric to acentric: the continuing assault to the egocentric". In: *Vistas in Astronomy* 17.1, pp. 65–83. DOI: 10.1016/0083-6656(75)90049-5.

Bergin, Edwin A. and Mario Tafalla (Sept. 2007). "Cold Dark Clouds: The Initial Conditions for Star Formation". In: 45.1, pp. 339–396. DOI: 10.1146/annurev.astro.45.071206.100404. arXiv: 0705.3765 [astro-ph].

Binney, J. J. et al. (Jan. 1997). "Dynamical Models of the COBE Bar". In: *IAU Joint Discussion*. Vol. 23. IAU Joint Discussion, 33, p. 33.

Binney, James and Cedric Lacey (Feb. 1988). "The diffusion of stars through phase space". In: 230, pp. 597–627. DOI: 10.1093/mnras/230.4.597.

Binney, James and Scott Tremaine (2008). *Galactic Dynamics: Second Edition*.

Bittner, Adrian et al. (Nov. 2020). "Inside-out formation of nuclear discs and the absence of old central spheroids in barred galaxies of the TIMER survey". In: 643, A65, A65. DOI: 10.1051/0004-6361/202038450. arXiv: 2009.01856 [astro-ph.GA].

Blanco-Cuaresma, Sergi (June 2019). "Modern stellar spectroscopy caveats". In: 486.2, pp. 2075–2101. DOI: 10.1093/mnras/stz549. arXiv: 1902.09558 [astro-ph.SR].

Bland-Hawthorn, Joss and Ortwin Gerhard (Sept. 2016). "The Galaxy in Context: Structural, Kinematic, and Integrated Properties". In: 54, pp. 529–596. DOI: 10.1146/annurev-astro-081915-023441. arXiv: 1602.07702 [astro-ph.GA].

Blitz, Leo and David N. Spergel (Oct. 1991). "Direct Evidence for a Bar at the Galactic Center". In: 379, p. 631. DOI: 10.1086/170535.

Block, D. L. et al. (Nov. 2002). "Gravitational torques in spiral galaxies: Gas accretion as a driving mechanism of galactic evolution". In: 394, pp. L35–L38. DOI: 10.1051/0004-6361:20021379. arXiv: astro-ph/0209406 [astro-ph].

Blum, R. D. et al. (Nov. 2003). "Really Cool Stars and the Star Formation History at the Galactic Center". In: 597.1, pp. 323–346. DOI: 10.1086/378380. arXiv: astro-ph/0307291 [astro-ph].

Böker, Torsten (Jan. 2010). "Nuclear star clusters". In: *Star Clusters: Basic Galactic Building Blocks Throughout Time and Space*. Ed. by Richard de Grijs and Jacques R. D. Lépine. Vol. 266, pp. 58–63. DOI: 10.1017/S1743921309990871. arXiv: 0910.4863 [astro-ph.CO].

Böker, Torsten et al. (Mar. 2002). "A Hubble Space Telescope Census of Nuclear Star Clusters in Late-Type Spiral Galaxies. I. Observations and Image Analysis". In: 123.3, pp. 1389–1410. DOI: 10.1086/339025. arXiv: astro-ph/0112086 [astro-ph].

Borucki, William J. et al. (Feb. 2010). "Kepler Planet-Detection Mission: Introduction and First Results". In: *Science* 327.5968, p. 977. DOI: 10.1126/science.1185402.

Bottema, Roelof (Sept. 2003). "Simulations of normal spiral galaxies". In: 344.2, pp. 358–384. DOI: 10.1046/j.1365-8711.2003.06613.x. arXiv: astro-ph/0303257 [astro-ph].

Bournaud, F. and F. Combes (Sept. 2002). "Gas accretion on spiral galaxies: Bar formation and renewal". In: 392, pp. 83–102. DOI: 10.1051/0004-6361:20020920. arXiv: astro-ph/0206273 [astro-ph].

Bournaud, F., F. Combes, and B. Semelin (Nov. 2005). "The lifetime of galactic bars: central mass concentrations and gravity torques". In: 364.1, pp. L18–L22. DOI: 10.1111/j.1745-3933.2005.00096.x. arXiv: astro-ph/0509126 [astro-ph].

Bovy, Jo (Feb. 2015). "galpy: A python Library for Galactic Dynamics". In: 216.2, 29, p. 29. DOI: 10.1088/0067-0049/216/2/29. arXiv: 1412.3451 [astro-ph.GA].

Brault, J. and R. Noyes (June 1983). "Solar emission lines near 12 microns". In: 269, pp. L61–L66. DOI: 10.1086/184056.

Brink, Jeandrew, Marisa Geyer, and Tanja Hinderer (Apr. 2015). "Astrophysics of resonant orbits in the Kerr metric". In: 91.8, 083001, p. 083001. DOI: 10.1103/PhysRevD.91.083001. arXiv: 1501.07728 [gr-qc].

Brooke, James S. A. et al. (Jan. 2016). "Line strengths of rovibrational and rotational transitions in the $X^2\,\Pi$ ground state of OH". In: 168, pp. 142–157. DOI: 10.1016/j.jqsrt.2015.07.021.

Brown, Gillen, Oleg Y. Gnedin, and Hui Li (Sept. 2018). "Nuclear Star Clusters in Cosmological Simulations". In: 864.1, 94, p. 94. DOI: 10.3847/1538-4357/aad595. arXiv: 1804.09819 [astro-ph.GA].

Buchholz, R. M., R. Schödel, and A. Eckart (May 2009). "Composition of the galactic center star cluster. Population analysis from adaptive optics narrow band spectral energy distributions". In: 499.2, pp. 483–501. DOI: 10.1051/0004-6361/200811497. arXiv: 0903.2135 [astro-ph.GA].

Buder, Sven et al. (Sept. 2021). "The GALAH+ survey: Third data release". In: 506.1, pp. 150–201. DOI: 10.1093/mnras/stab1242. arXiv: 2011.02505 [astro-ph.GA].

Bullock, James S. and Kathryn V. Johnston (Dec. 2005). "Tracing Galaxy Formation with Stellar Halos. I. Methods". In: 635.2, pp. 931–949. DOI: 10.1086/497422. arXiv: astro-ph/0506467 [astro-ph].

Burbidge, E. Margaret and G. R. Burbidge (July 1959). "Three Unusual so Galaxies." In: 130, p. 20. DOI: 10.1086/146691.

Bureau, M. and K. C. Freeman (July 1999). "The Nature of Boxy/Peanut-Shaped Bulges in Spiral Galaxies". In: 118.1, pp. 126–138. DOI: 10.1086/300922. arXiv: astro-ph/9904015 [astro-ph].

Buta, R. and F. Combes (Jan. 1996). "Galactic Rings". In: 17, pp. 95–281.

Caldwell, Nelson et al. (Aug. 1993). "Star Formation in Early-Type Galaxies in the Coma Cluster". In: 106, p. 473. DOI: 10.1086/116656.

Cameron, E. et al. (Nov. 2010). "Bars in early- and late-type discs in COSMOS". In: 409.1, pp. 346–354. DOI: 10.1111/j.1365-2966.2010.17314.x. arXiv: 1001.1736 [astro-ph.CO].

Capuzzo-Dolcetta, Roberto (Oct. 1993). "The Evolution of the Globular Cluster System in a Triaxial Galaxy: Can a Galactic Nucleus Form by Globular Cluster Capture?" In: 415, p. 616. DOI: 10.1086/173189. arXiv: astro-ph/9301006 [astro-ph].

Carpintero, Daniel D. and Luis A. Aguilar (July 1998). "Orbit classification in arbitrary 2D and 3D potentials". In: 298.1, pp. 1–21. DOI: 10.1046/j.1365-8711.1998.01320.x.

Carroll, Bradley W. and Dale A. Ostlie (2017). *An Introduction to Modern Astrophysics*. 2nd ed. Cambridge University Press.

Carson, Daniel J. et al. (May 2015). "The Structure of Nuclear Star Clusters in Nearby Late-type Spiral Galaxies from Hubble Space Telescope Wide Field Camera 3 Imaging". In: 149.5, 170, p. 170. DOI: 10.1088/0004-6256/149/5/170. arXiv: 1501.05586 [astro-ph.GA].

Casagrande, L. et al. (June 2011). "New constraints on the chemical evolution of the solar neighbourhood and Galactic disc(s). Improved astrophysical parameters for the Geneva-Copenhagen Survey". In: 530, A138, A138. DOI: 10.1051/0004-6361/201016276. arXiv: 1103.4651 [astro-ph.GA].

Catchpole, R. M., P. A. Whitelock, and I. S. Glass (Dec. 1990). "The Distribution of Stars Within Two Degrees of the Galactic Centre". In: 247, pp. 479–490.

Cavanagh, M. K. and K. Bekki (Sept. 2020). "Bars formed in galaxy merging and their classification with deep learning". In: 641, A77, A77. DOI: 10.1051/0004-6361/202037963. arXiv: 2006.14847 [astro-ph.GA].

Charbonnel, C. (Feb. 1994). "Clues for non-standard mixing on the red giant branch from 12C/13C and 12C/14N ratios in evolved stars." In: 282, pp. 811–820.

Charbonnel, C. and N. Lagarde (Nov. 2010). "Thermohaline instability and rotation-induced mixing. I. Low- and intermediate-mass solar metallicity stars up to the end of the AGB". In: 522, A10, A10. DOI: 10.1051/0004-6361/201014432. arXiv: 1006.5359 [astro-ph.SR].

Chatzopoulos, S. et al. (Feb. 2015a). "The old nuclear star cluster in the Milky Way: dynamics, mass, statistical parallax, and black hole mass". In: 447.1, pp. 948–968. DOI: 10.1093/mnras/stu2452. arXiv: 1403.5266 [astro-ph.GA].

— (Feb. 2015b). "The old nuclear star cluster in the Milky Way: dynamics, mass, statistical parallax, and black hole mass". In: 447.1, pp. 948–968. DOI: 10.1093/mnras/stu2452. arXiv: 1403.5266 [astro-ph.GA].

Chisholm, John et al. (Aug. 2017). "The mass and momentum outflow rates of photoionized galactic outflows". In: 469.4, pp. 4831–4849. DOI: 10.1093/mnras/stx1164. arXiv: 1702.07351 [astro-ph.GA].

Cimatti, Andrea, Filippo Fraternali, and Carlo Nipoti (2020). *Introduction to galaxy formation and evolution: from primordial gas to present-day galaxies*.

Cirasuolo, M. et al. (July 2014). "MOONS: the Multi-Object Optical and Near-infrared Spectrograph for the VLT". In: *Ground-based and Airborne Instrumentation for Astronomy V*. Ed. by Suzanne K. Ramsay, Ian S. McLean, and Hideki Takami. Vol. 9147. Society of Photo-Optical Instrumentation Engineers (SPIE) Conference Series, 91470N, 91470N. DOI: 10.1117/12.2056012.

Civiš, S. et al. (June 2013). "Infrared transitions and oscillator strengths of Ca and Mg". In: 554, A24, A24. DOI: 10.1051/0004-6361/201321052.

Clarkson, Will et al. (Sept. 2008). "Stellar Proper Motions in the Galactic Bulge from Deep Hubble Space Telescope ACS WFC Photometry". In: 684.2, pp. 1110–1142. DOI: 10.1086/590378. arXiv: 0809.1682 [astro-ph].

Combes, F. et al. (July 1990). "Box and peanut shapes generated by stellar bars." In: 233, p. 82.

Conroy, Charlie et al. (Apr. 2022). "Birth of the Galactic Disk Revealed by the H3 Survey". In: *arXiv e-prints*, arXiv:2204.02989, arXiv:2204.02989. DOI: 10.48550/arXiv.2204.02989. arXiv: 2204.02989 [astro-ph.GA].

Conselice, Christopher J. (Dec. 2006). "The fundamental properties of galaxies and a new galaxy classification system". In: 373.4, pp. 1389–1408. DOI: 10.1111/j.1365-2966.2006.11114.x. arXiv: astro-ph/0610016 [astro-ph].

Contopoulos, G. (Jan. 1980). "How far do bars extend". In: 81.1-2, pp. 198–209.

Contopoulos, G. and P. Grosbol (Nov. 1989). "Orbits in barred galaxies". In: 1.3-4, pp. 261–289. DOI: 10.1007/BF00873080.

Contursi, G. et al. (Feb. 2023). "The cerium content of the Milky Way as revealed by Gaia DR3 GSP-Spec abundances". In: 670, A106, A106. DOI: 10.1051/0004-6361/202244469. arXiv: 2207.05368 [astro-ph.GA].

Contursi, G. et al. (Mar. 2024). "Production of s-process elements in asymptotic giant branch stars as revealed by Gaia/GSP-Spec abundances". In: 683, A138, A138. DOI: 10.1051/0004-6361/202347188.

Crocker, R. M. et al. (May 2011). "Wild at Heart: the particle astrophysics of the Galactic Centre". In: 413.2, pp. 763–788. DOI: 10.1111/j.1365-2966.2010.18170.x. arXiv: 1011.0206 [astro-ph.GA].

de los Rios, Martín et al. (Jan. 2021). "ROGER: Reconstructing orbits of galaxies in extreme regions using machine learning techniques". In: 500.2, pp. 1784–1794. DOI: 10.1093/mnras/staa3339. arXiv: 2010.11959 [astro-ph.GA].

de Sá-Freitas, Camila et al. (Mar. 2023a). "A new method for age-dating the formation of bars in disc galaxies. The TIMER view on NGC1433's old bar and the inside-out growth of its nuclear disc". In: 671, A8, A8. DOI: 10.1051/0004-6361/202244667. arXiv: 2211.07670 [astro-ph.GA].

— (Mar. 2023b). "A new method for age-dating the formation of bars in disc galaxies. The TIMER view on NGC1433's old bar and the inside-out growth of its nuclear disc". In: 671, A8, A8. DOI: 10.1051/0004-6361/202244667. arXiv: 2211.07670 [astro-ph.GA].

de Sá-Freitas, Camila et al. (Oct. 2023c). "Disc galaxies are still settling. Discovery of the smallest nuclear discs and their young stellar bars". In: 678, A202, A202. DOI: 10.1051/0004-6361/202347028. arXiv: 2308.04482 [astro-ph.GA].

de Souza, R. E. and S. Dos Anjos (Sept. 1987). "Box-shaped galaxies : a complete list." In: 70, pp. 465–480.

de Vaucouleurs, Gerard Henri, Antoinette de Vaucouleurs, and Harlow Shapley (1964). *Reference catalogue of bright galaxies*.

de Zeeuw, P. T. et al. (Jan. 2002). "The SAURON project - II. Sample and early results". In: 329.3, pp. 513–530. DOI: 10.1046/j.1365-8711.2002.05059.x. arXiv: astro-ph/0109511 [astro-ph].

Debattista, Victor P. and J. A. Sellwood (Nov. 2000). "Constraints from Dynamical Friction on the Dark Matter Content of Barred Galaxies". In: 543.2, pp. 704–721. DOI: 10.1086/317148. arXiv: astro-ph/0006275 [astro-ph].

Debattista, Victor P. et al. (Aug. 2005). "The Kinematic Signature of Face-On Peanut-shaped Bulges". In: 628.2, pp. 678–694. DOI: 10.1086/431292. arXiv: astro-ph/0504530 [astro-ph].

Dékány, I. et al. (Oct. 2013). "VVV Survey Near-infrared Photometry of Known Bulge RR Lyrae Stars: The Distance to the Galactic Center and Absence of a Barred Distribution of the Metal-poor Population". In: 776.2, L19, p. L19. DOI: 10.1088/2041-8205/776/2/L19. arXiv: 1309.5933 [astro-ph.GA].

Dimitrijevic, M. S. and S Sahal-Bréchot (1996). "Stark Broadening of Solar MG I Lines." In: *A&AS* 117, pp. 127–129.

Dobbs, C. L. et al. (Apr. 2010). "Simulations of the grand design galaxy M51: a case study for analysing tidally induced spiral structure". In: 403.2, pp. 625–645. DOI: 10.1111/j.1365-2966.2009.16161.x. arXiv: 0912.1201 [astro-ph.GA].

Dong, H. et al. (Oct. 2011). "Hubble Space Telescope Paschen α survey of the Galactic Centre: data reduction and products". In: 417.1, pp. 114–135. DOI: 10.1111/j.1365-2966.2011.19013.x. arXiv: 1105.1703 [astro-ph.GA].

Drory, Niv and David B. Fisher (Aug. 2007). "A Connection between Bulge Properties and the Bimodality of Galaxies". In: 664.2, pp. 640–649. DOI: 10.1086/519441. arXiv: 0705.0973 [astro-ph].

Dumas, Gaëlle et al. (Aug. 2007). "Central kiloparsec of Seyfert and inactive host galaxies: a comparison of two-dimensional stellar and gaseous kinematics". In: 379.4, pp. 1249–1278. DOI: 10.1111/j.1365-2966.2007.12014.x. arXiv: 0705.4162 [astro-ph].

Dwek, E. et al. (June 1995). "Morphology, Near-Infrared Luminosity, and Mass of the Galactic Bulge from COBE DIRBE Observations". In: 445, p. 716. DOI: 10.1086/175734.

Edvardsson, B. et al. (Aug. 1993). "The Chemical Evolution of the Galactic Disk - Part One - Analysis and Results". In: 275, p. 101.

Ellison, Sara L. et al. (Sept. 2011). "The impact of gas inflows on star formation rates and metallicities in barred galaxies". In: 416.3, pp. 2182–2192. DOI: 10.1111/j.1365-2966.2011.19195.x. arXiv: 1106.1177 [astro-ph.CO].

Elmegreen, B. G. and D. M. Elmegreen (Jan. 1985). "Properties of barred spiral galaxies." In: 288, pp. 438–455. DOI: 10.1086/162810.

Elmegreen, Bruce G., Emmanuel Galliano, and Danielle Alloin (Oct. 2009). "Massive Clusters in the Inner Regions of NGC 1365: Cluster Formation and Gas Dynamics in Galactic Bars". In: 703.2, pp. 1297–1307. DOI: 10.1088/0004-637X/703/2/1297. arXiv: 0907.2602 [astro-ph.GA].

Emsellem, Eric and Glenn van de Ven (Feb. 2008). "Formation of Central Massive Objects via Tidal Compression". In: 674.2, pp. 653–659. DOI: 10.1086/524720. arXiv: 0710.3161 [astro-ph].

Emsellem, Eric et al. (Aug. 2004). "The SAURON project - III. Integral-field absorption-line kinematics of 48 elliptical and lenticular galaxies". In: 352.3, pp. 721–743. DOI: 10.1111/j.1365-2966.2004.07948.x. arXiv: astro-ph/0404034 [astro-ph].

Englmaier, Peter and Ortwin Gerhard (Apr. 1999). "Gas dynamics and large-scale morphology of the Milky Way galaxy". In: 304.3, pp. 512–534. DOI: 10.1046/j.1365-8711.1999.02280.x. arXiv: astro-ph/9810208 [astro-ph].

Erwin, Peter and Victor P. Debattista (June 2013). "Peanuts at an angle: detecting and measuring the three-dimensional structure of bars in moderately inclined galaxies". In: 431.4, pp. 3060–3086. DOI: 10.1093/mnras/stt385. arXiv: 1301.0638 [astro-ph.CO].

Erwin, Peter et al. (Feb. 2015). "Composite bulges: the coexistence of classical bulges and discy pseudo-bulges in S0 and spiral galaxies". In: 446.4, pp. 4039–4077. DOI: 10.1093/mnras/stu2376. arXiv: 1411.2599 [astro-ph.GA].

Feldmeier, A. et al. (Oct. 2014). "Large scale kinematics and dynamical modelling of the Milky Way nuclear star cluster". In: 570, A2, A2. DOI: 10.1051/0004-6361/201423777. arXiv: 1406.2849 [astro-ph.GA].

Feldmeier-Krause, A. (July 2022). "Stellar populations in the transition region of nuclear star cluster and nuclear stellar disc". In: 513.4, pp. 5920–5934. DOI: 10.1093/mnras/stac1227. arXiv: 2204.13723 [astro-ph.GA].

Feldmeier-Krause, A. et al. (Dec. 2015). "KMOS view of the Galactic centre. I. Young stars are centrally concentrated". In: 584, A2, A2. DOI: 10.1051/0004-6361/201526336. arXiv: 1509.04707 [astro-ph.GA].

Feldmeier-Krause, A. et al. (Jan. 2017a). "KMOS view of the Galactic Centre - II. Metallicity distribution of late-type stars". In: 464.1, pp. 194–209. DOI: 10.1093/mnras/stw2339. arXiv: 1610.01623 [astro-ph.GA].

Feldmeier-Krause, A. et al. (Apr. 2017b). "Triaxial orbit-based modelling of the Milky Way Nuclear Star Cluster". In: 466.4, pp. 4040–4052. DOI: 10.1093/mnras/stw3377. arXiv: 1701.01583 [astro-ph.GA].

— (Apr. 2017c). "Triaxial orbit-based modelling of the Milky Way Nuclear Star Cluster". In: 466.4, pp. 4040–4052. DOI: 10.1093/mnras/stw3377. arXiv: 1701.01583 [astro-ph.GA].

Feldmeier-Krause, A. et al. (Mar. 2020). "Asymmetric spatial distribution of sub-solar metallicity stars in the Milky Way nuclear star cluster". In: DOI: 10.1093/mnras/staa703. arXiv: 2003.05998 [astro-ph.GA].

Ferreras, Ignacio, Rosemary F. G. Wyse, and Joseph Silk (Nov. 2003). "The formation history of the Galactic bulge". In: 345.4, pp. 1381–1391. DOI: 10.1046/j.1365-2966.2003.07056.x. arXiv: astro-ph/0308165 [astro-ph].

Figer, Donald F. et al. (Jan. 2004). "An Extended Star Formation History for the Galactic Center from Hubble Space Telescope NICMOS Observations". In: 601.1, pp. 319–339. DOI: 10.1086/380392. arXiv: astro-ph/0309757 [astro-ph].

Fisher, David B. and Niv Drory (June 2011). "Demographics of Bulge Types within 11 Mpc and Implications for Galaxy Evolution". In: 733.2, L47, p. L47. DOI: 10.1088/2041-8205/733/2/L47. arXiv: 1104.0020 [astro-ph.CO].

Forsberg, R. et al. (Nov. 2019). "Abundances of disk and bulge giants from high-resolution optical spectra. IV. Zr, La, Ce, Eu". In: 631, A113, A113. DOI: 10.1051/0004-6361/201936343. arXiv: 1909.10535 [astro-ph.GA].

Forsberg, R. et al. (Jan. 2023). "First r-process enhanced star confirmed as a member of the Galactic bulge". In: 669, A17, A17. DOI: 10.1051/0004-6361/202244305. arXiv: 2210.05688 [astro-ph.SR].

Fragkoudi, F., E. Athanassoula, and A. Bosma (Oct. 2016). "A close look at secular evolution: boxy/peanut bulges reduce gas inflow to the central kiloparsec". In: 462.1, pp. L41–L45. DOI: 10.1093/mnrasl/slw120. arXiv: 1606.04540 [astro-ph.GA].

— (Apr. 2017). "Constraining the dark matter content of NGC 1291 using hydrodynamic gas response simulations". In: 466.1, pp. 474–488. DOI: 10.1093/mnras/stw3023. arXiv: 1611.09386 [astro-ph.GA].

Friedli, D. and W. Benz (Feb. 1993). "Secular evolution of isolated barred galaxies. I. Gravitational coupling between stellar bars and interstellar medium." In: 268, pp. 65–85.

Friske, Jennifer K S and Ralph Schönrich (Oct. 2023). "Chemical Evolution in Galactic Nuclear Discs". In: *arXiv e-prints*, arXiv:2310.01899, arXiv:2310.01899. DOI: 10.48550/arXiv.2310.01899. arXiv: 2310.01899 [astro-ph.GA].

Fritz, T. K. et al. (Apr. 2016). "The Nuclear Cluster of the Milky Way: Total Mass and Luminosity". In: 821.1, 44, p. 44. DOI: 10.3847/0004-637X/821/1/44. arXiv: 1406.7568 [astro-ph.GA].

Fritz, T. K. et al. (May 2021). "A KMOS survey of the nuclear disk of the Milky Way. I. Survey design and metallicities". In: 649, A83, A83. DOI: 10.1051/0004-6361/202040026. arXiv: 2012.00918 [astro-ph.GA].

Fulbright, Jon. P., Andrew McWilliam, and R. Michael Rich (June 2007). "Abundances of Baade's Window Giants from Keck HIRES Spectra. II. The Alpha and Light Odd Elements". In: 661.2, pp. 1152–1179. DOI: 10.1086/513710. arXiv: astro-ph/0609087 [astro-ph].

Gadotti, Dimitri A. et al. (Jan. 2019a). "Time Inference with MUSE in Extragalactic Rings (TIMER): properties of the survey and high-level data products". In: 482.1, pp. 506–529. DOI: 10.1093/mnras/sty2666. arXiv: 1810.01425 [astro-ph.GA].

— (Jan. 2019b). "Time Inference with MUSE in Extragalactic Rings (TIMER): properties of the survey and high-level data products". In: 482.1, pp. 506–529. DOI: 10.1093/mnras/sty2666. arXiv: 1810.01425 [astro-ph.GA].

Gadotti, Dimitri A. et al. (Nov. 2020). "Kinematic signatures of nuclear discs and bar-driven secular evolution in nearby galaxies of the MUSE TIMER project". In: 643, A14, A14. DOI: 10.1051/0004-6361/202038448. arXiv: 2009.01852 [astro-ph.GA].

Gaia Collaboration et al. (Nov. 2016a). "The Gaia mission". In: 595, A1, A1. DOI: 10.1051/0004-6361/201629272. arXiv: 1609.04153 [astro-ph.IM].

— (Nov. 2016b). "The Gaia mission". In: 595, A1, A1. DOI: 10.1051/0004-6361/201629272. arXiv: 1609.04153 [astro-ph.IM].

Gaia Collaboration et al. (June 2021). "Gaia Early Data Release 3. Summary of the contents and survey properties (Corrigendum)". In: 650, C3, p. C3. DOI: 10.1051/0004-6361/202039657e.

Gallego-Cano, E. et al. (Feb. 2020a). "New constraints on the structure of the nuclear stellar cluster of the Milky Way from star counts and MIR imaging". In: 634, A71, A71. DOI: 10.1051/0004-6361/201935303. arXiv: 2001.08182 [astro-ph.GA].

— (Feb. 2020b). "New constraints on the structure of the nuclear stellar cluster of the Milky Way from star counts and MIR imaging". In: 634, A71, A71. DOI: 10.1051/0004-6361/201935303. arXiv: 2001.08182 [astro-ph.GA].

Genzel, R. and C. H. Townes (Jan. 1987). "Physical conditions, dynamics, and mass distribution in the center of the galaxy." In: 25, pp. 377–423. DOI: 10.1146/annurev.aa.25.090187.002113.

Genzel, R. et al. (Nov. 1996). "The Dark Mass Concentration in the Central Parsec of the Milky Way". In: 472, p. 153. DOI: 10.1086/178051.

Genzel, Reinhard, Frank Eisenhauer, and Stefan Gillessen (Oct. 2010). "The Galactic Center massive black hole and nuclear star cluster". In: *Reviews of Modern Physics* 82.4, pp. 3121–3195. DOI: 10.1103/RevModPhys.82.3121. arXiv: 1006.0064 [astro-ph.GA].

Gillessen, S. et al. (Dec. 2009). "The Orbit of the Star S2 Around SGR A* from Very Large Telescope and Keck Data". In: 707.2, pp. L114–L117. DOI: 10.1088/0004-637X/707/2/L114. arXiv: 0910.3069 [astro-ph.GA].

Gilmore, G. and N. Reid (Mar. 1983). "New light on faint stars - III. Galactic structure towards the South Pole and the Galactic thick disc." In: 202, pp. 1025–1047. DOI: 10.1093/mnras/202.4.1025.

Gilmore, G. et al. (Mar. 2012). "The Gaia-ESO Public Spectroscopic Survey". In: *The Messenger* 147, pp. 25–31.

Gilroy, Kalpana Krishnaswamy (Dec. 1989). "Carbon Isotope Ratios and Lithium Abundances in Open Cluster Giants". In: 347, p. 835. DOI: 10.1086/168173.

Gnedin, Oleg Y., Jeremiah P. Ostriker, and Scott Tremaine (Apr. 2014). "Co-evolution of Galactic Nuclei and Globular Cluster Systems". In: 785.1, 71, p. 71. DOI: 10.1088/0004-637X/785/1/71. arXiv: 1308.0021 [astro-ph.CO].

Gonzalez, O. A. et al. (June 2011). "Alpha element abundances and gradients in the Milky Way bulge from FLAMES-GIRAFFE spectra of 650 K giants". In: 530, A54, A54. DOI: 10.1051/0004-6361/201116548. arXiv: 1103.6104 [astro-ph.GA].

Gonzalez, O. A. et al. (July 2012). "Reddening and metallicity maps of the Milky Way bulge from VVV and 2MASS. II. The complete high resolution extinction map and implications for Galactic bulge studies". In: 543, A13, A13. DOI: 10.1051/0004-6361/201219222. arXiv: 1204.4004 [astro-ph.GA].

Gonzalez, O. A. et al. (June 2020). "MOONS Surveys of the Milky Way and its Satellites". In: *The Messenger* 180, pp. 18–23. DOI: 10.18727/0722-6691/5196. arXiv: 2009.00635 [astro-ph.GA].

Gordon, David, Aletha de Witt, and Christopher S. Jacobs (Feb. 2023). "Position and Proper Motion of Sagittarius A* in the ICRF3 Frame from VLBI Absolute Astrometry". In: 165.2, 49, p. 49. DOI: 10.3847/1538-3881/aca65b. arXiv: 2212.00632 [astro-ph.GA].

Graham, Alister W. (Feb. 2001). "An Investigation into the Prominence of Spiral Galaxy Bulges". In: 121.2, pp. 820–840. DOI: 10.1086/318767. arXiv: astro-ph/0011256 [astro-ph].

Gran, F. et al. (July 2016). "Mapping the outer bulge with RRab stars from the VVV Survey". In: 591, A145, A145. DOI: 10.1051/0004-6361/201527511. arXiv: 1604.01336 [astro-ph.GA].

GRAVITY Collaboration et al. (Apr. 2020). "Detection of the Schwarzschild precession in the orbit of the star S2 near the Galactic centre massive black hole". In: 636, L5, p. L5. DOI: 10.1051/0004-6361/202037813. arXiv: 2004.07187 [astro-ph.GA].

Grevesse, N., M. Asplund, and A. J. Sauval (June 2007a). "The Solar Chemical Composition". In: 130.1-4, pp. 105–114. DOI: 10.1007/s11214-007-9173-7.

— (June 2007b). "The Solar Chemical Composition". In: 130.1-4, pp. 105–114. DOI: 10.1007/s11214-007-9173-7.

Grieco, V. et al. (Dec. 2012). "Chemical evolution of the Galactic bulge: different stellar populations and possible gradients". In: 548, A60, A60. DOI: 10.1051/0004-6361/201219761. arXiv: 1209.4462 [astro-ph.GA].

Grieco, V. et al. (June 2015). "Chemical evolution of the Galactic Centre". In: 450, pp. 2094–2103. DOI: 10.1093/mnras/stv729. arXiv: 1503.08949.

Gully-Santiago, Michael et al. (Sept. 2012a). "Near-infrared metrology of high-performance silicon immersion gratings". In: *Modern Technologies in Space- and Ground-based Telescopes and Instrumentation II*. Ed. by Ramón Navarro, Colin R. Cunningham, and Eric Prieto. Vol. 8450. Society of Photo-Optical Instrumentation Engineers (SPIE) Conference Series, 84502S, 84502S. DOI: 10.1117/12.926434.

Gully-Santiago, Michael et al. (Sept. 2012b). "Near-infrared metrology of high-performance silicon immersion gratings". In: *Modern Technologies in Space- and Ground-based Telescopes and Instrumentation II*. Ed. by Ramón Navarro, Colin R. Cunningham, and Eric Prieto. Vol. 8450. Society of Photo-Optical Instrumentation Engineers (SPIE) Conference Series, 84502S, 84502S. DOI: 10.1117/12.926434.

Gustafsson, B., B. Edvardsson, K. Eriksson, et al. (Aug. 2008a). "A grid of MARCS model atmospheres for late-type stars. I. Methods and general properties". In: 486, p. 951. eprint: arXiv:0805.0554.

Gustafsson, B. et al. (Aug. 2008b). "A grid of MARCS model atmospheres for late-type stars. I. Methods and general properties". In: 486.3, pp. 951–970. DOI: 10.1051/0004-6361:200809724. arXiv: 0805.0554 [astro-ph].

Hammer, F. et al. (Jan. 2005). "Did most present-day spirals form during the last 8 Gyr?. A formation history with violent episodes revealed by panchromatic observations". In: 430, pp. 115–128. DOI: 10.1051/0004-6361:20041471. arXiv: astro-ph/0410518 [astro-ph].

Hammersley, P. L. et al. (Aug. 1994). "Infrared signatures of the inner spiral arms and bar." In: 269, pp. 753–763. DOI: 10.1093/mnras/269.3.753.

Hasan, Hashima and Colin Norman (Sept. 1990). "Chaotic Orbits in Barred Galaxies with Central Mass Concentrations". In: 361, p. 69. DOI: 10.1086/169168.

Hasan, Hashima, Daniel Pfenniger, and Colin Norman (May 1993). "Galactic Bars with Central Mass Concentrations: Three-dimensional Dynamics". In: 409, p. 91. DOI: 10.1086/172644.

Hatchfield, H. Perry et al. (Nov. 2021). "Dynamically Driven Inflow onto the Galactic Center and its Effect upon Molecular Clouds". In: 922.1, 79, p. 79. DOI: 10.3847/1538-4357/ac1e89. arXiv: 2106.08461 [astro-ph.GA].

Haynes, M. P. and R. Giovanelli (July 1986). "The Pattern of H i Deficiency in the Virgo Cluster". In: 306, p. 466. DOI: 10.1086/164357.

Haywood, M. et al. (Sept. 2016). "Hiding its age: the case for a younger bulge". In: 593, A82, A82. DOI: 10.1051/0004-6361/201628816. arXiv: 1606.04092 [astro-ph.GA].

Haywood, M. et al. (Aug. 2018). "In Disguise or Out of Reach: First Clues about In Situ and Accreted Stars in the Stellar Halo of the Milky Way from Gaia DR2". In: 863.2, 113, p. 113. DOI: 10.3847/1538-4357/aad235.

Haywood, Misha et al. (Dec. 2013). "The age structure of stellar populations in the solar vicinity. Clues of a two-phase formation history of the Milky Way disk". In: 560, A109, A109. DOI: 10.1051/0004-6361/201321397. arXiv: 1305.4663 [astro-ph.GA].

Helmi, Amina (June 2008). "The stellar halo of the Galaxy". In: 15.3, pp. 145–188. DOI: 10.1007/s00159-008-0009-6. arXiv: 0804.0019 [astro-ph].

Helmi, Amina et al. (Oct. 2018). "The merger that led to the formation of the Milky Way's inner stellar halo and thick disk". In: 563.7729, pp. 85–88. DOI: 10.1038/s41586-018-0625-x. arXiv: 1806.06038 [astro-ph.GA].

Henshaw, J. D. et al. (Apr. 2016). "Molecular gas kinematics within the central 250 pc of the Milky Way". In: 457.3, pp. 2675–2702. DOI: 10.1093/mnras/stw121. arXiv: 1601.03732 [astro-ph.GA].

Henshaw, J. D. et al. (July 2023). "Star Formation in the Central Molecular Zone of the Milky Way". In: *Protostars and Planets VII*. Ed. by S. Inutsuka et al. Vol. 534. Astronomical Society of the Pacific Conference Series, p. 83. DOI: 10.48550/arXiv.2203.11223. arXiv: 2203.11223 [astro-ph.GA].

Hill, V. et al. (Oct. 2011). "The metallicity distribution of bulge clump giants in Baade's window". In: 534, A80, A80. DOI: 10.1051/0004-6361/200913757. arXiv: 1107.5199 [astro-ph.GA].

Hinkle, Kenneth, Lloyd Wallace, and William Livingston (Nov. 1995). "Infrared Atlas of the Arcturus Spectrum, 0.9-5.3 microns". In: 107, p. 1042. DOI: 10.1086/133660.

Hoang Binh, D. and Henri van Regemorter (1995). "The Impulse Approximation for the Broadening of Mg I Infrared Lines by Collisions with Neutral Hydrogen". In: *J. Phys. B: At. Mol. Opt. Phys.* 28.1, pp. 3147–3161. DOI: 10.1088/0953-4075/28/15/009.

— (1997). "Non-Hydrogenic Wavefunctions in Momentum Space". In: *J. Phys. B: At. Mol. Opt. Phys.* 30.1, pp. 2403–2416. DOI: 10.1088/0953-4075/30/10/014.

Howell, Steve B. et al. (Apr. 2014). "The K2 Mission: Characterization and Early Results". In: 126.938, p. 398. DOI: 10.1086/676406. arXiv: 1402.5163 [astro-ph.IM].

Hubble, E. P. (Dec. 1926). "Extragalactic nebulae." In: 64, pp. 321–369. DOI: 10.1086/143018.

Iben Icko, Jr. (Nov. 1965). "Stellar Evolution. II. The Evolution of a 3 M_{sun} Star from the Main Sequence Through Core Helium Burning." In: 142, p. 1447. DOI: 10.1086/148429.

Jenkins, A. and J. Binney (Oct. 1994). "Dynamics of gas near the Galactic Centre." In: 270, pp. 703–719. DOI: 10.1093/mnras/270.3.703.

Jeong, Ueejeong et al. (July 2014). "Characterization and optimization for detector systems of IGRINS". In: *High Energy, Optical, and Infrared Detectors for Astronomy VI*. Ed. by Andrew D. Holland and James Beletic. Vol. 9154. Society of Photo-Optical Instrumentation Engineers (SPIE) Conference Series, 91541X, p. 91541X. DOI: 10.1117/12.2055589.

Johnson, Christian I. et al. (Mar. 2013). "Metallicity Distribution Functions, Radial Velocities, and Alpha Element Abundances in Three Off-axis Bulge Fields". In: 765.2, 157, p. 157. DOI: 10.1088/0004-637X/765/2/157. arXiv: 1302.3679 [astro-ph.SR].

Johnson, Christian I. et al. (Oct. 2014). "Light, Alpha, and Fe-peak Element Abundances in the Galactic Bulge". In: 148.4, 67, p. 67. DOI: 10.1088/0004-6256/148/4/67. arXiv: 1407.2282 [astro-ph.SR].

Johnson, Christian I. et al. (Dec. 2020). "Blanco DECam Bulge Survey (BDBS) II: project performance, data analysis, and early science results". In: 499.2, pp. 2357–2379. DOI: 10.1093/mnras/staa2393. arXiv: 2008.09257 [astro-ph.GA].

Johnson, Christian I. et al. (Sept. 2022). "Blanco DECam Bulge Survey (BDBS) IV: Metallicity distributions and bulge structure from 2.6 million red clump stars". In: 515.1, pp. 1469–1491. DOI: 10.1093/mnras/stac1840. arXiv: 2206.14851 [astro-ph.GA].

Jönsson, H. et al. (Feb. 2017a). "Abundances of disk and bulge giants from high-resolution optical spectra. I. O, Mg, Ca, and Ti in the solar neighborhood and Kepler field samples". In: 598, A100, A100. DOI: 10.1051/0004-6361/201629128. arXiv: 1611.05462 [astro-ph.GA].

Jönsson, H. et al. (Feb. 2017b). "Abundances of disk and bulge giants from high-resolution optical spectra. I. O, Mg, Ca, and Ti in the solar neighborhood and Kepler field samples". In: 598, A100, A100. DOI: 10.1051/0004-6361/201629128. arXiv: 1611.05462 [astro-ph.GA].

Jönsson, Henrik et al. (Sept. 2018). "APOGEE Data Releases 13 and 14: Stellar Parameter and Abundance Comparisons with Independent Analyses". In: 156.3, 126, p. 126. DOI: 10.3847/1538-3881/aad4f5. arXiv: 1807.09784 [astro-ph.SR].

Kacharov, Nikolay et al. (Oct. 2018). "Stellar populations and star formation histories of the nuclear star clusters in six nearby galaxies". In: 480.2, pp. 1973–1998. DOI: 10.1093/mnras/sty1985. arXiv: 1807.08765 [astro-ph.GA].

Kaeufl, Hans-Ulrich et al. (Sept. 2004). "CRIRES: a high-resolution infrared spectrograph for ESO's VLT". In: *Ground-based Instrumentation for Astronomy*. Ed. by Alan F. M. Moorwood and Masanori Iye. Vol. 5492. Society of Photo-Optical Instrumentation Engineers (SPIE) Conference Series, pp. 1218–1227. DOI: 10.1117/12.551480.

Karakas, Amanda I. and John C. Lattanzio (July 2014). "The Dawes Review 2: Nucleosynthesis and Stellar Yields of Low- and Intermediate-Mass Single Stars". In: 31, e030, e030. DOI: 10.1017/pasa.2014.21. arXiv: 1405.0062 [astro-ph.SR].

Käufl, H. U. et al. (Dec. 2006). "Good Vibrations: Report from the Commissioning of CRIRES". In: *The Messenger* 126, pp. 32–36.

Kaulakys, B. (1985). "Analytical Expressions for Cross Sections of Rydberg-neutral Inelastic Collisions". In: *J. Phys. B: At. Mol. Phys.* 18.6, pp. L167–L170. DOI: 10.1088/0022-3700/18/6/004.

— (1991). "Free Electron Model for Collisional Angular Momentum Mixing of High Rydberg Atoms". In: *J. Phys. B: At. Mol. Phys.* 24.5, pp. L127–L132. DOI: 10.1088/0953-4075/24/5/004.

Kennicutt Jr., R. C. (May 1998). "The Global Schmidt Law in Star-forming Galaxies". In: 498, pp. 541–552. DOI: 10.1086/305588. eprint: astro-ph/9712213.

Kennicutt, Robert C. and Neal J. Evans (Sept. 2012). "Star Formation in the Milky Way and Nearby Galaxies". In: 50, pp. 531–608. DOI: 10.1146/annurev-astro-081811-125610. arXiv: 1204.3552 [astro-ph.GA].

Kim, Woong-Tae et al. (Mar. 2012). "Central Regions of Barred Galaxies: Two-dimensional Non-self-gravitating Hydrodynamic Simulations". In: 747.1, 60, p. 60. DOI: 10.1088/0004-637X/747/1/60. arXiv: 1112.6055 [astro-ph.GA].

Klypin, Anatoly et al. (Sept. 1999). "Where Are the Missing Galactic Satellites?" In: 522.1, pp. 82–92. DOI: 10.1086/307643. arXiv: astro-ph/9901240 [astro-ph].

Koleva, M. et al. (Dec. 2009). "Metallicity gradients: Mass dependency in dwarf elliptical galaxies". In: *Astronomische Nachrichten* 330, p. 960. DOI: 10.1002/asna.200911272. arXiv: 0910.2643 [astro-ph.CO].

Koppelman, Helmer H., Jorrit H. J. Hagen, and Amina Helmi (Mar. 2021). "Frequencies, chaos, and resonances: A study of orbital parameters of nearby thick-disc and halo stars". In: 647, A37, A37. DOI: 10.1051/0004-6361/202039390.

Kordopatis, G. et al. (Jan. 2023). "Stellar ages, masses, extinctions, and orbital parameters based on spectroscopic parameters of Gaia DR3". In: 669, A104, A104. DOI: 10.1051/0004-6361/202244283. arXiv: 2206.07937 [astro-ph.GA].

Kormendy, J. (Jan. 1993). "Kinematics of extragalactic bulges: evidence that some bulges are really disks". In: *Galactic Bulges*. Ed. by Herwig Dejonghe and Harm Jan Habing. Vol. 153, p. 209.

Kormendy, John and Jr. Kennicutt Robert C. (Sept. 2004a). "Secular Evolution and the Formation of Pseudobulges in Disk Galaxies". In: 42.1, pp. 603–683. DOI: 10.1146/annurev.astro.42.053102.134024. arXiv: astro-ph/0407343 [astro-ph].

— (Sept. 2004b). "Secular Evolution and the Formation of Pseudobulges in Disk Galaxies". In: 42.1, pp. 603–683. DOI: 10.1146/annurev.astro.42.053102.134024. arXiv: astro-ph/0407343 [astro-ph].

Kormendy, John et al. (July 2001). "The Nuclear Disk in the Dwarf Elliptical Galaxy NGC 4486A". In: *arXiv e-prints*, astro-ph/0107218, astro–ph/0107218. DOI: 10.48550/arXiv.astro-ph/0107218. arXiv: astro-ph/0107218 [astro-ph].

Krajnović, Davor et al. (Oct. 2008). "The SAURON project - XII. Kinematic substructures in early-type galaxies: evidence for discs in fast rotators". In: 390.1, pp. 93–117. DOI: 10.1111/j.1365-2966.2008.13712.x. arXiv: 0807.1505 [astro-ph].

Kraljic, Katarina, Frédéric Bournaud, and Marie Martig (Sept. 2012). "The Two-phase Formation History of Spiral Galaxies Traced by the Cosmic Evolution of the Bar Fraction". In: 757.1, 60, p. 60. DOI: 10.1088/0004-637X/757/1/60. arXiv: 1207.0351 [astro-ph.GA].

Kroupa, Pavel, Christopher A. Tout, and Gerard Gilmore (June 1993). "The Distribution of Low-Mass Stars in the Galactic Disc". In: 262, pp. 545–587. DOI: 10.1093/mnras/262.3.545.

Kruijssen, J. M. Diederik et al. (June 2014). "What controls star formation in the central 500 pc of the Galaxy?" In: 440.4, pp. 3370–3391. DOI: 10.1093/mnras/stu494. arXiv: 1303.6286 [astro-ph.GA].

Kubryk, M., N. Prantzos, and E. Athanassoula (Dec. 2013). "Radial migration in a bar-dominated disc galaxy - I. Impact on chemical evolution". In: 436.2, pp. 1479–1491. DOI: 10.1093/mnras/stt1667.

— (Aug. 2015a). "Evolution of the Milky Way with radial motions of stars and gas. I. The solar neighbourhood and the thin and thick disks". In: 580, A126, A126. DOI: 10.1051/0004-6361/201424171. arXiv: 1412.0585 [astro-ph.GA].

— (Aug. 2015b). "Evolution of the Milky Way with radial motions of stars and gas. II. The evolution of abundance profiles from H to Ni". In: 580, A127, A127. DOI: 10.1051/0004-6361/201424599. arXiv: 1412.4859 [astro-ph.GA].

Kuijken, Konrad and Michael R. Merrifield (Apr. 1995). "Establishing the Connection between Peanut-shaped Bulges and Galactic Bars". In: 443, p. L13. DOI: 10.1086/187824. arXiv: astro-ph/9501114 [astro-ph].

Kurucz, R. L. (2007). *Robert L. Kurucz on-line database of observed and predicted atomic transitions*.

— (2014). *Robert L. Kurucz on-line database of observed and predicted atomic transitions*.

Lagarde, N. et al. (July 2012). "Thermohaline instability and rotation-induced mixing. III. Grid of stellar models and asymptotic asteroseismic quantities from the pre-main sequence up to the AGB for low- and intermediate-mass stars of various metallicities". In: 543, A108, A108. DOI: 10.1051/0004-6361/201118331. arXiv: 1204.5193 [astro-ph.SR].

Larson, R. B. (July 1976). "Models for the formation of disc galaxies." In: 176, pp. 31–52. DOI: 10.1093/mnras/176.1.31.

Larson, Richard B. (Mar. 1974). "Dynamical models for the formation and evolution of spherical galaxies". In: 166, pp. 585–616. DOI: 10.1093/mnras/166.3.585.

Laskar, Jacques (May 1993). "Frequency Analysis of a Dynamical System". In: *Celestial Mechanics and Dynamical Astronomy* 56.1-2, pp. 191–196. DOI: 10.1007/BF00699731.

Launhardt, R., R. Zylka, and P. G. Mezger (Mar. 2002a). "The nuclear bulge of the Galaxy. III. Large-scale physical characteristics of stars and interstellar matter". In: 384, pp. 112–139. DOI: 10.1051/0004-6361:20020017. arXiv: astro-ph/0201294 [astro-ph].

— (Mar. 2002b). "The nuclear bulge of the Galaxy. III. Large-scale physical characteristics of stars and interstellar matter". In: 384, pp. 112–139. DOI: 10.1051/0004-6361:20020017. arXiv: astro-ph/0201294 [astro-ph].

Lebzelter, T. et al. (June 2015). "Oxygen isotopic ratios in intermediate-mass red giants". In: 578, A33, A33. DOI: 10.1051/0004-6361/201525832. arXiv: 1504.05377 [astro-ph.SR].

Lecureur, A. et al. (Apr. 2007). "Oxygen, sodium, magnesium, and aluminium as tracers of the galactic bulge formation". In: 465.3, pp. 799–814. DOI: 10.1051/0004-6361:20066036. arXiv: astro-ph/0610346 [astro-ph].

Ledo, H. R. et al. (Sept. 2010). "A census of nuclear stellar discs in early-type galaxies". In: 407.2, pp. 969–985. DOI: 10.1111/j.1365-2966.2010.16990.x.

Leenaarts, J. and M. Carlsson (Dec. 2009). "MULTI3D: A Domain-Decomposed 3D Radiative Transfer Code". In: *The Second Hinode Science Meeting: Beyond Discovery-Toward Understanding*. Ed. by B. Lites et al. Vol. 415. Astronomical Society of the Pacific Conference Series, p. 87.

Li, Gang et al. (Jan. 2015). "Rovibrational Line Lists for Nine Isotopologues of the CO Molecule in the X $^1\Sigma^+$ Ground Electronic State". In: 216.1, 15, p. 15. DOI: 10.1088/0067-0049/216/1/15.

Li, Zhi, Juntai Shen, and Woong-Tae Kim (June 2015). "Hydrodynamical Simulations of Nuclear Rings in Barred Galaxies". In: 806.2, 150, p. 150. DOI: 10.1088/0004-637X/806/2/150. arXiv: 1503.02594 [astro-ph.GA].

Lind, K. et al. (July 2017). "Non-LTE line formation of Fe in late-type stars - IV. Modelling of the solar centre-to-limb variation in 3D". In: 468.4, pp. 4311–4322. DOI: 10.1093/mnras/stx673. arXiv: 1703.04027 [astro-ph.SR].

Lindqvist, M., H. J. Habing, and A. Winnberg (June 1992a). "OH/IR stars close to the galactic centre. II. Their spatial and kinematics properties and the mass distribution within 5-100 PC from the galactic centre." In: 259, pp. 118–127.

— (June 1992b). "OH/IR stars close to the galactic centre. II. Their spatial and kinematics properties and the mass distribution within 5-100 PC from the galactic centre." In: 259, pp. 118–127.

Longmore, S. N. et al. (Sept. 2017). "H_2O Southern Galactic Plane Survey (HOPS): Paper III - properties of dense molecular gas across the inner Milky Way". In: 470.2, pp. 1462–1490. DOI: 10.1093/mnras/stx1226. arXiv: 1704.03253 [astro-ph.GA].

Lütticke, R., R. -J. Dettmar, and M. Pohlen (Sept. 2000). "Box- and peanut-shaped bulges. I. Statistics". In: 145, pp. 405–414. DOI: 10.1051/aas:2000354. arXiv: astro-ph/0006359 [astro-ph].

Lyapunov, A. M. (1992). "The general problem of the stability of motion". In: *International Journal of Control* 55.3, pp. 531–534. DOI: 10.1080/00207179208934253. eprint: https://doi.org/10.1080/00207179208934253. URL: https://doi.org/10.1080/00207179208934253.

Lynden-Bell, D. and M. J. Rees (Jan. 1971). "On quasars, dust and the galactic centre". In: 152, p. 461. DOI: 10.1093/mnras/152.4.461.

Mace, Gregory et al. (Aug. 2016). "300 nights of science with IGRINS at McDonald Observatory". In: *Ground-based and Airborne Instrumentation for Astronomy VI*. Ed. by Christopher J. Evans, Luc Simard, and Hideki Takami. Vol. 9908. Society of Photo-Optical Instrumentation Engineers (SPIE) Conference Series, 99080C, p. 99080C. DOI: 10.1117/12.2232780.

Mace, Gregory et al. (July 2018). "IGRINS at the Discovery Channel Telescope and Gemini South". In: *Ground-based and Airborne Instrumentation for Astronomy VII*. Ed. by Christopher J. Evans, Luc Simard, and Hideki Takami. Vol. 10702. Society of Photo-Optical Instrumentation Engineers (SPIE) Conference Series, 107020Q, 107020Q. DOI: 10.1117/12.2312345.

Madore, Barry F. (Jan. 2016). "Bulges: Seen from a Philosophically-Informed Historical Perspective". In: *Galactic Bulges*. Ed. by Eija Laurikainen, Reynier Peletier, and Dimitri Gadotti. Vol. 418. Astrophysics and Space Science Library, p. 1. DOI: 10.1007/978-3-319-19378-6_1.

Majewski, S. R., APOGEE Team, and APOGEE-2 Team (Sept. 2016). "The Apache Point Observatory Galactic Evolution Experiment (APOGEE) and its successor, APOGEE-2". In: *Astronomische Nachrichten* 337.8-9, p. 863. DOI: 10.1002/asna.201612387.

Majewski, Steven R. et al. (Sept. 2017). "The Apache Point Observatory Galactic Evolution Experiment (APOGEE)". In: 154.3, 94, p. 94. DOI: 10.3847/1538-3881/aa784d. arXiv: 1509.05420 [astro-ph.IM].

Malhan, Khyati, Rodrigo A. Ibata, and Nicolas F. Martin (Dec. 2018). "Ghostly tributaries to the Milky Way: charting the halo's stellar streams with the Gaia DR2 catalogue". In: 481.3, pp. 3442–3455. DOI: 10.1093/mnras/sty2474. arXiv: 1804.11339 [astro-ph.GA].

Martínez-Arranz, Á. et al. (Apr. 2022). "Distance to the Brick cloud using stellar kinematics". In: 660, L3, p. L3. DOI: 10.1051/0004-6361/202243263. arXiv: 2204.02109 [astro-ph.GA].

Martinez-Valpuesta, Inma and Ortwin Gerhard (June 2011). "Unifying A Boxy Bulge and Planar Long Bar in the Milky Way". In: 734.1, L20, p. L20. DOI: 10.1088/2041-8205/734/1/L20. arXiv: 1105.0928 [astro-ph.GA].

Matsunaga, Noriyuki et al. (Sept. 2011). "Three classical Cepheid variable stars in the nuclear bulge of the Milky Way". In: 477.7363, pp. 188–190. DOI: 10.1038/nature10359. arXiv: 1111.6359 [astro-ph.SR].

Matsunaga, Noriyuki et al. (Feb. 2013). "Cepheids and other short-period variables near the Galactic Centre". In: 429.1, pp. 385–397. DOI: 10.1093/mnras/sts343. arXiv: 1211.0151 [astro-ph.SR].

Matteucci, F. et al. (Aug. 2019). "The origin of stellar populations in the Galactic bulge from chemical abundances". In: 487.4, pp. 5363–5371. DOI: 10.1093/mnras/stz1647. arXiv: 1903.12440 [astro-ph.GA].

Matteucci, Francesca (Dec. 2021). "Modelling the chemical evolution of the Milky Way". In: 29.1, 5, p. 5. DOI: 10.1007/s00159-021-00133-8. arXiv: 2106.13145 [astro-ph.GA].

Matteucci, Francesca and Enzo Brocato (Dec. 1990). "Metallicity Distribution and Abundance Ratios in the Stars of the Galactic Bulge". In: 365, p. 539. DOI: 10.1086/169508.

Mauerhan, J. C. et al. (Dec. 2010). "Isolated Wolf-Rayet Stars and O Supergiants in the Galactic Center Region Identified Via Paschen-α Excess". In: 725.1, pp. 188–199. DOI: 10.1088/0004-637X/725/1/188. arXiv: 1009.2769 [astro-ph.SR].

McGinn, M. T. et al. (Mar. 1989). "Stellar Kinematics in the Galactic Center". In: 338, p. 824. DOI: 10.1086/167239.

McMillan, Paul J. and James J. Binney (Oct. 2008). "Disassembling the Galaxy with angle-action coordinates". In: 390.1, pp. 429–437. DOI: 10.1111/j.1365-2966.2008.13767.x. arXiv: 0806.0319 [astro-ph].

McWilliam, Andrew (Jan. 1997). "Abundance Ratios and Galactic Chemical Evolution". In: 35, pp. 503–556. DOI: 10.1146/annurev.astro.35.1.503.

McWilliam, Andrew and R. Michael Rich (Apr. 1994). "The First Detailed Abundance Analysis of Galactic Bulge K Giants in Baade's Window". In: 91, p. 749. DOI: 10.1086/191954.

McWilliam, Andrew and Manuela Zoccali (Dec. 2010). "Two Red Clumps and the X-shaped Milky Way Bulge". In: 724.2, pp. 1491–1502. DOI: 10.1088/0004-637X/724/2/1491. arXiv: 1008.0519 [astro-ph.GA].

Meléndez, J. et al. (June 2008). "Chemical similarities between Galactic bulge and local thick disk red giant stars". In: 484.3, pp. L21–L25. DOI: 10.1051/0004-6361:200809398. arXiv: 0804.4124 [astro-ph].

Méndez-Abreu, J. et al. (Dec. 2014). "Secular- and merger-built bulges in barred galaxies". In: 572, A25, A25. DOI: 10.1051/0004-6361/201423955. arXiv: 1409.2876 [astro-ph.GA].

Méndez-Abreu, J. et al. (Jan. 2019). "Inner bars also buckle. The MUSE TIMER view of the double-barred galaxy NGC 1291". In: 482.1, pp. L118–L122. DOI: 10.1093/mnrasl/sly196. arXiv: 1811.03855 [astro-ph.GA].

Merritt, David (Feb. 1999). "Elliptical Galaxy Dynamics". In: 111.756, pp. 129–168. DOI: 10.1086/316307. arXiv: astro-ph/9810371 [astro-ph].

Mezger, Peter G., Wolfgang J. Duschl, and Robert Zylka (Jan. 1996). "The Galactic Center: a laboratory for AGN?" In: 7.4, pp. 289–388. DOI: 10.1007/s001590050007.

Mikolaitis, Š. et al. (May 2012). "C, N, O abundances and carbon isotope ratios in evolved stars of the open clusters Collinder 261 and NGC 6253". In: 541, A137, A137. DOI: 10.1051/0004-6361/201218831. arXiv: 1203.6514 [astro-ph.SR].

Milosavljević, Miloš (Apr. 2004). "On the Origin of Nuclear Star Clusters in Late-Type Spiral Galaxies". In: 605.1, pp. L13–L16. DOI: 10.1086/420696. arXiv: astro-ph/0310574 [astro-ph].

Minchev, I. and B. Famaey (Oct. 2010). "A New Mechanism for Radial Migration in Galactic Disks: Spiral-Bar Resonance Overlap". In: 722.1, pp. 112–121. DOI: 10.1088/0004-637X/722/1/112. arXiv: 0911.1794 [astro-ph.GA].

Minniti, D. et al. (July 2010). "VISTA Variables in the Via Lactea (VVV): The public ESO near-IR variability survey of the Milky Way". In: 15, pp. 433–443. DOI: 10.1016/j.newast.2009.12.002. arXiv: 0912.1056 [astro-ph.GA].

Mo, Houjun, Frank C. van den Bosch, and Simon White (2010). *Galaxy Formation and Evolution*.

Molinari, S. et al. (July 2011). "A 100 pc Elliptical and Twisted Ring of Cold and Dense Molecular Clouds Revealed by Herschel Around the Galactic Center". In: 735.2, L33, p. L33. DOI: 10.1088/2041-8205/735/2/L33. arXiv: 1105.5486 [astro-ph.GA].

Molla, Mercedes and Federico Ferrini (Dec. 1995). "Evolution of Spiral Galaxies. V. The Galactic Bulge". In: 454, p. 726. DOI: 10.1086/176524.

Montelius, M. et al. (Sept. 2022). "Chemical evolution of ytterbium in the Galactic disk". In: 665, A135, A135. DOI: 10.1051/0004-6361/202243140. arXiv: 2202.00691 [astro-ph.GA].

Moon, Bongkon et al. (Sept. 2012). "Immersion grating mount design for IGRINS and GMTNIRS". In: *Modern Technologies in Space- and Ground-based Telescopes and Instrumentation II*. Ed. by Ramón Navarro, Colin R. Cunningham, and Eric Prieto. Vol. 8450. Society of Photo-Optical Instrumentation Engineers (SPIE) Conference Series, 845048, p. 845048. DOI: 10.1117/12.925702.

Moorwood, A., J. -G. Cuby, and C. Lidman (Mar. 1998a). "SOFI sees first light at the NTT." In: *The Messenger* 91, pp. 9–13.

Moorwood, A. et al. (Dec. 1998b). "ISAAC sees first light at the VLT." In: *The Messenger* 94, pp. 7–9.

Moorwood, Alan (Jan. 2005). "CRIRES: Context and Status". In: *High Resolution Infrared Spectroscopy in Astronomy*, pp. 15–24. DOI: 10.1007/10995082_2.

Morris, Mark and Eugene Serabyn (Jan. 1996). "The Galactic Center Environment". In: 34, pp. 645–702. DOI: 10.1146/annurev.astro.34.1.645.

Nandakumar, G. et al. (Oct. 2017). "Effects of the selection function on metallicity trends in spectroscopic surveys of the Milky Way". In: 606, A97, A97. DOI: 10.1051/0004-6361/201731099. arXiv: 1707.09932 [astro-ph.GA].

Nandakumar, G. et al. (Aug. 2018). "Chemical characterization of the inner Galactic bulge:North-South symmetry". In: 478.4, pp. 4374–4389. DOI: 10.1093/mnras/sty1255. arXiv: 1805.05037 [astro-ph.GA].

Nandakumar, G. et al. (Dec. 2022). "The Galactic chemical evolution of phosphorus observed with IGRINS". In: 668, A88, A88. DOI: 10.1051/0004-6361/202244724. arXiv: 2210.04940 [astro-ph.SR].

Nataf, D. M. et al. (Sept. 2010). "The Split Red Clump of the Galactic Bulge from OGLE-III". In: 721.1, pp. L28–L32. DOI: 10.1088/2041-8205/721/1/L28. arXiv: 1007.5065 [astro-ph.GA].

Navarro, Julio F., Carlos S. Frenk, and Simon D. M. White (Dec. 1997). "A Universal Density Profile from Hierarchical Clustering". In: 490.2, pp. 493–508. DOI: 10.1086/304888. arXiv: astro-ph/9611107 [astro-ph].

Ness, M. and K. Freeman (June 2016). "The Metallicity Distribution of the Milky Way Bulge". In: 33, e022, e022. DOI: 10.1017/pasa.2015.51. arXiv: 1511.07438 [astro-ph.GA].

Ness, M. et al. (Sept. 2012). "The Origin of the Split Red Clump in the Galactic Bulge of the Milky Way". In: 756.1, 22, p. 22. DOI: 10.1088/0004-637X/756/1/22. arXiv: 1207.0888 [astro-ph.GA].

Ness, M. et al. (Apr. 2013a). "ARGOS - III. Stellar populations in the Galactic bulge of the Milky Way". In: 430.2, pp. 836–857. DOI: 10.1093/mnras/sts629. arXiv: 1212.1540 [astro-ph.GA].

— (Apr. 2013b). "ARGOS - III. Stellar populations in the Galactic bulge of the Milky Way". In: 430.2, pp. 836–857. DOI: 10.1093/mnras/sts629. arXiv: 1212.1540 [astro-ph.GA].

Neumayer, Nadine, Anil Seth, and Torsten Böker (July 2020). "Nuclear star clusters". In: 28.1, 4, p. 4. DOI: 10.1007/s00159-020-00125-0. arXiv: 2001.03626 [astro-ph.GA].

Neumayer, Nadine and C. Jakob Walcher (Jan. 2012). "Are Nuclear Star Clusters the Precursors of Massive Black Holes?" In: *Advances in Astronomy* 2012, 709038, p. 709038. DOI: 10.1155/2012/709038. arXiv: 1201.4950 [astro-ph.CO].

Nierenberg, A. M. et al. (Nov. 2016). "The missing satellite problem in 3D". In: 462.4, pp. 4473–4481. DOI: 10.1093/mnras/stw1860. arXiv: 1603.01614 [astro-ph.GA].

Nieuwmunster, N. et al. (May 2024). "Orbital analysis of stars in the nuclear stellar disc of the Milky Way". In: 685, A93, A93. DOI: 10.1051/0004-6361/202349000. arXiv: 2403.00761 [astro-ph.GA].

Nishiyama, S. and R. Schödel (Jan. 2013). "Young, massive star candidates detected throughout the nuclear star cluster of the Milky Way". In: 549, A57, A57. DOI: 10.1051/0004-6361/201219773. arXiv: 1210.6125 [astro-ph.GA].

Nishiyama, Shogo et al. (Feb. 2006). "Interstellar Extinction Law in the J, H, and K_s Bands toward the Galactic Center". In: 638.2, pp. 839–846. DOI: 10.1086/499038. arXiv: astro-ph/0601174 [astro-ph].

Nishiyama, Shogo et al. (June 2008). "The Interstellar Extinction Law toward the Galactic Center. II. V, J, H, and K_s Bands". In: 680.2, pp. 1174–1179. DOI: 10.1086/587791. arXiv: 0802.3559 [astro-ph].

Nishiyama, Shogo et al. (June 2013). "Magnetically Confined Interstellar Hot Plasma in the Nuclear Bulge of Our Galaxy". In: 769.2, L28, p. L28. DOI: 10.1088/2041-8205/769/2/L28. arXiv: 1305.0347 [astro-ph.GA].

Nissen, Poul Erik and Bengt Gustafsson (Oct. 2018). "High-precision stellar abundances of the elements: methods and applications". In: 26.1, 6, p. 6. DOI: 10.1007/s00159-018-0111-3. arXiv: 1810.06535 [astro-ph.SR].

Noguchi, Masafumi (Mar. 1999). "Early Evolution of Disk Galaxies: Formation of Bulges in Clumpy Young Galactic Disks". In: 514.1, pp. 77–95. DOI: 10.1086/306932. arXiv: astro-ph/9806355 [astro-ph].

Nogueras-Lara, F. (Dec. 2022a). "A first glimpse at the line-of-sight structure of the Milky Way's nuclear stellar disc". In: 668, L8, p. L8. DOI: 10.1051/0004-6361/202244934. arXiv: 2212.00047 [astro-ph.GA].

— (Dec. 2022b). "A first glimpse at the line-of-sight structure of the Milky Way's nuclear stellar disc". In: 668, L8, p. L8. DOI: 10.1051/0004-6361/202244934. arXiv: 2212.00047 [astro-ph.GA].

— (Oct. 2022c). "Kinematic data rebuild the nuclear star cluster as the most metal-rich region of the Galaxy". In: 666, A72, A72. DOI: 10.1051/0004-6361/202244411. arXiv: 2208.13218 [astro-ph.GA].

— (Jan. 2024). "Hunting young stars in the Galactic centre. Hundreds of thousands of solar masses of young stars in the Sagittarius C region". In: 681, L21, p. L21. DOI: 10.1051/0004-6361/202348712. arXiv: 2401.07900 [astro-ph.GA].

Nogueras-Lara, F., R. Schödel, and N. Neumayer (Sept. 2021a). "Distance and extinction to the Milky Way spiral arms along the Galactic centre line of sight". In: 653, A33, A33. DOI: 10.1051/0004-6361/202040073. arXiv: 2106.04529 [astro-ph.GA].

— (Sept. 2021b). "GALACTICNUCLEUS: A high-angular-resolution JHK$_s$ imaging survey of the Galactic centre. IV. Extinction maps and de-reddened photometry". In: 653, A133, A133. DOI: 10.1051/0004-6361/202140996. arXiv: 2107.00021 [astro-ph.GA].

Nogueras-Lara, F. et al. (Mar. 2018a). "GALACTICNUCLEUS: A high angular resolution JHK$_s$ imaging survey of the Galactic centre. I. Methodology, performance, and near-infrared extinction towards the Galactic centre". In: 610, A83, A83. DOI: 10.1051/0004-6361/201732002. arXiv: 1709.09094 [astro-ph.GA].

— (Mar. 2018b). "GALACTICNUCLEUS: A high angular resolution JHK$_s$ imaging survey of the Galactic centre. I. Methodology, performance, and near-infrared extinction towards the Galactic centre". In: 610, A83, A83. DOI: 10.1051/0004-6361/201732002. arXiv: 1709.09094 [astro-ph.GA].

Nogueras-Lara, F. et al. (Nov. 2019a). "GALACTICNUCLEUS: A high-angular-resolution JHK$_s$ imaging survey of the Galactic centre. II. First data release of the catalogue and the most detailed CMDs of the GC". In: 631, A20, A20. DOI: 10.1051/0004-6361/201936263. arXiv: 1908.10366 [astro-ph.GA].

Nogueras-Lara, F. et al. (Oct. 2019b). "Variability of the near-infrared extinction curve towards the Galactic centre". In: 630, L3, p. L3. DOI: 10.1051/0004-6361/201936322. arXiv: 1909.02494 [astro-ph.SR].

Nogueras-Lara, F. et al. (Mar. 2023a). "Evidence of an age gradient along the line of sight in the nuclear stellar disc of the Milky Way". In: 671, L10, p. L10. DOI: 10.1051/0004-6361/202345941. arXiv: 2302.02890 [astro-ph.GA].

— (Mar. 2023b). "Evidence of an age gradient along the line of sight in the nuclear stellar disc of the Milky Way". In: 671, L10, p. L10. DOI: 10.1051/0004-6361/202345941. arXiv: 2302.02890 [astro-ph.GA].

Nogueras-Lara, F. et al. (Dec. 2023c). "Smooth kinematic and metallicity gradients reveal that the Milky Way's nuclear star cluster and disc might be part of the same structure". In: 680, A75, A75. DOI: 10.1051/0004-6361/202347421. arXiv: 2309.07219 [astro-ph.GA].

Nogueras-Lara, Francisco, Rainer Schödel, and Nadine Neumayer (Oct. 2021a). "The Nuclear Star Cluster and Nuclear Stellar Disk of the Milky Way: Different Stellar Populations and Star Formation Histories". In: 920.2, 97, p. 97. DOI: 10.3847/1538-4357/ac185e. arXiv: 2107.13003 [astro-ph.GA].

Nogueras-Lara, Francisco, Rainer Schödel, and Nadine Neumayer (Oct. 2021b). "The Nuclear Star Cluster and Nuclear Stellar Disk of the Milky Way: Different Stellar Populations and Star Formation Histories". In: 920.2, 97, p. 97. DOI: 10.3847/1538-4357/ac185e. arXiv: 2107.13003 [astro-ph.GA].

— (Aug. 2022). "Detection of an excess of young stars in the Galactic Centre Sagittarius B1 region". In: *Nature Astronomy* 6, pp. 1178–1184. DOI: 10.1038/s41550-022-01755-3. arXiv: 2207.02227 [astro-ph.GA].

Nogueras-Lara, Francisco et al. (Jan. 2020a). "Early formation and recent starburst activity in the nuclear disk of the Milky Way". In: *Nature Astronomy* 4, pp. 377–381. DOI: 10.1038/s41550-019-0967-9. arXiv: 1910.06968 [astro-ph.GA].

— (Dec. 2020b). "Early formation and recent starburst activity in the nuclear disk of the Milky Way". In: *Nature Astronomy* 4, pp. 377–381. DOI: 10.1038/s41550-019-0967-9. arXiv: 1910.06968 [astro-ph.GA].

— (Jan. 2020c). "Early formation and recent starburst activity in the nuclear disk of the Milky Way". In: *Nature Astronomy* 4, pp. 377–381. DOI: 10.1038/s41550-019-0967-9. arXiv: 1910.06968 [astro-ph.GA].

Norman, Colin A., J. A. Sellwood, and Hashima Hasan (May 1996). "Bar Dissolution and Bulge Formation: an Example of Secular Dynamical Evolution in Galaxies". In: 462, p. 114. DOI: 10.1086/177133.

Nowak, N. et al. (Apr. 2010). "Do black hole masses scale with classical bulge luminosities only? The case of the two composite pseudo-bulge galaxies NGC 3368 and NGC 3489". In: 403.2, pp. 646–672. DOI: 10.1111/j.1365-2966.2009.16167.x. arXiv: 0912.2511 [astro-ph.CO].

Ordenes-Briceño, Yasna et al. (June 2018). "The Next Generation Fornax Survey (NGFS). IV. Mass and Age Bimodality of Nuclear Clusters in the Fornax Core Region". In: 860.1, 4, p. 4. DOI: 10.3847/1538-4357/aac1b8. arXiv: 1805.00491 [astro-ph.GA].

Ortolani, Sergio et al. (Oct. 1995). "Near-coeval formation of the Galactic bulge and halo inferred from globular cluster ages". In: 377.6551, pp. 701–704. DOI: 10.1038/377701a0.

Osorio, Y. et al. (July 2015). "Mg Line Formation in Late-Type Stellar Atmospheres. I. The Model Atom". In: *A&A* 579, A53. ISSN: 0004-6361. DOI: 10.1051/0004-6361/201525846.

Park, Chan et al. (July 2014). "Design and early performance of IGRINS (Immersion Grating Infrared Spectrometer)". In: *Ground-based and Airborne Instrumentation for Astronomy V*. Ed. by Suzanne K. Ramsay, Ian S. McLean, and Hideki Takami. Vol. 9147. Society of Photo-Optical Instrumentation Engineers (SPIE) Conference Series, 91471D, p. 91471D. DOI: 10.1117/12.2056431.

Paudel, Sanjaya, Thorsten Lisker, and Harald Kuntschner (May 2011). "Nuclei of early-type dwarf galaxies: insights from stellar populations". In: 413.3, pp. 1764–1776. DOI: 10.1111/j.1365-2966.2011.18256.x. arXiv: 1012.4092 [astro-ph.GA].

Pedregosa, Fabian et al. (Oct. 2011). "Scikit-learn: Machine Learning in Python". In: *Journal of Machine Learning Research* 12, pp. 2825–2830. DOI: 10.48550/arXiv.1201.0490. arXiv: 1201.0490 [cs.LG].

Perets, Hagai B. and Alessandra Mastrobuono-Battisti (Apr. 2014). "Age and Mass Segregation of Multiple Stellar Populations in Galactic Nuclei and their Observational Signatures". In: 784.2, L44, p. L44. DOI: 10.1088/2041-8205/784/2/L44. arXiv: 1401.1824 [astro-ph.GA].

Perret, V. et al. (Feb. 2014). "Evolution of the mass, size, and star formation rate in high redshift merging galaxies. MIRAGE - A new sample of simulations with detailed stellar feedback". In: 562, A1, A1. DOI: 10.1051/0004-6361/201322395. arXiv: 1307.7130 [astro-ph.CO].

Perret, Valentin (July 2016). *DICE: Disk Initial Conditions Environment*. Astrophysics Source Code Library, record ascl:1607.002.

Pfenniger, D. and D. Friedli (Dec. 1991). "Structure and dynamics of 3D N-body barred galaxies." In: 252, pp. 75–93.

Pfuhl, O. et al. (Nov. 2011). "The Star Formation History of the Milky Way's Nuclear Star Cluster". In: 741.2, 108, p. 108. DOI: 10.1088/0004-637X/741/2/108. arXiv: 1110.1633 [astro-ph.GA].

Pietrukowicz, P. et al. (Oct. 2015). "Deciphering the 3D Structure of the Old Galactic Bulge from the OGLE RR Lyrae Stars". In: 811.2, 113, p. 113. DOI: 10.1088/0004-637X/811/2/113. arXiv: 1412.4121 [astro-ph.GA].

Pinsonneault, Marc H. et al. (Dec. 2014). "The APOKASC Catalog: An Asteroseismic and Spectroscopic Joint Survey of Targets in the Kepler Fields". In: 215.2, 19, p. 19. DOI: 10.1088/0067-0049/215/2/19. arXiv: 1410.2503 [astro-ph.SR].

Piskunov, Nikolai and Jeff A. Valenti (Jan. 2017a). "Spectroscopy Made Easy: Evolution". In: 597, A16, A16. DOI: 10.1051/0004-6361/201629124. arXiv: 1606.06073 [astro-ph.IM].

— (Jan. 2017b). "Spectroscopy Made Easy: Evolution". In: 597, A16, A16. DOI: 10.1051/0004-6361/201629124. arXiv: 1606.06073 [astro-ph.IM].

Pizzella, A. et al. (July 2002). "Nuclear Stellar Disks in Spiral Galaxies". In: 573.1, pp. 131–137. DOI: 10.1086/340486. arXiv: astro-ph/0203038 [astro-ph].

Poincaré, Henri (1892). *Les méthodes nouvelles de la mécanique céleste*. DOI: 10.3931/e-rara-421.

— (2017). *The Three-Body Problem and the Equations of Dynamics: Poincaré's Foundational Work on Dynamical Systems Theory*. Vol. 443. DOI: 10.1007/978-3-319-52899-1.

Portail, Matthieu et al. (Sept. 2017a). "Chemodynamical modelling of the galactic bulge and bar". In: 470.1, pp. 1233–1252. DOI: 10.1093/mnras/stx1293. arXiv: 1704.07821 [astro-ph.GA].

Portail, Matthieu et al. (Feb. 2017b). "Dynamical modelling of the galactic bulge and bar: the Milky Way's pattern speed, stellar and dark matter mass distribution". In: 465.2, pp. 1621–1644. DOI: 10.1093/mnras/stw2819. arXiv: 1608.07954 [astro-ph.GA].

Portegies Zwart, Simon F. et al. (Jan. 2002). "The Lives and Deaths of Star Clusters near the Galactic Center". In: 565.1, pp. 265–279. DOI: 10.1086/324141. arXiv: astro-ph/0102259 [astro-ph].

Price-Whelan, Adrian M. (June 2015). *SuperFreq*. DOI: 10.5281/zenodo.18787. URL: https://doi.org/10.5281/zenodo.18787.

Price-Whelan, Adrian M. et al. (Jan. 2016). "Chaotic dispersal of tidal debris". In: 455.1, pp. 1079–1098. DOI: 10.1093/mnras/stv2383. arXiv: 1507.08662 [astro-ph.GA].

Queiroz, A. B. A. et al. (June 2020). "From the bulge to the outer disc: StarHorse stellar parameters, distances, and extinctions for stars in APOGEE DR16 and other spectroscopic surveys". In: 638, A76, A76. DOI: 10.1051/0004-6361/201937364. arXiv: 1912.09778 [astro-ph.GA].

Ramírez, I. and C. Allende Prieto (Dec. 2011). "Fundamental Parameters and Chemical Composition of Arcturus". In: 743.2, 135, p. 135. DOI: 10.1088/0004-637X/743/2/135. arXiv: 1109.4425 [astro-ph.SR].

Ramos, P. et al. (June 2020). "Full 5D characterisation of the Sagittarius stream with Gaia DR2 RR Lyrae". In: 638, A104, A104. DOI: 10.1051/0004-6361/202037819. arXiv: 2002.11142 [astro-ph.GA].

Randich, S. et al. (June 2022). "The Gaia-ESO Public Spectroscopic Survey: Implementation, data products, open cluster survey, science, and legacy". In: *arXiv e-prints*, arXiv:2206.02901, arXiv:2206.02901. arXiv: 2206.02901 [astro-ph.GA].

Rauer, H. et al. (Nov. 2014). "The PLATO 2.0 mission". In: *Experimental Astronomy* 38.1-2, pp. 249–330. DOI: 10.1007/s10686-014-9383-4. arXiv: 1310.0696 [astro-ph.EP].

Reid, Mark J. (Jan. 1993). "The distance to the center of the Galaxy." In: 31, pp. 345–372. DOI: 10.1146/annurev.aa.31.090193.002021.

Renaud, Florent et al. (June 2021a). "VINTERGATAN - II. The history of the Milky Way told by its mergers". In: 503.4, pp. 5846–5867. DOI: 10.1093/mnras/stab250. arXiv: 2006.06011 [astro-ph.GA].

Renaud, Florent et al. (June 2021b). "VINTERGATAN III: how to reset the metallicity of the Milky Way". In: 503.4, pp. 5868–5876. DOI: 10.1093/mnras/stab543. arXiv: 2006.06012 [astro-ph.GA].

Renzini, Alvio et al. (Aug. 2018). "The WFC3 Galactic Bulge Treasury Program: Relative Ages of Bulge Stars of High and Low Metallicity". In: 863.1, 16, p. 16. DOI: 10.3847/1538-4357/aad09b. arXiv: 1806.11556 [astro-ph.GA].

Rich, R. M. et al. (Dec. 2017). "Detailed Abundances for the Old Population near the Galactic Center. I. Metallicity Distribution of the Nuclear Star Cluster". In: 154.6, 239, p. 239. DOI: 10.3847/1538-3881/aa970a. arXiv: 1710.08477 [astro-ph.GA].

Rich, R. Michael and Livia Origlia (Dec. 2005). "The First Detailed Abundances for M Giants in Baade's Window from Infrared Spectroscopy". In: 634.2, pp. 1293–1299. DOI: 10.1086/432592. arXiv: astro-ph/0506051 [astro-ph].

Ricker, George R. et al. (Jan. 2015). "Transiting Exoplanet Survey Satellite (TESS)". In: *Journal of Astronomical Telescopes, Instruments, and Systems* 1, 014003, p. 014003. DOI: 10.1117/1.JATIS.1.1.014003.

Rix, Hans-Walter et al. (Dec. 2022). "The Poor Old Heart of the Milky Way". In: 941.1, 45, p. 45. DOI: 10.3847/1538-4357/ac9e01. arXiv: 2209.02722 [astro-ph.GA].

Rojas-Arriagada, A. et al. (Sept. 2014). "The Gaia-ESO Survey: metallicity and kinematic trends in the Milky Way bulge". In: 569, A103, A103. DOI: 10.1051/0004-6361/201424121. arXiv: 1408.4558.

Rojas-Arriagada, A. et al. (May 2017a). "The Gaia-ESO Survey: Exploring the complex nature and origins of the Galactic bulge populations". In: 601, A140, A140. DOI: 10.1051/0004-6361/201629160. arXiv: 1704.03325 [astro-ph.GA].

— (May 2017b). "The Gaia-ESO Survey: Exploring the complex nature and origins of the Galactic bulge populations". In: 601, A140, A140. DOI: 10.1051/0004-6361/201629160. arXiv: 1704.03325 [astro-ph.GA].

Rojas-Arriagada, Alvaro et al. (Nov. 2020a). "How many components? Quantifying the complexity of the metallicity distribution in the Milky Way bulge with APOGEE". In: 499.1, pp. 1037–1057. DOI: 10.1093/mnras/staa2807. arXiv: 2007.13967 [astro-ph.GA].

— (Nov. 2020b). "How many components? Quantifying the complexity of the metallicity distribution in the Milky Way bulge with APOGEE". In: 499.1, pp. 1037–1057. DOI: 10.1093/mnras/staa2807. arXiv: 2007.13967 [astro-ph.GA].

Rojas-Arriagada, A. et al. (2014). "The Gaia-ESO Survey: metallicity and kinematic trends in the Milky Way bulge". In: *A&A* 569, A103. DOI: 10.1051/0004-6361/201424121. URL: https://doi.org/10.1051/0004-6361/201424121.

Romano, D. et al. (Nov. 2010). "Quantifying the uncertainties of chemical evolution studies. II. Stellar yields". In: 522, A32, A32. DOI: 10.1051/0004-6361/201014483. arXiv: 1006.5863 [astro-ph.GA].

Roškar, Rok et al. (Sept. 2008). "Riding the Spiral Waves: Implications of Stellar Migration for the Properties of Galactic Disks". In: 684.2, p. L79. DOI: 10.1086/592231. arXiv: 0808.0206 [astro-ph].

Ryabchikova, T. et al. (May 2015). "A major upgrade of the VALD database". In: 90.5, 054005, p. 054005. DOI: 10.1088/0031-8949/90/5/054005.

Ryde, N. and M. Schultheis (Jan. 2015). "Chemical abundances of M giants in the Galactic centre: A single metal-rich population with low [α/Fe]". In: 573, A14, A14. DOI: 10.1051/0004-6361/201424486.

Ryde, N. et al. (Jan. 2010). "Chemical abundances of 11 bulge stars from high-resolution, near-IR spectra". In: 509, A20, A20. DOI: 10.1051/0004-6361/200912687. arXiv: 0910.0448 [astro-ph.GA].

Ryde, N. et al. (Jan. 2016a). "Chemical Evolution of the Inner 2 Degrees of the Milky Way Bulge: [α/Fe] Trends and Metallicity Gradients". In: 151.1, 1, p. 1. DOI: 10.3847/0004-6256/151/1/1. arXiv: 1510.02622 [astro-ph.GA].

Ryde, N. et al. (Nov. 2016b). "Detailed Abundance Analysis of a Metal-poor Giant in the Galactic Center". In: 831.1, 40, p. 40. DOI: 10.3847/0004-637X/831/1/40. arXiv: 1608.07562 [astro-ph.GA].

Ryde, Nils et al. (Apr. 2020). "Fluorine in the Solar Neighborhood: The Need for Several Cosmic Sources". In: 893.1, 37, p. 37. DOI: 10.3847/1538-4357/ab7eb1. arXiv: 2003.04656 [astro-ph.GA].

Sahal-Bréchot, S. et al. (May 2015). "The STARK-B Database VAMDC Node: A Repository for Spectral Line Broadening and Shifts Due to Collisions with Charged Particles". In: *Phys. Scr.* 90, p. 054008. ISSN: 0031-8949. DOI: 10.1088/0031-8949/90/5/054008.

Saito, R. K. et al. (Jan. 2012). "VVV DR1: The first data release of the Milky Way bulge and southern plane from the near-infrared ESO public survey VISTA variables in the Vía Láctea". In: 537, A107, A107. DOI: 10.1051/0004-6361/201118407. arXiv: 1111.5511 [astro-ph.GA].

Saito, R. K. et al. (June 2024). "The VISTA Variables in the Vía Láctea eXtended (VVVX) ESO public survey: Completion of the observations and legacy". In: *arXiv e-prints*, arXiv:2406.16646, arXiv:2406.16646. DOI: 10.48550/arXiv.2406.16646. arXiv: 2406.16646 [astro-ph.GA].

Salpeter, Edwin E. (Jan. 1955). "The Luminosity Function and Stellar Evolution." In: 121, p. 161. DOI: 10.1086/145971.

Sambhus, Niranjan and S. Sridhar (Oct. 2000). "Stellar Orbits in Triaxial Clusters around Black Holes in Galactic Nuclei". In: 542.1, pp. 143–160. DOI: 10.1086/309497. arXiv: astro-ph/0007355 [astro-ph].

Samland, M. and O. E. Gerhard (Mar. 2003). "The formation of a disk galaxy within a growing dark halo". In: 399, pp. 961–982. DOI: 10.1051/0004-6361:20021842. arXiv: astro-ph/0301499 [astro-ph].

Sánchez-Janssen, Rubén et al. (June 2019). "The Next Generation Virgo Cluster Survey. XXIII. Fundamentals of Nuclear Star Clusters over Seven Decades in Galaxy Mass". In: 878.1, 18, p. 18. DOI: 10.3847/1538-4357/aaf4fd. arXiv: 1812.01019 [astro-ph.GA].

Sanders, Jason L. et al. (Nov. 2022a). "Mira variables in the Milky Way's nuclear stellar disc: discovery and classification". In: 517.1, pp. 257–280. DOI: 10.1093/mnras/stac2274. arXiv: 2208.04966 [astro-ph.GA].

Sanders, Jason L. et al. (Aug. 2022b). "The extinction law in the inner 3×3 deg^2 of the Milky Way and the red clump absolute magnitude in the inner bar-bulge". In: 514.2, pp. 2407–2424. DOI: 10.1093/mnras/stac1367. arXiv: 2205.10378 [astro-ph.GA].

Sanders, Jason L. et al. (May 2024). "The epoch of the Milky Way's bar formation: dynamical modelling of Mira variables in the nuclear stellar disc". In: 530.3, pp. 2972–2993. DOI: 10.1093/mnras/stae711. arXiv: 2311.00035 [astro-ph.GA].

Santiago, Basílio X. et al. (Jan. 2016). "Spectro-photometric distances to stars: A general purpose Bayesian approach". In: 585, A42, A42. DOI: 10.1051/0004-6361/201323177. arXiv: 1501.05500 [astro-ph.IM].

Santos-Peral, P. et al. (July 2020). "The AMBRE Project: Spectrum normalisation influence on Mg abundances in the metal-rich Galactic disc". In: 639, A140, A140. DOI: 10.1051/0004-6361/202037522. arXiv: 2006.08544 [astro-ph.GA].

Schödel, R. et al. (Feb. 2010). "Peering through the veil: near-infrared photometry and extinction for the Galactic nuclear star cluster. Accurate near infrared H, Ks, and L' photometry and the near-infrared extinction-law toward the central parsec of the Galaxy". In: 511, A18, A18. DOI: 10.1051/0004-6361/200913183.

Schödel, R. et al. (June 2014a). "Surface brightness profile of the Milky Way's nuclear star cluster". In: 566, A47, A47. DOI: 10.1051/0004-6361/201423481. arXiv: 1403.6657 [astro-ph.GA].

— (June 2014b). "Surface brightness profile of the Milky Way's nuclear star cluster". In: 566, A47, A47. DOI: 10.1051/0004-6361/201423481. arXiv: 1403.6657 [astro-ph.GA].

Schödel, R. et al. (Dec. 2014c). "The nuclear cluster of the Milky Way: our primary testbed for the interaction of a dense star cluster with a massive black hole". In: *Classical and Quantum Gravity* 31.24, 244007, p. 244007. DOI: 10.1088/0264-9381/31/24/244007. arXiv: 1411.4504 [astro-ph.GA].

Schödel, R. et al. (Sept. 2020a). "The Milky Way's nuclear star cluster: Old, metal-rich, and cuspy. Structure and star formation history from deep imaging". In: 641, A102, A102. DOI: 10.1051/0004-6361/201936688.

— (Sept. 2020b). "The Milky Way's nuclear star cluster: Old, metal-rich, and cuspy. Structure and star formation history from deep imaging". In: 641, A102, A102. DOI: 10.1051/0004-6361/201936688. arXiv: 2007.15950 [astro-ph.GA].

Schödel, R. et al. (Apr. 2023). "The formation history of our Galaxy's nuclear stellar disc constrained from HST observations of the Quintuplet field". In: 672, L8, p. L8. DOI: 10.1051/0004-6361/202346335. arXiv: 2304.01791 [astro-ph.GA].

Schönrich, Ralph, Michael Aumer, and Stuart E. Sale (Oct. 2015a). "Kinematic Detection of the Galactic Nuclear Disk". In: 812.2, L21, p. L21. DOI: 10.1088/2041-8205/812/2/L21. arXiv: 1507.02695 [astro-ph.GA].

— (Oct. 2015b). "Kinematic Detection of the Galactic Nuclear Disk". In: 812.2, L21, p. L21. DOI: 10.1088/2041-8205/812/2/L21. arXiv: 1507.02695 [astro-ph.GA].

Schultheis, M., N. Ryde, and G. Nandakumar (May 2016). "Temperatures and metallicities of M giants in the Galactic bulge from low-resolution K-band spectra". In: 590, A6, A6. DOI: 10.1051/0004-6361/201628266. arXiv: 1603.02633 [astro-ph.SR].

Schultheis, M. et al. (Feb. 2009). "Interstellar extinction and long-period variables in the Galactic centre". In: 495.1, pp. 157–168. DOI: 10.1051/0004-6361:200810342. arXiv: 0811.2902 [astro-ph].

Schultheis, M. et al. (Apr. 2017). "Baade's window and APOGEE. Metallicities, ages, and chemical abundances". In: 600, A14, A14. DOI: 10.1051/0004-6361/201630154. arXiv: 1702.01547 [astro-ph.GA].

Schultheis, M. et al. (June 2021). "The nuclear stellar disc of the Milky Way: A dynamically cool and metal-rich component possibly formed from the central molecular zone". In: 650, A191, A191. DOI: 10.1051/0004-6361/202140499. arXiv: 2104.10439 [astro-ph.GA].

Schwarz, Gideon (July 1978). "Estimating the Dimension of a Model". In: *Annals of Statistics* 6.2, pp. 461–464.

Scorza, Cecilia and Frank C. van den Bosch (Oct. 1998). "Nuclear stellar discs in early-type galaxies - II. Photometric properties". In: 300.2, pp. 469–478. DOI: 10.1046/j.1365-8711.1998.01922.x. arXiv: astro-ph/9806078 [astro-ph].

Searle, L. and R. Zinn (Oct. 1978). "Composition of halo clusters and the formation of the galactic halo." In: 225, pp. 357–379. DOI: 10.1086/156499.

Sellwood, J. A. (Jan. 2014). "Secular evolution in disk galaxies". In: *Reviews of Modern Physics* 86.1, pp. 1–46. DOI: 10.1103/RevModPhys.86.1. arXiv: 1310.0403 [astro-ph.GA].

Sellwood, J. A. and J. J. Binney (Nov. 2002). "Radial mixing in galactic discs". In: 336.3, pp. 785–796. DOI: 10.1046/j.1365-8711.2002.05806.x. arXiv: astro-ph/0203510 [astro-ph].

Sellwood, J. A. and A. Wilkinson (Feb. 1993). "Dynamics of barred galaxies". In: *Reports on Progress in Physics* 56.2, pp. 173–256. DOI: 10.1088/0034-4885/56/2/001. arXiv: astro-ph/0608665 [astro-ph].

Seo, Woo-Young et al. (Feb. 2019). "Effects of Gas on Formation and Evolution of Stellar Bars and Nuclear Rings in Disk Galaxies". In: 872.1, 5, p. 5. DOI: 10.3847/1538-4357/aafc5f. arXiv: 1901.02021 [astro-ph.GA].

Seth, Anil C. et al. (Dec. 2006). "Clues to Nuclear Star Cluster Formation from Edge-on Spirals". In: 132.6, pp. 2539–2555. DOI: 10.1086/508994. arXiv: astro-ph/0609302 [astro-ph].

Shahzamanian, B. et al. (June 2022). "A proper motion catalogue for the Milky Way's nuclear stellar disc". In: 662, A11, A11. DOI: 10.1051/0004-6361/202142687. arXiv: 2108.11847 [astro-ph.GA].

Shapley, H. (Feb. 1918). "Globular Clusters and the Structure of the Galactic System". In: 30.173, p. 42. DOI: 10.1086/122686.

Sharples, R. et al. (Mar. 2013). "First Light for the KMOS Multi-Object Integral-Field Spectrometer". In: *The Messenger* 151, pp. 21–23.

Shen, Jeff et al. (Jan. 2022). "The Mass of the Milky Way from the H3 Survey". In: 925.1, 1, p. 1. DOI: 10.3847/1538-4357/ac3a7a. arXiv: 2111.09327 [astro-ph.GA].

Shen, Juntai and J. A. Sellwood (Apr. 2004). "The Destruction of Bars by Central Mass Concentrations". In: 604.2, pp. 614–631. DOI: 10.1086/382124. arXiv: astro-ph/0310194 [astro-ph].

Shimizu, T. Taro et al. (Dec. 2019). "The multiphase gas structure and kinematics in the circumnuclear region of NGC 5728". In: 490.4, pp. 5860–5887. DOI: 10.1093/mnras/stz2802. arXiv: 1907.03801 [astro-ph.GA].

Shlosman, Isaac, Mitchell C. Begelman, and Julian Frank (June 1990). "The fuelling of active galactic nuclei". In: 345.6277, pp. 679–686. DOI: 10.1038/345679a0.

Skokos, Ch., P. A. Patsis, and E. Athanassoula (July 2002). "Orbital dynamics of three-dimensional bars - I. The backbone of three-dimensional bars. A fiducial case". In: 333.4, pp. 847–860. DOI: 10.1046/j.1365-8711.2002.05468.x. arXiv: astro-ph/0204077 [astro-ph].

Smith, Beverly J., Stephan D. Price, and Rachel I. Baker (Oct. 2004). "The COBE DIRBE Point Source Catalog". In: 154.2, pp. 673–704. DOI: 10.1086/423248. arXiv: astro-ph/0406177 [astro-ph].

Smith, L. C. et al. (Feb. 2018). "VIRAC: the VVV Infrared Astrometric Catalogue". In: 474.2, pp. 1826–1849. DOI: 10.1093/mnras/stx2789. arXiv: 1710.08919 [astro-ph.SR].

Smith, Verne V. et al. (Mar. 2013a). "Chemical Abundances in Field Red Giants from High-resolution H-band Spectra Using the APOGEE Spectral Linelist". In: 765.1, 16, p. 16. DOI: 10.1088/0004-637X/765/1/16. arXiv: 1212.4091 [astro-ph.SR].

— (Mar. 2013b). "Chemical Abundances in Field Red Giants from High-resolution H-band Spectra Using the APOGEE Spectral Linelist". In: 765.1, 16, p. 16. DOI: 10.1088/0004-637X/765/1/16. arXiv: 1212.4091 [astro-ph.SR].

Sneden, Christopher et al. (Oct. 2014). "Line Lists for the A $^2\Pi$-X $^2\Sigma^+$ (Red) and B $^2\Sigma^+$-X $^2\Sigma^+$ (Violet) Systems of CN, $^{13}C^{14}N$, and $^{12}C^{15}N$, and Application to Astronomical Spectra". In: 214.2, 26, p. 26. DOI: 10.1088/0067-0049/214/2/26. arXiv: 1408.3828 [astro-ph.SR].

Soderblom, David R (2010). "The ages of stars". In: *Annual Review of Astronomy and Astrophysics* 48, pp. 581–629.

Sofue, Yoshiaki, Mareki Honma, and Toshihiro Omodaka (Feb. 2009). "Unified Rotation Curve of the Galaxy – Decomposition into de Vaucouleurs Bulge, Disk, Dark Halo, and the 9-kpc Rotation Dip –". In: 61, p. 227. DOI: 10.1093/pasj/61.2.227. arXiv: 0811.0859 [astro-ph].

Sormani, Mattia C. and Ashley T. Barnes (Mar. 2019). "Mass inflow rate into the Central Molecular Zone: observational determination and evidence of episodic accretion". In: 484.1, pp. 1213–1219. DOI: 10.1093/mnras/stz046. arXiv: 1901.00867 [astro-ph.GA].

Sormani, Mattia C., Emanuele Sobacchi, and Jason L. Sanders (Sept. 2023). "Nuclear rings are the inner edge of a gap around the Lindblad Resonance". In: *arXiv e-prints*, arXiv:2309.14093, arXiv:2309.14093. DOI: 10.48550/arXiv.2309.14093. arXiv: 2309.14093 [astro-ph.GA].

— (Mar. 2024). "Nuclear rings are the inner edge of a gap around the Lindblad Resonance". In: 528.4, pp. 5742–5762. DOI: 10.1093/mnras/stae082. arXiv: 2309.14093 [astro-ph.GA].

Sormani, Mattia C. et al. (Nov. 2018a). "A dynamical mechanism for the origin of nuclear rings". In: 481.1, pp. 2–19. DOI: 10.1093/mnras/sty2246. arXiv: 1805.07969 [astro-ph.GA].

Sormani, Mattia C. et al. (Apr. 2018b). "A theoretical explanation for the Central Molecular Zone asymmetry". In: 475.2, pp. 2383–2402. DOI: 10.1093/mnras/stx3258. arXiv: 1707.03650 [astro-ph.GA].

Sormani, Mattia C. et al. (Sept. 2020). "Jeans modelling of the Milky Way's nuclear stellar disc". In: 499.1, pp. 7–24. DOI: 10.1093/mnras/staa2785. arXiv: 2007.06577 [astro-ph.GA].

Sormani, Mattia C. et al. (May 2022). "Self-consistent modelling of the Milky Way's nuclear stellar disc". In: 512.2, pp. 1857–1884. DOI: 10.1093/mnras/stac639. arXiv: 2111.12713 [astro-ph.GA].

Soto, M., R. M. Rich, and K. Kuijken (Aug. 2007). "Evidence of a Metal-rich Galactic Bar from the Vertex Deviation of the Velocity Ellipsoid". In: 665.1, pp. L31–L34. DOI: 10.1086/521098. arXiv: astro-ph/0611433 [astro-ph].

Spitoni, E. et al. (June 2022). "Beyond the two-infall model with Gaia DR3 α-element abundances". In: *arXiv e-prints*, arXiv:2206.12436, arXiv:2206.12436. arXiv: 2206.12436 [astro-ph.GA].

Springel, Volker, Carlos S. Frenk, and Simon D. M. White (Apr. 2006). "The large-scale structure of the Universe". In: 440.7088, pp. 1137–1144. DOI: 10.1038/nature04805. arXiv: astro-ph/0604561 [astro-ph].

Stebbins, Joel and A. E. Whitford (Jan. 1947). "Infrared radiation from the region of the galactic center." In: 52, p. 130. DOI: 10.1086/106022.

Stolovy, S. et al. (Dec. 2006). "A mid-infrared survey of the inner 2 × 1.5 degrees of the Galaxy with Spitzer/IRAC". In: *Journal of Physics Conference Series*. Vol. 54. Journal of Physics Conference Series. IOP, pp. 176–182. DOI: 10.1088/1742-6596/54/1/030.

Surot, F. et al. (Mar. 2019). "Mapping the stellar age of the Milky Way bulge with the VVV. I. The method". In: 623, A168, A168. DOI: 10.1051/0004-6361/201833550. arXiv: 1902.01695 [astro-ph.GA].

Tautvaišienė, Gražina et al. (Oct. 2016). "CNO abundances and carbon isotope ratios in evolved stars of the open clusters NGC 2324, NGC 2477, and NGC 3960". In: 595, A16, A16. DOI: 10.1051/0004-6361/201629273. arXiv: 1608.08398 [astro-ph.GA].

Telting, J. H. et al. (Jan. 2014). "FIES: The high-resolution Fiber-fed Echelle Spectrograph at the Nordic Optical Telescope". In: *Astronomische Nachrichten* 335.1, p. 41. DOI: 10.1002/asna.201312007.

Teyssier, R. (Apr. 2002). "Cosmological hydrodynamics with adaptive mesh refinement. A new high resolution code called RAMSES". In: 385, pp. 337–364. DOI: 10.1051/0004-6361:20011817. arXiv: astro-ph/0111367 [astro-ph].

Thorsbro, B. et al. (May 2020). "Detailed Abundances in the Galactic Center: Evidence of a Metal-rich Alpha-enhanced Stellar Population". In: 894.1, 26, p. 26. DOI: 10.3847/1538-4357/ab8226. arXiv: 2003.11085 [astro-ph.GA].

Toomre, A. (May 1964). "On the gravitational stability of a disk of stars." In: 139, pp. 1217–1238. DOI: 10.1086/147861.

Toomre, Alar and Juri Toomre (Dec. 1972). "Galactic Bridges and Tails". In: 178, pp. 623–666. DOI: 10.1086/151823.

Trager, S. C. et al. (Apr. 2000). "The Stellar Population Histories of Local Early-Type Galaxies. I. Population Parameters". In: 119.4, pp. 1645–1676. DOI: 10.1086/301299. arXiv: astro-ph/0001072 [astro-ph].

Tremaine, S. D., J. P. Ostriker, and Jr. Spitzer L. (Mar. 1975). "The formation of the nuclei of galaxies. I. M31." In: 196, pp. 407–411. DOI: 10.1086/153422.

Tress, Robin G. et al. (Dec. 2020). "Simulations of the Milky Way's central molecular zone - I. Gas dynamics". In: 499.3, pp. 4455–4478. DOI: 10.1093/mnras/staa3120. arXiv: 2004.06724 [astro-ph.GA].

Trujillo, I. et al. (Apr. 2004). "Evidence for a New Elliptical-Galaxy Paradigm: Sérsic and Core Galaxies". In: 127.4, pp. 1917–1942. DOI: 10.1086/382712. arXiv: astro-ph/0403659 [astro-ph].

Tsatsi, Athanasia et al. (Jan. 2017a). "On the rotation of nuclear star clusters formed by cluster inspirals". In: 464.3, pp. 3720–3727. DOI: 10.1093/mnras/stw2593. arXiv: 1610.01162 [astro-ph.GA].

— (Jan. 2017b). "On the rotation of nuclear star clusters formed by cluster inspirals". In: 464.3, pp. 3720–3727. DOI: 10.1093/mnras/stw2593. arXiv: 1610.01162 [astro-ph.GA].

Valenti, E. et al. (Nov. 2013). "Stellar ages through the corners of the boxy bulge". In: 559, A98, A98. DOI: 10.1051/0004-6361/201321962. arXiv: 1309.4570 [astro-ph.GA].

Valenti, J. A. and N. Piskunov (Sept. 1996a). "Spectroscopy made easy: A new tool for fitting observations with synthetic spectra." In: 118, pp. 595–603.

— (Sept. 1996b). "Spectroscopy made easy: A new tool for fitting observations with synthetic spectra." In: 118, pp. 595–603.

Valluri, Monica and David Merritt (Oct. 1998). "Regular and Chaotic Dynamics of Triaxial Stellar Systems". In: 506.2, pp. 686–711. DOI: 10.1086/306269.

Valluri, Monica et al. (Mar. 2010). "The orbital evolution induced by baryonic condensation in triaxial haloes". In: 403.1, pp. 525–544. DOI: 10.1111/j.1365-2966.2009.16192.x.

Valluri, Monica et al. (Jan. 2012). "Probing the shape and history of the Milky Way halo with orbital spectral analysis". In: 419.3, pp. 1951–1969. DOI: 10.1111/j.1365-2966.2011.19853.x.

Valluri, Monica et al. (Feb. 2016). "A Unified Framework for the Orbital Structure of Bars and Triaxial Ellipsoids". In: 818.2, 141, p. 141. DOI: 10.3847/0004-637X/818/2/141. arXiv: 1512.03467 [astro-ph.GA].

van Albada, T. S., C. G. Kotanyi, and M. Schwarzschild (Jan. 1982). "A model for elliptical radio galaxies with dust lanes." In: 198, pp. 303–310. DOI: 10.1093/mnras/198.2.303.

van der Marel, Roeland P. et al. (July 2012). "The M31 Velocity Vector. II. Radial Orbit toward the Milky Way and Implied Local Group Mass". In: 753.1, 8, p. 8. DOI: 10.1088/0004-637X/753/1/8. arXiv: 1205.6864 [astro-ph.GA].

van Dokkum, Pieter G. et al. (July 2013). "The Assembly of Milky-Way-like Galaxies Since z ~2.5". In: 771.2, L35, p. L35. DOI: 10.1088/2041-8205/771/2/L35. arXiv: 1304.2391 [astro-ph.CO].

van Donkelaar, Floor et al. (Apr. 2024). "Stellar cluster formation in a Milky Way-sized galaxy at z > 4 - II. A hybrid formation scenario for the nuclear star cluster and its connection to the nuclear stellar ring". In: 529.4, pp. 4104–4116. DOI: 10.1093/mnras/stae804. arXiv: 2303.12828 [astro-ph.GA].

Vasiliev, Eugene (Oct. 2013). "A new code for orbit analysis and Schwarzschild modelling of triaxial stellar systems". In: 434.4, pp. 3174–3195. DOI: 10.1093/mnras/stt1235. arXiv: 1307.8116 [astro-ph.GA].

— (Dec. 2014). "Rates of capture of stars by supermassive black holes in non-spherical galactic nuclei". In: *Classical and Quantum Gravity* 31.24, 244002, p. 244002. DOI: 10.1088/0264-9381/31/24/244002. arXiv: 1411.1760 [astro-ph.GA].

— (Jan. 2019). "AGAMA: action-based galaxy modelling architecture". In: 482.2, pp. 1525–1544. DOI: 10.1093/mnras/sty2672. arXiv: 1802.08239 [astro-ph.GA].

Wallace, L. and W. Livingston (2003). *An atlas of the solar spectrum in the infrared from 1850 to 9000 cm-1 (1.1 to 5.4 micrometer)*.

Wang, Weisong et al. (July 2010). "Manufacturing of silicon immersion gratings for infrared spectrometers". In: *Modern Technologies in Space- and Ground-based Telescopes and Instrumentation*. Ed. by Eli Atad-Ettedgui and Dietrich Lemke. Vol. 7739. Society of Photo-Optical Instrumentation Engineers (SPIE) Conference Series, 77394L, p. 77394L. DOI: 10.1117/12.857164.

Wegg, C. and O. Gerhard (Dec. 2013). "The Milky Way's Box/Peanut Bulge: Measuring its Three-dimensional Structure Using the VVV Survey". In: *The Messenger* 154, pp. 54–56.

Wegg, Christopher and Ortwin Gerhard (Nov. 2013). "Mapping the three-dimensional density of the Galactic bulge with VVV red clump stars". In: 435.3, pp. 1874–1887. DOI: 10.1093/mnras/stt1376. arXiv: 1308.0593 [astro-ph.GA].

Wegg, Christopher, Ortwin Gerhard, and Matthieu Portail (July 2015). "The structure of the Milky Way's bar outside the bulge". In: 450.4, pp. 4050–4069. DOI: 10.1093/mnras/stv745. arXiv: 1504.01401 [astro-ph.GA].

Weiland, J. L. et al. (Apr. 1994). "COBE Diffuse Background Experiment Observations of the Galactic Bulge". In: 425, p. L81. DOI: 10.1086/187315.

Weinberg, M. D. (Mar. 1985). "Evolution of barred galaxies by dynamical friction." In: 213, pp. 451–471. DOI: 10.1093/mnras/213.3.451.

Wylie, Shola M., Jonathan P. Clarke, and Ortwin E. Gerhard (Mar. 2022). "The Milky Way's middle-aged inner ring". In: 659, A80, A80. DOI: 10.1051/0004-6361/202142343. arXiv: 2110.03658 [astro-ph.GA].

Xiang, Maosheng and Hans-Walter Rix (Mar. 2022). "A time-resolved picture of our Milky Way's early formation history". In: 603.7902, pp. 599–603. DOI: 10.1038/s41586-022-04496-5. arXiv: 2203.12110 [astro-ph.GA].

Yavetz, Tomer D. et al. (Sept. 2023). "Stream Fanning and Bifurcations: Observable Signatures of Resonances in Stellar Stream Morphology". In: 954.2, 215, p. 215. DOI: 10.3847/1538-4357/ace7b9. arXiv: 2212.11006 [astro-ph.GA].

Yuk, In-Soo et al. (July 2010). "Preliminary design of IGRINS (Immersion GRating INfrared Spectrograph)". In: *Ground-based and Airborne Instrumentation for Astronomy III*. Ed. by Ian S. McLean, Suzanne K. Ramsay, and Hideki Takami. Vol. 7735. Society of Photo-Optical Instrumentation Engineers (SPIE) Conference Series, 77351M, p. 77351M. DOI: 10.1117/12.856864.

Zasov, Anatoly V. and A. V. Moiseev (Jan. 1999). "Nuclear kpc-sized Disks of Spiral Galaxies". In: *Activity in Galaxies and Related Phenomena*. Ed. by Y. Terzian, E. Khachikian, and D. Weedman. Vol. 194, p. 279. DOI: 10.48550/arXiv.astro-ph/9812121. arXiv: astro-ph/9812121 [astro-ph].

Zasowski, G. et al. (Jan. 2019). "APOGEE DR14/DR15 Abundances in the Inner Milky Way". In: 870.2, 138, p. 138. DOI: 10.3847/1538-4357/aaeff4. arXiv: 1811.01097 [astro-ph.GA].

Zhao, Hongsheng, David N. Spergel, and R. Michael Rich (Dec. 1994). "Signature of Bulge Triaxiality From Kinematics in Baade's Window". In: 108, p. 2154. DOI: 10.1086/117227. arXiv: astro-ph/9409024 [astro-ph].

Zoccali, M. et al. (Mar. 2003). "Age and metallicity distribution of the Galactic bulge from extensive optical and near-IR stellar photometry". In: 399, pp. 931–956. DOI: 10.1051/0004-6361:20021604. arXiv: astro-ph/0210660 [astro-ph].

Zoccali, M. et al. (Jan. 2008). "Chemical abundances in the Galactic bulge". In: 79, p. 503.

Zoccali, M. et al. (Feb. 2014). "The GIRAFFE Inner Bulge Survey (GIBS). I. Survey description and a kinematical map of the Milky Way bulge". In: 562, A66, A66. DOI: 10.1051/0004-6361/201323120. arXiv: 1401.4878 [astro-ph.GA].

Zoccali, M. et al. (Mar. 2017). "The GIRAFFE Inner Bulge Survey (GIBS). III. Metallicity distributions and kinematics of 26 Galactic bulge fields". In: 599, A12, A12. DOI: 10.1051/0004-6361/201629805. arXiv: 1610.09174 [astro-ph.GA].

Zoccali, M. et al. (Apr. 2024). "Observed kinematics of the Milky Way nuclear stellar disk region". In: 684, A214, A214. DOI: 10.1051/0004-6361/202347923. arXiv: 2402.16800 [astro-ph.GA].